Anthracycline Analogs that Target Abasic Sites in DNA

By

Joshua M. Elder

Dissertation

Submitted to the Faculty of the

Graduate School of Vanderbilt University

in partial fulfillment of the requirements

for the degree of

DOCTOR OF PHILOSOPHY

In

Chemistry

December 17, 2022

Nashville, Tennessee

Approved:

Carmelo Rizzo, Ph.D.

Michael Stone, Ph.D.

Gary Sulikowski, Ph.D.

Martin Egli, Ph.D.

To my fiancée Cleo Evans, without whose love and support I never could have completed this program. I cannot wait to spend our lives together.

ACKNOWLEDGEMENTS

This dissertation would not have been possible without the support of many people. Firstly, I would like to thank Dr. Carmelo Rizzo for his support and guidance throughout graduate school, especially in the first year. I always felt as though I had someone watching out for my best interest in the department, both personally and professionally. His guidance on this project, support through difficult times, and his professional camaraderie have made my graduate school experience that much better; I feel very lucky to have gotten to work in his lab. He has helped shape me into the scientist that I am today, and for that I owe him plenty. I'm especially grateful for him letting me use his office to sleep in during overnight HPLC experiments!

I next would like to thank my committee members – Drs. Michael Stone, Gary Sulikowski, and Martin Egli – on their guidance and input throughout these past years. Dr. Stone's office door almost always was open if I needed to come by and ask questions or talk. Dr. Sulikowski's course on organic reactions remains to this day one of the more interesting classes I have taken. Lastly, Dr. Egli has been a constant in my time at Vanderbilt, as he always was available during PPG meetings for questions regarding many aspects of my project.

It is important that I acknowledge each and every member of the Rizzo lab, past and present, during my time at Vanderbilt. Firstly, I would like to thank Dr. Francesca Gruppi for getting me set up in the lab all those years ago. Her help teaching me to use the HPLCs made the entirety of the kinetic experiments possible. Next, I would like to thank Ben Sexton. Ben was my first mentee in the lab. I genuinely enjoyed our time working together, exchanging "witty" banter, and bouncing ideas off each other. I know he will continue to go on to do great things, even if he ended up going to the University of Voldemort. Hongkai (Bruce) Wang, my second mentee, contributed greatly to the outcome of this project. Much of the legwork with the syntheses was done by him. His dedication to the project made all of the kinetic experiments possible, and I could not have done all of this work without his help. I wish him the best of luck at graduate school, even if he and Ben together acted like the little children I never had.

Dr. Arjun Kafle's time in the lab, although relatively short so far, has been a great joy of my final year at Vanderbilt. His smile is contagious, his attitude about chemistry is infectious, and I have come to consider him a friend. His advice with some synthetic steps made the final deprotection possible; I owe him a lot! Dr. Jotirling Mali also helped me a lot along the way. After the pandemic, when it mostly was just us two in lab during rotations, his guidance and advice helped me kick some of the research quality up a notch. I had the pleasure of bringing him and his wife home from the hospital with their newborn baby, and that's a memory I'll get to keep for a while! I'm saddened to see him return to India, and I hope he and his family will keep in touch! Lastly in the Rizzo lab, I would like to thank John Terrell. My entire time at Vanderbilt, John has been a constant on whom I always could rely. Being the only two graduate students in the lab, he and I have spent many a weekend together in that HPLC room chatting while we work. Additionally, his insight on the chemistry helped get the groundwork set for me to come into lab and take over that part of the project. He is a good man, and I'm lucky to have gotten to work with him.

The trajectory of my career always felt concrete, but it has not been until recently (after I started my teaching job) that I realized how tenuous it was at any given time. But it was a path I walked proudly as it was laid before me. For that, I would like to thank Mrs. Heather Hernandez for her mentorship and guidance since my time away from Highland Park High School. She is a big reason I got into Chemistry and my aspiration as a high school teacher. Even if she makes me call her Heather now, I will always think of her first as Mrs. Hernandez as she deserves as much respect as I can muster. I also would like to thank Professors Catherine Oertel, Robert Thompson, Albert Matlin, Michael Nee, and Cortland Hill at Oberlin College for the many opportunities they provided me to hone my Chemistry craft, both in the lab and in the classroom. Lastly, I would like to thank the administration and science department at Nolensville High School. They all have welcomed me with such open arms and have been understanding about my finishing this program *while* taking night classes *while* teaching full time. Namely, I would like to thank Teresa Poole, Rebekah Groves, and Chris Ladd for their help, mentorship, and picking up some of my slack during the final weeks of my writing this dissertation.

There are many people to thank outside of lab and class, as well. Firstly, I would like to thank my cohort at Vanderbilt for the many great times we have had. Namely, I would like to acknowledge Dr. Katie Almasy, Dr. Micaella Jorge, Dr. Cal Larson, Danielle Penk, Dr. Johny Nguyen, and Shelby & CJ Chance for their friendship. Between food excursions, game nights, baseball games, movie watching, and so many memes, I know that I have made friends I will want to keep for as long as possible. I was nervous when moving to Nashville, so far from so many things I knew well. But their friendships have made my time outside of lab fun and enjoyable, and I'm glad they all are in my life now.

My close friends from childhood and Oberlin all deserve attention in their own right, but that would make this section longer than my dissertation. My OCMB and Oberlin science friends have been there when I have needed them, and I could not ask for anything more. So, thank you Dr. Lisa Learman, Dr. Andrea Goltz, Sammy Moores, Naviya Schuster-Little, Dr. Alex Sutherland, Emily Rizzo, and Ryan Walton. And thank you to everyone else in the OCMB for reminding me to always stay suave! My other Oberlin friends have been my surrogate family since I left Highland Park for college. Nick Music, Ellyn Butler, and Althea Levine are three of my all-time favorite people. Each of them has made me a better person having known them, and I love each of them more dearly than words can express.

Lastly of this crew, I would like to acknowledge Rebecca Flicher, Scott Beck, Max Schwartz, and Ben Lieberman for being living extensions of my soul. The four of them are four of the best friends for which I ever could have asked. I love each and every one of them for the support and camaraderie they have provided, even virtually. And, I love that we all can go a long time without seeing each other, but go back to being like no time has passed at all. I know I can count on them for anything, and I hope they know how much they mean to me.

In the way of family, I want to begin by acknowledging my in-laws. When Cleo and I began dating, I had never felt such strong love from people who never had met me. Each of them has accepted me and invited me into their family as if I was always one of their own. With that in-mind, I also would like to thank Sabbata, Grandma and Len, Uncle Ira and Aunt Laura, Uncle Ben and Aunt Rachel, Uncle Chuck and Aunt Leslie, and Aunt Beth and Uncle Paul for their love and support. And I love all my cousins who have made all the family gatherings so fun.

Noah and Eli are the two best brothers in the world. They are funny and make me smile both inside and out, even when they drive me crazy. The day I became your brother was the luckiest day of my life, and I love you guys for all your support and friendship. My parents deserve an entire dissertation for acknowledgments. I am overwhelmed simply by thinking about what to say to them through this acknowledgement. As such, all I can bring myself to say is, “Thank you.” Thank you for raising me to be the man I am today, the person you both knew I always could be (even when I did not). I love both of them intensely.

Lastly, I would like to acknowledge the dedicatee of the dissertation, my fiancée Cleo Evans. Cleo, you are the soul of this dissertation and my motivation to be the person you see in me. I will save most of what I have to say for our vows in March, but I hope you know that I love you more than anything and anyone else in the whole world (sorry Mom and Dad!). You are brilliant, cute, funny, and the best possible person out there for me. I owe you everything, and I hope this dissertation in your honor is the start of that.

TABLE OF CONTENTS

APPENDIX

LIST OF FIGURES

LIST OF TABLES

Page

LIST OF EQUATIONS

Page

LIST OF ABBREVIATIONS

[substance]	Concentration of "substance"
$[\text{substance}]_{\text{eff}}$	Effective concentration of "substance"
˚C	Degress Celcius
±	Plus or minus
1,N^6-εA	1,N^6-Ethano-2'-deoxyadenosine
^{13}C	Carbon-13
^{1}H	Proton
3-meA	3-Methyl-2'-deoxyadenosine
3-meG	3-Methyl-2'-deoxyguanosine
3,N^4-εC	3,N^4-Ethano-2'-deoxycytosine
5-FU	5-Fluorouracil
5-hmU	5-Hydroxymethyl-2'-deoxyuracil
5-hoC	5-Hydroxy-2'-deoxycytosine
5-hoU	5-Hydroxy-2'-deoxyuracil
7-AFB-G	7-(Aflatoxin B1)-2'-deoxyguanosine
7-meG	7-Methyl-2'-deoxyguanosine
8-hoG	8-Hydroxy-2'-deoxyguanosine
8-oxoG	8-Oxo-2'-deoxyguanosine
A	Adenosine
Å	Angstrom(s)
A_{260}	Absorbance units at wavelength = 260 nm
AC	Adriamycin/cyclophosphamide
AD	*anno Domini*

ADP	Adenosine 5'-diphosphate
AIDS	Acquired immunodeficiency syndrome
AP	Abasic/apurinic/apyrimidinic
ApG	5'-dA-dG-3' DNA sequence
APmer	5'-GTTGC-AP-CGTATG-3'
Ar	Aromatic moiety
ATP	Adenosine 5'-triphosphate
ATPase	Adenosine 5'-triphosphatase
AV	Adriamycin/vincristine
BCG	Bacillus Calmette-Guérin
BER	Base excision repair
Boc	*tert*-Butyloxy carbonyl
Boc-AOAcOH	*N*-Boc-2-aminoxyacetic acid
br	Broad
C	Cytosine
CC-1065	5-hydroxy-2-[5-hydroxy-4-methoxy-2-(3-methyl-7-oxo-5,10-diazatetracyclo[7.4.0.01,12.02,6]trideca-2(6),3,8-triene-10-carbonyl)-7,8-dihydro-3*H*-pyrrolo[3,2-e]indole-6-carbonyl]-4-methoxy-7,8-dihydro-3*H*-pyrrolo[3,2-e]indole-6-carboxamide
CID	Collision-induced dissociation
cm	Centimeter(s)
CMF	Cyclophosphamide/methotrexate/5-fluorouracil
Coeff.	Coefficient
comp	5'-CATACGCGCAAC-3'
COPASI	Complex pathway simulator
COSY	Correlated spectroscopy

CPA	Cyclophosphamide
CpG	5'-dC-dG-3' DNA sequence
CSV	Comma-separated values
CT	Calf-thymus
CYP2B6	Cytochrome P450 enzyme 2B6
δ	Chemical shift for NMR
d	Doublet
dA	2'-Deoxyadenosine
DAU	Daunorubicin
DBF	Dibenzofulvene
dC	2'-Deoxycytosine
DCC	*N*,*N*'-Dicyclohexylcarbodiimide
dd	Doublet of doublets
dG	2'-Deoxyguanosine
DMF	*N,N*-Dimethylformamide
DMSO	Dimethylsulfoxide
DMSO-d_6	Deuterated DMSO
DNA	Deoxyribonucleic acid
DNAse	Deoxyribonuclease
Dnr S	Daunosamine glycosyltransferase
dN	2’-Deoxynucleoside
dNTP	2'-Deoxynucleoside triphosphate
DOX	Doxorubicin
DOXol	C^{13}-reduced doxorubicin
dR	2'-Deoxy-*D*-ribose

DS	Double-stranded
dT	2'-Deoxythymine
dTbpy	4,4'-Di-tert-butyl-2,2'-bipyridine
dU	2'Deoxyuracil
E	x 10^___
e.g.	*exempli gratia*
ε_{260}	Extinction coefficient at wavelength = 260 nm
EMCH	*N*-(e-maleimidocaproic acid) hydrazide
Eq.	Equation
ESI	Electrospray ionization
et al.	*et alia*
Et-	CH_3CH_2-
EtOAc	Ethyl acetate
Ext. Coeff.	Extinction coefficient
FAPy-G	N^6-(2-Deoxy-*D*-*erythro*-pentofuranosyl)-2,6-diamino-3,4-dihydro-4-oxo-N^5-formamidopyrimidine
FCC	Flash column chromatography
FDA	U.S. Food and Drug Administration
Fe^{2+}	Iron(II) ion
Fe^{3+}	Iron(III) ion
FEN1	Flap endonuclease 1
Fmoc	Fluorenylmethyloxy carbonyl
FPG	DNA-formamidopyrimidine glycosylase
G	Guanosine
G-HN1-G	Bis-(2-chloroethyl)ethylamine 2'-deoxyguanosine crosslink

G-HN2-G	Bis-(2-chloromethyl)ethylamine 2'-deoxyguanosine crosslink
GpC	5'-dG-dC-3' DNA sequence
GpG	5'-dG-dG-3' DNA sequence
H_2O	Water
H_2O_2	Hydrogen peroxide
HBTU	3-[Bis(dimethylamino)methyliumyl]-3*H*-benzotriazol-1-oxide hexafluorophosphate
HCl	Hydrochloric acid
HeLa	Henrietta Lacks
HEPES	4-(2-hydroxyethyl)-1-piperazineethanesulfonic acid
HMBC	Heteronuclear multiple bond correlation
HOBt	1-Hydroxybenzotriazole
HPLC	High performance liquid chromatography
hr	Hour(s)
HSQC	Heteronuclear single quantum coherence
Hx	2-Deoxy-*D*-*erythro*-pentafuranosyl-1,7-dihydro-*6H*-purin-6-one (Hypoxanthine)
Hz	Hertz
i.e.	*id est*
IP	Intraperitoneal
^iPr	$(CH_3)_2CH$-
IRP1	Iron regulatory protein 1
kg	Kilogram(s)
L	Liter(s)
LC	Liquid chromatography
LD_{50}	Median lethal dose

Lig I	DNA ligase I
LTQ	Linear trap quadrupole
m	Meter(s)
M	Molar
m/z	Mass to charge ratio
M_1G	2-Deoxy-D-erythro-pentafuranosyl-pyrimido[1,2-*a*]purin-10(*3H*)-one
MAR70	4'-Epi-4'-(2-deoxyfucose)daunomycin
Me-	CH_3-
MeCN	Acetonitrile
meFAPy-G	N^6-(2-Deoxy-*D*-*erythro*-pentofuranosyl)-2,6-diamino-3,4-dihydro-4-oxo-N^5-methylformamidopyrimidine
MEN 10755	4-Demethoxy-7-*O*-[2,6-dideoxy-4-*O*-(2,3,6-trideoxy-3- amino-a-*L*-*lyxo*-hexopyranosyl)-a-*L*-*lyxo*-hexopyranosyl]-adriamycinone
MeOH	Methanol
METC	Mitochondrial electron transport chain
mg	Milligram(s)
μg	Microgram(s)
Mg^{2+}	Magnesium ion
$MgCl_2$	Magnesium chloride
MHz	Megahertz
min	Minute(s)
mL	Milliliter(s)
μL	Microliter(s)
mM	Millimolar
μM	Micromolar

mm	Millimeter(s)
μm	Micrometer(s)
mmol	Millimole(s)
μmol	Micromole(s)
mRNA	Messenger ribonucleic acid
MS	Mass spectrometry
MS^2	MS-MS
MS^3	MS-MS-MS
MTX	Mitoxantrone
N^2-BP-G	N^2-(10*R*(+)-*trans*-*anti*-benzo[*a*]pyrene)-2'-deoxyguanosine
Na^+	Sodium ion
Na_2EDTA	Ethylenedinitrilotetraacetic acid disodium salt
NaCl	Sodium chloride
$NADP^+$	Nicotinamide adenine dinucleotide phosphate
NADPH	Reduced nicotinamide adenine dinucleotide phosphate
NCI	National Cancer Institute
NER	Nucleotide excision repair
ng	Nanogram(s)
NHS	*N*-Hydroxysuccinimide
NL	Total mass spectrometric ion count
nm	Nanometer(s)
NMR	Nuclear magnetic resonance
NOR	Nornitrogen mustard
O_2	Molecular oxygen
$O_2^{-\cdot}$	Superoxide radical

O^4-meT	O^4-Methyl-2'-deoxythymine
O^6-meG	O^6-Methyl-2'-deoxyguanosine
OH·	Hydroxide radical
OTf	Triflate
P	Phosphate
PCNA	Proliferating cell nuclear antigen
pD	Potential of deuterium
PGC1	Peroxisome proliferator-activated receptor-g coactivator 1
pH	Potential of hydrogen
Ph-	H_5C_6-
PM	Phosphoramide mustard
PMOA	*O*-(pyridin-3-yl-methyl)hydroxylamine
pol-β	DNA polymerase β
pol-δ	DNA polymerase δ
pol-ε	DNA polymerase ε
ppm	Parts per million
PXT	Pixantrone
PyBOP	(Benzotriazol-1-yloxy)tripyrrolidinophosphonium hexafluorophosphate
q	Quartet
R·	Hydrocarbon radical
R^2	Coefficient of determination
redox	Reduction-oxidation
RNA	Ribonucleic acid
ROS	Reactive oxygen species
RP	Reverse-phase

RPM	Rotations per minute
rt	Room temperature
s	Singlet
s.d.	Standard deviation
SAR	Structure-activity relationship
sec	Second(s)
S_NAr	Nucleophilic aromatic substitution
SPE	Solid-phase extraction
SS	Single-stranded
T	Thymine
t	Triplet
$t_{1/2}$	Half-life
^{t}Bu-	$(CH_3)_3C$-
td	Triplet of doublets
TEMPO	2,2,6,6-tetramethylpiperidine-1-oxyl radical
TFA	2,2,2-Trifluoroacetic acid
Tg	5,6–dihydroxy-5,6–dihydro-pyrimidine (Thymine glycol)
THF	Tetrahydrofuran
THFmer	5'-GTTGC-THF-CGTATG-3'
TLC	Thin layer chromatography
T_m	Thermal melting temperature
TMS	Trimethylsilyl
Top2	Topoisomerase II
TXT	Text document file
U	Uracil

UDG	Uracil DNA glycosylase
Umer	5'-GTTGC-U-CGTATG-3'
UPLC	Ultra performance liquid chromatography
UV	Ultraviolet
v/v	By volume
vis	Visible
vs.	Versus

CHAPTER 1: Introduction

Background

Cancers and the problems they pose have plagued this planet's inhabitants since the prehistoric era.[1] Population screening of dinosaur fragments by fluoroscopy and other radiologic surveying techniques has shown that various types of tumors existed in the vertebrae of *Cretaceous hadrosaurs*. Other studies prior to this discovery show scattered instances of tumors in other pre-Cenozoic species, such as osteoma in mosasaurs, and hemangioma and metastatic cancers in other dinosaurs.[2]

The first mention of human tumors dates to the Edwin Smith and George Ebers papyri of ancient Egypt. As Smith's artifact mentions, "…tumors with prominent head in his breast" must be treated by cauterization if formed from an injury, though it is grave if it comes from disease.[3–5] Since Ebers' acquisition of his papyrus in 1872, the document has been transliterated and translated as describing ways for preparing herbal and mystical medicines for different treatments.[6] Other evidence was found that further supported the ancient Egyptians' knowledge of tumors. Growths from the Ptolemaic era of ancient Egypt were found in a mummy. Digital radiography and tomography scans determined that these growths originated in the prostate and then distributed throughout the body.[1] Additionally, tumors found on a Siberian mummy of a Scythian king from the Iron Age were identified as terminal prostate carcinoma by scanning-electron microscopy and 1- and 2-D electrophoreses.[7] Starting with these examples, one can trace the history of cancer from ancient Greece and the Roman empire in Hippocrates' time to the Middle Ages, all the way to World War II. It was Hippocrates who first called these malignancies καρκίνος ("karkinos": crab), which later became "cancer" around 1600 AD.[5,8]

Reported instances of tumors increase with the chaos and complexity of civilization throughout history. By the end of the 1930s, cancer had become so prevalent that it finally was addressed on a national scale in the United States.[1] In 1937, President Roosevelt signed into law the National Cancer Act, which began a 40-year increase in cancer research by establishing the National Cancer Institute (NCI). The NCI's research amounted to little in the way of curing cancer during this time. President Nixon enacted the National Cancer Act of 1971, but only as a political tactic. His dislike of the Kennedy name prevented him signing it until Senator Edward Kennedy resigned his name from the bill. Despite being a political tactic by Nixon, this act did increase the money available to finance cancer research drastically; and, it started what has been known as the "War on Cancer."[9]

Cancer

Despite the failure of the War on Cancer to cure the disease, research has uncovered the true nature of cancer, as well as the biological processes by which it forms and affects the body.[10] Cancer occurs when abnormal cells grow uncontrollably. As the number of cells increases rapidly, they form lumps of tissue, called tumors, that wreak havoc on the organism. Tumors invade nearby tissue, wrap themselves within and around blood vessels, hijack immune responses to hide their presence, and even feed using other cells' nutrients. Not all tissue abrasions are cancer; however, those that are either can be malignant or benign. If a tumor is malignant, cells from the infected lump break away and spread throughout the body via blood vessels. These broken off cells can find a new home and multiply to create other tumors. This process is called metastasizing. Benign tumors are those that do not metastasize.[11]

The uncontrolled cellular growth of tumor cells is attributed to mutations in certain genes. Oncogenes are genes that promote cell growth. When this cell growth is controlled, the genes are referred to as proto-oncogenes. However, when these proto-oncogenes are mutated, cell growth is no longer controlled, leading to increased proliferation.[11,12] Tumor suppressor genes are the other main type of gene that is mutated in many types of cancer, the most commonly affected of which is called p53. Tumor suppressor genes signal apoptosis (i.e., programmed cell death), and help stabilize the cell cycle and genome. Specifically, p53 can activate DNA-repair proteins to fix malignant DNA damage during replication and initiate apoptosis if that damage is irreparable. If p53 is mutated, then the genes that it signals to initiate apoptosis are not activated, leading to excessive replication of the damaged cells.[13] Mutations to the proteins involved in apoptosis and in DNA-repair also are viewed as key to the proliferation of cancer cells.

DNA Damage: Sources and its Repair Mechanisms

Mutations, including the ones previously mentioned, arise from both endogenous and exogenous sources. Errors that occur in the division of cells, whether naturally or genetically, are examples of endogenous sources of DNA damage. For example, even if the genetic defects are not inherited, lifestyle choices like one's diet can create changes in bile acids, reactive oxygen species (ROSs), and other damaging agents. Exogenously, DNA damage can be caused by chemicals, smoking, UV radiation, and other things we are now taught to avoid as best we can.[11] If the DNA damage induced by any of these sources is not repaired, then the damages will accumulate in the cell, cause further mutations to occur, and eventually lead to formation of a tumor.

Regardless of the source, mutations caused by DNA damage can be categorized into oxidative, hydrolytic, or alkylative. Examples of these lesions are shown in Figure 1.1. When these damages occur, many downstream effects are observed. DNA replication is stalled, leading to cell death or a stop in the DNA biosynthetic process.[14] They also can create mispairings by mis-incorporating bases *during* replication. When these adducts form, hydrolysis may occur, which can lead directly to strand cleavage.[15]

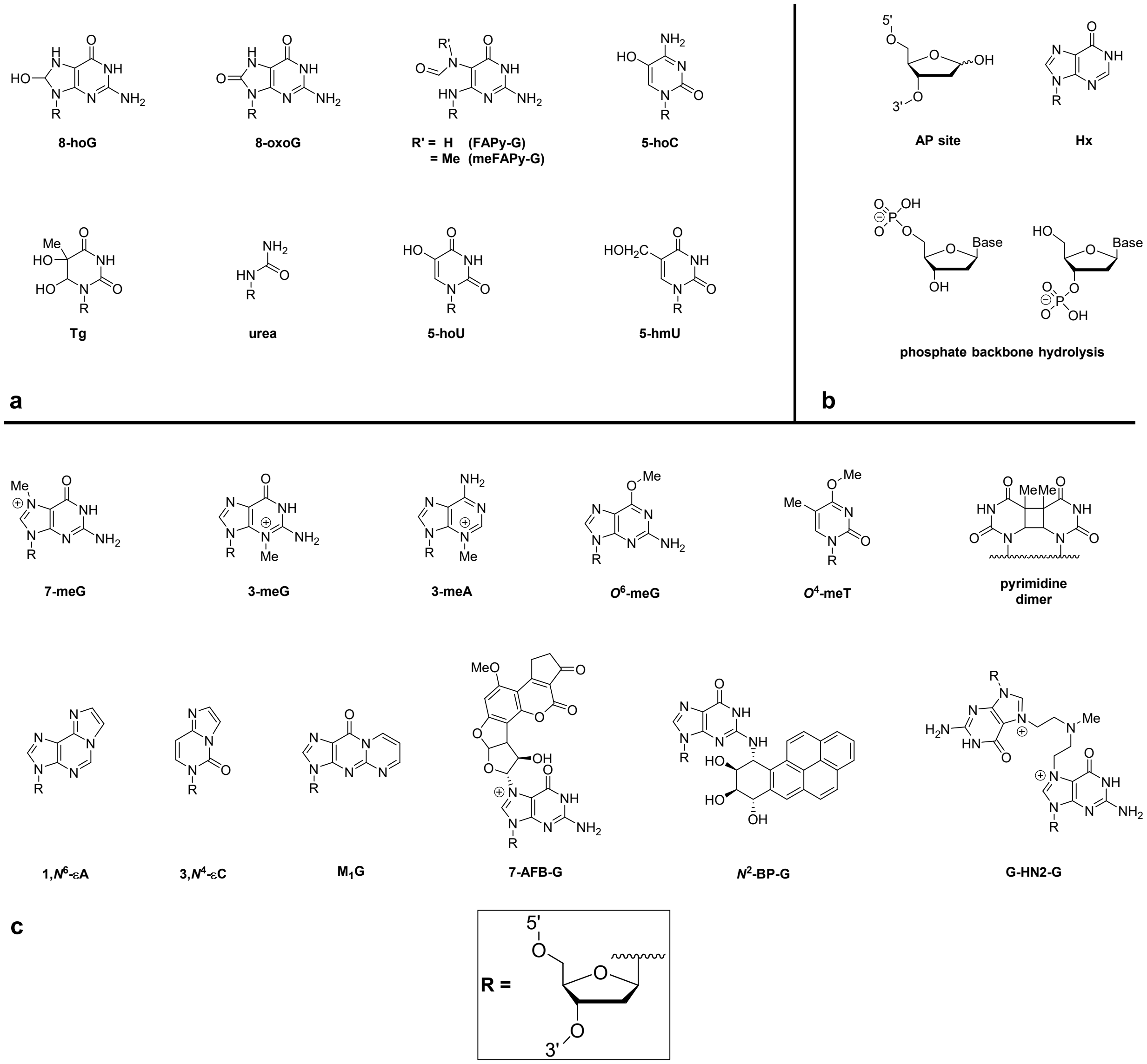

Figure 1.1: Examples of kinds of DNA damage. a) Oxidative; b) Hydrolytic; c) Alkylative

Oxidation can occur from radiation, metabolic byproducts that create hydroxyl and superoxide radicals, or radicals formed in the mitochondria and endoplasmic reticulum.[16] These ROSs can cause damage by forming covalent links with nucleobases; or, they can take part in the metabolism of other carcinogens to form more reactive, electrophilic compounds that react with DNA. Oxidative adducts are the most commonly seen lesion in mammalian cells.[17]

Hydrolytic damage typically occurs either at the glycosidic bond of a nucleotide or at the phosphodiester backbone of the double helix. Hydrolysis of the backbone results in strand cleavage, whereas the former creates an abasic/apyrimidinic (AP) site. This type of lesion can occur spontaneously, or by the deglycosylation of damaged DNA bases.[18] AP sites are another common lesion in mammalian cells, matching oxidative damage in occurrence with great toxicity.[19] This specific lesion is essential to understanding the work in this dissertation; thus, the toxicity of AP sites will be explored in greater detail in later sections.

Metabolic oxidation is not the only way electrophiles are introduced into cells; some carcinogens are naturally electrophilic.[20] These electrophilic hydrocarbons are capable of reacting with nucleophilic sites on DNA to form adducts. The most commonly adducted site on DNA is the N^7-position of dG, followed by the N^3-positions of dG and dA.[15] When the N^7-position of dG is alkylated, many reactions can occur to make up for the decrease in electron density around the ring system. Namely, these reactions are (1) loss of the C^8 proton, (2) depurination, (3) formation of a FAPy-G lesion (see Figure 1.1), (4) decomposition of the guanine residue, and (5) rearrangement to form C^8 adducts.[21]

Once its genome is damaged, a cell will either mutate, or it will activate one of its innate mechanisms to fix it. The cell can initiate different repair pathways depending on the specific type of damage. These responses include direct reversal of base damage; excision of damaged, mispaired, or even correct bases; strand break repair; interstrand crosslink repair; and, tolerance of base damage. Each of these responses to DNA damage deserve further attention and understanding; however, as they can result in deglycosylation of a damaged base, the focus of this overview will be the excision of said bases.

When a nucleobase is damaged, mutated, or mispaired, there are multiple pathways the cell can activate to excise the lesion. When DNA replicates, errors often occur in the daughter strand. Some errors include the addition of an extra nucleotide, the absence of a necessary nucleotide, strands “slipping” while they are in the process of being repaired, or the incorporation of an incorrect nucleotide.[22,23] Enzymes are called to the DNA strand in these instances to locate and isolate the mismatch, create and excise a nick in the daughter strand, and resynthesize the nicked portion.[23]

When a lesion is bulky and causes significant structural distortion, the DNA undergoes nucleotide excision repair (NER). There is a wide variety of structurally unrelated lesions that may require this repair pathway. Some of these include UV damage, mutations from tobacco smoke, pyrimidine dimers, and bulky crosslinks. This mechanism requires over 30 enzymes in humans; and, although complex, much of this mechanism has been elucidated over the past 100 years.[24] The NER pathway starts with the assembly of a multi-protein machine. Then, the proteins recognize and verify the damage and remove a 24-32 nucleotide segment of DNA containing the bulky lesion. The gap caused by the excision of nucleotides is re-synthesized using the opposite strand as a template.[25]

The most common pathway employed in the excision of small modifications to nucleobases is base excision repair (BER). This mechanism targets lesions that occur from oxidation (e.g., 8-oxoG), sterically small alkylations (e.g., 3-meA), and even some bases that are unmodified but do not belong in a DNA strand (e.g., dU). The BER pathway is split into two overall steps: removal of the damaged base, and base replacement. The actual mechanism of these two steps depends heavily on the type of lesion being excised and, therefore, the DNA glycosylase needed. Briefly put, if the glycosylase enzyme is a hydrolase, then it is considered "monofunctional." If the enzyme uses an active site amine instead of water to excise the base, then it is considered "bifunctional."

A monofunctional glycosylase will hydrolyze the lesion at the deoxyribose anomeric carbon, excising the base from the sugar and leaving behind an AP site. The toxic AP site is cleaved hydrolytically from the 5'-DNA strand by AP endonuclease,[26,27] followed by β-elimination from the 3'-DNA strand. The remaining strands act as a template for pol-β to replace the missing dN,[28] which is re-ligated to afford the undamaged strand.[29] Bifunctional glycosylases behave similarly; however, instead of hydrolysis, an amine in the active site cleaves the base, forms a Schiff base with the sugar backbone,[30] and induces β- or β,δ-elimination to afford the strand-scission products that are substrates for polymerase and ligase enzymes (Figure 1.2). While the complete mechanisms of these BER pathways are much more complex,[31] the overall

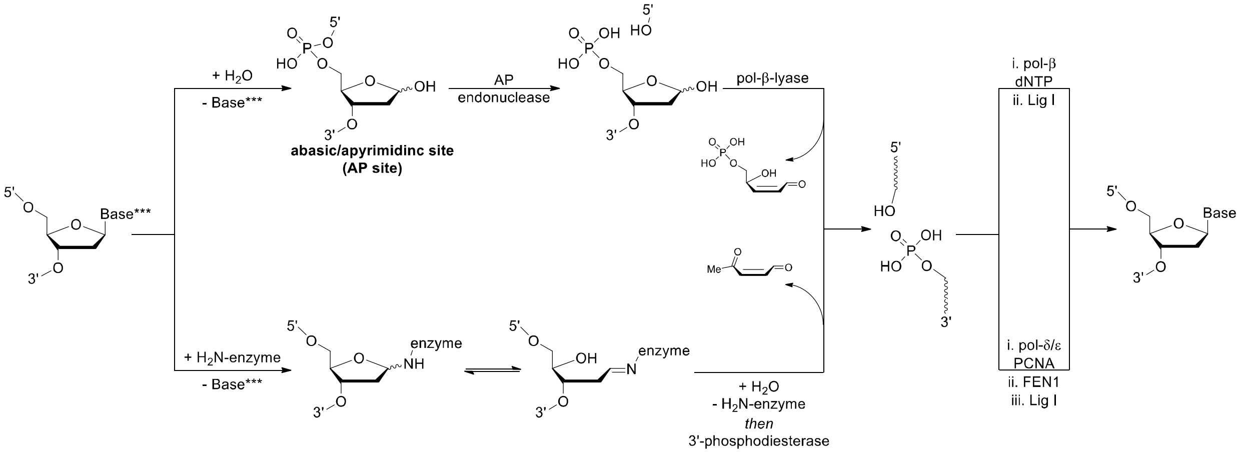

Figure 1.2: Summarized mechanism of the two pathways of BER. The top is with a monofunctional glycosylase, and the bottom is with a bifunctional glycosylase. Adapted from Figure 1 of Stivers & Jiang.[29]

idea behind this excision pathway is the removal of a damaged base, and sometimes a few of the surrounding bases, too, followed by replacement of undamaged bases.[29]

Anti-Cancer Regimens

While our cells have processes in place to repair damage to DNA, some damage evades these mechanisms. In some instances, tumors form, requiring therapeutic intervention. As our knowledge of how cancer proliferates and harms us has increased, so too has the number of options regarding how it is treated. While the Smith and Ebers papyri only mention options such as surgeries,[3,4,6] non-surgical options have become much more common. Some of these options are radiation, hormonal, and targeted immunotherapies, as well as chemotherapy. These options are used either alone or in conjunction with surgery.

Beginning with the discovery that radiation could cure head and neck cancers in 1928, radiotherapy has become a popular form of a treatment and is used commonly to treat solid tumors. In 1950, cobalt teletherapy began the modern era of radiation therapy.[10] In this form of cancer therapy, the DNA of cancerous cells is damaged with ionizing radiation, either directly from charged particles or indirectly by free hydroxyl radicals generated by high energy photons reacting with water. When the DNA damage is irreparable, the cell will stop dividing and die.

Radiotherapies are categorized as either internal or external. Internal radiation therapy involves treatment using sources of radiation. When that source is a solid instead of a liquid, it commonly is referred to as brachytherapy. In this treatment, the radioactive isotope is implanted near the tumor and gives off radiation over a longer period. The more commonly used radiative technique is external radiation therapy. In this technique, a machine aims radiation at the area affected by cancer from outside the body. As it is outside the patient, the radiation source can be positioned to attack the tumor from different angles. However, because radiation cannot differentiate healthy cells from cancerous ones, there is a limit to the amount of radiation a patient can receive over the course of their lifetime.[32]

Hormonal therapy is another common cancer treatment. This regimen utilizes steroid-based therapeutics to target the endocrine system. These therapeutics could be the hormone, itself, or an antagonist of said hormone. The latter is used as a means of inhibiting the hormone or affecting how the hormone behaves in the body.[33] Antagonists to hormones necessary for cell growth and gene expression in cancer cells lead to a suppression in tumor growth or even cell death. By the late-1890s, estrogen had been observed to have an effect on breast cancer,[34] and reports of estrogen-based hormonal therapy for prostate cancer in men date back to the late-1930s/early-1940s.[35] More recently, aromatase inhibitors were developed as a breast cancer treatment in postmenopausal women. Aromatase is a key enzyme in the biosynthesis of estrogen; so, starving estrogen-dependent cancer cells of this enzyme is desirable in oncological practices.[36]

Another method of treating tumors is by taking advantage of immune responses already present in the body. As previously mentioned, malignant cells are capable of hijacking many of these processes. Immunotherapy for cancer focuses on blocking or reversing those immune-escape mechanisms that allow cancer cells to evade notice from the body's forces that seek to destroy them. The regulation of the activation of T lymphocytes, a type of white blood cell, and their effects is the product of numerous co-stimulatory and inhibitory molecules designed to control immune responses at numerous "checkpoints" throughout the body.[37] These checkpoints act as suppressors for the immune system to prevent responses that are too strong. Some immunotherapy drugs inhibit these checkpoints to allow the immune system to "go wild" when fighting cancer. Other strategies employed in immunotherapy are the enhancing of T-cell proliferation *in vitro*, treatment vaccines, immune system modulators, and monoclonal antibody treatment to make cancer cells more visible to immune responses.[38,39]

Lastly, chemotherapy is a regimen that uses anti-cancer drugs to combat the malignancy or, at the very least, treat the symptoms in a palliative approach. While hormonal therapy and immunotherapy are technically a type of chemotherapy, a chemotherapeutic approach to treating cancer, palliative or curative, does not need a specific target, such as a specific biomolecule or gene. A deeper discussion of chemotherapy in general is warranted as this dissertation provides the results of research conducted towards the synthetic modification of some chemotherapeutics.

Chemotherapy

With his theory of targeted drug therapy and his use of chemicals to treat diseases, Paul Ehrlich is considered the creator of chemotherapy. In fact, it was he who coined the term in the early-1900s.[40] His "magic bullet" concept came from using German dyes to map receptors of invading parasites that are not shared by the host.[41] In 1908, these strategies led to the discovery that organoarsenic compounds could treat syphilis in rabbit models. By World War I, Ehrlich's ideas had inspired Alexander Flemming in his discovery that penicillin worked as a strong bacterial chemotherapeutic. Alas, even Ehrlich saw the application of chemotherapy to fighting cancer as a hopeless cause;[40,41] the idea of targeting cancer cells while avoiding healthy cells is still a challenge in much of the current chemotherapy research.

The first report of anti-cancer drugs working in a human are those from the end of World War II involving mustard gas and other nitrogen mustards to treat a number of malignancies.[1,40,42] This discovery led to a burst in alkylative compounds being tested as chemotherapeutics. Another World War II-related program followed Flemming's work with penicillin to examine its and other antibiotics' effects on wound infections. From this research came the discovery in 1959 that the antibiotic actinomycin D had significant antitumor properties,[43] beginning the surge of antitumor antibiotic use clinically. Many of these antibiotics still are used today.[40]

While the complete history of chemotherapy goes far beyond what is discussed in this dissertation, the key points from this overview lend themselves to a further discussion of commonly used metal- and nonmetal-based chemotherapies. As such, the following section is devoted to exploring the use of cisplatin and the adjuvant combination regimen referred to as "AC Chemotherapy."

Cisplatin first was synthesized with a fully elucidated structure by 1893. However, its antitumor properties were not discovered until much later.[44] In 1965, while exploring the effect of electric fields on bacterial growth, Rosenberg *et al.* found that electrolysis products of group VIIIb transition metals inhibited the cellular division process. These electrolysis products came from the electrodes in their experimental apparatus, and they found that the inhibition occurred at metal concentrations from 1-10 ppm. The focus on platinum-based chemotherapeutics came from their discovery that platinum compounds, like cisplatin, were responsible for the results.[45]

Most commonly, cisplatin is used for the treatment of testicular cancers, as well as ovarian, cervical, head, neck, and non-small-cell lung cancers. When cisplatin enters a cell, the chloride ions are replaced by loosely-bound water molecules. The water ligands of this new platinum complex are displaced by nucleophilic biomolecules, such as DNA.[46,47] The major cisplatin-DNA adducts are 1,2-intrastrand crosslinks within GpG or ApG sequences, with a smaller percentage represented by 1,3-intrastrand crosslinks between non-adjacent dG nucleotides, and an even smaller amount of interstrand crosslinking. In all cases, the metallic complex formed at the N^7-positions of the purine bases.[48] As previously noted, these adducts can block cellular division and induce apoptosis. However, while these DNA adducts are considered large contributors to cisplatin's cytotoxicity, platinum-based drugs, like those shown in Figure 1.3, also have been shown to induce oxidative stress and disrupt cellular function through changes in calcium homeostasis, formation of DNA-protein crosslinks, and many other mechanisms of cellular damage.[44,46]

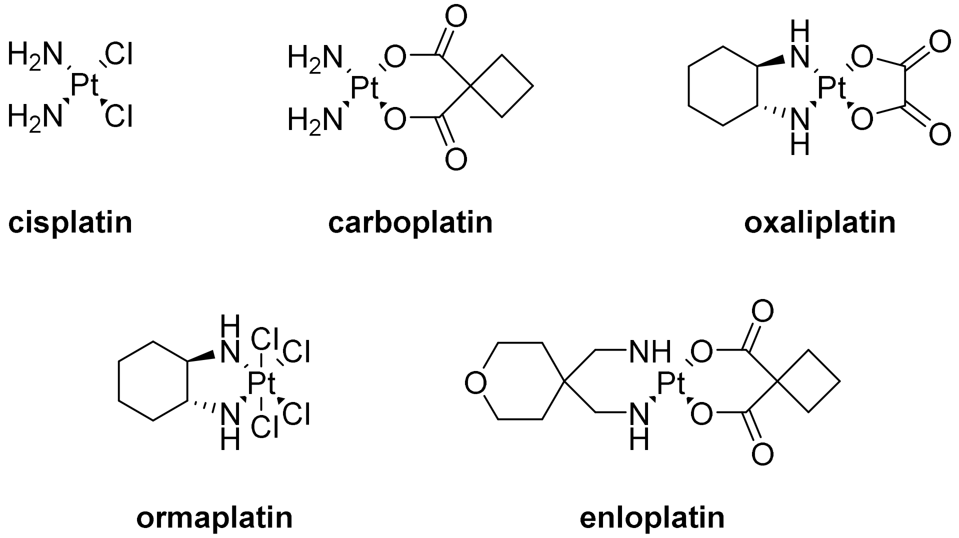

cisplatin **carboplatin** **oxaliplatin**

ormaplatin **enloplatin**

Figure 1.3: Examples of platinum-based chemotherapeutics

Although cisplatin is used to combat many different types of cancer, it cannot be used as the only drug for *all* cancers. There exist many kinds of tumors that are cisplatin-resistant. Some proposed mechanisms-of-resistance include changes in cisplatin influx and efflux, increased detoxification systems, and an increase in DNA repair pathway efficiency, namely that of NER.[46,49] Because of these cisplatin-resistant diseases, cisplatin often is used in combination with other, nonmetal-based chemotherapeutics. A review of the different drugs with which cisplatin typically is paired can be found in Dasari & Tchounwou.[44]

This strategy of treating with multiple drugs to circumvent any drug resistance has been applied to chemotherapy since 1965. It was discovered that cotreatment of methotrexate, 6-mercaptopurine, vincristine, and prednisone significantly reduced the tumor load and increased remission of acute lymphocytic leukemia in children.[50] This technique, dubbed "combination therapy," focuses on eliciting either synergistic or additive effects from drugs that function via different pathways.[51]

When combination therapy is used to augment the effects of an initial treatment, the regimen is dubbed "adjuvant." One of the most common adjuvant combination therapies for stage II and stage III breast cancers is Adriamycin/Cyclophosphamide (AC) chemotherapy. A further exploration of the drugs involved in this combination therapy regimen follows.

Adriamycin/Cyclophosphamide Chemotherapy

While combination therapies have been employed in chemotherapy regimens since 1965,[50] the first report of an adjuvant combination treatment came in the 1970s. This regimen,

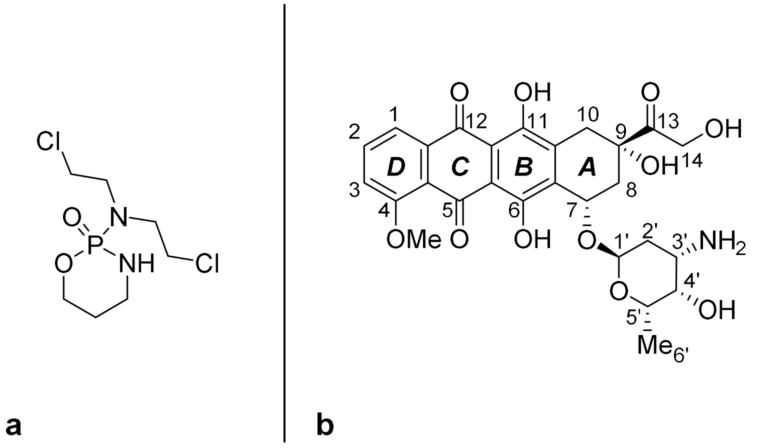

Figure 1.4: Structures of the drugs included in AC chemotherapy. a) Cyclophosphamide (CPA); b) Doxorubicin (DOX), with traditional ring and number assignments

often referred to as "CMF," included cyclophosphamide (CPA) (Figure 1.4a), methotrexate, and fluorouracil (5-FU) as an adjuvant to mastectomies.[52] Even though the study was developed by the National Cancer Institute, most cancer centers in the United States were not willing to try combination therapy as an adjuvant at that time. This changed very quickly after cancer centers in Milan reported positive results from the treatment.[10]

Because of its success and popularity in single-agent chemotherapeutic regimens, doxorubicin (DOX) (Figure 1.4b), usually called Adriamycin, was included in many combination regimens studied thereafter. One example of these regimens is treatment with 5-FU, DOX, CPA, and a vaccine for tuberculosis called "BCG vaccine." This treatment increased the survival rate in patients with stage II and III breast cancer regardless of menopausal status and, in cases of recurrence, prolonged the time it took for the disease to return.[53] Another example from the same time period is that of DOX and vincristine (AV), which showed comparable levels of remission as CMF. In fact, treatment with CMF *after* eight cycles of AV chemotherapy doubled the rate of complete remission in patients with advanced breast cancer to approximately 16%.[54] This treatment also benefitted from the addition of CPA to its regimen, which raised the complete response rate to 28% with a *total* response rate of 72%.[55,56]

Many of the adjuvants studied during this time included DOX and CPA. In fact, many of the studies compare their results to those of AC chemotherapy, the treatment containing only DOX and CPA (Figure 1.4). This was one of the earliest examples of adjuvant treatments after the first reports in the mid-1970s. In 1975, Corbett *et al*. reported the improved effect of this combination compared to the individual drugs. They also determined that this regimen allowed for a 30-50% reduction in the amount of DOX used while still maintaining a higher tumor cell death rate.[57] Jones *et al*. reported a total response rate of approximately 80% after two cycles of

AC chemotherapy. Additionally, it was determined that, if there was to be a response to the regimen, then 4 cycles of AC chemotherapy was optimal.[58] Each of the 4 to 6 recommended cycles of AC chemotherapy involves administration of 60 mg/m^2 of body surface area of DOX intravenously over 15 to 60 min. This is followed immediately by 600 mg/m^2 of body surface area of CPA administered intravenously over 30 to 60 min. In between each cycle, the patient has 3 weeks to recover.[58–60] Because of their efficacy as a combination, as well as their ubiquity in other adjuvant treatments and this dissertation, it is important to examine how CPA and DOX function individually to better understand how current regimens might be improved.

Cyclophosphamide

CPA (Figure 1.4a) is a type of oxazaphosphorine called a nitrogen mustard. As with mustard gas, which is a type of thioether (Figure 1.5a), nitrogen mustards characteristically feature β-chloroethylene substituents on the central heteroatom. The haloalkane substituents make excellent reagents for DNA alkylation. While it is not required to be considered a mustard, most nitrogen mustards are di-substituted with respect to the β-chloroethylene; the third substituent differentiates one nitrogen mustard from another (Figure 1.5b).

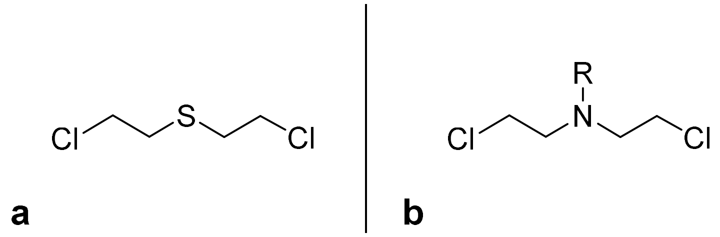

Figure 1.5: General structures of different mustards. a) Mustard gas; b) Nitrogen mustard

Earlier in this dissertation, a very brief summation of the history of mustards in oncological practices was presented. To review, in 1946, it was discovered that victims exposed to nitrogen mustards showed deep myeloid and lymphoid suppression. This observation was critical as it jumpstarted an exploration into how these agents worked.[61,62] Shortly thereafter, researchers elucidated and reported the clinical uses of nitrogen mustards.[42]

Nitrogen mustards, like CPA, most commonly are used in the treatment of Hodgkin's disease, non-Hodgkin's lymphoma, leukemia, numerous bone and soft tissue sarcomas, and solid tumors.[42,63,64] On its own, CPA is inactive as a therapeutic, setting it apart from many other alkylating agents;[65] CPA is a prodrug. The metabolites of CPA are the source of cytotoxicity

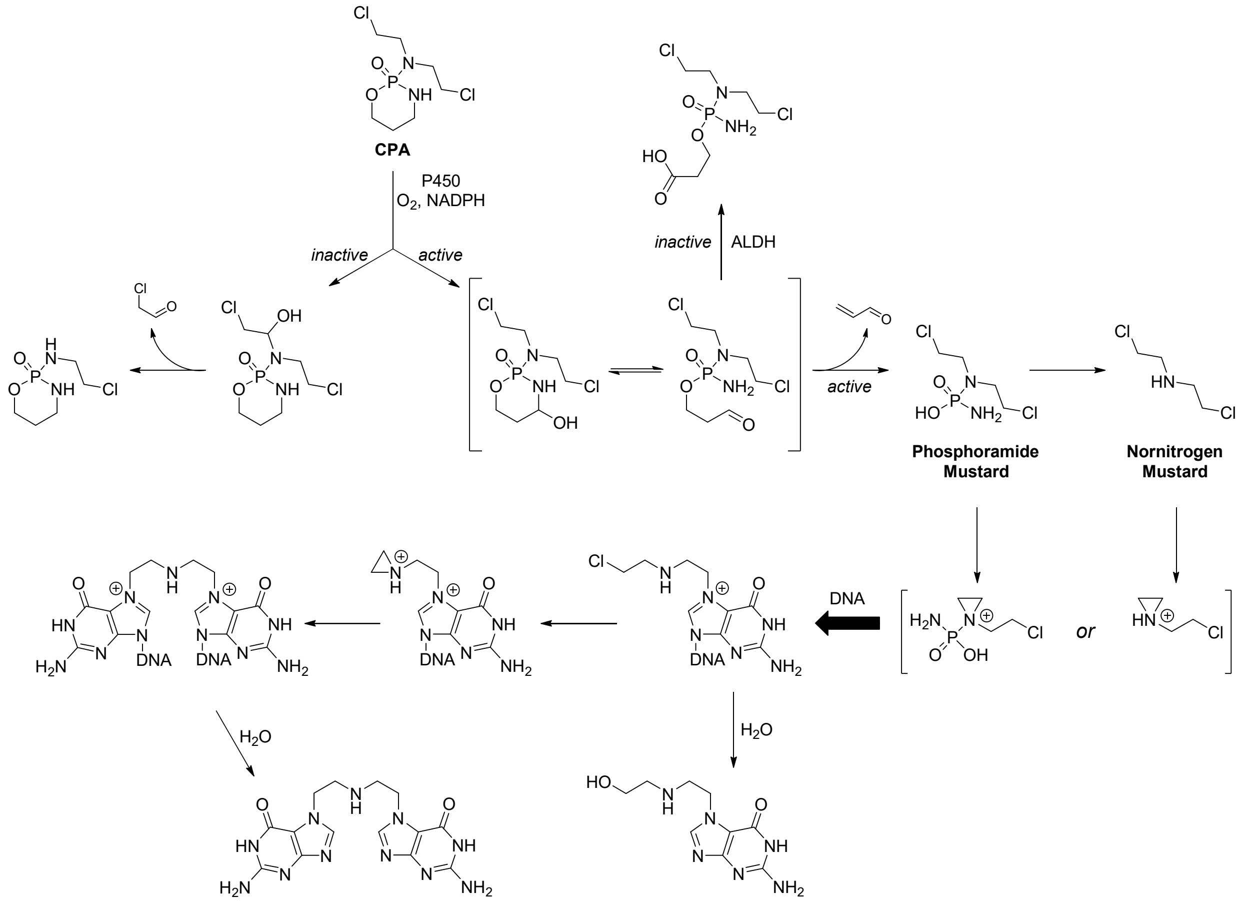

Figure 1.6: Metabolic pathway of CPA

exhibited by the mustard. These metabolites are phosphoramide mustard (PM) and nornitrogen mustard (NOR). The active metabolic pathway that produces these reactive species is well-known (Figure 1.6). CPA is oxidized metabolically by the Cytochrome P450 enzyme CYP2B6 to form 4-hydroxycyclophosphamide, which is thought to be in equilibrium with its ring-opened tautomer aldophosphamide. This tautomer eliminates acrolein to form PM, which either moves forward as the reactive species or dephosphorylates to make NOR.

Both PM and NOR are capable of alkylating DNA.[66] This is achieved primarily by displacement of a chloride ion by neighboring group participation of the central nitrogen to generate a highly reactive aziridinium ion that is susceptible to nucleophilic attack by the N^7-position of dG. This forms a cationic dG adduct (Figure 1.6). There is evidence to suggest that there is a significant amount of nitrogen mustard adducts of the phosphodiester backbone;[67] however, the N^7-position of dG is considered the primary site of nucleophilic attack. The mono-dG adduct of these mustards is hydrolytically unstable. As such, water may displace the second chloride ion, most likely through a second aziridinium ion to form a hydrolyzed mono-dG adduct; or, the second aziridinium ion may be attacked by another dG nucleotide to form an intra- or interstrand crosslink within the double helix.[63,68,69]

There had been some debate as to which of the metabolites is more active. Overall, CPA has a half-life of approximately 6-9 hr, and the peak levels of PM are reached in approximately half that time.[64] The dephosphorylation of PM to NOR proceeds at physiological conditions with a half-life of 100 min. Many believed that NOR is more active because of PM's lack of stability.[70] However, it has been shown that PM is more than capable of alkylating DNA without undergoing dephosphorylation at biological pH.[66] Therefore, it most commonly is accepted that

PM is the more-active metabolite, undergoing dephosphorylation after alkylating DNA to form the NOR adduct as previously discussed.

Once the cationic dG adducts form, there are numerous downstream pathways the DNA can undergo. Primarily, there are those that are common to cationic dG adducts.[21] In the past, our lab, in conjunction with collaborators at the Masonic Cancer Center at the University of Minnesota, had characterized the extent to which the FAPy-G adduct of the nitrogen mustard bis-(2-chloroethyl)ethylamine (HN-1) forms.[71] The interstrand crosslink dG-HN1-dG accounted for a small amount of the adducts in cellular DNA compared to others. The hydrolyzed mono-dG adduct accounted for about 4 times as many lesions as the dG-HN1-dG adduct and about 4-5 times as many lesions as the hydrolyzed mono-FAPy-G adduct. This possibly is due to the presence of histones and other proteins that make the cellular environment less favorable for nonspecific and interhelix crosslinking.[71]

These HN-1 adducts, especially those of FAPy-G, were shown to be good substrates for BER glycosylase enzymes. In fact, when treated with the glycosylase enzyme FPG, higher levels of the hydrolyzed mono-FAPy-G adduct *and* the HN-1 crosslink between FAPy-G and G were detected. This is significant as it suggests that cationic G is removed hydrolytically from one side of a crosslink, leaving behind an AP site.[71] Secondly, glycosylase enzymes also hydrolytically excise the modified base, leaving an AP site in the strand.[29] This hypothesized process, outlined in Figure 1.7, would leave two AP sites on opposite strands in close proximity, leading to a highly toxic double-strand break.[71]

The toxicity resulting from these cationic adducts comes from multiple sources. For one, it has been shown that nitrogen mustard adducts are capable of causing point mutations in the genome due to mismatched base pairing.[72] Additionally, instead of hydrolyzing or crosslinking

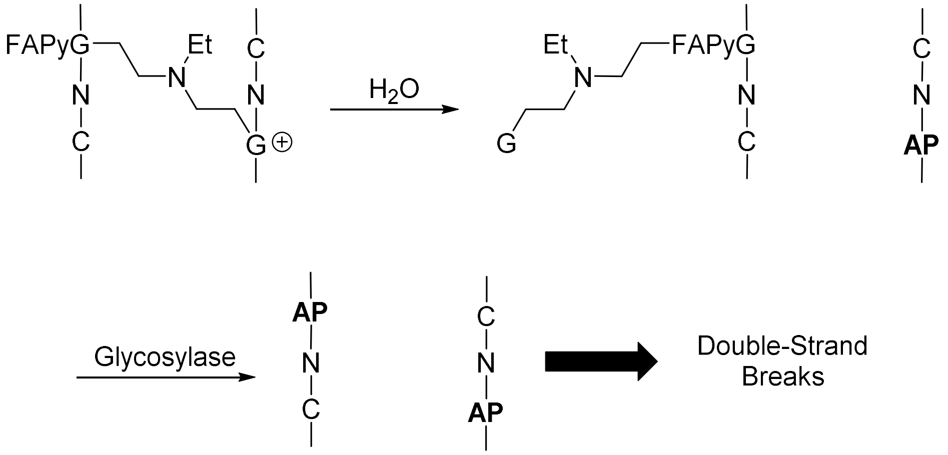

Figure 1.7: Proposed mechanism of double-strand breaks caused by HN-1. Adapted from Gruppi *et al.*[71]

to the other DNA strand, the mono-dG adducts of nitrogen mustards can form DNA-protein crosslinks.[62] As it currently is understood, the most significant contributor to nitrogen mustard toxicity is the interstrand crosslink between strands of DNA. While these adducts only account for a small percentage of the total number of adducts, they can cause a variety of issues. Primarily, these crosslinks stall replication at the replication fork. During this process, the crosslink prevents the strands from separating, causing cell-cycle arrest, activation of apoptotic pathways of cell repair, and cell death.[73] Additionally, the DNA strand cleaves via β- or β,δ-elimination because of the AP sites formed, as previously described.[62,71] Because of these pathways, nitrogen mustards, such as CPA, are key components to anti-cancer regimens.

Doxorubicin

DOX commonly is used to treat breast cancer. Additionally, it often is used in combination with other chemotherapeutics, some of which have been cited previously in this dissertation.[53–56] Other human malignancies that have responded well to DOX and its multiple combination therapies include soft tissue/bone sarcomas, Hodgkin's disease, lymphosarcoma, bladder adenocarcinoma, thyroid cancer, solid tumors in pediatric patients, acute leukemias, bronchogenic carcinoma, AIDS-related Kaposi's sarcoma, and ovarian cancer, among many others.[74–78] DOX and its congeners are among the most useful antitumor drugs in the world.[75]

The parental precursor to DOX, daunorubicin (DAU), often referred to as Daunomycin, was isolated in 1963 as the hydrochloride salt from cultures of *Streptomyces peucetius*. It concurrently was reported that daily doses of 1-2 mg/kg of DAU showed activity against solid tumors and those from excess abdominal fluid. Additionally, mitotic activity of healthy and cancerous cells was inhibited *in vitro* at concentrations as low as 0.01-0.1 μg/mL.[79,80] Clinically, DAU had proven itself to be a powerful antitumor antibiotic against childhood leukemia, with some amount of remission appearing in 83% of previously untreated patients and 38% of patients resistant to other treatments.[81]

The belief was that, if DAU had favorable pharmacological properties compared to other anthracyclines of the time, then even more successful antitumor antibiotics might be found by investigating new compounds with a similar structure. This came in the form of examining mutants of *Streptomyces peucetius*.[82] DOX was isolated as a metabolite of *Streptomyces peucetius* var. *caesius*, a mutant of the original strain. Soon after its isolation, the structure of DOX was confirmed to be that shown in Figure 1.4b,[83] and its cytotoxic properties were shown to be an improvement on those of DAU.[82,84]

In *Streptomyces peucetius*, biosynthesis of anthracycline aglycones occurs via a Type II polyketide synthase starting with one unit of propionate and nine units of acetate.[85] While the following biosynthetic steps had been debated over time, the more commonly accepted pathway comes from Yoshimoto *et al*.[75] For a detailed figure showing the overall mechanism, reference the studies cited by Yoshimoto *et al*.[86,87] To summarize, the decaketide formed by the polyketide synthase became aklavinone and, eventually, ε-rhodomycinone. They proposed that daunomycinone came from ε-rhodomycinone via removal of the methoxycarbonyl group followed by subsequent oxidations. It later was determined that the Cytochrome P450 oxidase DoxA was responsible for these oxidations *and* the conversion of DAU into DOX.[88] During the biosynthesis of the aglycone, daunosamine glycosyltransferase (Dnr S) added the sugar moiety to the compound.[89]

Because of its utility as an antitumor antibiotic, DOX was a prime candidate for the target of a total synthesis. While first syntheses focus on DAU, Arcamone *et al*. reported in 1969 a 7-step conversion from DAU to DOX, making DOX as synthetically attainable as DAU.[90] The first synthesis of the anthracycline aglycone of DAU was reported in 1972 by Wong *et al*. The aglycone is produced in about 21 steps from 2,5-methoxybenzaldehyde, the source of the anthracycline B ring (Figure 1.8a).[91] While this is the original synthetic route to the aglycone and referenced in much of the literature, many have devised other routes. For example, a more recent approach involves di-convergent Diels-Alder reactions onto 2,3,5,6-tetramethylidene-7-oxanorbornane, the source of the B ring. This oxanorborane is synthesized in 5 steps beginning with a Diels-Alder reaction between furan and maleic anhydride (Figure 1.8a).[92,93] This approach is more versatile than that reported for daunorubicinone, specifically; Vogel's approach can be used to access many modified derivatives of the aglycone, as well. For more details regarding these aglycone syntheses, I defer to the literature.[90–93]

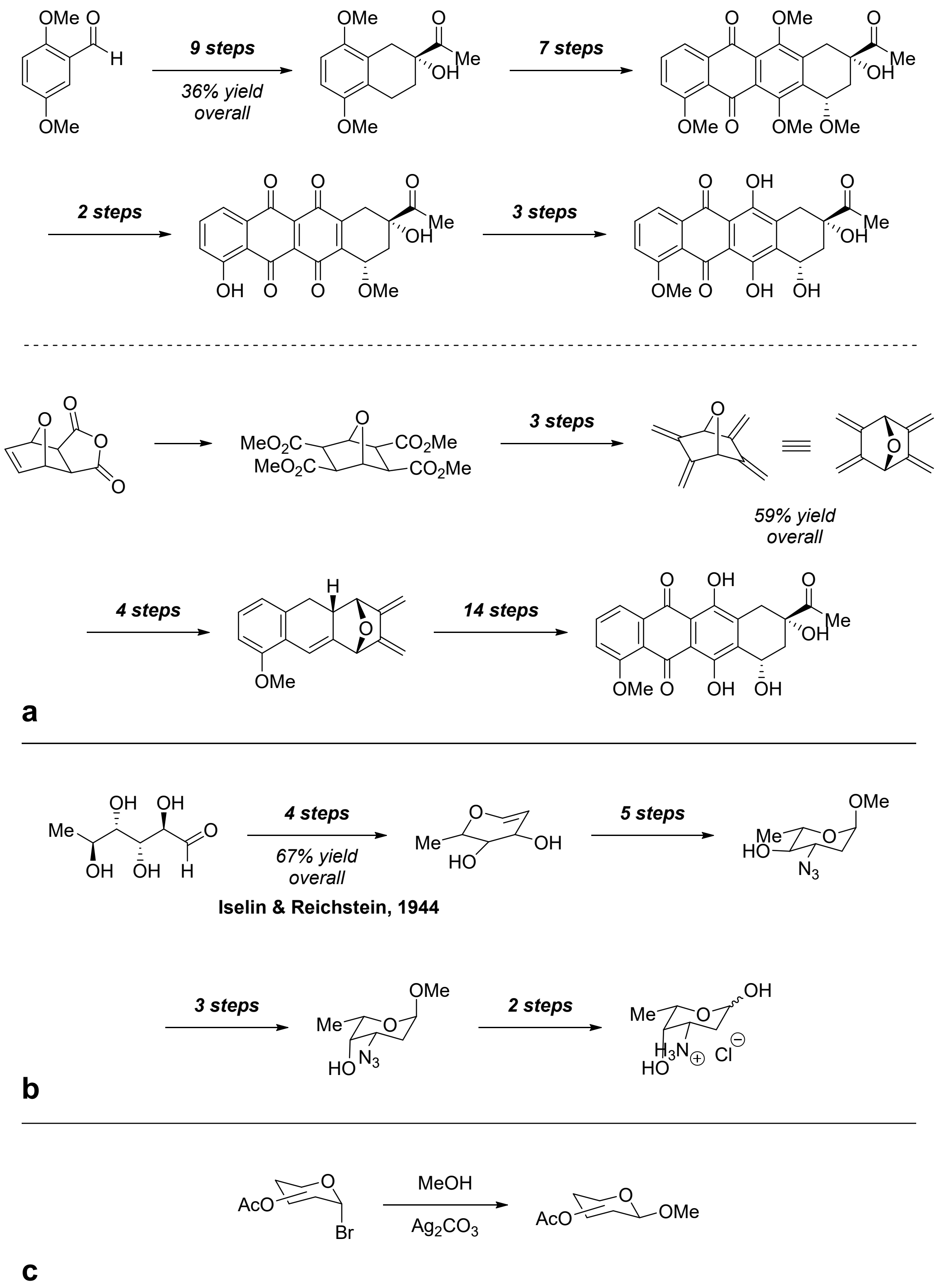

Figure 1.8: Representative syntheses of the different parts of DAU. a) Synthesis of the aglycone by (top) Wong *et al.*[91] and (bottom) Vogel *et al.*;[92] b) Synthesis of daunosamine by Iselin *et al.*[94] and Marsh *et al.*;[95] and c) Koenigs-Knorr glycosylation conditions.

The first reported synthesis of the daunosamine moiety begins with the conversion of L-rhamnose to L-rhamnal over 4 steps.[94] From this precursor, the hydrochloride salt of the sugar found on both DAU and DOX is synthesized in about 10 steps (Figure 1.8b).[95] For the glycosylation to occur, the sugar's amino group must be protected as a trifluoroacetyl group. Similarly, both hydroxyl groups typically are protected as *p*-nitrobenzoyl groups. After conversion of the anomeric ester to an anomeric halide, the glycosylation can occur. Typically, the glycosylation is performed using modified Koenigs-Knorr conditions (Figure 1.8c).[92] However, the first reported glycosylation of the aglycone core onto L-daunosamine uses mercuric cyanide and mercuric bromide in anhydrous conditions to make the protected DAU with high α-selectivity.[96] Other routes have activated the *p*-nitrobenzoyl protected glycosyl donors with trimethylsilyl triflate instead of converting it into the halide, first.[97] More recently, Biao Yu's gold(I)-mediated glycosylation has been a popular choice due to its milder conditions and its compatibility with many desirable anthracycline functionalities.[98] For example, PPh_3AuNTf_2, the gold(I) catalyst used by Yu, also was used to perform structure-activity relationship (SAR) studies on modified versions of DOX and aclarubicin. Derivatives combining features of these two anthracyclines were synthesized to deduce certain structural aspects responsible for different mechanisms-of-action.[99]

There are many potential mechanisms by which DOX effects a cytotoxic response. The most accepted mechanisms are as a topoisomerase II (Top2) poison through DNA intercalation and by redox cycling of the anthracycline core. DNA intercalation is the noncovalent process by which a small, planar, aromatic molecule, dubbed an "intercalator," is inserted in the space between base pairs of DNA, perpendicularly to the DNA helical axis (e.g., Figure 1.9).[100] Once inserted, intercalators cause numerous downstream biological effects. In 1961, Lerman reported

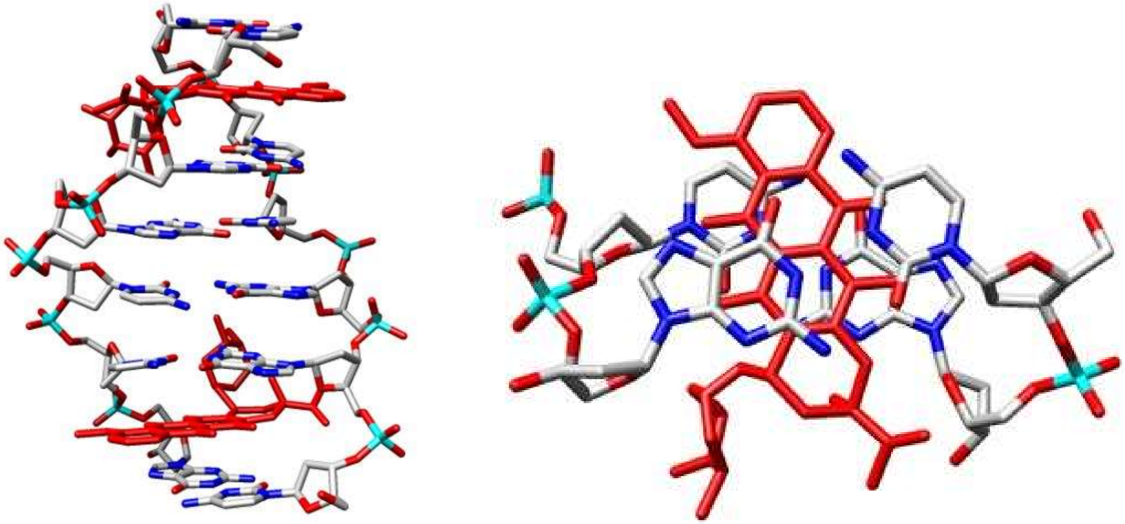

Figure 1.9: DAU (red) intercalated into a DNA oligo hexamer. Viewed from the major groove (left) and above (right). Created in Chimera (PDB: 110D) and adapted from Leonard *et al*.[100]

that planar acridine molecules caused DNA to become longer and stiffer post-intercalation.[101] Additionally, drugs that intercalate DNA block binding sites for numerous DNA-dependent enzymes. Examples of enzymes blocked by intercalators are DNA and RNA polymerases and nucleases. Competition with these enzymes results in the inhibition of DNA replication and transcription.[102] Another way DNA replication and transcription are blocked is via single-strand breaks along the molecule. Intercalators like DOX have been shown to induce this DNA damage.[103,104] Lastly, frameshift mutations also are possible when compounds intercalate DNA. As briefly mentioned earlier in this dissertation, a frameshift mutation is one where a nucleotide base in DNA either is mis-inserted or is deleted from a DNA strand, leading to improper protein synthesis due to a misread codon in the mRNA.[104]

In 1987, Wang *et al*. provided 1.2 Å-resolution crystal structures of DAU complexed to a self-complementary DNA hexamer. From these studies, they determined that DAU preferentially intercalates DNA at 5’-CpG-3’ sequences, projecting the daunosamine ring into the minor groove. Rings B-D are those that intercalate, whereas the A ring and its substituents anchor the drug to the double helix via hydrogen bonding between the O^9-hydroxyl of DAU and the N^2- and N^3-positions of the dG residue in the 5’-CpG-3’ sequence. Additionally, a molecule of water binds the O^{13}-position of DAU with the O^2-position of the dC residue in that same sequence (Figure 1.10).[105,106] DOX is understood to behave similarly, as the only structural difference is the substituent on the C^{14}-position of the aglycone.

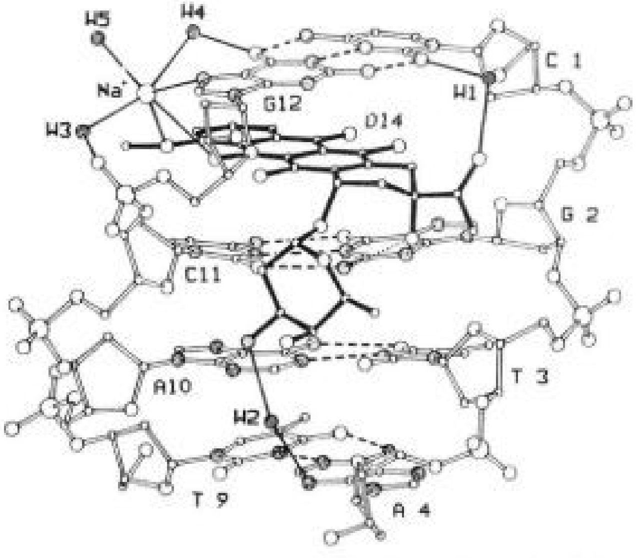

Figure 1.10: Diagram of the DAU/DNA crystal structure. Hydrogen bonds are represented by dashed lines, water is represented by “W,” sodium ions are labeled as “Na^+,” nucleotides are represented by their letter and their spot in the hexamer duplex, and the relevant atoms on DAU are labeled as they are. Diagram copied from Wang *et al.*[105]

The reported crystal structures and the fact that the non-intercalated portion of the drugs resides in the minor groove indicate that intercalation of DAU or DOX occurs from the minor-groove side of DNA.[104] The overall mechanism-of-intercalation has been studied extensively.[104,107,108] Figure 1.11, adapted from Mukherjee & Sasikala,[104] who borrowed the figure from Macgregor *et al.*,[109] shows different possible pathways of intercalation. Using

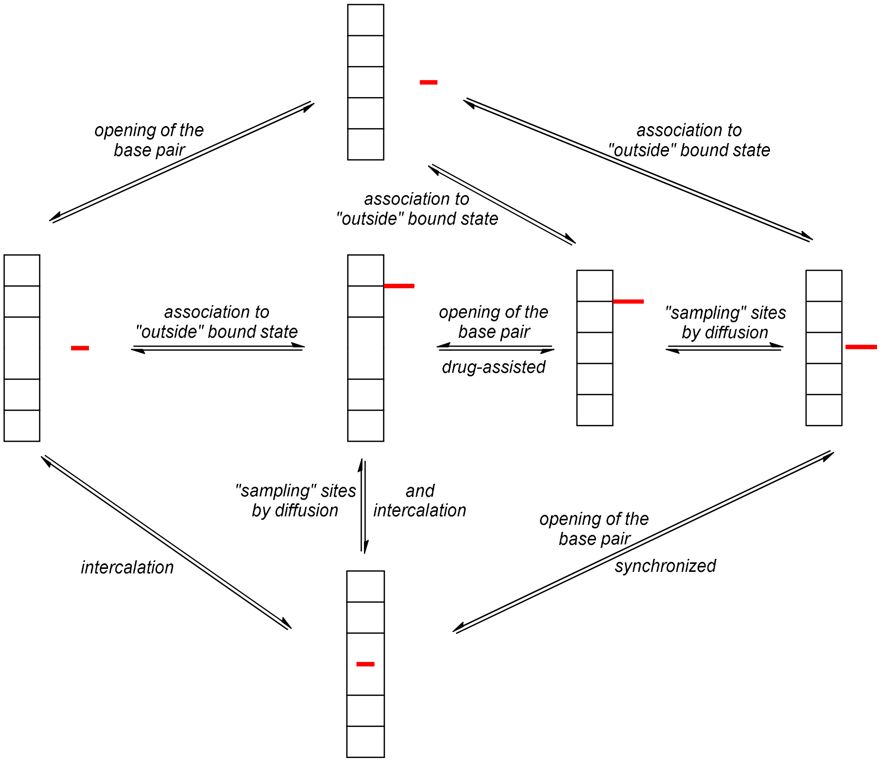

Figure 1.11: Possible mechanisms of intercalation. Ladder is the DNA duplex; red line is the drug. Adapted from Mukherjee & Sasikala[104] and Macgregor *et al.*[109]

stopped-flow and temperature-jump relaxation methods, Chaires *et al.* were able to calculate rate constants of a proposed mechanism-of-interaction of DAU with DNA. In their analysis, they proposed a mechanism that follows one of the pathways proposed by Macgregor *et al.*[109] A complex between DAU and DNA *outside* the double helix forms rapidly, followed by a slower intercalation process from that bound state.[108] However, these studies have some shortcomings, including the lack of elucidation of a direct path between the bound and intercalative states.[104]

Intercalation is an essential property for DOX's commonly accepted mechanism-of-action as a Top2 poison. Top2 is a class of enzyme essential in the DNA replication process. It most commonly is cited for its utility in relieving stress on the chromosome caused by DNA supercoiling.[110,111] Supercoiling is the extent to which DNA is twisted at a given time, quantitatively determined by a formula;[112–114] and, it is classified as either “positive” or “negative” depending on the amount of tension relative to its normal state, “relaxed B-form” DNA. While negative supercoiling is necessary for many processes in the nucleus, positive supercoiling can inhibit those same processes.[115]

Structurally, Top2 is a heart-shaped dimeric protein with a large cavity in the center. Each monomer folds into a crescent shape made of two subfragments, called A’ and B’, connected by a disordered linker of approximately 48 residues. The monomers are joined together at the A’ subfragments, creating a hydrophobic core inaccessible to solvents. On top of each of the B’ subunits lies an ATPase-domain at the N-terminus of each monomer.[116] Of the Top2 enzymes, there are two isoforms present in mammalian cells. While they structurally are similar and cleave DNA in similar manners, there are differences in their phosphorylation states and how their genes are expressed during the cell cycle.[117] As will be discussed later on, these isoforms, dubbed Top2α and Top2β, function independently and in different ways from each other.

From these structural insights, a model for Top2’s catalytic reaction has been proposed (Figure 1.12). DNA binds in the grooves of the A’ subfragments with the B’ subunits clamping around it as the result of a conformational change. ATP binds to the ATPase domains, causing them to open for a separate DNA strand (called the T-segment) to pass through the enzyme.[116] In order for this to occur, two tyrosine residues on the A’ subfragments in the active site of Top2 each bind to DNA by nucleophilic attack on the phosphodiester backbones of the duplex to cause nicks in each strand of the DNA resulting in a DNA-protein crosslink intermediate. This occurs by a general acid-base mechanism for DNA cleavage mediated by two Mg^{2+} ions and other residues in the active site. These residues are believed to be aspartates, glutamates, and histidine,

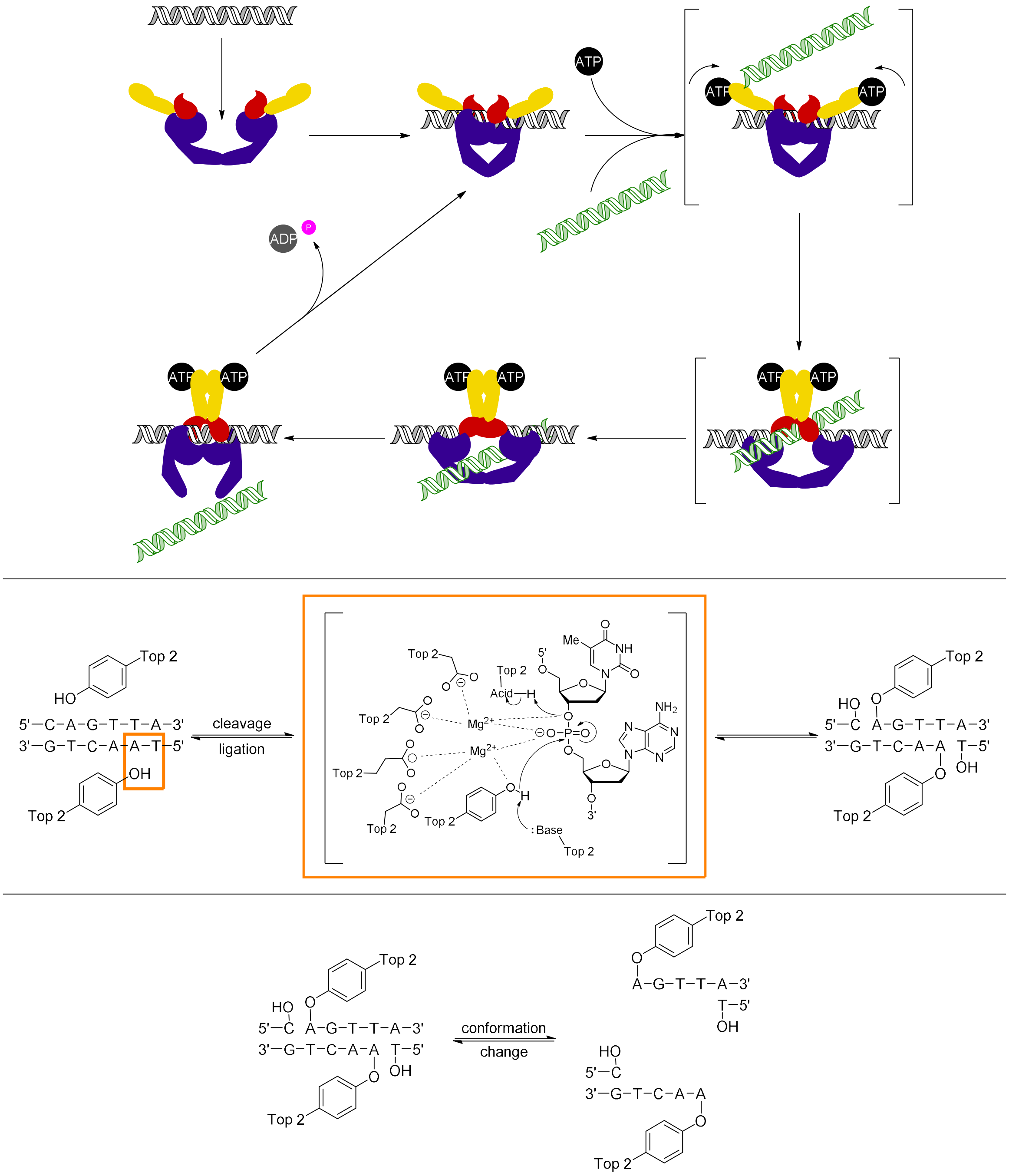

Figure 1.12: Proposed mechanism-of-action of Top2. Blue = A' subfragments; red = B' subfragments; yellow = ATPase domains; black helix = DNA (G-segment); black = ATP; green helix = DNA (T-segment); grey = ADP; pink = phosphate. The overall mechanism is shown on the top; the binding of Top2 to DNA is shown in the middle; the topological change that separates the double-strand break is on the bottom. Adapted from Deweese[115] and Berger.[116]

but this has not been confirmed experimentally.[115,118] This intermediate and its overall structure is referred to as the "cleavable complex." As the T-segment is passed through the enzyme into the cavity at the center of Top2, the nicked DNA is pulled apart by conformational changes to clear a path. These conformational changes dimerize the two ATPase domains. As the cleavable complex re-ligates the nicked strands, the A' subfragments separate to allow the T-segment to exit the enzyme.[116] This most likely occurs as a reversal of the acid-base mechanism previously described, where the 3'-hydroxyls of the nicks nucleophilically attack the phosphodiester backbones to break the phosphotyrosyl bonds.[115,118] Upon redimerizing the A' subfragments, ATP is hydrolyzed and released, monomerizing the ATPase domains to complete the enzymatic mechanism.[116]

If a replication or transcription complex tries to skip over a cleavable complex, the transient double-strand breaks caused by Top2 can become permanent. This typically occurs if there are too many cleavable complexes present in the given system. Because double-strand breaks in DNA are toxic, the levels of cleavable complex in the cell must be maintained as a delicate balance. If there are too few cleavable complexes, then the supercoiling is not corrected, and the chromosome will remain tangled post-replication. This eventually leads to mitotic failure and cell death. However, transient double-strand breaks become permanent if there are too many cleavable complexes, triggering repair pathways in the cell. If the number of breaks becomes too overwhelming, the cell activates apoptotic pathways and kills the cell. If the apoptotic pathways are not activated, then chromosomal translocations will form and persist, increasing the risk of some acute leukemias.[115,119]

These observations are the basis of the toxicity of what are called Top2 poisons (e.g., DOX). By interacting with the cleavable complex in the Top2 pathway, the equilibrium between cleavage and ligation, which usually favors ligation about 99:1,[115] shifts to favor the cleavage by stabilizing the complex and inhibiting re-ligation. This ternary complex between the drug, DNA, and Top2 forms as a result of the drug's ability to interact noncovalently with DNA (e.g., intercalate) within the active site of Top2.[119–124] There is precedence for site-specificity in how these poisons affect strand cleavage. For example, cleavage by DOX-stabilized cleavable complex requires that at least one of the nicks in the duplex have a dA nucleotide on the 3'-terminus of the strand (as shown in the middle portion of Figure 1.12).[125] DOX is believed primarily to affect the Top2α isoform because it is expressed only in proliferating and tumor cells; the high efficacy of DOX often is linked to the overexpression of Top2α in cancer cells.[126]

Although it is highly effective as a cancer drug, DOX is plagued by many toxic side effects. Primarily, patients treated with DOX are at a high risk of developing off-site, life-threatening cardiotoxicity.[126–129] The assumed culprits of this cardiotoxicity are ROSs, which also have shown to effect a cytotoxic response. Although the source of the cardiotoxicity is not known definitively, this side effect most commonly is attributed to redox cycling of the anthracycline core because of DOX's interaction with iron within the mitochondria. DOX can bind Fe^{3+} ions to form a hydrated Fe^{3+}-complex. In the presence of O_2, it cycles between the Fe^{3+} and Fe^{2+} oxidation states, generating superoxide radicals. When the complex is reduced by NADPH Cytochrome P450 reductase and the mitochondrial electron transport chain (METC), DOX either cycles to a semiquinone radical or reduces to doxorubicinol (DOXol), a 13-hydroxy metabolite of DOX.[130,131] Both pathways damage the cell. The DOX-Fe^{3+}complex and DOXol have been found to affect IRP1 RNA binding activity and iron homeostasis, while the doxorubicin semiquinone deglycosylates to form a C^7-radical of DOX that causes DNA damage and lipid peroxidation in its own right (Figure 1.13).[130,132–134] However, it should be noted that

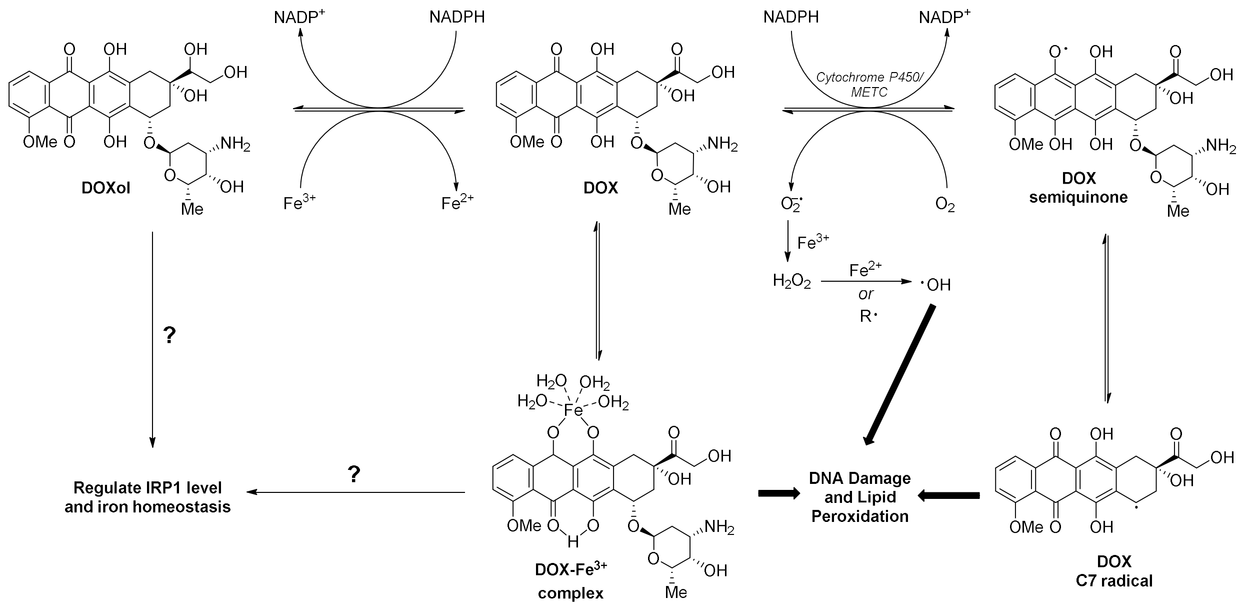

Figure 1.13: Possible mechanisms-of-action of DOX cardiotoxicity via (left) interactions with iron(III) ions and (right) redox cycling by Cytochrome P450 and the mitochondrial electron transport chain (METC). Adapted from Xu *et al.*[130] and Zhu *et al.*[131]

these observations regarding DOX redox cycling have been made at pharmacologically irrelevant concentrations of the drug,[131] indicating that the iron-mediated pathways may be more biologically relevant. Additionally, there is evidence to suggest that intercalated anthracyclines produce less superoxide and are poor substrates for enzymatic reduction.[135,136] The lack of evidence to support biologically relevant redox cycling of DOX further contributes to the mystery of DOX's induced cardiomyopathy.

Another source of cardiotoxicity explored in the literature is the interaction of DOX with the Top2β isoform. While Top2α is expressed in proliferating cells and needed for cellular survival, Top2β is inactive and present in *every* cell and is not necessary for survival.[117] Additionally, only Top2β is expressed in the adult heart.[137] Lyu *et al.* have shown that Top2β may be involved in DOX's cardiotoxic side effects, as they proved that dexrazoxane, a Top2 catalytic inhibitor, decreased the cardiotoxic effect of DOX in mouse embryonic fibroblasts.[126] Additionally, deletion of the gene that encodes Top2β protects cardiomyocytes from DOX-induced double-strand breaks and transcriptome changes responsible for ROS production.[138] Whether by activation of p53 or by a mediatory route, Top2β affected by DOX decreases the expression of PGC1α and PGC1β, enzymes responsible for mitochondrial biogenesis. This leads to mitochondrial dysfunction and a decrease in antioxidant production, key roles of the PGC1 enzymes.[139] All of this results in an increase of ROS production from the METC and, therefore, cardiotoxicity (Figure 1.14).[131]

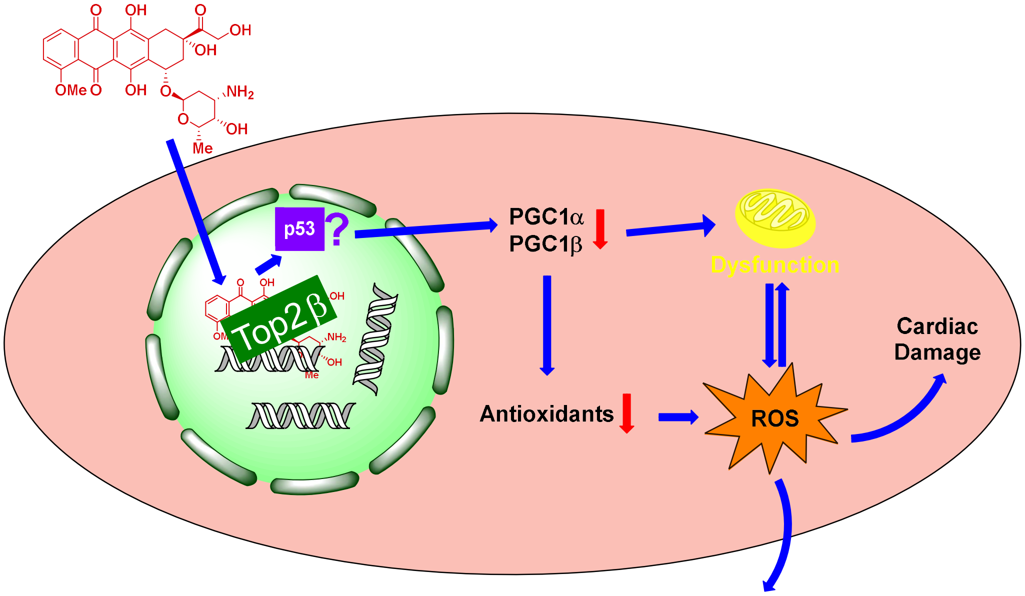

Figure 1.14: Interaction between DOX and Top2β and its potential involvement in the induced cardiotoxicity of DOX. Adapted from Zhu *et al.*[131]

The cumulative cardiotoxicity that stems from DOX treatment has forced a lifetime cap upon the amount of drug a patient is able to receive. This cap is for doses greater than 500 mg/m^2 of body surface area.[126–129] Because of this, understanding how DOX induces cardiotoxicity is paramount to improving the overall effectiveness of the drug. Antioxidants have been researched as adjuvants to DOX chemotherapy to no avail.[131] Similarly, while dexrazoxane has shown a decrease in the cardiotoxic effect of DOX on mouse embryonic fibroblasts by inhibiting Top2β's activity,[126] it also showed a decrease in DOX cytotoxicity in the clinic. Because of this, the FDA has approved dexrazoxane as an adjuvant only for metastatic breast cancer patients who need DOX beyond a dose of 300 mg/m^2 of body surface area.[140] As this issue prevails, there is a clinical need to improve on the very effective cancer drug, DOX. Improvement on DOX will create a better situation for many cancer patients, and research into circumventing these cardiotoxic side effects will help to better inform drug design in the future.

Drug Modifications

DOX was discovered as a metabolite of *Streptomyces peucetius* var. *caesius* during a push to find effective anticancer antibiotics that were structurally similar to DAU.[82] One other

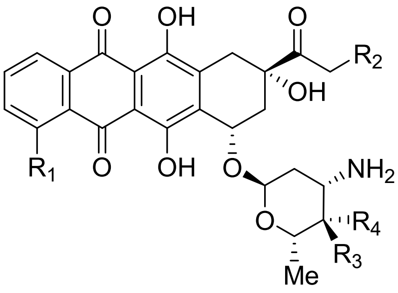

Name	R_1	R_2	R_3	R_4
Daunorubicin	OMe	H	H	OH
Doxorubicin	OMe	OH	H	OH
Epirubicin	OMe	OH	OH	H
Idarubicin	H	H	H	OH

Figure 1.15: Structural comparison of common anthracycline antibiotics to DAU.

example of a drug from this effort is epirubicin. Epirubicin (Figure 1.15), a 4'-epimer of DOX, often is used clinically instead of DOX because it has fewer and less intense side effects, especially with regard to cardiotoxicity.[141–143] Similarly, idarubicin, demethoxylated DAU (Figure 1.15), has been a popular choice in the treatment of acute leukemias and has shown a greater cytotoxicity *in vitro* than both DOX and DAU. Idarubicin also is preferred to DOX in some clinical cases because it is less susceptible to multidrug resistance; there is only partial cross-resistance between DOX and idarubicin.[144,145] As briefly demonstrated, DOX is not the only antibiotic structurally-related to DAU discovered from these microbial studies. Further examples of these drugs are summarized hereafter.

In 1965, nogalamycin (Figure 1.16a) was fermented and isolated from the bacterial species *Streptomyces nogalater* var. *nogalater*.[146] Nogalamycin shows significant cytotoxicity in HeLa-derived KB cells. At concentrations as low as 5 ng/mL, nogalamycin inhibited the growth of these cells by 50% over a 3-day period. At 600 ng/mL, this antibiotic inhibited RNA synthesis

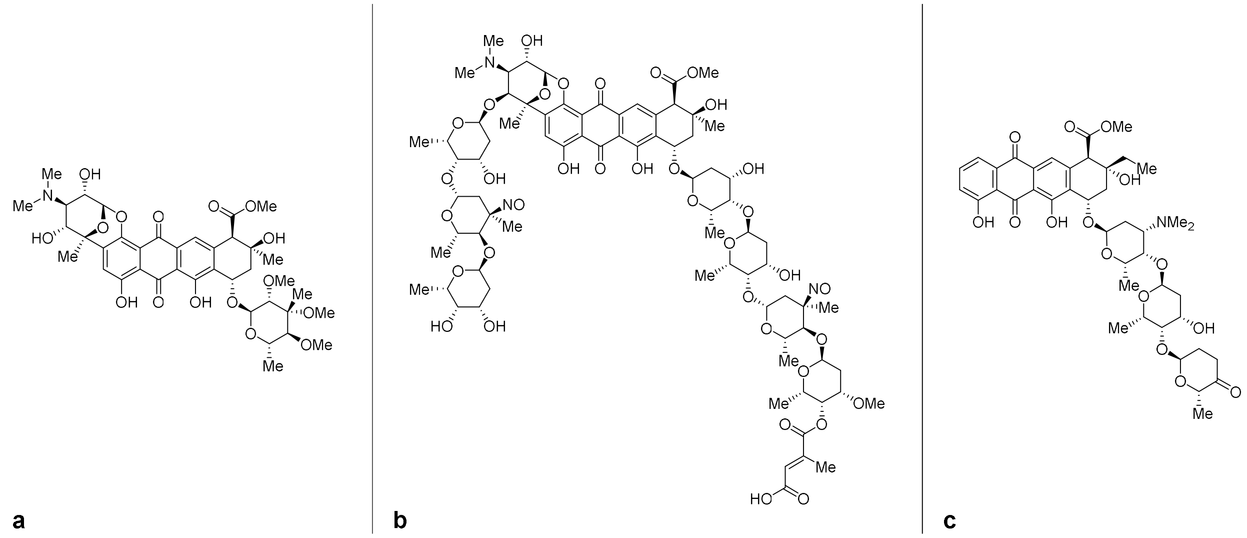

Figure 1.16: Other microbial antibiotics with similar structures as DAU and DOX. a) Nogalamycin; b) Viriplanin A; and c) Aclarubicin.

by 74%, DNA synthesis by 31%, and protein synthesis by 2%.[147] *In vivo*, nogalamycin increased the lifespan of mice implanted with L1210 leukemia cells by 32% (at a dose of 1 mg/kg administered by IP injection over 7 days).[148] Nogalamycin originally was believed to bind to dA and dT residues in DNA to effect these changes because of its higher effect on RNA synthesis compared to other biomolecular syntheses.[147] However, in 1989, Liaw *et al*. showed with 1.3- and 1.7-Å resolution crystal structures that nogalamycin binds to DNA with the bicyclic amino sugar on the D ring in the major groove and the nogalose sugar on the A ring in the minor groove, a result in contrast with drugs like DOX and DAU that only bind to the minor groove. They used these results to reconcile discrepancies in the literature regarding nogalamycin's site specificity. The crystal structure shows a preference for GC sequences, but the fact that there is binding to both grooves suggests that AT sequences surrounding the GC sequence are necessary to make room, transiently, for intercalation to occur.[149] These observations have been corroborated by other studies.[150–153]

The length of the sugar moiety also differs between these antibiotics. For example, viriplanin A (Figure 1.16b) was isolated from the *Ampullariella regularis* strain SE 47 in 1986. Viriplanin A is toxic to leukemia P388 cells in mice at a concentration of 500 μg/kg. The intravenous LD_{50} was found to be about twice this dose. The structure of viriplanin A is similar to that of nogalamycin, except the bicyclic sugar on the D ring is glycosylated with a trisaccharide, and the nogalose sugar is replaced with another oligosaccharide chain.[154]

Aclacinomycin A, often referred to as aclarubicin (Figure 1.16c), was isolated from *Streptomyces galilaeus* in 1981. This anthracycline has an aklavinone core with a trisaccharide in the C^7-position of the aglycone.[155] Even though aclarubicin has a greater redox potential than DOX, this drug did not induce a cardiotoxic response in mice and human cardiac microtissue.[156,157] This has led researchers to believe that aclarubicin, though an intercalator, does not induce double-strand breaks in DNA.[157] Today, aclarubicin is approved only in Japan and China for the treatment of acute myeloid leukemia.[99]

These have been just a few of the plethora of examples of antibiotics discovered through microbial studies. Each of these compounds presents its own, unique challenges to its total synthesis *ex vivo*. However, synthetic organic chemistry has provided a library of compounds for research in addition to those compounds fermented and isolated from bacteria. In the late 1970s, Arcamone *et al*. patented a process of synthesizing 14-aminodaunomycin derivatives, (Figure 1.17, Site "a") where the C^{14}-position is substituted by an amine. This is accomplished using the 14-bromo substituted DAU intermediate. This route provided five compounds that were less effective *in vitro*, but less toxic to mice *in vivo*.[158] This method also has been employed to synthesize 14-thio- and 14-seleno-derivates of DAU (Figure 1.17, Site "b").[159] DOX and DAU also can be modified at the daunosamine ring.[160] Reductive amination of aldehydes and ketones by DOX or DAU has provided *N*-alkylated derivatives of these anthracyclines (Figure 1.17, Site "c"). Many of these alkylated derivatives maintained their cytotoxicity, but showed improved inhibition of RNA synthesis. Notably, DAU modified with two benzyl groups showed increased efficacy against P388 leukemia cells in mice and a ten-fold reduction of cardiotoxicity.[161]

Hydrazines and hydrazides, semicarbazides, and alkoxyamines condense onto the C^{13}-position of DOX or DAU to create modified anthracyclines (Figure 1.17, site "d"). These functional groups are called hydrazones, semicarbazones, and oximes, respectively, and are stable at physiological pH (unlike their imine counterparts). As these functional groups are the main focus of this dissertation, more detail about how they form and their stability will be presented later. However, given that some modifications at the C^{13}-position have been reported

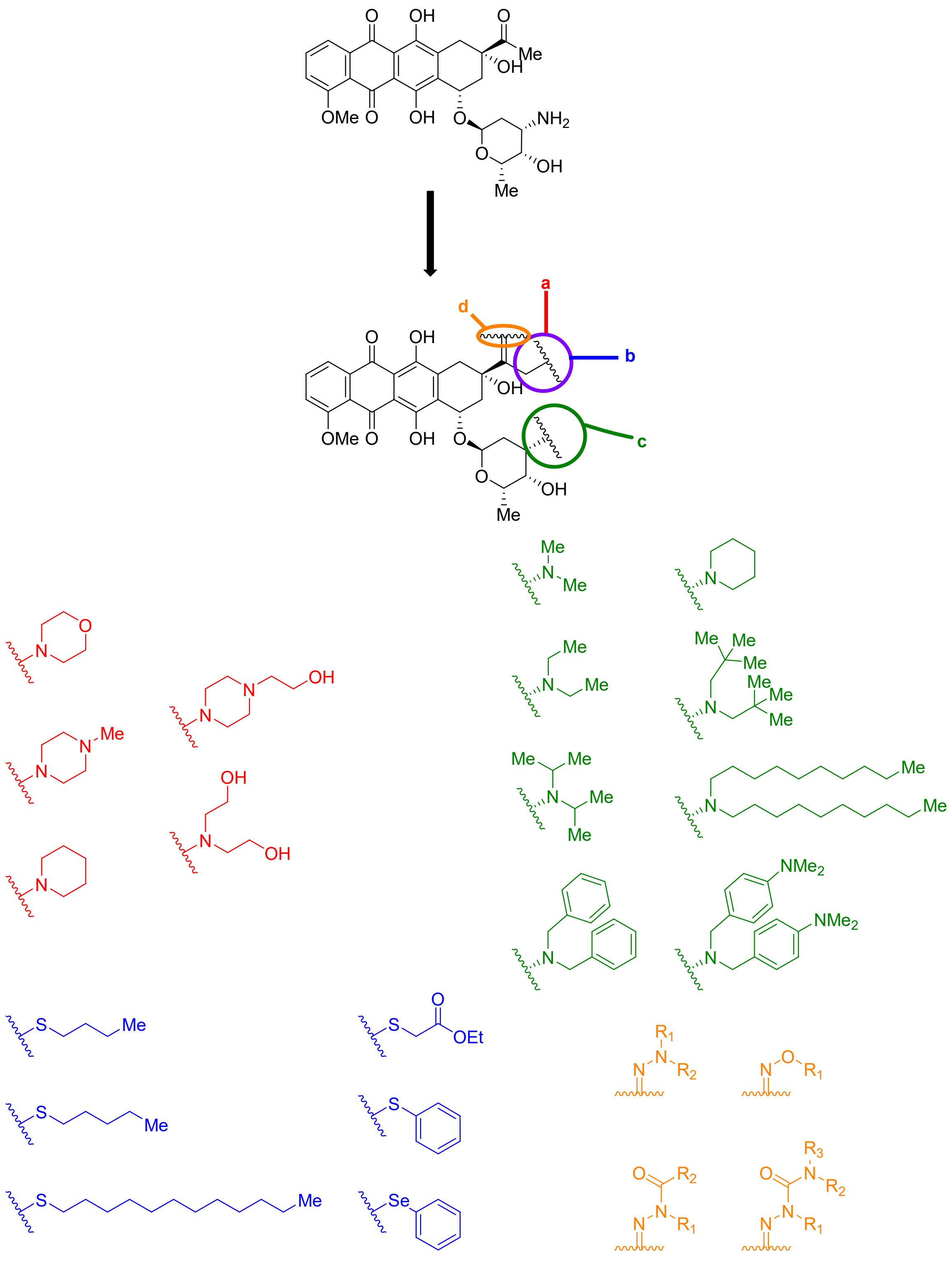

Figure 1.17: Different sites of DAU targeted for synthetic modification in the literature. Examples at each site are provided in the corresponding colors.

in the literature (Yamamoto *et al.*,[160] for example), a quick review of these examples is warranted at this time.

Affixing these functional groups to the C^{13}-carbonyl of DOX or DAU most notably has been used in the synthesis of prodrugs of the anthracyclines. Prodrugs are metabolized in vivo to form the active compound. Prodrugs also are employed often in the study of drug delivery systems. For example, condensation of (6-maleimidocaproyl)hydrazide onto DOX created a derivative of the drug capable of forming a drug-protein crosslink between DOX and albumin. This prodrug, dubbed DOX-EMCH (Figure 1.18a), showed improved cytotoxic effects with decreased cardiotoxicity compared to free DOX in mouse models. This was the first albumin-binding prodrug introduced in the clinic.[162] DOX-EMCH and its successful binding to albumin have inspired prodrugs that use DOX-EMCH to attach peptides to the maleimide moiety. These examples are well-documented in the literature.[163–165] Similarly, many prodrugs have been synthesized by forming an oxime. For example, *N*-(6-thiohexoxy)amine has been used to bridge two units of DOX to a bifunctionalized porphyrazine derivative to improve cellular uptake (Figure 1.18b). While dissociation of DOX is insufficient at physiological pH, the authors of this study have proposed different uses of said linkers.[166] Other handles affixed to the C^{13}-position of DOX via oximes have been used to help promote drug-protein linkages and arms for binding to antibodies by click-chemistry.[167–173]

Methods similar to the ones described have been used in numerous ways to assess the relationship between an anthracycline's structure and its biological activity. Work performed by Mervyn Israel in the 1980s focused heavily on modifying DOX and DAU in specific ways to determine if drug efficacy could be improved. For example, Potti and Israel emphasized the importance of the C^9-hydroxyl by showing that the 9,10-anhydro-modified anthracyclines

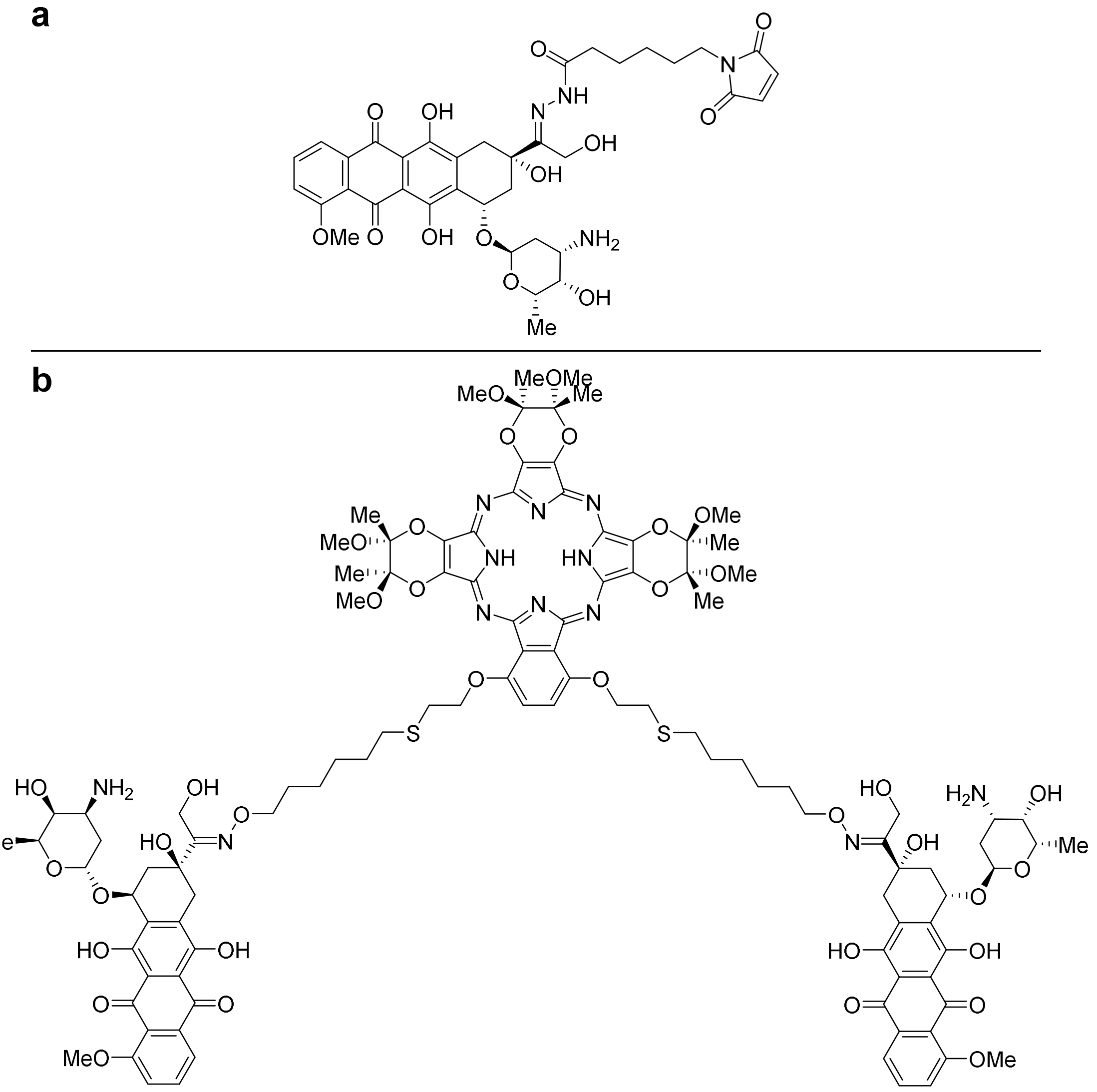

Figure 1.18: *C*^{13}-modified DOX by hydrazone and oxime condensations. a) DOX-EMCH; and b) Porphyrazine-modified DOX.

exhibited significantly less activity.[174] In the same vein, the importance of the stereochemistry of DOX and epirubicin's sugars have been elucidated.[175] Additionally, the length of the saccharide chain attached to the aglycone has been examined. For example, Arcamone *et al*. synthesized a demethoxylated disaccharide derivative of DOX called MEN 10755 (Figure 1.19a). They

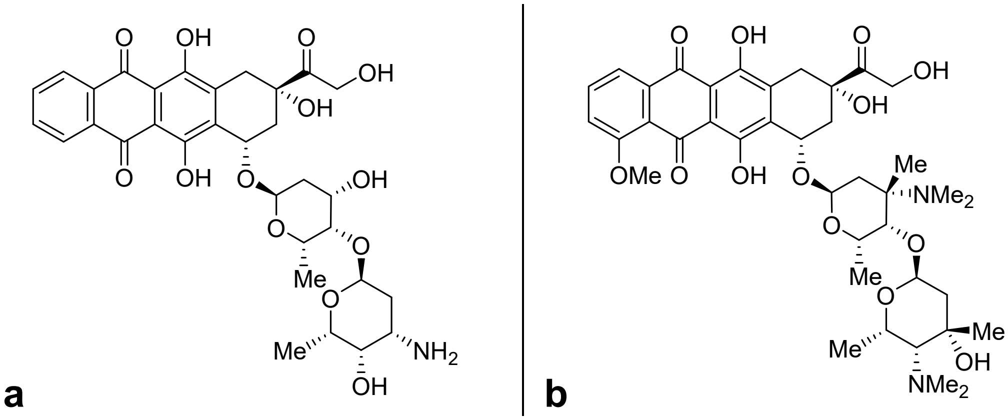

Figure 1.19: DOX derivatives with new glycosides. a) MEN 10755; and b) DOX-Arimetamycin A derivative.

showed that this derivative poisons Top2 more effectively than does DOX, and it caused significant cytotoxicity in MX-1, a DOX-resistant breast cancer cell line.[176]

This is one example of researchers combining aglycones and sugars from different drugs to improve cytotoxicity. An example of this is the study previously mentioned in this dissertation that compared DOX with aclarubicin. Wander *et al.* examined the aglycone structure, saccharide length, and the amino group's methylation status to elucidate which features are most important to these drugs' activities. They found that dimethylated amines improved the cytotoxicity of their non-methylated counterparts.[99] When considering the increased cytotoxic effects of natural products like aclarubicin or arimetamycin A,[177] dimethylated amines might prove to be the source. Similarly to Wander *et al.*, Huseman *et al.* affixed the disaccharide of arimetamycin A with the aglycones of DOX and DAU (Figure 1.19b) to create more potent hybrids than arimetamycin A on its own.[178] These are two of the many examples in the literature where these strategies have been employed.

Another mechanism-of-action exhibited by some of these drugs is covalent crosslinking. The remainder of this section is devoted to further exploring the effect of those adducts.

Drug-DNA Covalent Adducts

Many anticancer antibiotics function by forming covalent crosslinks between strands of DNA or between DNA and proteins. An example is mitomycin C (Figure 1.20a), a toxic antibiotic active against numerous types of cancer.[179] Soon after its discovery in 1956,[180,181] it was shown that mitomycin C inhibited DNA synthesis and caused DNA degradation.[179] It was proposed that this drug forms a crosslink within DNA at the O^6-position of dG.[181,182] It later was determined that the crosslink actually formed between the N^2-position of dG residues in complementary 5'-CpG-3' sequences.[183] Similarly, the antibiotic CC-1065 (Figure 1.20b) covalently binds to the N^3-position of dA residues in AT-rich sequences of DNA to induce a strand break, in addition to noncovalently binding to the minor groove of DNA.[184] In each of these cases, the covalent adduct is cited as a key contributor to the overall toxicity.

MAR70 (Figure 1.21) is a synthetic derivative of DAU where the 4'-hydroxyl of the daunosamine ring is glycosylated by 4'-epi-2'-deoxyfucose. In 1991, Gao *et al.* sought to

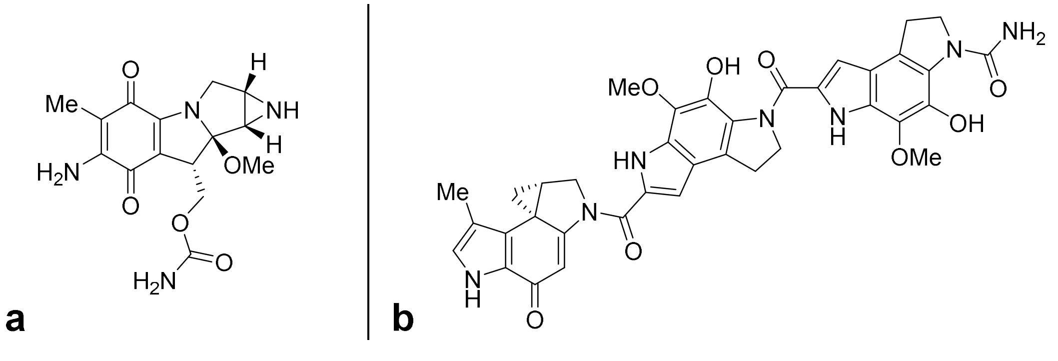

Figure 1.20: Some antibiotics that form DNA-protein crosslinks. a) Mitomycin C; and b) CC-1065.

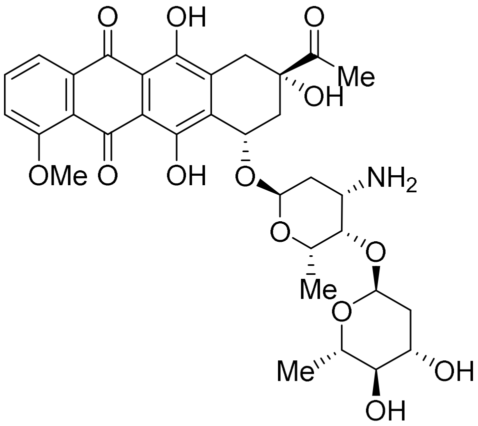

Figure 1.21: MAR70, a synthetic DAU disaccharide derivative.

determine the crystal structure of MAR70 interacting with a DNA oligo hexamer to elucidate its DNA-binding affinity and sequence specificity. However, they fortuitously discovered that trace amounts of formaldehyde in their crystallization buffer formed a methylene crosslink between the 3'-amine of MAR70 and the *N*^{2}-position of 2-aminoadenosine. Crystal structures of this crosslink showed that, with the disaccharide of MAR70 projected into the minor groove (just like DAU, shown in Figure 1.8), the two amino moieties were positioned with the optimal spacing to promote efficient formaldehyde addition.[185] This discovery led them to prove that this crosslink forms between both DAU and DOX and the *N*^{2}-positions of either dG or 2-aminoadenosine (Figure 1.22).[186,187] The *C*^{9}-hydroxyls of DAU and DOX help stabilize the duplex in these structures with strong, non-covalent attractions to the opposite strand.[188] Further evidence of this mechanism of action for anthracyclines like DOX exists, as ^{14}C-labeled DOX-formaldehyde-DNA adducts have been detected in MCF-7 breast cancer cells by accelerator mass spectrometry using clinically relevant concentrations of ^{14}C-labeled DOX.[189] Crosslinks formed by formaldehyde in this manner have been shown to induce a cytotoxic response in tumor cells that

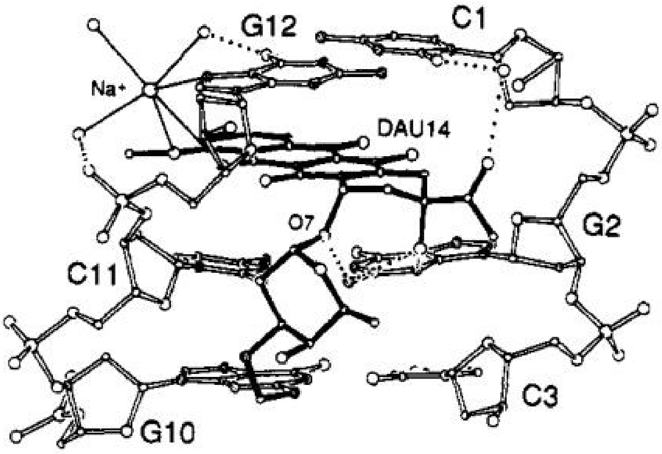

Figure 1.22: Crystal structure of the formaldehyde-mediated covalent crosslink between DAU and a self-complementary DNA hexamer. Sequence is d(CGCGCG). The tight fit of the drug in the minor groove results in a 14.6° buckling of the G2-C11 base pair. Taken from Wang *et al.*[186]

are resistant to DOX. This has led to the belief that the cytotoxicity does *not* come from Top2 poisoning in these cases.[190,191]

These discoveries have opened an interest in certain drug modifications that either release formaldehyde or mimic its reactivity upon hydrolysis or enzymatic activation.[192–195] Of note, in 1997, Fenick *et al*. synthesized two prodrugs called Doxoform and Daunoform (Figure 1.23). These compounds are dimers of the base drugs, bound together by a methylene bridge, where each sugar is modified such that the 3'-amine and 4'-hydroxyl are bound together by a methylene bridge to form an oxazolidine ring. Each of these drugs exhibited greater and faster cytotoxicity than the drugs introduced separately with exogenous formaldehyde. Additionally, Doxoform induced a 150-times greater cytotoxic response than did DOX in MCF-7 breast cancer cells. Its cytotoxic profile extended to MCF-7 cells resistant to DOX.[190] Similarly, a prodrug made from epirubicin and formaldehyde, Epidoxoform (Figure 1.23), has been shown to be more cytotoxic than epirubicin alone in those same cell lines.[196,197]

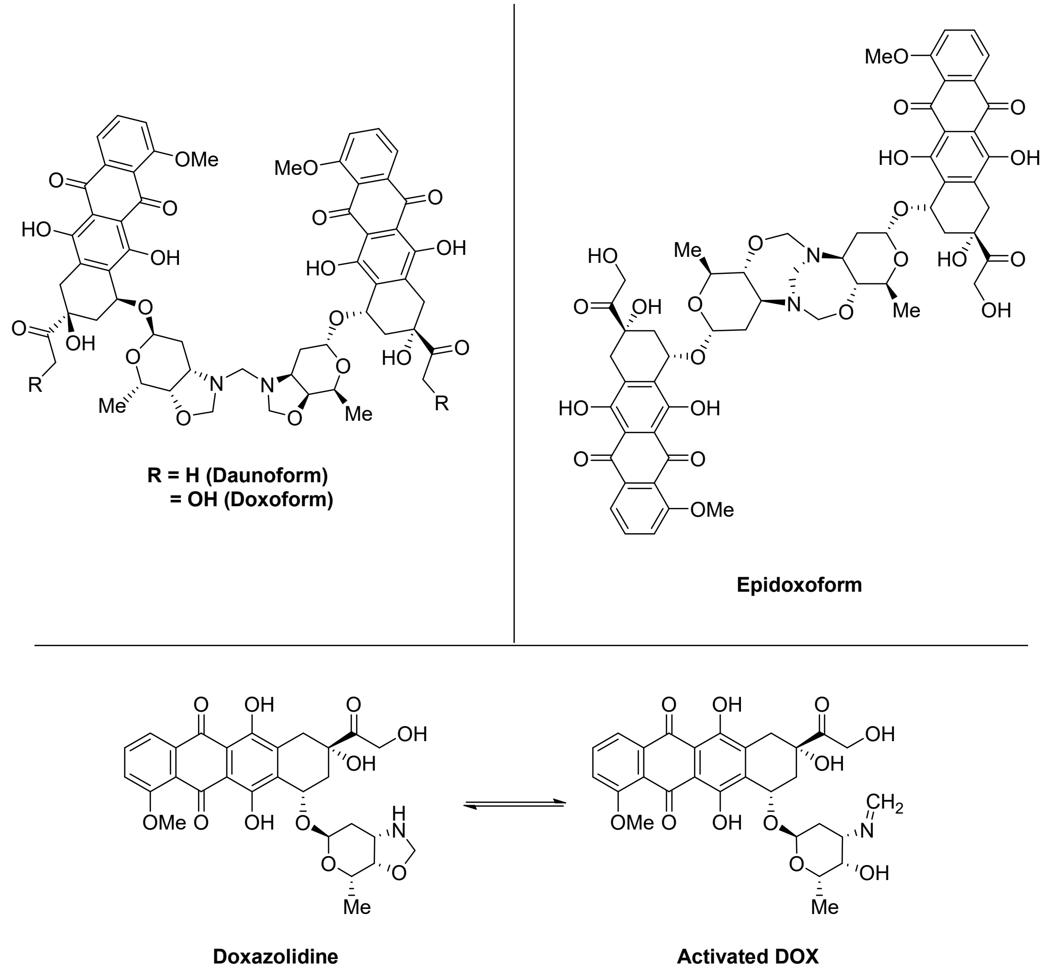

Figure 1.23: Synthetic prodrugs of DOX designed to release formaldehyde upon metabolic activation or hydrolysis. Top left: Daunoform and Doxoform; Top right: Epidoxoform; Bottom: Hydrolytic equilibrium between Doxazolidine and the imine form of activated DOX.

As shown in Figure 1.23, drugs like Doxoform are in tautomeric equilibrium between the oxazolidine and the imine forms.[192] There are many other examples of anthracycline derivatives designed to exhibit similar reactivity. The antibiotic barminomycin (Figure 1.24a) is a derivative of DAU that contains an eight-membered carbinolamine ring attached to the daunosamine residue. A natural anthracycline derivative, it was first isolated from *Actinomadura (microtetraspora) roseoviolacea* var. *miuraensis* in 1985.[198,199] Barminomycin, often referred to

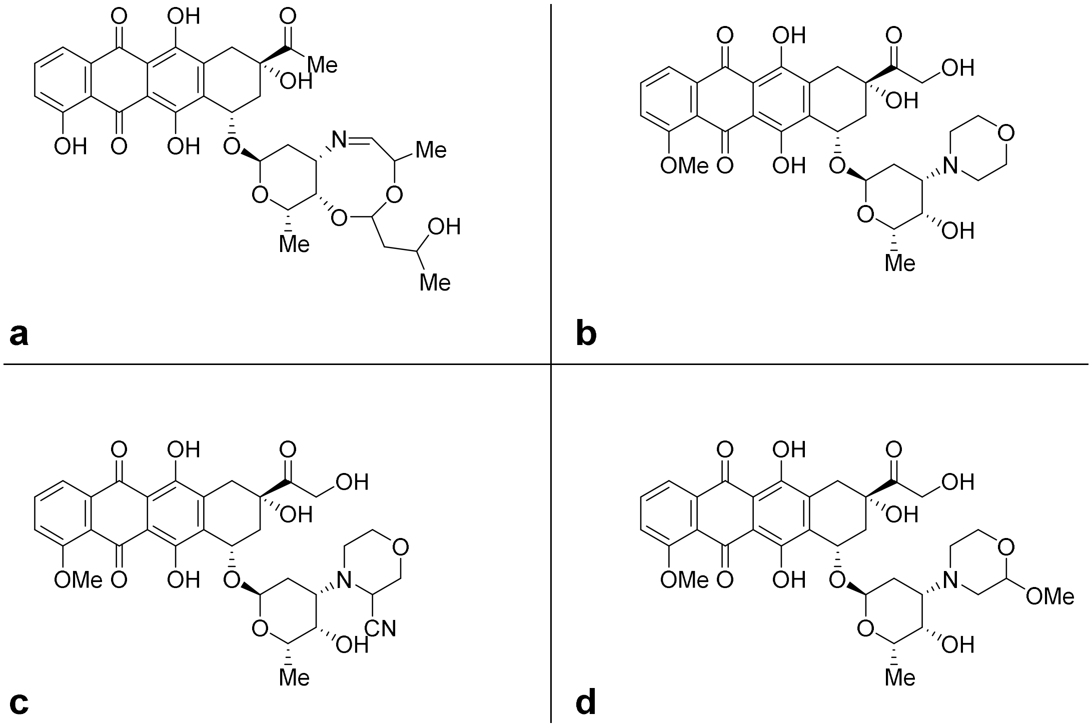

Figure 1.24: DOX modifications designed to form a methylene bridge between the drug and DNA. a) Barminomycin; b) Morpholinodoxorubicin; c) Cyanomorpholinodoxorubicin; and d) Nemorubicin.

as SN-07, is cytotoxic to HeLa cervical cancer cells, among many others.[199,200] DNA adducts form rapidly with barminomycin at a concentration 50-times lower than that of formaldehyde-activated DOX. In addition, it has been shown that barminomycin is 1000-times more cytotoxic to P388 leukemia cells than free DOX, preferentially binding to 5'-GpC-3' sequences in DNA.[199,201] This toxicity is attributed to crosslinks, as the carbinolamine moiety mimics the structure and reactivity of formaldehyde-activated DAU.[199,202]

While studying the alkylation of DOX and DAU by reductive amination onto 2,2'-oxybis(acetaldehyde), Acton *et al.* found a new type of morpholino derivative of anthracyclines (Figure 1.24b-d). A nucleophilic nitrile ion can attack the intermediate of the amination to form cyanomorpholino-modified DOX.[203] Cyanomorpholinodoxorubicin (Figure 1.24c) is 1000-times more potent against leukemia L1210 cells than is DOX.[203,204] While not as active, the 4’-hydroxyl of DOX is capable of adding into the morpholino ring forming a fused daunosamine-oxazolidine-morpholine system.[205] Displacement of the cyanide moiety creates an iminium ion similar to that of formaldehyde-activated DOX, making it susceptible to attack by the N^2-position of dG to form a “methylene” crosslink.[206,207] A similar drug to cyanomorpholinodoxorubicin is called nemorubicin, (Figure 1.24d) the methylated hemiacetal of morpholinodoxorubicin. First synthesized in 1990, it was shown to induce an *in vitro* cytotoxicity in multiple cell lines, inhibiting 50% of growth at drug concentrations 3-times lower than those required of DOX. When metabolically activated by Cytochrome P450 enzymes, a similar pathway as the cyano-modified drug occurs with the activation similar to that of formaldehyde-activated DOX.[208]

Other synthetic drugs with different structures than DAU and DOX also have been shown to covalently conjugate to DNA using formaldehyde (Figure 1.25).[209–214] Of the examples shown in Figure 1.25, those of interest to this report are mitoxantrone and pixantrone. Mitoxantrone (MTX) is a synthetic anthracenedione derivative of the compound amentantrone.[215] The anthraquinone hydroxyls of MTX were added as the result of structure-activity studies showing that MTX exhibited enhanced anticancer activity against P388-leukemia cells and B-16 melanoma systems.[216] MTX is used clinically to treat breast and prostate cancers, lymphomas, and leukemias.[215] In addition to its antineoplastic properties, MTX is used to treat patients with progressive-relapsing multiple sclerosis via immunomodulatory mechanisms.[217] MTX-DNA crosslinks mediated by formaldehyde form *in vitro* and stabilize the DNA duplex by virtual interstrand crosslinks. While the covalent conjugate is stable, the interstrand crosslink is heat-labile with a half-life of 10 min at 60 °C.[210]

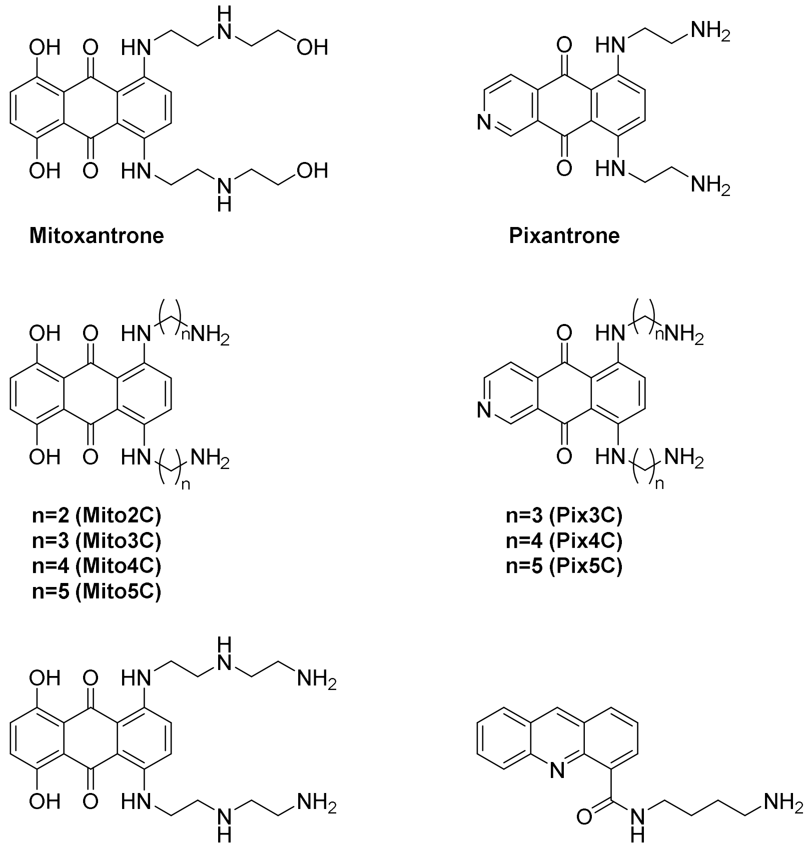

Mitoxantrone

Pixantrone

n=2 (Mito2C)
n=3 (Mito3C)
n=4 (Mito4C)
n=5 (Mito5C)

n=3 (Pix3C)
n=4 (Pix4C)
n=5 (Pix5C)

WEHI-150

Acridine-4-carboxamide

Figure 1.25: Some synthetic drugs reported to form covalent links with DNA mediated by formaldehyde.

Pixantrone (PXT) is another synthetic anthracenedione with a similar structure to MTX. However, the hydroquinone is replaced with a heteroaromatic ring. Additionally, the alkyl chains are shorter in length, terminating with primary amines instead of the *N*-(2-hydroxyethyl)-ethylenediamine. While MTX induced cardiotoxic responses in anthracycline-pretreated animals and patients, PXT did not.[218] Namely, PXT exhibits a marked efficacy against lymphomas and leukemias.[211] However, while PXT is approved for the treatment of non-Hodgkin's B-cell lymphoma in Europe, it currently is stuck in clinical trials in the United States.[219] PXT-DNA crosslinks mediated by formaldehyde form *in vitro*, just like those of MTX. Additionally, PXT-formaldehyde adducts stabilize the duplex in denaturing conditions. However, PXT adducts are shown to form 10- to 100-times more readily than those of MTX and exist with a greater half-life.[211] Site specificity of the PXT-formaldehyde-DNA adducts also has been elucidated.[212]

As previously mentioned, the covalent bond between the drug and DNA is cited as the main source of cytotoxicity for these compounds that induce toxicity in DOX-resistant cell lines. However, these compounds are designed to be hydrolytically unstable as a means of producing endogenous formaldehyde or to metabolically activate to mimic formaldehyde's reactivity (Figure 1.23). Unfortunately, formaldehyde is toxic in its own right and cannot be used in a treatment clinically.[220] As is discussed in the next section of this chapter, an improved treatment regimen can be implemented to enhance covalent crosslinking between drugs and DNA without the use of formaldehyde.

AP Site Covalent Conjugates

Many of the drug modifications discussed in the previous section involve modifying drugs with moieties that mimic formaldehyde's reactivity. In other words, an electrophilic handle is affixed to the drug to promote binding by the nucleophilic sites on DNA (e.g., the N^2-position of dG). However, for reasons previously discussed, these conjugates are not feasible in the clinic due to the release of formaldehyde,[220] either enzymatically or hydrolytically. As such, a new method of covalent binding is necessary for the implementation of these findings to a clinical setting.

AP sites are an electrophilic lesion in an otherwise nucleophilic DNA biomolecule. As previously discussed, a consequence of DNA alkylation by nitrogen mustards is the formation of AP sites. Previous work done by Chen *et al.*, in collaboration with our lab, has shown that the level of naturally occurring AP sites in nuclear DNA of female mice livers are lower than previously reported. This is due to artificial AP site formation during the experimental work-up. In addition, treatment of female mice with the nitrogen mustard HN-1 increased the number of AP sites by 3.7-times over the newly determined baseline of the lesion's natural occurrence.[221,222]

A typical regimen of AC chemotherapy is 4 to 6 cycles of 60 mg/m^2 of DOX over 15 to 60 min and 600 mg/m^2 of CPA over 30 to 60 min, in that order, every 3 weeks.[58–60] However, the nucleophilic moiety of DOX (i.e., the amino sugar) theoretically can bind electrophilic functional groups covalently. For example, amines are known to form Schiff bases in the presence of aldehydes and ketones. AP sites exist as the open-chain aldehyde, albeit in a 1:99 ratio between that and the closed furanose form (Figure 1.26).[223] Therefore, a Schiff base link between AP sites and the amine of DOX is a possibility. By reversing the order in which the drugs are administered during AC chemotherapy and allowing CPA to induce AP sites before introducing DOX, a new mechanism-of-action for this regimen based on the formation of covalent conjugates may result in a yet-to-be-elucidated improvement to current treatment regimens if the AP-DOX conjugate display similar cytotoxicity as DOX-formaldehyde-DNA conjugates. These would form without formaldehyde or formaldehyde-releasing prodrugs (Figure 1.27).

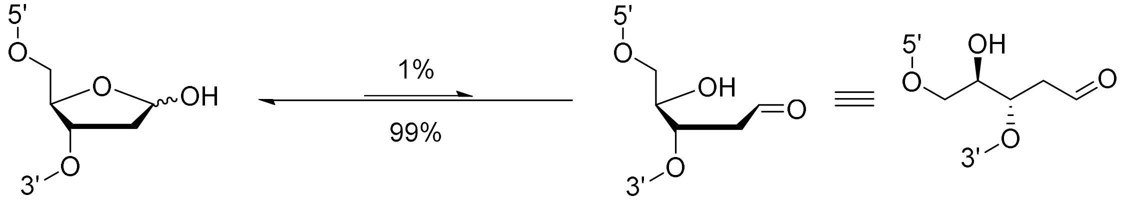

Figure 1.26: Equilibrium between the open-chain and furanose forms of an AP site in DNA.

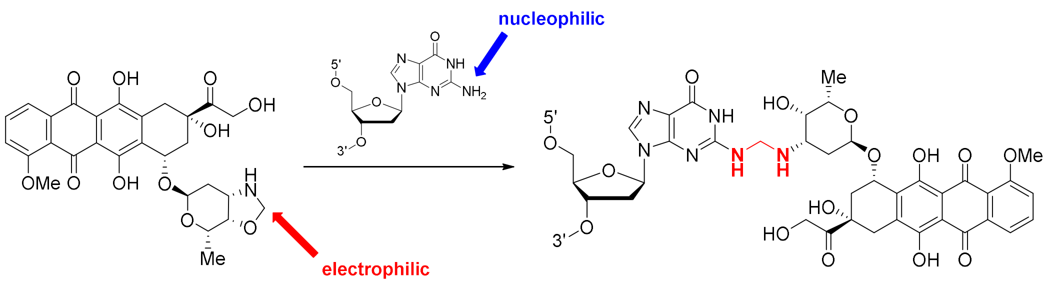

Modifications in the Literature

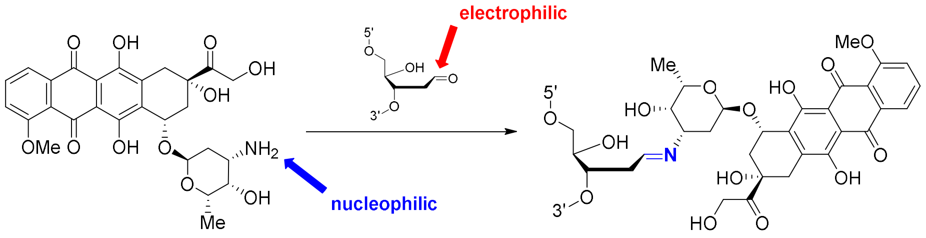

Our hypothesis

Figure 1.27: Comparison of doxazolidine and its reaction with DNA to the proposed Schiff base conjugate of DOX with AP sites in DNA. Covalent linkers are highlighted in color.

We hypothesize that the drugs used in AC chemotherapy can work synergistically to increase the level of AP sites to which the anthracycline can bind covalently. Additionally, we predict that these will be bulky lesions that inhibit DNA synthesis and as a result be cytotoxic. The idea that a nucleophilic agent can bind to AP sites in DNA is supported in the literature and the clinic. For example, methoxyamine sometimes is added to treatment regimens involving temozolomide. Namely, it was shown that temozolomide and methoxyamine induce toxicity in mismatch repair-deficient, temozolomide-resistant HCT116 colon cancer cells.[224,225] Additionally, this strategy for combination therapy has led to the use of methoxyamine for potentiating other agents, as well.[226] Temozolomide is an methylating agent most commonly used in the treatment of astrocytoma, glioblastoma, brain metastases from solid tumors, and melanoma.[227] And, methoxyamine is known to block BER in treated cells.[228,229] The restoration of alkylative damage of temozolomide by methoxyamine in temozolomide-resistant cells is attributed to the oxime conjugates formed between the BER blocker and AP sites induced by the alkylating agent.[227] These examples demonstrate the ability of therapeutic agents and small molecules to covalently bind to induced AP sites in DNA in the manner in which we describe.

Work done by Madjda Bellamri at the University of Minnesota and John T. Terrell in our lab has shown that the anthracyclines DOX and epirubicin, as well as MTX and PXT, are capable of binding AP sites in a 12-base pair DNA duplex and calf-thymus (CT) DNA (*Publication in-progress*). The conjugates observed by reductive amination of MTX and PXT onto an induced AP site in a 12-base pair DNA duplex formed more readily than those of DOX and epirubicin (following the pattern PXT > MTX > epirubicin > DOX). Additionally, the Schiff base formation between MTX and CT DNA was elucidated and quantitated by enzymatic digestion and isotope dilution LC-MS^2 analysis of the hydrolysate.

When treated with both NOR and MTX, breast cancer MDA-MB-231 cells experienced an increased cytotoxic response in a time- and concentration-dependent manner to a greater extent than treatment with NOR on its own. An increase in the number of AP sites as a result of NOR treatment is observed in this cell line, especially in dividing cells. Additionally, quantitation by UPLC-ESI/MS^3 shows that, after 18 hr, levels of MTX conjugate reached as high as 1.50 adducts per 10^5 bases. As these levels were similar to those of AP sites induced by NOR alone, high conversion of AP sites to MTX conjugates can be inferred. These data support our general hypothesis of a new mechanism-of-action for the drugs in this chemotherapeutic regimen (*Publication in-progress*).

Dissertation Aims

As previously discussed, covalent crosslinks between DNA and chemotherapeutics like DOX, mediated by formaldehyde, have been cited as a source of cytotoxicity independent from Top2. The components of AC chemotherapy already exhibit the reactivity necessary to form covalent crosslinks without formaldehyde. AP sites form when DNA is alkylated by NOR (a metabolite of CPA). Additionally, nucleophilic moieties of certain drugs and small molecules are capable of binding to AP sites (Figure 1.27). This is a new, synergistic mechanism-of-action for these drugs which may contribute to the overall toxicity of the regimen.

Previous work in our lab, in collaboration with Dr. Robert Turesky's lab of the Masonic Cancer Center and Department of Medicinal Chemistry at the University of Minnesota, has shown that the chemotherapeutics DOX, epirubicin, MTX, and PXT are capable of binding to AP sites (formed naturally or by deglycosylation of alkylated bases) in DNA in the manner in which we have described. However, the Schiff base conjugates proposed are hydrolytically unstable at physiological pH; that is why Bellamri *et al*. (*Publication in-progress*) had to reduce the Schiff base conjugate with sodium cyanoborohydride before mass spectrometric analysis. The aim of this dissertation is to synthetically modify chemotherapeutics with "stronger" nucleophilic moieties. Doing so will result in more stable conjugates with AP sites that will not hydrolyze at physiological pH. Because of the complexity of DOX and the related chemotherapeutics, this dissertation focuses mainly on two anthraquinone derivatives (Figure 1.28).

In Chapter II, the modification examined is that of 2-aminoxyacetamides. The syntheses of these modified anthraquinones are examined. Their reactivity with AP sites in a 12-base pair

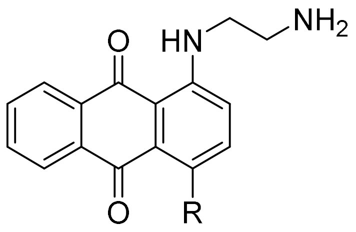

R = OH (2-5)

= $NH(CH_2)_2NH_2$ (2-8)

Figure 1.28: Anthraquinone derivatives used as base drugs in this dissertation.

DNA duplex are characterized by LC-MS^2, and the kinetic profile of the reactions are modeled using data from HPLC and the modeling software COPASI.[230] The aims of this chapter are:

1. Synthesize the desired aminoxyacetamide-modified anthraquinones.
2. Model and characterize the anthraquinones' reactivity with AP sites using a 12-base pair DNA duplex.
3. Examine the reactions between the anthraquinones and the 12-base pair DNA duplex to elucidate a rate law governing their reactivity.

References

1. Faguet, G. An Historical Overview: From Prehistory to WWII. in *The Conquest of Cancer: A distant goal* 13–33 (Springer Netherlands, 2015). doi:10.1007/978-94-017-9165-6_2
2. Rothschild, B. M., Tanke, D. H., Helbling, M. & Martin, L. D. Epidemiologic study of tumors in dinosaurs. *Naturwissenschaften* **90**, 495–500 (2003).
3. Breasted, J. H. Case Thirty-Nine: Tumors or Ulcers in the Breast Perhaps Resulting from Injury. in *The Edwin Smith Surgical Papyrus* **1: Hierogl**, 363–369 (University of Chicago,

Oriental Institute, 1930).

4. Breasted, J. H. Case Forty-Five: Bulging Tumors on the Breast. in *The Edwin Smith Surgical Papyrus* **1: Hierogl**, 403–406 (University of Chicago, Oriental Institute, 1930).
5. Hajdu, S. I. A note from history: Landmarks in history of cancer, part 1. *Cancer* **117**, 1097–1102 (2011).
6. Bolton, H. C. *Papyrus Ebers: the earliest medical work extant*. (Weekly Drug News Press, 1884).
7. Schultz, M., Parzinger, H., Posdnjakov, D. V., Chikisheva, T. A. & Schmidt-Schultz, T. H. Oldest known case of metastasizing prostate carcinoma diagnosed in the skeleton of a 2,700-year-old Scythian king from Arzhan (Siberia, Russia). *Int. J. Cancer* **121**, 2591–2595 (2007).
8. cancer | Etymology, origin and meaning of cancer by etymonline. Available at: https://www.etymonline.com/word/cancer. (Accessed: 14th May 2022)
9. Faguet, G. The Four-Decade Journey to the National Cancer Act of 1971. in *The Conquest of Cancer: A distant goal* 3–9 (Springer Netherlands, 2015). doi:10.1007/978-94-017-9165-6_1
10. DeVita, V. T. & Rosenberg, S. A. Two Hundred Years of Cancer Research. *N. Engl. J. Med.* **366**, 2207–2214 (2012).
11. What Is Cancer? - NCI. Available at: https://www.cancer.gov/about-cancer/understanding/what-is-cancer. (Accessed: 14th May 2022)
12. What are oncogenes? *Office for Science and Society - McGill University* Available at: https://www.mcgill.ca/oss/article/health-you-asked/what-are-oncogenes. (Accessed: 14th May 2022)

13. The p53 tumor suppressor protein. *Genes and Disease [Internet]* (1998). Available at: https://www.ncbi.nlm.nih.gov/books/NBK22268/. (Accessed: 14th May 2022)

14. Moore, P. & Strauss, B. S. Sites of inhibition of in vitro DNA synthesis in carcinogen- and UV-treated Φ174 DNA. *Nature* **278**, 664–666 (1979).

15. Marnett, L. J. & Burcham, P. C. Endogenous DNA Adducts: Potential and Paradox. *Chem. Res. Toxicol.* **6**, 771–785 (1993).

16. Cadenas, E. Biochemistry of Oxygen Toxicity. *Annu. Rev. Biochem.* **58**, 79–110 (1989).

17. Ames, B. N. & Gold, L. S. Endogenous mutagens and the causes of aging and cancer. *Mutat. Res.* **250**, 3–16 (1991).

18. Marnett, L. J. & Plastaras, J. P. Endogenous DNA damage and mutation. *Trends Genet.* **17**, 214–221 (2001).

19. Roberts, K. P., Sobrino, J. A., Payton, J., Mason, L. B. & Turesky, R. J. Determination of Apurinic/Apyrimidinic Lesions in DNA with High-Performance Liquid Chromatography and Tandem Mass Spectrometry. *Chem. Res. Toxicol.* **19**, 300–309 (2006).

20. Hemminki, K. Nucleic acid adducts of chemical carcinogens and mutagens. *Arch. Toxicol.* **52**, 249–285 (1983).

21. Gates, K. S., Nooner, T. & Dutta, S. Biologically relevant chemical reactions of N7-alkylguanine residues in DNA. *Chemical Research in Toxicology* **17**, 839–856 (2004).

22. de Jong, W. W. & Rydén, L. Causes of more frequent deletions than insertions in mutations and protein evolution. *Nature* **290**, 157–159 (1981).

23. Iyer, R. R., Pluciennik, A., Burdett, V. & Modrich, P. L. DNA mismatch repair: Functions and mechanisms. *Chem. Rev.* **106**, 302–323 (2006).

24. Gillet, L. C. J. & Schärer, O. D. Molecular mechanisms of mammalian global genome

nucleotide excision repair. *Chem. Rev.* **106**, 253–276 (2006).

25. Lindahl, T. & Wood, R. D. Quality control by DNA repair. *Science (80-.).* **286**, 1897–1905 (1999).

26. Wilson III, D. M., Takeshita, M., Grollman, A. P. & Demple, B. Incision Activity of Human Apurinic Endonuclease (Ape) at Abasic Site Analogs in DNA. *J. Biol. Chem.* **270**, 16002–16007 (1995).

27. Mol, C. D., Izumi, T., Mitra, S. & Tainer, J. A. DNA-bound structures and mutants reveal abasic DNA binding by APE1 DNA repair and coordination. *Nature* **403**, 451–456 (2000).

28. Mullen, G. P. & Wilson, S. H. DNA polymerase β in abasic site repair: A structurally conserved helix- hairpin-helix motif in lesion detection by base excision repair enzymes. *Biochemistry* **36**, 4713–4717 (1997).

29. Stivers, J. T. & Jiang, Y. L. A mechanistic perspective on the chemistry of DNA repair glycosylases. *Chemical Reviews* **103**, 2729–2759 (2003).

30. Piersen, C. E., McCullough, A. K. & Lloyd, R. S. AP lyases and dRPases: commonality of mechanism. *Mutat. Res.* **459**, 43–53 (2000).

31. Klungland, A. & Lindahl, T. Second pathway for completion of human DNA base excision-repair: reconstitution with purified proteins and requirement for DNase IV (FEN1). *EMBO J.* **16**, 3341–3348 (1997).

32. Radiation Therapy to Treat Cancer - NCI. Available at: https://www.cancer.gov/about-cancer/treatment/types/radiation-therapy#TCRT. (Accessed: 24th May 2022)

33. Hormone Therapy for Cancer - NCI. Available at: https://www.cancer.gov/about-cancer/treatment/types/hormone-therapy. (Accessed: 27th May 2022)

34. Beatson, G. T. On the Treatment of Inoperable Cases of Carcinoma of the Mamma:

Suggestions for a New Method of Treatment, with Illustrative Cases. *Lancet* **148**, 104–107 (1896).

35. Huggins, C. & Hodges, C. V. Studies on Prostatic Cancer. I. The Effect of Castration, of Estrogen and of Androgen Injection on Serum Phosphatases in Metastatic Carcinoma of the Prostate. *Cancer Res.* **1**, 293–297 (1941).
36. Smith, I. E. & Dowsett, M. Aromatase Inhibitors in Breast Cancer. *N. Engl. J. Med.* **348**, 2431–2442 (2003).
37. Syn, N. L., Teng, M. W. L., Mok, T. S. K. & Soo, R. A. De-novo and acquired resistance to immune checkpoint targeting. *Lancet Oncol.* **18**, e731–e741 (2017).
38. Immunotherapy for Cancer - NCI. Available at: https://www.cancer.gov/about-cancer/treatment/types/immunotherapy. (Accessed: 28th May 2022)
39. Immunotherapy | Memorial Sloan Kettering Cancer Center. Available at: https://www.mskcc.org/cancer-care/diagnosis-treatment/cancer-treatments/immunotherapy. (Accessed: 28th May 2022)
40. DeVita, V. T. & Chu, E. A History of Cancer Chemotherapy. *Cancer Res.* **68**, 8643–8653 (2008).
41. Strebhardt, K. & Ullrich, A. Paul Ehrlich's magic bullet concept: 100 years of progress. *Nat. Rev. Cancer* **8**, 473–480 (2008).
42. Goodman, L. S. *et al.* Nitrogen Mustard Therapy: Use of Methyl-Bis(Beta-Chloroethyl)amine Hydrochloride and Tris(Beta-Chloroethyl)amine Hydrochloride for Hodgkin's Disease, Lymphosarcoma, Leukemia and Certain Allied and Miscellaneous Disorders. *J. Am. Med. Assoc.* **132**, 126–132 (1946).
43. Pinkel, D. Actinomycin D in Childhood Cancer: A Preliminary Report. *Pediatrics* **23**,

342–347 (1959).

44. Dasari, S. & Bernard Tchounwou, P. Cisplatin in cancer therapy: Molecular mechanisms of action. *Eur. J. Pharmacol.* **740**, 364–378 (2014).

45. Rosenberg, B., Van Camp, L. & Krigas, T. Inhibition of Cell Division in Escherichia coli by Electrolysis Products from a Platinum Electrode. *Nature* **205**, 698–699 (1965).

46. Jamieson, E. R. & Lippard, S. J. Structure, recognition, and processing of cisplatin-DNA adducts. *Chem. Rev.* **99**, 2467–2498 (1999).

47. Goodsell, D. S. The Molecular Perspective: Cisplatin. *Stem Cells* **24**, 514–515 (2006).

48. Fichtinger-Schepman, A. M. J., van der Veer, J. L., den Hartog, J. H. J., Lohman, P. H. M. & Reedijk, J. Adducts of the Antitumor Drug cis-Diamminedichloroplatinum(II) with DNA: Formation, Identification, and Quantitation. *Biochemistry* **24**, 707–713 (1985).

49. Gottesman, M. M., Fojo, T. & Bates, S. E. Multidrug resistance in cancer: role of ATP–dependent transporters. *Nat. Rev. Cancer* **2**, 48–58 (2002).

50. Frei III, E. *et al.* The Effectiveness of Combinations of Antileukemic Agents in Inducing and Maintaining Remission in Children with Acute Leukemia. *Blood* **26**, 642–656 (1965).

51. Mokhtari, R. B. *et al.* Combination therapy in combating cancer. *Oncotarget* **8**, 38022–38043 (2017).

52. Bonadonna, G. *et al.* Combination Chemotherapy as an Adjuvant Treatment in Operable Breast Cancer. *N. Engl. J. Med.* **294**, 405–410 (1976).

53. Buzdar, A. U. *et al.* Postoperative Adjuvant Chemotherapy With Fluorouracil, Doxorubicin, Cyclophosphamide, and BCG Vaccine: A Follow-up Report. *J. Am. Med. Assoc.* **242**, 1509–1513 (1979).

54. Brambilla, C., De Lena, M., Rossi, A., Valagussa, P. & Bonadonna, G. Response and

survival in advanced breast cancer after two non-cross-resistant combinations. *Br. Med. J.* **1**, 801–804 (1976).

55. Rainey, J. M., Jones, S. E. & Salmon, S. E. Combination chemotherapy for advanced breast cancer utilizing vincristine, adriamycin, and cyclophosphamide (VAC). *Cancer* **43**, 66–71 (1979).

56. Perlow, L. S. & Holland, J. F. Chemotherapy of breast cancer. *Med. Oncol. Tumor Pharmacother.* **1**, 169–192 (1984).

57. Corbett, T. H., Griswold, D. P., Mayo, J. G., Laster, W. R. & Schabel Jr, F. M. Cyclophosphamide-Adriamycin Combination Chemotherapy of Transplantable Murine Tumors. *Cancer Res.* **35**, 1568–1573 (1975).

58. Jones, S. E., Durie, B. G. M. & Salmon, Y. E. Combination chemotherapy with adriamycin and cyclophosphamide for advanced breast cancer. *Cancer* **36**, 90–97 (1975).

59. Breast Cancer Now: The research & care charity. AC chemotherapy. (2018). Available at: https://breastcancernow.org/information-support/facing-breast-cancer/going-through-breast-cancer-treatment/chemotherapy/ac-chemotherapy. (Accessed: 6th July 2022)

60. Brenner, T., Duggal, S. & Natale, J. Treatment protocols for breast cancer. *UpToDate* (2020). Available at: https://www.uptodate.com/contents/treatment-protocols-for-breast-cancer?search=ac chemotherapy&sectionRank=1&usage_type=default&anchor=H931995934&source=machineLearning&selectedTitle=1~150&display_rank=1#H931995934. (Accessed: 6th July 2022)

61. Gilman, A. & Philips, F. S. The biological actions and therapeutic applications of the B-chloroethyl amines and sulfides. *Science (80-.).* **103**, 409–436 (1946).

62. Diethelm-Varela, B., Ai, Y., Liang, D. & Xue, F. Nitrogen Mustards as Anticancer Chemotherapies: Historic Perspective, Current Developments and Future Trends. *Curr. Top. Med. Chem.* **19**, 691–712 (2019).

63. Malayappan, B. *et al.* Quantitative high-performance liquid chromatography-electrospray ionization tandem mass spectrometry analysis of bis- n 7-guanine DNA-DNA cross-links in white blood cells of cancer patients receiving cyclophosphamide therapy. *Anal. Chem.* **82**, 3650–3658 (2010).

64. Boddy, A. V. & Yule, S. M. Metabolism and pharmacokinetics of oxazaphosphorines. *Clinical Pharmacokinetics* **38**, 291–304 (2000).

65. Mehta, J. R., Przybylski, M. & Ludlum, D. B. Alkylation of Guanosine and Deoxyguanosine by Phosphoramide Mustard. *Cancer Res.* **40**, 4183–4186 (1980).

66. Colvin, M., Brundrett, R. B., Kan, M. N., Jardine, I. & Fenselau, C. Alkylating properties of phosphoramide mustard. *Cancer Res.* **36**, 1126 (1976).

67. Maccubbin, A. E., Caballes, L., Riordan, J. M., Huang, D. H. & Gurtoo, H. L. A Cyclophosphamide/DNA Phosphoester Adduct Formed in Vitro and in Vivo. *Cancer Res.* **51**, 886–892 (1991).

68. Hemminki, K., Alhonen, A., Linkola, E. & Hesso, A. Kinetics of hydrolysis in vitro of nornitrogen mustard, a metabolite of phosphoramide mustard and cyclophosphamide. *Arch. Toxicol.* **61**, 126–130 (1987).

69. Johnson, L. A. *et al.* Formation of Cyclophosphamide Specific DNA Adducts in Hematological Diseases. *Pediatr. Blood Cancer* **58**, 708–714 (2012).

70. Hemminki, K. Reactions of ethyleneimine with guanosine and deoxyguanosine. *Chem. Biol. Interact.* **48**, 249–260 (1984).

71. Gruppi, F. *et al.* Characterization of Nitrogen Mustard Formamidopyrimidine Adduct Formation of Bis(2-chloroethyl)ethylamine with Calf Thymus DNA and a Human Mammary Cancer Cell Line. *Chem. Res. Toxicol.* **28**, 1850–1860 (2015).

72. Klamerth, O. L. Abnormal base pairing under the influence of nitrogen mustard. *FEBS Lett.* **29**, 35–37 (1973).

73. Osawa, T., Davies, D. & Hartley, J. A. Mechanism of cell death resulting from DNA interstrand cross-linking in mammalian cells. *Cell Death Dis.* **2**, e187–e187 (2011).

74. Arcamone, F. New antitumor anthracyclines. *Lloydia* **40**, 45–66 (1977).

75. Fujiwara, A., Hoshino, T. & Westley, J. W. Anthracycline Antibiotics. *Crit. Rev. Biotechnol.* **3**, 133–157 (1985).

76. American Society of Health-System Pharmacists. DOXOrubicin. *Drugs.com - Monograph for Professionals* (2021). Available at: https://www.drugs.com/monograph/doxorubicin.html?references=1. (Accessed: 19th June 2022)

77. Gill, P. S. *et al.* Systemic treatment of AIDS-related kaposi's sarcoma: Results of a randomized trial. *Am. J. Med.* **90**, 427–433 (1991).

78. Vogelzang, N. J. *et al.* Methotrexate, Vinblastine, Doxorubicin and Cisplatin followed by Radiotherapy or Surgery for Muscle Invasive Bladder Cancer: The University of Chicago Experience. *J. Urol.* **149**, 753–757 (1993).

79. Di Marco, A., Soldati, M., Fioretti, A. & Dasdia, T. Activity of Daunomycin, a New Antitumor Antibiotic, on Normal and Neoplastic Cells Grown in vitro. *Cancer Chemother. Reports* **38**, 39–47 (1964).

80. Di Marco, A. *et al.* 'Daunomycin', a New Antibiotic of the Rhodomycin Group. *Nature*

201, 706–707 (1964).

81. Tan, C., Tasaka, H., Yu, K.-P., Murphy, M. L. & Karnofsky, D. A. Daunomycin, an antitumor antibiotic, in treatment of neoplastic disease: Clinical Evaluation with Special Reference to Childhood Leukemia. *Cancer* **20**, 333–353 (1967).
82. Arcamone, F. *et al.* Adriamycin, 14-hydroxydaimomycin, a new antitumor antibiotic from S. Peucetius var. caesius. *Biotechnol. Bioeng.* **11**, 1101–1110 (1969).
83. Arcamone, F., Franceschi, G., Penco, S. & Selva, A. Adriamycin (14-hydroxydaunomycin), a novel antitumor antibiotic. *Tetrahedron Lett.* **10**, 1007–1010 (1969).
84. Di Marco, A., Gaetani, M. & Scarpinato, B. Adriamycin (NSC-123,127): a New Antibiotic with Antitumor Activity. *Cancer Chemother. Reports* **53**, 33–38 (1969).
85. Casey, M. L., Paulick, R. C. & Whitlock, H. W. Carbon-13 Nuclear Magnetic Resonance Study of the Biosynthesis of Daunomycin and Islandicin. *J. Org. Chem.* **43**, 1627–1634 (1978).
86. Yoshimoto, A., Oki, T., Takeuchi, T. & Umezawa, H. Microbial Conversion of Anthracyclinones to Daunomycin by Blocked Mutants of Streptomyces coeruleorubidus. *J. Antibiot. (Tokyo).* **33**, 1158–1166 (1980).
87. Yoshimoto, A., Oki, T. & Umezawa, H. Biosynthesis of daunomycinone from aklavinone and E-rhodomycinone. *J. Antibiot. (Tokyo).* **33**, 1199–1201 (1980).
88. Walczak, R. J., Dickens, M. L., Priestley, N. D. & Strohl, W. R. Purification, properties, and characterization of recombinant Streptomyces sp. strain C5 DoxA, a cytochrome P-450 catalyzing multiple steps in doxorubicin biosynthesis. *J. Bacteriol.* **181**, 298–304 (1999).

89. Otten, S. L., Liu, X., Ferguson, J. & Hutchinson, C. R. Cloning and characterization of the Streptomyces peucetius dnrQS genes encoding a daunosamine biosynthesis enzyme and a glycosyl transferase involved in daunorubicin biosynthesis. *J. Bacteriol.* **177**, 6688–6692 (1995).

90. Arcamone, F., Barbieri, W., Franceschi, G. & Penco, S. Conversion of daunomycin to adriamycin. *Chim. e l'Industria* **51**, 834–835 (1969).

91. Wong, C. M., Schwenk, R., Popien, D. & Ho, T.-L. The Total Synthesis of Daunomycinone. *Can. J. Chem.* **51**, 466–467 (1973).

92. Vogel, P. Combinatorial Synthesis of Linearly Condensed Polycyclic Compounds, IncludingAnthracyclinones, Through Tandem Diels–Alder Additions. in *Anthracycline Chemistry and Biology 1. Topics in Current Chemistry* (ed. Krohn, K.) **282**, 187–214 (Springer-Verlag Berlin Heidelberg, 2007).

93. Mahaim, C., Carrupt, P., Hagenbuch, J., Florey, A. & Vogel, P. An Efficient Synthesis of 2,3,5,6-Tetramethylidene-7-oxanorbornane. *Helv. Chim. Acta* **63**, 1149–1157 (1980).

94. Iselin, B. & Reichstein, T. Krystallisierte 2-Desoxy-l-rhamnose (2-Desoxy-l-chinovose). Desoxyzucker. 2. Mitteilung. *Helv. Chim. Acta* **27**, 1146–1149 (1944).

95. Marsh, J. P., Mosher, C. W., Acton, E. M. & Goodman, L. The synthesis of daunosamine. *Chem. Commun.* 973b – 975 (1967). doi:10.1039/C1967000973B

96. Acton, E. M., Fujiwara, A. N. & Henry, D. W. Total Synthesis of the Antitumor Antibiotic Daunorubicin. Coupling of the Sugar and Aglycone. *J. Med. Chem.* **17**, 659–660 (1974).

97. Kimura, Y., Suzuki, M., Matsumoto, T., Abe, R. & Terashima, S. Novel Glycosidation of 4-Demethoxyanthracyclinones by the Use of Trimethylsilyl Triflate. Syntheses of

Optically Active 4-Demethoxydaunorubicin and 4-Demethoxyadriamycin. *Bull. Chem. Soc. Jpn.* **59**, 423–431 (1986).

98. Yu, B. Gold(I)-Catalyzed Glycosylation with Glycosyl o-Alkynylbenzoates as Donors. *Acc. Chem. Res.* **51**, 507–516 (2018).

99. Wander, D. P. A. *et al.* Doxorubicin and Aclarubicin: Shuffling Anthracycline Glycans for Improved Anticancer Agents. *J. Med. Chem.* **63**, 12814–12829 (2020).

100. Leonard, G. A., Hambley, T. W., McAuley-Hecht, K., Brown, T. & Hunter, W. N. Anthracycline-DNA interactions at unfavourable base-pair triplet-binding sites: structures of d(CGGCCG)/daunomycin and d(TGGCCA)/adriamycin complexes. *Acta Crystallogr. Sect. D* **49**, 458–467 (1993).

101. Lerman, L. S. Structural considerations in the interaction of DNA and acridines. *J. Mol. Biol.* **3**, 18–30 (1961).

102. Berman, H. M. & Young, P. R. The Interaction of Intercalating Drugs with Nucleic Acids. *Annu. Rev. Biophys. Bioeng.* **10**, 87–114 (1981).

103. Capranico, G., Soranzo, C. & Zunino, F. Single-strand DNA breaks induced by chromophore-modified anthracyclines in P388 leukemia cells. *Cancer Res.* **46**, 5499–5503 (1986).

104. Mukherjee, A. & Sasikala, W. D. Drug-DNA intercalation: From discovery to the molecular mechanism. in *Advances in Protein Chemistry and Structural Biology* **92**, 1–62 (Academic Press Inc., 2013).

105. Wang, A. H., Ughetto, G., Quigley, G. J. & Rich, A. Interactions between an Anthracycline Antibiotic and DNA: Molecular Structure of Daunomycin Complexed to d(CpGpTpApCpG) at 1.2-Å Resolution. *Biochemistry* **26**, 1152–1163 (1987).

106. Quigley, G. J. *et al.* Molecular structure of an anticancer drug-DNA complex: Daunomycin plus d(CpGpTpApCpG). *Proc. Natl. Acad. Sci. U. S. A.* **77**, 7204–7208 (1980).

107. Mukherjee, A., Lavery, R., Bagchi, B. & Hynes, J. T. On the molecular mechanism of drug intercalation into DNA: A simulation study of the intercalation pathway, free energy, and DNA structural changes. *J. Am. Chem. Soc.* **130**, 9747–9755 (2008).

108. Chaires, J. B., Dattagupta, N. & Crothers, D. M. Kinetics of the Daunomycin-DNA Interaction. *Biochemistry* **24**, 260–267 (1985).

109. Macgregor, R. B., Clegg, R. M. & Jovin, T. M. Viscosity Dependence of Ethidium-DNA Intercalation Kinetics. *Biochemistry* **26**, 4008–4016 (1987).

110. Gellert, M. DNA Topoisomerases. *Annu. Rev. Biochem.* **50**, 879–910 (1981).

111. Wang, J. C. DNA Topoisomerases. *Annu. Rev. Biochem.* **54**, 665–697 (1985).

112. White, J. H. Self-Linking and the Gauss Integral in Higher Dimensions. *Am. J. Math.* **91**, 693–728 (1969).

113. Lavery, R., Lebrun, A., Allemand, J.-F., Bensimon, D. & Croquette, V. Structure and mechanics of single biomolecules: experiment and simulation. *J. Phys. Condens. Matter* **14**, R383–R414 (2002).

114. Shimada, J. & Yamakawa, H. Ring-Closure Probabilities for Twisted Wormlike Chains. Application to DNA. *Macromolecules* **17**, 689–698 (1984).

115. Deweese, J. E. & Osheroff, N. The DNA cleavage reaction of topoisomerase II: wolf in sheep's clothing. *Nucleic Acids Res.* **37**, 738–748 (2009).

116. Berger, J. M., Gamblin, S. J., Harrison, S. C. & Wang, J. C. Structure and mechanism of DNA topoisomerase II. *Nature* **379**, 225–232 (1996).

117. Cornarotti, M. *et al.* Drug sensitivity and sequence specificity of human recombinant DNA topoisomerases IIα (p170) and IIβ (p180). *Mol. Pharmacol.* **50**, 1463–1471 (1996).

118. Wang, J. C. Cellular roles of DNA topoisomerases: a molecular perspective. *Nat. Rev. Mol. Cell Biol.* **3**, 430–440 (2002).

119. McClendon, A. K. & Osheroff, N. DNA topoisomerase II, genotoxicity, and cancer. *Mutat. Res.* **623**, 83–97 (2007).

120. Liu, L. F. DNA Topoisomerase Poisons as Antitumor Drugs. *Annu. Rev. Biochem.* **58**, 351–375 (1989).

121. Tewey, K. M., Chen, G. L., Nelson, E. M. & Liu, L. F. Intercalative Antitumor Drugs Interfere with the Breakage-Reunion Reaction of Mammalian DNA Topoisomerase II. *J. Biol. Chem.* **259**, 9182–9187 (1984).

122. Tewey, K. M., Rowe, T. C., Yang, L., Halligan, B. D. & Liu, L. F. Adriamycin-induced DNA damage mediated by mammalian DNA topoisomerase II. *Science (80-.).* **226**, 466–468 (1984).

123. Chen, G. L. *et al.* Nonintercalative antitumor drugs interfere with the breakage-reunion reaction of mammalian DNA topoisomerase II. *J. Biol. Chem.* **259**, 13560–13566 (1984).

124. Nitiss, J. L. & Wang, J. C. Mechanisms of cell killing by drugs that trap covalent complexes between DNA topoisomerases and DNA. *Mol. Pharmacol.* **50**, 1095–1102 (1996).

125. Capranico, G., Kohn, K. W. & Pommier, Y. Local sequence requirements for DNA cleavage by mammalian topoisomerase II in the presence of doxorubicin. *Nucleic Acids Res.* **18**, 6611–6619 (1990).

126. Lyu, Y. L. *et al.* Topoisomerase IIβ-mediated DNA double-strand breaks: Implications in

doxorubicin cardiotoxicity and prevention by dexrazoxane. *Cancer Res.* **67**, 8839–8846 (2007).

127. Singal, P. K., Iliskovic, N., Li, T. & Kumar, D. Adriamycin cardiomyopathy: pathophysiology and prevention. *FASEB J.* **11**, 931–936 (1997).
128. De Beer, E. L., Bottone, A. E. & Voest, E. E. Doxorubicin and mechanical performance of cardiac trabeculae after acute and chronic treatment: a review. *Eur. J. Pharmacol.* **415**, 1–11 (2001).
129. Wallace, K. B. Doxorubicin-Induced Cardiac Mitochondrionopathy. *Pharmacol. Toxicol.* **93**, 105–115 (2003).
130. Xu, X., Persson, H. L. & Richardson, D. R. Molecular Pharmacology of the Interaction of Anthracyclines with Iron. *Mol. Pharmacol.* **68**, 261–271 (2005).
131. Zhu, H. *et al.* Doxorubicin Redox Biology: Redox Cycling, Topoisomerase Inhibition, and Oxidative Stress. *React. Oxyg. Species* **1**, 189–198 (2016).
132. Bird, D. M., Boldt, M. & Koch, T. H. Leucodaunomycin, a Tautomer of Daunomycin Hydroquinone. *J. Am. Chem. Soc.* **111**, 1148–1150 (1989).
133. Lea, J. S., Rushton, F. A. P., Land, E. J. & Swallow, A. J. The Reductive Deglycosylation Of Adriamycin In Aqueous Medium: A Pulse Radiolysis Study. *Free Radic. Res. Commun.* **8**, 241–249 (1990).
134. Wallace, K. B. Adriamycin-induced interference with cardiac mitochondrial calcium homeostasis. *Cardiovasc. Toxicol.* **7**, 101–107 (2007).
135. Kalyanaraman, B., Perez-Reyes, E. & Mason, R. P. Spin-trapping and direct electron spin resonance investigations of the redox metabolism of quinone anticancer drugs. *Biochim. Biophys. Acta* **630**, 119–130 (1980).

136. Sato, S., Handa, K., Tamura, Y. & Iwaizumi, M. Electron Spin Resonance Study on the Mode of Generation of Free Radicals of Daunomycin, Adriamycin, and Carboquone in NAD(P)H-Microsome System. *GANN Japanese J. Cancer Res.* **68**, 603–608 (1977).

137. Capranico, G., Tinelli, S., Austin, C. A., Fisher, M. L. & Zunino, F. Different patterns of gene expression of topoisomerase II isoforms in differentiated tissues during murine development. *Biochim. Biophys. Acta - Gene Struct. Expr.* **1132**, 43–48 (1992).

138. Zhang, S. *et al.* Identification of the molecular basis of doxorubicin-induced cardiotoxicity. *Nat. Med.* **18**, 1639–1642 (2012).

139. Finkel, T. Cell Biology: A clean energy programme. *Nature* **444**, 151–152 (2006).

140. Vejpongsa, P. & Yeh, E. T. H. Prevention of Anthracycline-Induced Cardiotoxicity: Challenges and Opportunities. *J. Am. Coll. Cardiol.* **64**, 938–945 (2014).

141. Khasraw, M., Bell, R. & Dang, C. Epirubicin: Is it like doxorubicin in breast cancer? A clinical review. *The Breast* **21**, 142–149 (2012).

142. Bonadonna, G. *et al.* Drugs ten years later: Epirubicin. *Ann. Oncol.* **4**, 359–369 (1993).

143. Untch, M. *et al.* First-line trastuzumab plus epirubicin and cyclophosphamide therapy in patients with human epidermal growth factor receptor 2-positive metastatic breast cancer: Cardiac safety and efficacy data from the herceptin, cyclophosphamide, and epirubicin (HERCULES) trial. *J. Clin. Oncol.* **28**, 1473–1480 (2010).

144. Robert, J. Clinical Pharmacokinetics of Idarubicin. *Clin. Pharmacokinet.* **24**, 275–288 (2012).

145. Schott, B. & Robert, J. Comparative cytotoxicity, DNA synthesis inhibition and drug incorporation of eight anthracyclines in a model of doxorubicin-sensitive and -resistant rat glioblastoma cells. *Biochem. Pharmacol.* **38**, 167–172 (1989).

146. Bhuyan, B. K. & Dietz, A. Fermentation, taxonomic, and biological studies on nogalamycin. *Antimicrob. Agents Chemother.* **5**, 836–844 (1965).

147. Bhuyan, B. K. & Smith, C. G. Differential interaction of nogalamycin with DNA of varying base composition. *Proc. Natl. Acad. Sci. U. S. A.* **54**, 566–572 (1965).

148. Bhuyan, B. K. & Reusser, F. Comparative Biological Activity of Nogalamycin and Its Analogs. *Cancer Res.* **30**, 984–989 (1970).

149. Liaw, Y. C. *et al.* Antitumor Drug Nogalamycin Binds DNA in Both Grooves Simultaneously: Molecular Structure of Nogalamycin-DNA Complex. *Biochemistry* **28**, 9913–9918 (1989).

150. Williams, L. D. *et al.* Structure of nogalamycin bound to a DNA hexamer. *Proc. Natl. Acad. Sci. U. S. A.* **87**, 2225–2229 (1990).

151. Robinson, H., Liaw, Y.-C., van der Marel, G. A., van Boom, J. H. & Wang, A. H. J. NMR studies on the binding of antitumor drug nogalamycin to DNA hexamer d(CGTACG). *Nucleic Acids Res.* **18**, 4851–4858 (1990).

152. Searle, M. S., Hall, J. G., Denny, W. A. & Wakelin, L. P. G. NMR Studies of the Interaction of the Antibiotic Nogalamycin with the Hexadeoxyribonucleotide Duplex d(5’-GCATGC)2. *Biochemistry* **27**, 4340–4349 (1988).

153. Zhang, X. & Patel, D. J. Solution Structure of the Nogalamycin-DNA Complex. *Biochemistry* **29**, 9451–9466 (1990).

154. Hütter, K. *et al.* Viriplanin A, a New Anthracycline Antibiotic of the Nogalamycin Group. *J. Antibiot. (Tokyo).* **39**, 1193–1204 (1986).

155. Oki, T., Takeuchi, T., Oka, S. & Umezawa, H. New anthracycline antibiotic aclacinomycin A: experimental studies and correlations with clinical trials. in *New Drugs*

in Cancer Chemotherapy. Recent Results in Cancer Research (eds. Carter, S. K., Sakurai, Y. & Umezawa, H.) **76**, 21–40 (Springer, Berlin, Heidelberg, 1981).

156. Hashimoto, K., Ito, K. & Ishimori, Y. Novel DNA sensor for electrochemical gene detection. *Anal. Chim. Acta* **286**, 219–224 (1994).

157. Qiao, X. *et al.* Uncoupling DNA damage from chromatin damage to detoxify doxorubicin. *Proc. Natl. Acad. Sci. U. S. A.* **117**, 15182–15192 (2020).

158. Arcamone, F., Bernardi, L., Patelli, B. & di Marco, A. 14-Aminodaunomycins, their preparation and use. (1977).

159. Seshadri, R., Israel, M. & Pegg, W. J. Adriamycin Analogues. Preparation and Biological Evaluation of Some Novel 14-Thiaadriamycins1. *J. Med. Chem.* **26**, 11–15 (1983).

160. Yamamoto, K., Acton, E. M. & Henry, D. W. Antitumor Activity of Some Derivatives of Daunorubicin at the Amino and Methyl Ketone Functions. *J. Med. Chem.* **15**, 872–875 (1972).

161. Tong, G. L., Wu, H. Y., Smith, T. H. & Henry, D. W. Adriamycin Analogues. 3. Synthesis of N-Alkylated Anthracyclines with Enhanced Efficacy and Reduced Cardiotoxicity. *J. Med. Chem.* **22**, 912–918 (1979).

162. Kratz, F. DOXO-EMCH (INNO-206): the first albumin-binding prodrug of doxorubicin to enter clinical trials. *Expert Opin. Investig. Drugs* **16**, 855–866 (2007).

163. Wang, J., Chen, M., Li, S. & Ye, R. D. Targeted Delivery of a Ligand-Drug Conjugate via Formyl Peptide Receptor 1 through Cholesterol-Dependent Endocytosis. *Mol. Pharm.* **16**, 2636–2647 (2019).

164. Li, S.-Y. *et al.* A pH-responsive prodrug for real-time drug release monitoring and targeted cancer therapy. *Chem. Commun.* **50**, 11852–11855 (2014).

165. Li, J. *et al.* Strategies to release doxorubicin from doxorubicin delivery vehicles. *J. Drug Target.* **26**, 9–26 (2017).

166. Trivedi, E. R. *et al.* Multi-gram synthesis of a porphyrazine platform for cellular translocation, conjugation to Doxorubicin, and cellular uptake. *Tetrahedron Lett.* **53**, 5475–5478 (2012).

167. Ingallinella, P., Di Marco, A., Taliani, M., Fattori, D. & Pessi, A. A New Method for Chemoselective Conjugation of Unprotected Peptides to Dauno- and Doxorubicin. *Bioorg. Med. Chem. Lett.* **11**, 1343–1346 (2001).

168. Lelle, M. & Peneva, K. An amino acid-based heterofunctional cross-linking reagent. *Amino Acids* **46**, 1243–1251 (2014).

169. Lelle, M., Frick, S. U., Steinbrink, K. & Peneva, K. Novel cleavable cell-penetrating peptide–drug conjugates: synthesis and characterization. *J. Pept. Sci.* **20**, 323–333 (2014).

170. Lelle, M. *et al.* Overcoming drug resistance by cell-penetrating peptide-mediated delivery of a doxorubicin dimer with high DNA-binding affinity. *Eur. J. Med. Chem.* **130**, 336–345 (2017).

171. Lelle, M., Freidel, C., Kaloyanova, S., Müllen, K. & Peneva, K. Multivalency: Key Feature in Overcoming Drug Resistance with a Cleavable Cell-Penetrating Peptide-Doxorubicin Conjugate. *Int. J. Pept. Res. Ther.* **24**, 355–367 (2018).

172. Polgár, L. *et al.* Drug targeting to decrease cardiotoxicity – determination of the cytotoxic effect of GnRH-based conjugates containing doxorubicin, daunorubicin and methotrexate on human cardiomyocytes and endothelial cells. *Beilstein J. Org. Chem.* **14**, 1583–1594 (2018).

173. Ohata, J. & Ball, Z. T. A Hexa-rhodium Metallopeptide Catalyst for Site-Specific

Functionalization of Natural Antibodies. *J. Am. Chem. Soc.* **139**, 12617–12622 (2017).

174. Potti, G. & Israel, M. Adriamycin Analogues. Preparation of 9,10-Anhydrodaunorubicin, 9,10-Anhydroadriamycin, and Some Related Compounds. *J. Med. Chem.* **25**, 478–481 (1982).

175. Di Marco, A., Casazza, A. M., Gambetta, R., Supino, R. & Zunino, F. Relationship between Activity and Amino Sugar Stereochemistry of Daunorubicin and Adriamycin Derivatives. *Cancer Res.* **36**, 1962–1966 (1976).

176. Arcamone, F. *et al.* Doxorubicin Disaccharide Analogue: Apoptosis-Related Improvement of Efficacy In Vivo. *J. Natl. Cancer Inst.* **89**, 1217–1223 (1997).

177. Kang, H.-S. & Brady, S. F. Arimetamycin A: Improving Clinically Relevant Families of Natural Products through Sequence-Guided Screening of Soil Metagenomes. *Angew. Chemie Int. Ed.* **52**, 11063–11067 (2013).

178. Huseman, E. D. *et al.* Synthesis and Cytotoxic Evaluation of Arimetamycin A and Its Daunorubicin and Doxorubicin Hybrids. *ACS Cent. Sci.* **7**, 1327–1337 (2021).

179. Millard, J. T., Weidner, M. F., Raucher, S. & Hopkins, P. B. Determination of the DNA Cross-Linking Sequence Specificity of Reductively Activated Mitomycin C at Single-Nucleotide Resolution: Deoxyguanosine Residues at CpG Are Cross-Linked Preferentially. *J. Am. Chem. Soc.* **112**, 3637–3641 (1990).

180. Hata, T. *et al.* Mitomycin, a new antibiotic from Streptomyces. I. *J. Antibiot.* **9**, 141–146 (1956).

181. Carter, S. K. Mitomycin C (NSC-26980) -- Clinical Brochure. *Cancer Chemother. Reports, Part 3* **1**, 99–114 (1968).

182. Iyer, V. N. & Szybalski, W. A Molecular Mechanism of Mitomycin Action: Linking of

Complementary DNA Strands. *Proc. Natl. Acad. Sci. U. S. A.* **50**, 355–362 (1963).

183. Tomasz, M., Chawla, A. K. & Liman, R. Mechanism of Monofunctional and Bifunctional Alkylation of DNA by Mitomycin C. *Biochemistry* **27**, 3182–3187 (1988).

184. Warpehoski, M. A. & Hurley, L. H. Sequence Selectivity of DNA Covalent Modification. *Chem. Res. Toxicol.* **1**, 315–333 (1988).

185. Gao, Y. G. *et al.* Facile formation of a crosslinked adduct between DNA and the daunorubicin derivative MAR70 mediated by formaldehyde: Molecular structure of the MAR70-d(CGT(n)ACG) covalent adduct. *Proc. Natl. Acad. Sci. U. S. A.* **88**, 4845–4849 (1991).

186. Wang, A. H.-J., Gao, Y.-G., Liaw, Y.-C. & Li, Y. Formaldehyde Cross-Links Daunorubicin and DNA Efficiently: HPLC and X-ray Diffraction Studies. *Biochemistry* **30**, 3812–3815 (1991).

187. Taatjes, D. J., Gaudiano, G., Resing, K. & Koch, T. H. Alkylation of DNA by the anthracycline, antitumor drugs adriamycin and daunomycin. *J. Med. Chem.* **39**, 4135–4138 (1996).

188. Zeman, S. M., Phillips, D. R. & Crothers, D. M. Characterization of covalent adriamycin-DNA adducts. *Proc. Natl. Acad. Sci. U. S. A.* **95**, 11561–11565 (1998).

189. Coldwell, K. E., Cutts, S. M., Ognibene, T. J., Henderson, P. T. & Phillips, D. R. Detection of Adriamycin–DNA adducts by accelerator mass spectrometry at clinically relevant Adriamycin concentrations. *Nucleic Acids Res.* **36**, e100 (2008).

190. Fenick, D. J., Taatjes, D. J. & Koch, T. H. Doxoform and Daunoform: Anthracycline-Formaldehyde Conjugates Toxic to Resistant Tumor Cells. *J. Med. Chem.* **40**, 2452–2461 (1997).

191. Swift, L. P., Rephaeli, A., Nudelman, A., Phillips, D. R. & Cutts, S. M. Doxorubicin-DNA adducts induce a non-topoisomerase II-mediated form of cell death. *Cancer Res.* **66**, 4863–4871 (2006).

192. Post, G. C., Barthel, B. L., Burkhart, D. J., Hagadorn, J. R. & Koch, T. H. Doxazolidine, a proposed active metabolite of doxorubicin that cross-links DNA. *J. Med. Chem.* **48**, 7648–7657 (2005).

193. Swift, L. P., Cutts, S. M., Rephaeli, A., Nudelman, A. & Phillips, D. R. Activation of adriamycin by the pH-dependent formaldehyde-releasing prodrug hexamethylenetetramine. *Mol. Cancer Ther.* **2**, 198 (2003).

194. Nudelman, A., Levovich, I., Cutts, S. M., Phillips, D. R. & Rephaeli, A. The role of intracellularly released formaldehyde and butyric acid in the anticancer activity of acyloxyalkyl esters. *J. Med. Chem.* **48**, 1042–1054 (2005).

195. Taatjes, D. & Koch, T. Nuclear Targeting and Retention of Anthracycline Antitumor Drugs in Sensitive and Resistant Tumor Cells. *Curr. Med. Chem.* **8**, 15–29 (2001).

196. Taatjes, D. J., Fenick, D. J. & Koch, T. H. Epidoxoform: A hydrolytically more stable anthracycline-formaldehyde conjugate toxic to resistant tumor cells. *J. Med. Chem.* **41**, 1306–1314 (1998).

197. Cutts, S. M., Nudelman, A., Rephaeli, A. & Phillips, D. R. The power and potential of doxorubicin-DNA adducts. *IUBMB Life* **57**, 73–81 (2005).

198. Kimura, K.-I. *et al.* SN-07 Chromaphone: An Anthracycline Antibiotic from the Macromolecular Antibiotic SN-07. *J. Antibiot. (Tokyo).* **40**, 1353–1355 (1987).

199. Moufarij, M. A., Cutts, S. M., Neumann, G. M., Kimura, K. I. & Phillips, D. R. Barminomycin functions as a potent pre-activated analogue of Adriamycin. *Chem. Biol.*

Interact. **138**, 137–153 (2001).

200. Kimura, K.-I. *et al.* A New Anthracycline Antibiotic SN-706. *J. Antibiot. (Tokyo).* **41**, 1918–1921 (1988).

201. Perrin, L. C., Cullinane, C., Kimura, K. I. & Phillips, D. R. Barminomycin forms GC-specific adducts and virtual interstrand crosslinks with DNA. *Nucleic Acids Res.* **27**, 1781–1787 (1999).

202. Cutts, S. M., Parker, Belinda, S., Swift, L. P., Kimura, K. & Phillips, D. R. Structural requirements for the formation of anthracycline-DNA adducts. *Anticancer. Drug Des.* **15**, 373–386 (2000).

203. Acton, E. M., Tong, G. L., Mosher, C. W. & Wolgemuth, R. L. Intensely potent morpholinyl anthracyclines. *J. Med. Chem.* **27**, 638–645 (1984).

204. Westendorf, J., Groth, G., Steinheider, G. & Marquardt, H. Formation of DNA-adducts and induction of DNA-crosslinks and chromosomal aberrations by the new potent anthracycline antitumor antibiotics: morpholinodaunomycin, cyanomorpholinodaunomycin and cyanomorhpolinoadriamycin. *Cell Biol. Toxicol.* **1**, 87–101 (1985).

205. Acton, E. M., Tong, G. L., Taylor, D. L., Filppi, J. A. & Wolgemuth, R. L. New Cyanomorpholinyl Byproduct of Doxorubicin Reductive Alkylation. *J. Med. Chem.* **29**, 1225–1230 (1986).

206. Cullinane, C. & Phillips, D. R. Thermal stability of DNA adducts induced by cyanomorpholinoadriamycin in vitro. *Nucleic Acids Res.* **21**, 1857–1862 (1993).

207. Cutts, S., Swift, L., Rephaeli, A., Nudelman, A. & Phillips, D. Recent Advances in Understanding and Exploiting the Activation of Anthracyclines by Formaldehyde. *Curr.*

Med. Chem. Agents **5**, 431–447 (2005).

208. Broggini, M. Nemorubicin. in *Anthracycline Chemistry and Biology II. Topics in Current Chemistry* (ed. Krohn, K.) **283**, 191–206 (Springer, Berlin, Heidelberg, 2007).

209. Ankers, E. A., Evison, B. J., Phillips, D. R., Brownlee, R. T. C. & Cutts, S. M. Design, synthesis, and DNA sequence selectivity of formaldehyde-mediated DNA-adducts of the novel N-(4-aminobutyl) acridine-4-carboxamide. *Bioorg. Med. Chem. Lett.* **24**, 5710–5715 (2014).

210. Parker, B. S., Cullinane, C. & Phillips, D. R. Formation of DNA adducts by formaldehyde-activated mitoxantrone. *Nucleic Acids Res.* **27**, 2918–2923 (1999).

211. Evison, B. J., Mansour, O. C., Menta, E., Phillips, D. R. & Cutts, S. M. Pixantrone can be activated by formaldehyde to generate a potent DNA adduct forming agent. *Nucleic Acids Res.* **35**, 3581–3589 (2007).

212. Evison, B. J., Chiu, F., Pezzoni, G., Phillips, D. R. & Cutts, S. M. Formaldehyde-Activated Pixantrone Is a Monofunctional DNA Alkylator That Binds Selectively to CpG and CpA Doublets. *Mol. Pharmacol.* **74**, 184–194 (2008).

213. Mansour, O. C. *et al.* New anthracenedione derivatives with improved biological activity by virtue of stable drug-DNA adduct formation. *J. Med. Chem.* **53**, 6851–6866 (2010).

214. Pumuye, P. P. *et al.* Formaldehyde-activated WEHI-150 induces DNA interstrand crosslinks with unique structural features. *Bioorg. Med. Chem.* **28**, 115260 (2020).

215. Evison, B. J., Sleebs, B. E., Watson, K. G., Phillips, D. R. & Cutts, S. M. Mitoxantrone, More than Just Another Topoisomerase II Poison. *Med. Res. Rev.* **36**, 248–299 (2016).

216. Zee-Cheng, R. K. Y. & Cheng, C. C. Antineoplastic Agents. Structure-Activity Relationship Study of Bis(substituted aminoalkylamino)anthraquinones. *J. Med. Chem.*

21, 291–294 (1978).

217. Scott, L. J. & Figgitt, D. P. Mitoxantrone: A review of its use in multiple sclerosis. *CNS Drugs* **18**, 379–396 (2004).

218. Salvatorelli, E. *et al.* The novel anthracenedione, pixantrone, lacks redox activity and inhibits doxorubicinol formation in human myocardium: Insight to explain the cardiac safety of pixantrone in doxorubicin-treated patients. *J. Pharmacol. Exp. Ther.* **344**, 467–478 (2013).

219. Péan, E. *et al.* The European Medicines Agency Review of Pixantrone for the Treatment of Adult Patients With Multiply Relapsed or Refractory Aggressive Non-Hodgkin's B-Cell Lymphomas: Summary of the Scientific Assessment of the Committee for Medicinal Products for Human Use. *Oncologist* **18**, 625–633 (2013).

220. Cogliano, V. J. *et al.* Meeting Report: Summary of IARC Monographs on Formaldehyde, 2-Butoxyethanol, and 1-tert-Butoxy-2-Propanol. *Environ. Health Perspect.* **113**, 1205–1208 (2005).

221. Chen, H., Yao, L., Brown, C., Rizzo, C. J. & Turesky, R. J. Quantitation of Apurinic/Apyrimidinic Sites in Isolated DNA and in Mammalian Tissue with a Reduced Level of Artifacts. *Anal. Chem.* **91**, 7403–7410 (2019).

222. Chen, H. *et al.* Kinetics of DNA Adducts and Abasic Site Formation in Tissues of Mice Treated with a Nitrogen Mustard. *Chem. Res. Toxicol.* **33**, 988–998 (2020).

223. Wilde, J. A., Bolton, P. H., Mazumder, A., Manoharan, M. & Gerlt, J. A. Characterization of the Equilibrating Forms of the Aldehydic Abasic Site in Duplex DNA by Oxygen-17 NMR. *J. Am. Chem. Soc.* **111**, 1894–1896 (1989).

224. Taverna, P. *et al.* Methoxyamine potentiates DNA single strand breaks and double strand

breaks induced by temozolomide in colon cancer cells. *Mutat. Res. Repair* **485**, 269–281 (2001).

225. Liu, L., Nakatsuru, Y. & Gerson, S. L. Base Excision Repair as a Therapeutic Target in Colon Cancer. *Clin. Cancer Res.* **8**, 2985–2991 (2002).

226. Liu, L., Yan, L., Donze, J. R. & Gerson, S. L. Blockage of abasic site repair enhances antitumor efficacy of 1,3-bis-(2-chloroethyl)-1-nitrosourea in colon tumor xenografts. *Mol. Cancer Ther.* **2**, 1061–1066 (2003).

227. Rinne, M., Caldwell, D. & Kelly, M. R. Transient adenoviral N-methylpurine DNA glycosylase overexpression imparts chemotherapeutic sensitivity to human breast cancer cells. *Mol. Cancer Ther.* **3**, 955–967 (2004).

228. Fishel, M. L. & Kelley, M. R. The DNA base excision repair protein Ape1/Ref-1 as a therapeutic and chemopreventive target. *Mol. Aspects Med.* **28**, 375–395 (2007).

229. Heijink, D. M. *et al.* Perspectives for tailored chemoprevention and treatment of colorectal cancer in Lynch syndrome. *Crit. Rev. Oncol. Hematol.* **80**, 264–277 (2011).

230. Hoops, S. *et al.* COPASI - a COmplex PAthway SImulator. *Bioinformatics* **22**, 3067–3074 (2006).

CHAPTER 2: Aminoxyacetamides and their Reactivity with DNA

Background

Oximes most commonly are found in antidotes for organophosphorus nerve agents. Namely, oximes react with acetylcholinesterase inhibited by the nerve agents. The organophosphorus compound phosphorylates the enzyme's active site, inhibiting it and causing a buildup of acetylcholine in the synapses. The oxime antidotes dephosphorylate the active site to allow for the enzyme to continue functioning.[231] Additionally, oximes serve a biological function in plant general metabolism. In these cases, oximes are derived from amino acids either as the end metabolite or an intermediate to a nitrile metabolite.[232,233] Oximes also are present in drug conjugates synthesized for combatting bacterial infections, such as tuberculosis, and exhibiting anti-inflammatory properties, activity against some cancers, and therapeutic responses against neurodegenerative disorders.[233–240]

As mentioned in the previous chapter, oximes are the resulting functional group when alkoxyamines condense onto a carbonyl moiety. However, unlike their imine counterpart, oximes do not hydrolyze at physiological pH. NMR studies have provided pD-rate profiles (as deuterated solvent was used) by tracking the rate of hydrolysis of imine-like conjugates as a function of solution acidity. In fact, the rate of hydrolysis of the oxime formed between methoxyamine and pivaldehyde is too slow to measure at a pD greater than 7. At pD 7, the rate of hydrolysis of this oxime is measured to be on the order of 10^{-4} with a half-life of approximately 25 days.[241] The greater stability of conjugates like oximes is believed to be due to either the release of repulsive electronic strain between the lone pairs of the nitrogen and oxygen or the presence of a partial negative charge on the oxime carbon due to resonance.[241,242]

Also mentioned in the previous chapter was the ability of methoxyamine to potentiate the cytotoxic effects of temozolomide in temozolomide-resistant cells. Methoxyamine inhibits BER by binding to the aldehydic form of AP sites, preventing the necessary lyase action of the BER pathway. Similarly, methoxyamine binds to AP sites formed by temozolomide, blocking the repair of the damage caused by the alkylator in resistant cells.[224,243,244] We hypothesize that synthetically affixing chemotherapeutics with alkoxyamine handles will result in stronger covalent conjugates between the drug and AP sites in DNA, providing improved results upon those reported by Bellamri *et al*. (*Publication in-progress*) The effectiveness of the combination of temozolomide and methoxyamine stands in-support of the findings of Kalia & Raines[241] as well as our hypothesis.

Synthetic Strategies

Because of their utility in conjugation reactions, several synthetic strategies for the synthesis of alkoxyamines have been proposed. For example, alkoxyamines of 2,2,6,6-tetramethylpiperidine-1-oxyl radical (TEMPO) have been synthesized for use as initiators in the polymerization of styrene. This was accomplished via a radical-mediated substitution between TEMPO and bromoalkanes mediated by copper metal and a copper(I) catalyst.[245] More recently, Braslau *et al.* proposed a similar radical-mediated alkylation of TEMPO initiated with *tert*-butyl hyponitrile and tris(trimethyl)silane.[246] Unfortunately, radical alkylations of an *N*-protected nitroxide (Figure 2.1a) are not feasible for our compounds as the anthracycline and anthraquinone cores react with radicals.

Another method of synthesizing alkoxyamines is via the direct amination of alcohols. Typically, this is done using *O*-(mesitylsulfonyl)hydroxylamine, a reagent used in the amination

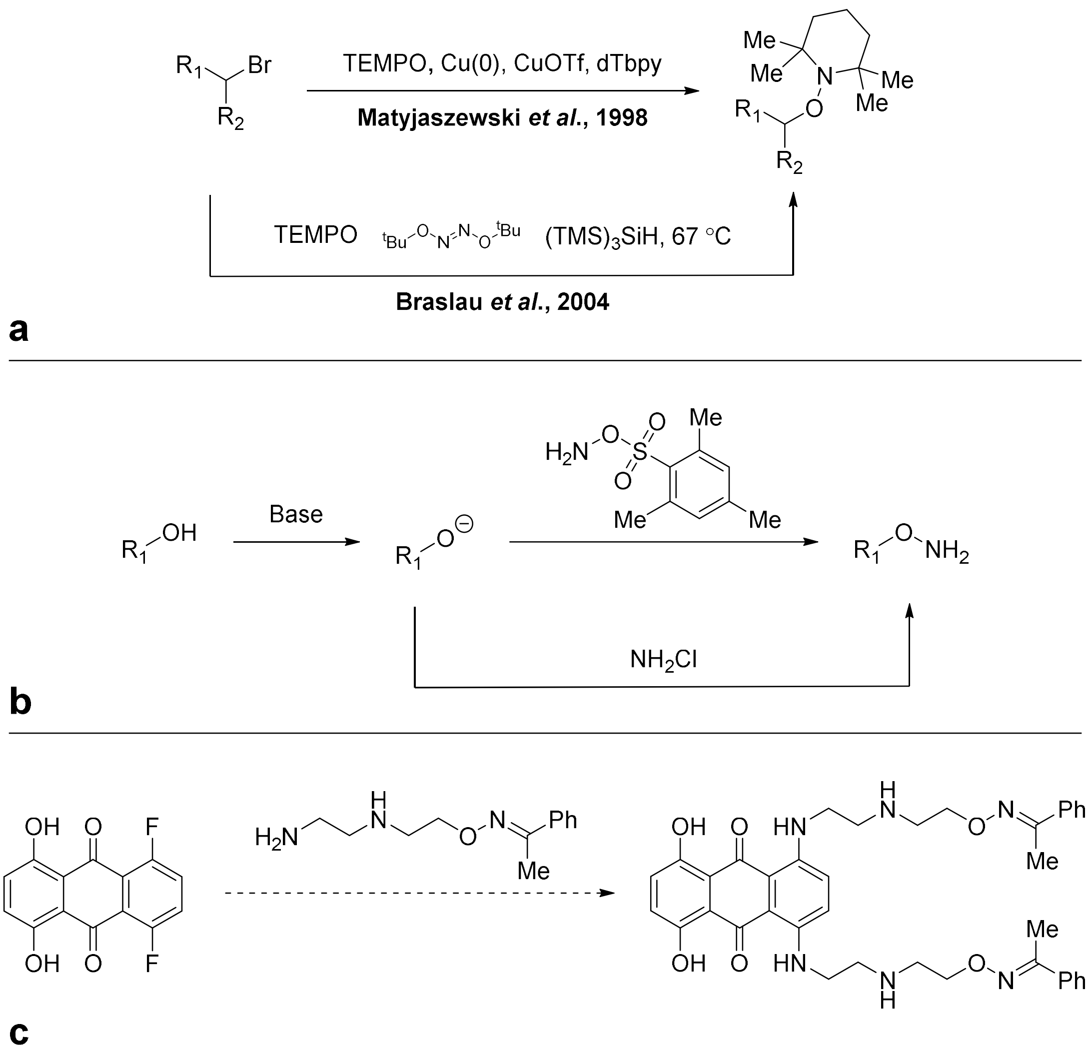

Figure 2.1: Reported synthetic routes toward the alkoxyamine moiety. a) Radical substitution (R_1,R_2 = H, alkyl, aryl); b) Direct amination of an alkoxide (R_1 = H, alkyl, aryl); c) S_NAr of anthraquinone core (the nucleophile is synthesized with the alkyl bromide and acetophenone oxime) – our originally proposed route.

of many nucleophilic heteroatoms and carbanions.[247,248] In the case of hydroxyl amination, deprotonation to the alkoxide is necessary for amination to occur (Figure 2.1b).[249] While this may be a suitable route for some potential compounds, the aglycone hydroxyls of DOX and the phenols of MTX pose chemoselectivity issues for the modification of those compounds since they, too, deprotonate. Another mean of directly aminating heteroatoms is by nucleophilic substitution of chloramine (Figure 2.1b).[250,251] However, this method is used most commonly in the synthesis of hydrazines (the amination of an amine). As there are more nucleophilic sites on our drugs than alcohols, this route is not feasible, either.

Our original proposal for the synthesis of alkoxyamine derivatives of MTX had us attach two aliphatic arms of the drug to the anthraquinone core by nucleophilic aromatic substitution (Figure 2.1c).[252,253] The aliphatic amine to be substituted onto the core already would have been modified with a protected alkoxyamine.[254,255] While past members of our lab had attempted the synthesis of the MTX arm using acetophenone oxime and the alkyl bromide as described in the literature,[254,255] substitution of the bromide proved elusive. As such, other ways of synthesizing this moiety were required. Additionally, while it has been hypothesized by John T. Terrell in our lab, Buchwald-Hartwig coupling of the aliphatic arm to the anthraquinone core has not been attempted at this time due to the aforementioned issues with synthesizing the aliphatic arms.

2-Aminoxyacetamides

Acylating ethylenediamine arms affixed onto an anthraquinone core with 2-aminoxyacetic acid to form 2-aminoxyacetamides circumvents many of the theoretical and observed issues discussed in the previous section (Figure 2.2). A common use of this functional group is in the synthesis of aldehyde-reactive probes for biological studies and fluorescent labeling.[256–262] Additionally, the high reactivity of alkoxyamines has led to 2-aminoxyacetamides' employment in crosslinking peptides to different anchors such as sugars to make anticancer vaccines,[263,264] cytotoxic peptides and oligonucleotides,[265] etc. They even have been used in conjugation onto AP sites.[257,258] Modifying our drugs as 2-aminoxyacetamides would be a 2-step process of amidation and deprotection. This route is feasible since the

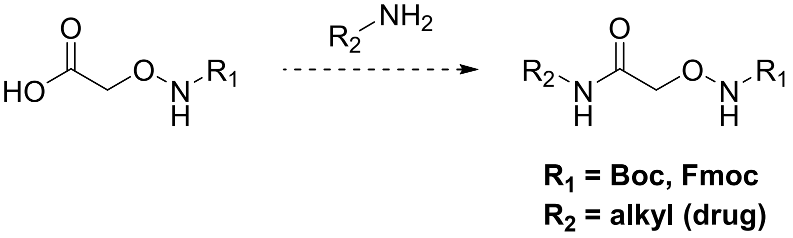

Figure 2.2: Formation of 2-aminoxyacetamides.

carboxylic acid precursor to this functional group is commercially available. Therefore, we proceeded with this modification.

Results and Discussion

Synthesis and Spectral Characterization of Mono- and Bis-Substituted Anthraquinone Aminoxyacetamides

The 2-aminoxyacetamide-modified anthraquinones were accessed over 4 steps from anthracene-1,4,9,10-tetraol with an overall yield of 11% for the mono-substituted **2-1** and 2% for the bis-substituted **2-2**. The yields presented in this dissertation are not optimized. The final compounds were isolated as the HCl salts as shown in Figure 2.3. Compounds **2-5** and **2-8** were synthesized as reported in the literature.[266,267] The 1,4-dioxo-tautomer of the anthracene starting material reacted with Boc-protected ethylenediamine to form a mono- or bis-imine that tautomerized to the 1,4-dianiline anthracene core. Air oxidation of the reaction mixture stops the reaction by converting the 1,4-(di)aniline-9,10-diol into the 9,10-anthraquinone core equipped with Boc-protected ethylenediamine arms at positions 1 or positions 1 *and* 4 to afford the mono- and bis-substituted products (compounds **2-4** and **2-7**). After separating these intermediates, the Boc-group was removed with trifluoroacetic acid in methylene chloride, which afforded **2-5** and

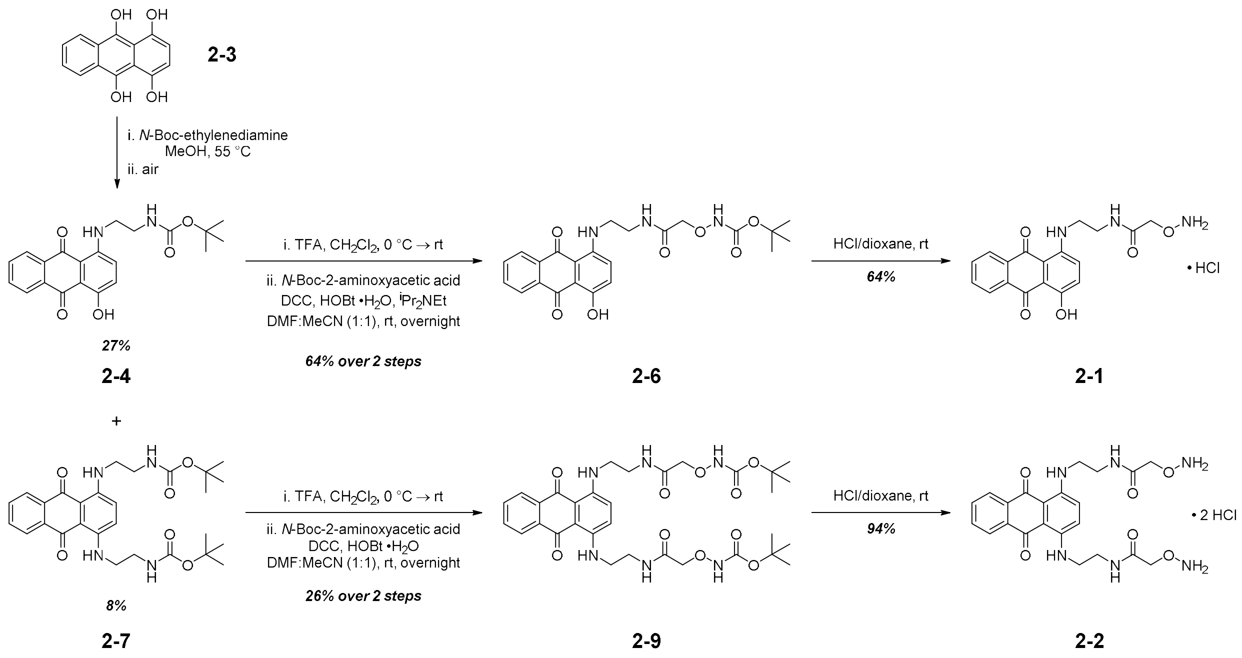

Figure 2.3: Synthetic route toward compounds **2-1** and **2-2**. Compounds **2-5** and **2-9** are the products from the first reaction of **2-4** and **2-7**, respectively.

2-8. While **2-5** was pure after the deprotection, **2-8** required purification by reverse-phase flash column chromatography (FCC) to separate the product from the mono-deprotected byproduct and **2-5** impurity from the previous step. As such, **2-5** was isolated as the trifluoroacetate salt, and **2-8** was isolated as the free diamine.

The crucial step to the synthesis was the coupling between *N*-Boc-2-aminoxyacetic acid (Boc-AOAcOH) and compounds **2-5** and **2-8**. *N*,*N*'-dicyclohexylcarbodiimide (DCC) was activated in 1:1 *N*,*N*-dimethylformamide (DMF):acetonitrile (MeCN) with *N*-hydroxybenzotriazole (HOBt) monohydrate. The HOBt-activated DCC was reacted with Boc-AOAcOH to form the activated ester. Separately, our intermediates were neutralized with Hunig's base (^{i}Pr$_2$NEt) in DMF and added dropwise into the activated ester solution. After reacting overnight, intermediates **2-6** and **2-9** were purified by FCC. Final deprotection of the Boc-aminoxyacetamides occurred via reaction with HCl/dioxane, yielding **2-1** and **2-2** as the mono- and bis-hydrochloride salts, respectively. The compounds were confirmed and characterized by ^{1}H and ^{13}C NMR spectroscopy and ESI/MS^{2} (Appendix I and II).

Our original amidation strategy involved a two-step process of synthesizing the *N*-hydroxysuccinimide (NHS) ester of Boc-AOAcOH. There is precedence for this synthetic route toward the synthesis of 2-aminoxyacetamides from the amino moieties of small molecules and peptide oligomers.[262,263,265] Originally, we selected an Fmoc-protected substrate since the acidic conditions of a Boc-deprotection could lead to deglycosylation when applied to drugs like DOX. While esterification with NHS proceeded with ease, the amidation of the ester with our drug was low-yielding. Additionally, the Fmoc-deprotection of what was purified from the amidation could not be purified effectively as the product was too polar for FCC. Attempts to purify the reaction by means of reverse-phase chromatography failed as well. Separation did not occur by reverse-phase FCC, nor did it occur with solid-phase extraction (SPE). Reverse-phase HPLC seemed promising at first, but the dibenzofulvene (DBF) byproducts' peak intensities overtook those of the products.

The route described in the previous paragraph was performed using Boc-AOAcOH as well. However, the 2-step yield for the amidation, as described previously, was comparable to that of the DCC coupling in our reported synthesis. As such, we opted for the route with fewer

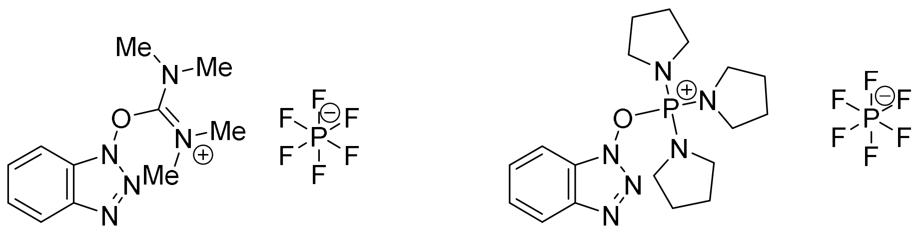

HBTU **PyBOP**

Figure 2.4: Other peptide-coupling reagents used in the optimization of our synthetic route.

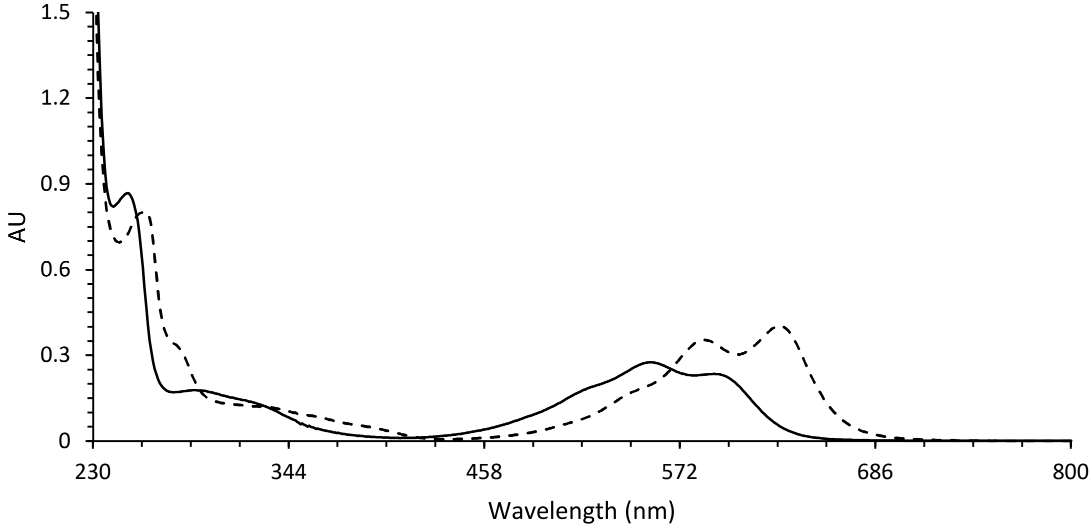

Figure 2.5: UV-vis spectra of 40 µM **2-1** (solid) and **2-2** (dashed).

total steps, although the longest linear sequence of the branched route would be the same. A one-step amide coupling, similar to a DCC coupling, was attempted with two different coupling reagents: HBTU (3-[Bis(dimethylamino)methyliumyl]-3*H*-benzotriazol-1-oxide hexafluorophosphate) and PyBOP ((Benzotriazol-1-yloxy)tripyrrolidinophosphonium hexafluorophosphate) (Figure 2.4). However, in both cases, reactions were lower-yielding than the DCC reaction, and the phosphine oxide byproduct of the PyBOP reaction was present even after FCC. The low yield made further purification to remove the byproduct unfeasible.

We determined the extinction coefficients of compounds **2-1** and **2-2** using UV-vis spectroscopy. This characterization was in addition to the NMR and mass spectrometric characterization presented in the Experimental section of the chapter. Five stock solutions of varying concentrations (six for **2-2**) were made in triplicate of each compound in no-more-than 4% (v/v) aqueous dimethylsulfoxide (DMSO). Each of the 15 or 18 samples was scanned at a range of 800 nm to 230 nm with absorbance measurements recorded at each point. Sample UV-vis absorption spectra are presented in Figure 2.5, overlaid to demonstrate the changes in absorption as a result of adding a second aliphatic arm to the anthraquinone core. These absorbance data were compiled and plotted as a function of concentration (Figure 2.6). Trendlines were calculated using the Microsoft Excel LINEST function, and the extinction coefficient at any desired wavelength was determined using an automated process in Excel that employed said LINEST function. A sample of this process for compound **2-1** at a wavelength of 260 nm is presented in Table 2.1, and the results in this table are those presented in Figure 2.6.

Table 2.1. Data for the graph shown in Figure 2.6. The table was automated using Microsoft Excel. The formulas used are presented in Appendix III. Note that these values are rounded from the long string of digits provided by Excel.

Wavelength (nm)	Conc. (M)	Abs	Abs s.d.	LINEST		Ext. Coeff. (M^{-1} cm^{-1})	Ext. Coeff. s.d. (M^{-1} cm^{-1})
260	0.000005	0.08	0.01	12600	0.026	12600	200
	0.000010	0.15	0.03	200	0.008		
	0.000020	0.29	0.05	0.999	0.0114		
	0.000040	0.54	0.08	4567	3		
	0.000080	1.0	0.1	0.5901	0.000388		

Synthesis and Spectral Characterization of Aminoxyacetamide Oximes with 2-Deoxy-D-Ribose

The next objective was to model the compounds' reactivity with AP sites in DNA. During the synthesis of **2-2**, there were instances when the main product of the final deprotection was not **2-2**, but rather an oxime formed between **2-2** and residual acetone in the glassware. Fortuitously, this impurity lent itself as the first model system for the reactivity of these specific aminoxyacetamides with AP sites in DNA. However, as **2-2** was needed for future experiments and the acetone oxime was not, flame-drying glassware became a norm for these syntheses. As

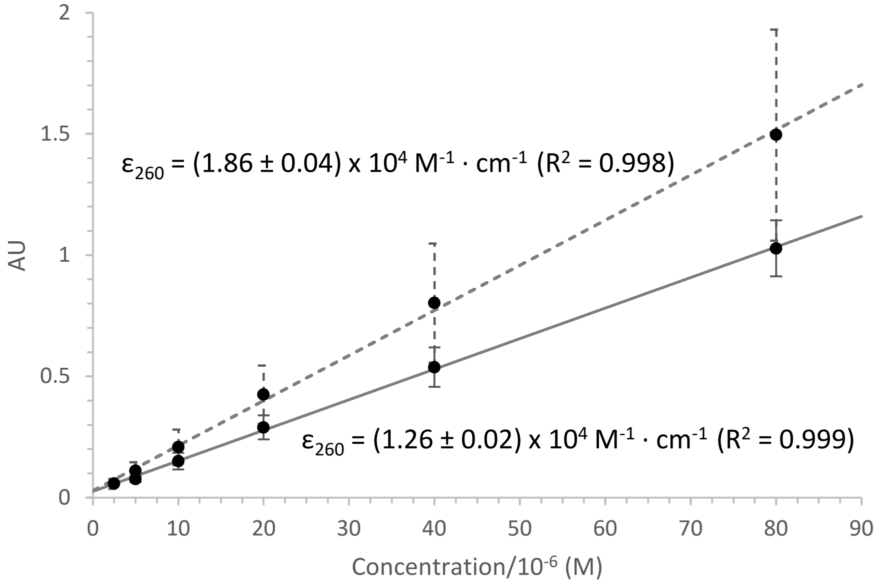

Figure 2.6: Absorbance of **2-1** (solid) and **2-2** (dashed) at 260 nm as a function of concentration. The slope of each curve is the extinction coefficient at 260 nm.

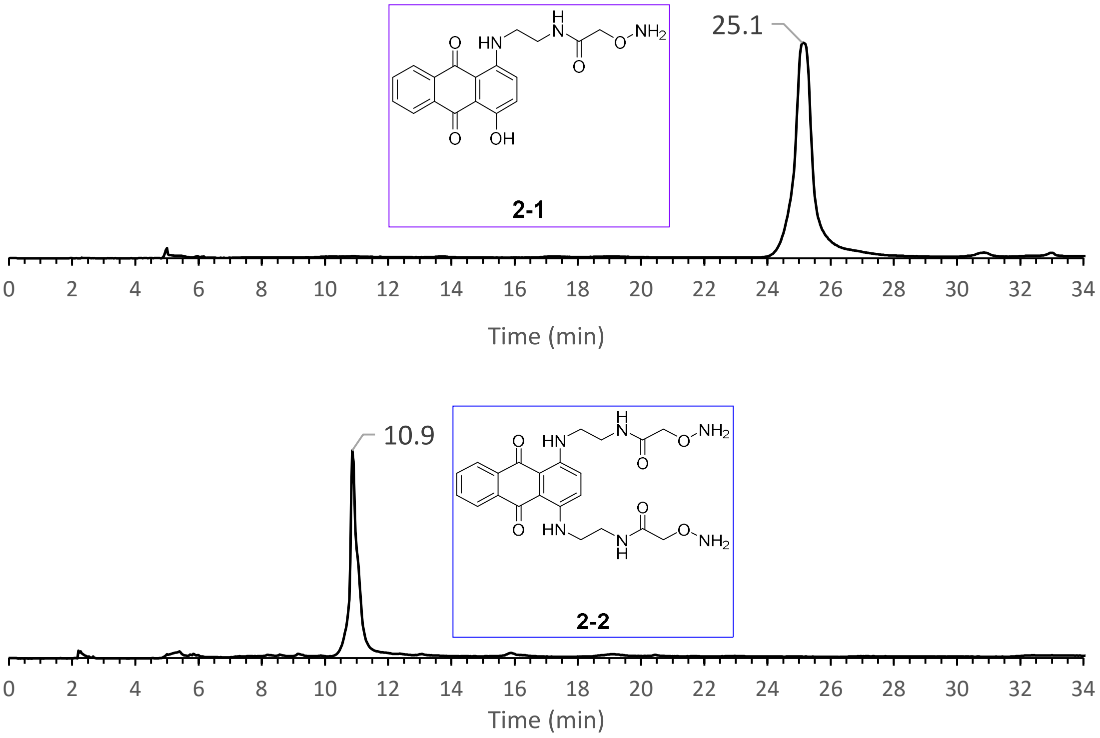

Figure 2.7: Purity of compounds **2-1** (top) and **2-2** (bottom) by reverse-phase HPLC and UV detection at 254 nm.

the first *intentional* introductory model system, we sought to show reactivity between these aminoxyacetamides and 2-deoxy-D-ribose (dR), the nucleoside equivalent of an AP site.

With compounds **2-1** and **2-2** in-hand, a 2 mM solution in DMSO was made of each compound. The purity of each solution was checked by reverse-phase HPLC, as shown in Figure 2.7. For the synthesis of the dR oxime of **2-1**, an aliquot of the 2 mM DMSO solution was added to an Eppendorf tube and placed on a heat block set to 37 °C. To this solution was added a small spatula scoop of dR. The solution was vortexed and sonicated to promote solubility of the excess dR. After reacting on the heat block for 1 hour, the reaction was purified by reverse-phase HPLC (Figure 2.8a). The purified samples were lyophilized multiple times to remove the chromatography buffer salt, and the product was analyzed by ESI/MS^2.

A similar procedure was followed in the synthesis of the bis-dR oxime of **2-2**. Having an excess amount of dR helped to promote conversion to the bis-oxime at 10 min (Figure 2.8b). The peak at 11 min is unreacted **2-2**. However, synthesis of the mono-oxime required an excess of **2-2**. To accomplish this, a solution of dR was prepared, and an aliquot of the 2 mM **2-2** solution was added such that there was an excess of anthraquinone. The solution was allowed to react on the 37 °C heat block for 12 hr before purification by reverse-phase HPLC (Figure 2.8c). The conjugate eluted at 9.5 min, just before **2-2** elutes at 11 min. Purification of this sample was difficult due to the close and early retention times of both conjugates. Like the oxime of **2-1**, the mono- and bis-oximes were lyophilized to remove excess buffer salt, and the products were analyzed by ESI/MS^2.

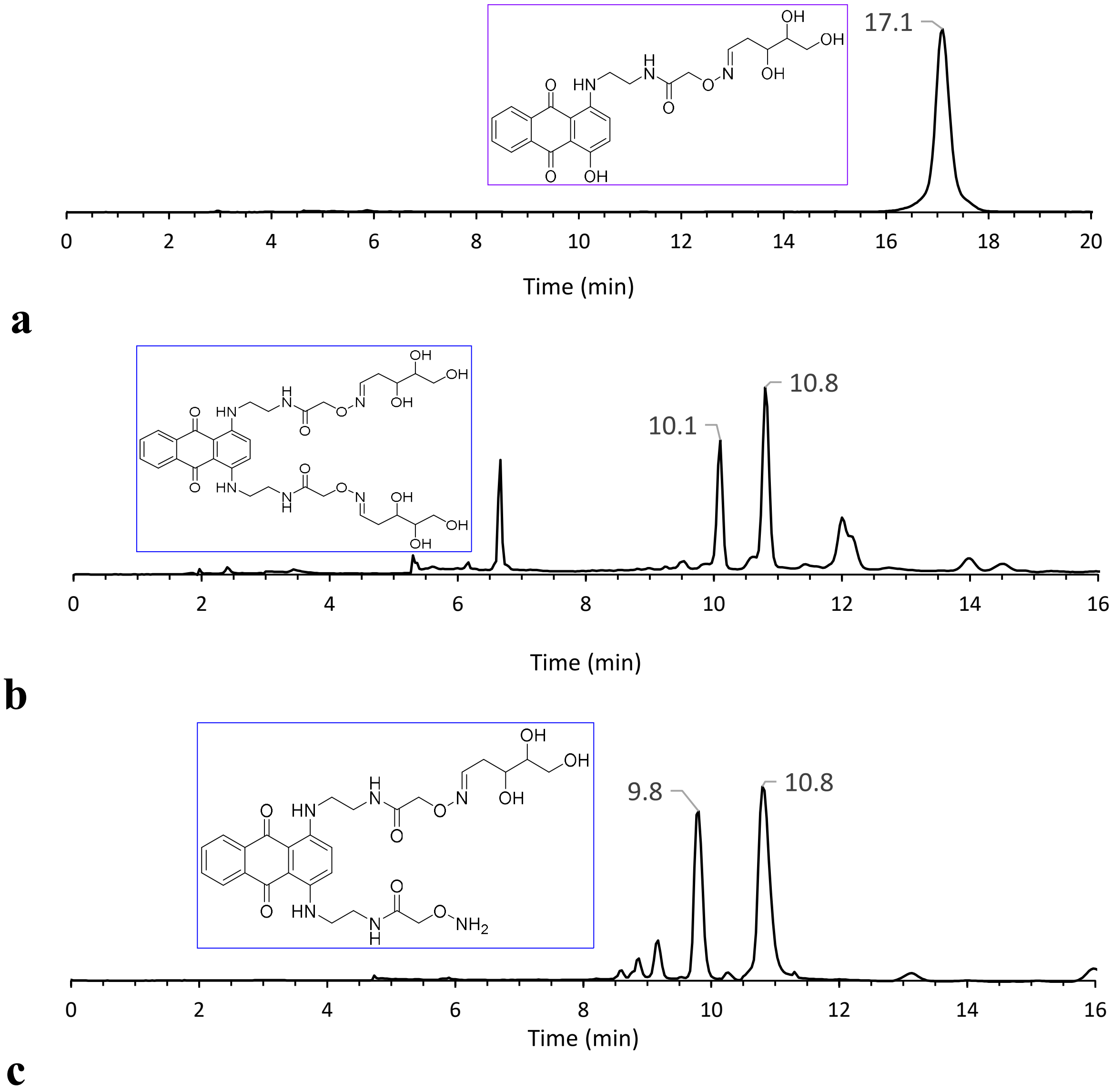

Figure 2.8: HPLC chromatograms of dR oximes of compounds **2-1** and **2-2** before purification. a) **2-1**; b) bis-dR oxime of **2-2** (10.1 min); and c) mono-dR oxime of **2-2** (9.8 min). Peak at 10.8 min in b) and c) is **2-2**.

Isotopically labeled dR adducts are required to quantitate the extent of adduct formation *in vitro* (e.g., CT DNA and cell culture) and *in vivo* by isotope dilution LC-ESI/MS^3 analysis. In preparation for such analyses, progress was made in the synthesis of $^{13}C_5$-labeled dR oximes of

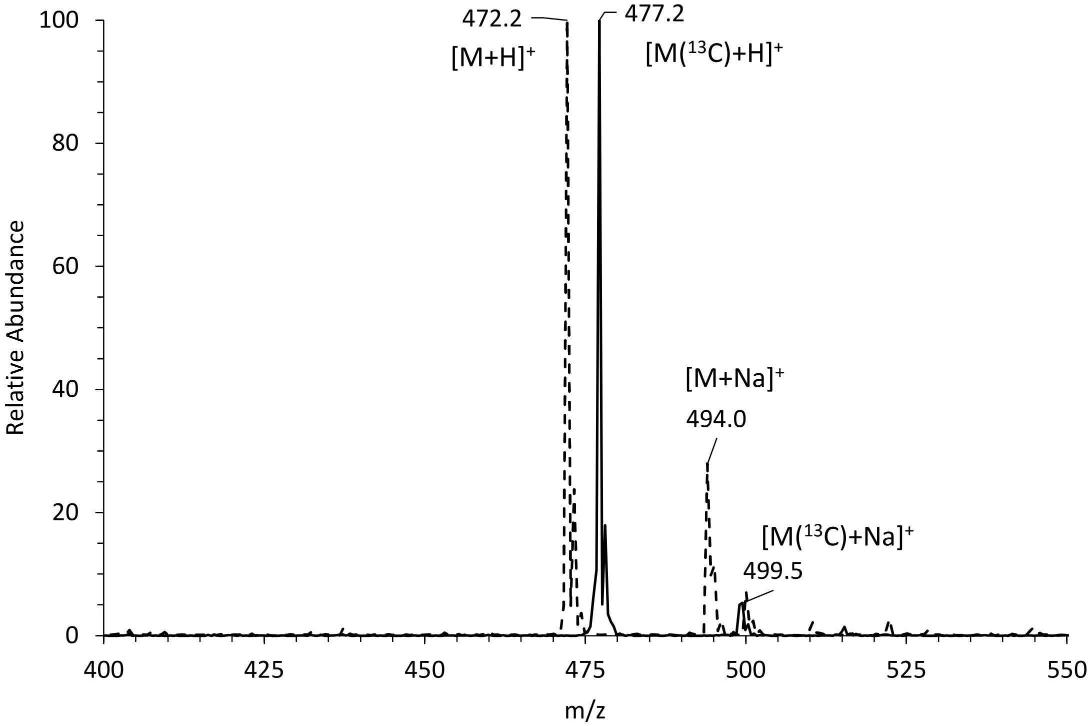

Figure 2.9: Mass spectra of the dR oxime of **2-1** (dashed) and the ^{13}C-labeled dR oxime of **2-1** (solid). Note that the $[M+H]^+$ ions and $[M+Na]^+$ ions for each compound are 5 m/z units apart from their labeled counterparts.

compounds **2-1** and **2-2**. Because of the cost of isotopically labeled dR, using a crude mixture of aminoxyacetamide and dR was not feasible like it was for the dR oxime of **2-1** previously outlined. As such, a similar procedure to that of the mono-oxime of **2-2** was followed, where a solution of $^{13}C_5$-labeled dR was prepared and an aliquot of drug solution was added in excess. Qualitative mass spectrometry showed a product 5 mass units greater than that of the unlabeled oxime (Figure 2.9), suggesting successful conjugation of the drug to the isotopically labeled sugar. At this time, no $^{13}C_5$-labeled dR oximes have been made using **2-2**.

Conjugation and Spectral Characterization of Aminoxyacetamide Drugs with a 12-Base Pair DNA Oligonucleotide

The next model system for the reactivity of the aminoxyacetamide anthraquinones with AP sites in DNA was a 12-base pair DNA oligonucleotide. By designing an oligonucleotide with a single dU nucleotide, we can enzymatically induce deglycosylation to form a site-specific AP site within the strand. Having a single AP site is beneficial for numerous reasons. Because the molecule is small, we can monitor these reactions by reverse-phase HPLC. Additionally, being able to monitor the reaction allows us to monitor reaction kinetics, analyze the entire oligonucleotide conjugate by LC-ESI/MS^2, and measure stabilizing effects of the conjugate on the oligonucleotide duplex.

The oligonucleotide used in these studies was the 12mer 5'– GTT GCU CGT ATG –3' (Umer), and all DNA duplexes contained the complementary strand 5'– CAT ACG CGC AAC – 3'. When reacting the drugs with the Umer, first the duplex needed to be formed. As such, Umer and complement were annealed in HEPES buffer. After annealing, the duplex was subjected to uracil DNA glycosylase (UDG) to deglycosylate the dU nucleotide *specifically*, creating an AP site (APmer). After the AP site was formed, the drug was added as an aliquot from a 2 mM stock solution and allowed to react at 37 °C for a few hours. The reaction was monitored periodically by reverse-phase HPLC (Figure 2.10). When the peak representing the APmer at 18.6 min disappeared or ceased to change, the peaks on the chromatogram were purified, lyophilized, and characterized by LC-ESI/MS^2.

Aliquots for HPLC monitoring require quenching. Past work done by our lab in collaboration with Dr. Robert Turesky's lab employed butyraldehyde as an alkoxyamine-scavenging reagent to remove excess *O*-(pyridin-3-yl-methyl)hydroxylamine (PMOA). In those experiments, PMOA was used to covalently capture AP sites so that they could be quantified.[221]

While initial experiments for this dissertation employed butyraldehyde to scavenge excess aminoxyacetamide when taking aliquots to monitor the reactions of the drug and APmer, we ultimately settled on the use of acetone to quench the reaction. The use of acetone to quench the reactions resulted in fewer diastereomers of the oxime compared to that of the asymmetrical butyraldehyde.

For our oligonucleotide reactions, the Umer and complement were annealed at 25 μM in HEPES buffer. Past work in our lab has determined that an optimal concentration of UDG is 0.25 units/μL, added as an aliquot of a stock solution of 5 units/μL. When the anthraquinone is added, we typically add an aliquot such that the concentration of the drug is 40 μM; however, this is changed as the reaction conditions require. When these conditions were utilized in the conjugation of **2-1** to the APmer, the reaction lasted 4 hours before requiring purification by HPLC. For reasons discussed later in this chapter, the reaction with **2-2** was run at an

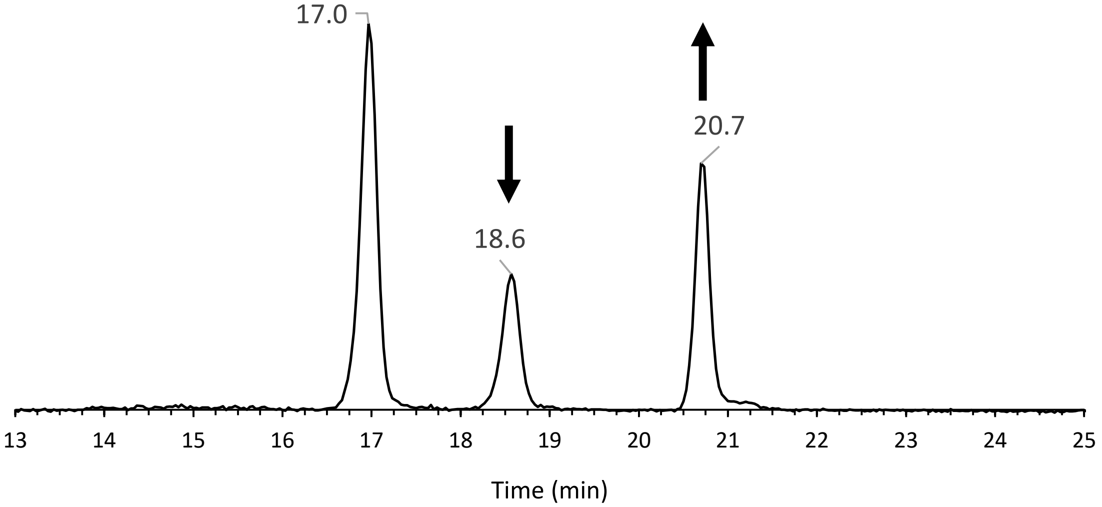

Figure 2.10: HPLC chromatogram monitoring the progress of the conjugation reaction of 40 μM **2-1** to duplex APmer. The complementary strand elutes at 17.0 min, the APmer elutes at 18.6 min, and the oxime conjugate elutes at 20.7 min. Arrows indicate the growth or decrease in peaks over time.

anthraquinone concentration of 200 μM. This reaction lasted 3 hours before requiring purification.

After lyophilizing the purified samples several times to remove excess chromatography buffer, the samples were dissolved in LCMS-grade water and characterized by LC-ESI/MS^2. As shown in Figure 2.11a, the HPLC peak at 20.7 min (Figure 2.10) is purified **2-1** conjugated to the APmer. Figure 2.11b shows the selected ion collision-induced dissociation (CID) fragmentation of the $[M\text{-}4H]^{-4}$ ion. Upon CID fragmentation, the MS^2 spectrum shows a fragmentation pattern similar to what one would expect based on the APmer sequence (Table 2.2). Based on the presence and accuracy of the $[a_7\text{-}B]^{-2}$, $[w_7]^{-2}$, and $[w_7]^{-3}$ fragments, we concluded that the conjugate formed at the AP site in the oligonucleotide as expected.

As previously mentioned, compound **2-2** required different conditions for the conjugation of the drug to the APmer. When the reaction was performed with the same conditions as **2-1**, we observed multiple peaks eluting closely together where the conjugate was expected to elute (Figure 2.12). The identity of those peaks were unknown, so further experiments were needed to determine their identity. The APmer conjugation reaction was performed as previously described. When purifying the reaction by HPLC, all of the peaks from 20.0-22.0 min were collected in the same tube. Once the samples were dried by lyophilization, the sample was subjected to enzymatic digestion as described in the Experimental section of this chapter. Once the sample was enriched by SPE, the fractions were analyzed by LC-ESI/MS^2. To our surprise, as shown in Figure 2.13, there was evidence of the bis-dR oxime of **2-2** in relatively significant amounts. As the reaction was purified to remove unreacted APmer, the presence of the bis-oxime suggests that, at 40 μM, a cross-linking between two APmer duplexes facilitated by **2-2** competes with the desired mono-conjugation.

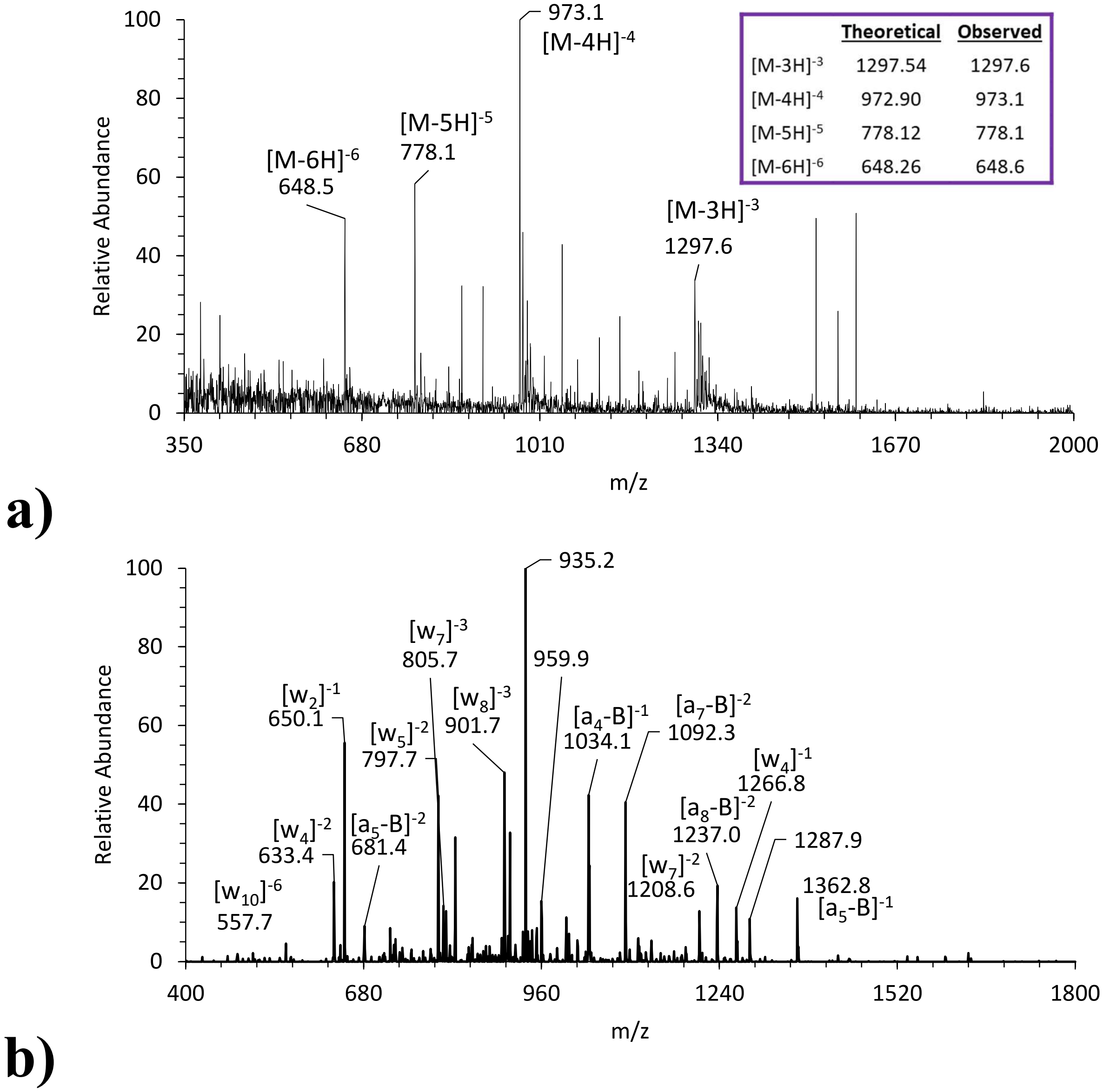

	Theoretical	Observed
$[M-3H]^{-3}$	1297.54	1297.6
$[M-4H]^{-4}$	972.90	973.1
$[M-5H]^{-5}$	778.12	778.1
$[M-6H]^{-6}$	648.26	648.6

Figure 2.11: Mass spectrometric data of HPLC-purified **2-1** oxime conjugate to APmer. a) Full mass spectrum and table of important m/z data; and b) CID fragmentation MS^2 of m/z 972.9. Important m/z data and the representative fragments are emphasized.

Table 2.2. Theoretical and observed mass spectrometric data for the CID fragmentation of the **2-1** oxime conjugate to the APmer. Theoretical values calculated by Mongo Oligo Mass Calculator v2.06. Names of the fragments and the sequences they represent are provided. Note that not all peaks are labeled in Figure 2.10. X = conjugated AP site.

		Theoretical	**Observed**
GTT	$[a_3\text{-B}]^{-1}$	730.50	730.1
GTTG	$[a_4\text{-B}]^{-1}$	1034.70	1034.1
GTTGC	$[a_5\text{-B}]^{-1}$	1363.91	1362.8
	$[a_5\text{-B}]^{-2}$	681.45	681.4
GTTGC**X**C	$[a_7\text{-B}]^{-2}$	1092.24	1092.3
GTTGC**X**CG	$[a_8\text{-B}]^{-2}$	1236.83	1237.0
	$[a_8\text{-B}]^{-3}$	824.22	824.6
pTTGC**X**CGTATG	$[w_{11}]^{-4}$	910.59	910.5
TTGC**X**CGTATG	$[y_{11}]^{-3}$	1187.80	1186.8
pTGC**X**CGTATG	$[w_{10}]^{-3}$	1113.06	1112.6
	$[w_{10}]^{-6}$	556.03	557.7
pC**X**CGTATG	$[w_8]^{-3}$	901.92	901.7
p**X**CGTATG	$[w_7]^{-2}$	1208.80	1208.6
	$[w_7]^{-3}$	805.53	805.7
pGTATG	$[w_5]^{-2}$	798.01	797.7
pTATG	$[w_4]^{-1}$	1267.82	1266.8
	$[w_4]^{-2}$	633.41	633.4
pTG	$[w_2]^{-1}$	650.41	650.1

As a means of promoting mono-conjugation over the cross-linking reaction, the concentration of **2-2** was increased to 200 μM in the APmer reaction. Doing so significantly reduced the size of the other product peaks in the chromatogram relative to the major product peak (Figure 2.14). Because the reaction is quenched with acetone as it was with the **2-1** reaction, the conjugate is not **2-2** bound to the APmer but rather **2-10** bound to the APmer.

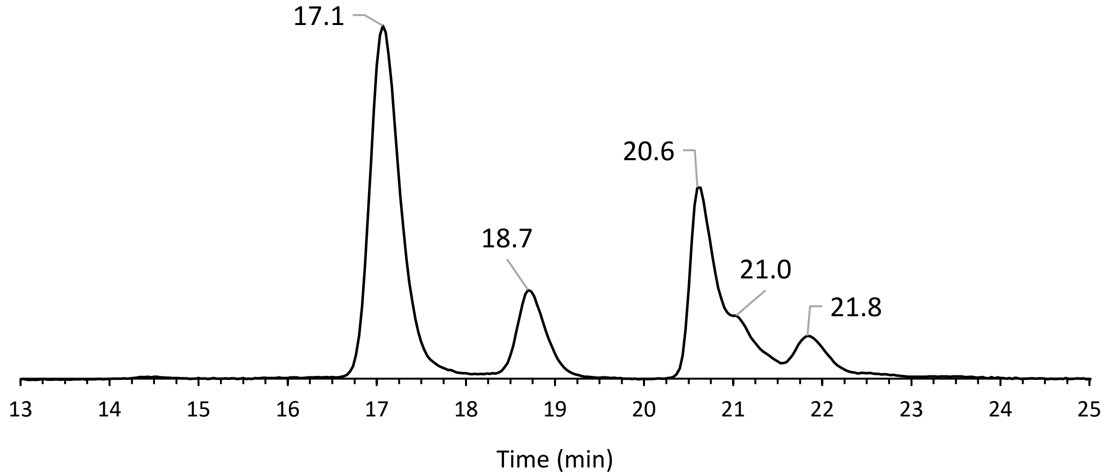

Figure 2.12: HPLC chromatogram monitoring the progress of the conjugation reaction of 40 μM **2-2** to duplex APmer. The complementary strand elutes at 17.1 min, the APmer elutes at 18.7 min, and the oxime conjugate elutes at 20.6 min. The other eluants within that minute are currently-unwanted byproducts.

Compound **2-10** is formed when the free alkoxyamine reacts with the acetone quench to form the acetone oxime. This prevents further reaction of the conjugate, leading to an even neater HPLC chromatogram (Figure 2.15). Qualitative mass spectrometric analysis showed that the purified peak is the conjugate between **2-2** and the APmer with the unbound alkoxylamine capped with acetone (i.e., **2-10** and the APmer). As shown in Figure 2.16 and Table 2.3, the acetone conjugate is pure, and the CID fragmentation pattern indicates that our oxime is attached to the AP site in the sequence.

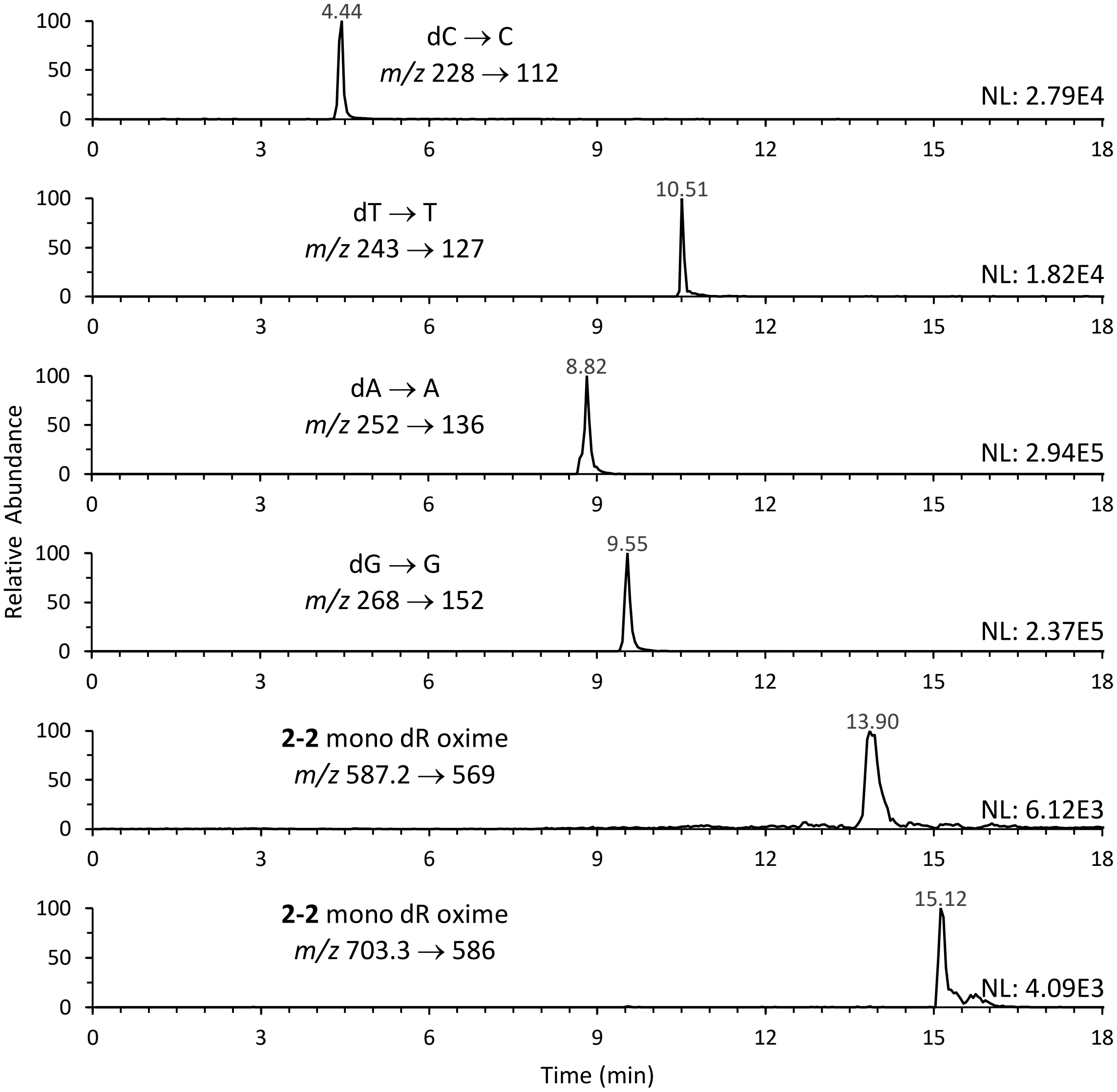

Figure 2.13: LC-ESI/MS^2 chromatogram of the SPE-enriched enzymatic digestion of the reaction between **2-2** and the APmer. Chromatograms show the fragmented loss of dR for the natural nucleosides. Ion counts are presented to the right of each trace (NL).

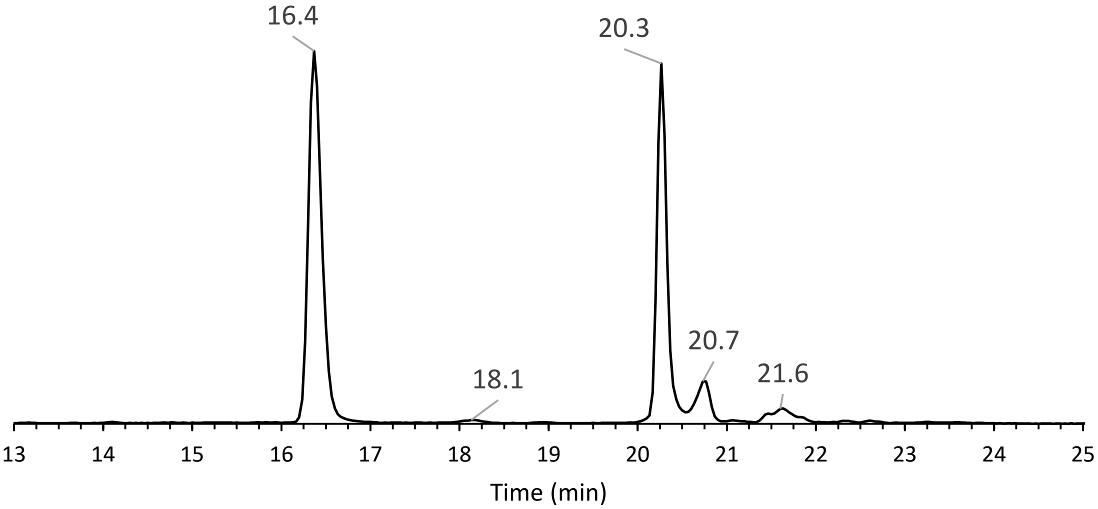

Figure 2.14: HPLC chromatogram monitoring the progress of the conjugation reaction of 200 µM **2-2** to 25 µM duplex APmer. The complementary strand elutes at 16.4 min, the APmer elutes at 18.1 min, and the oxime conjugate elutes at 20.3 min. The other eluants within that minute are the same unwanted byproducts. Note that they are smaller relative to the peak at 20.3 min. The sharper peaks and better separation are due to the use of a newer column than that used for the previous

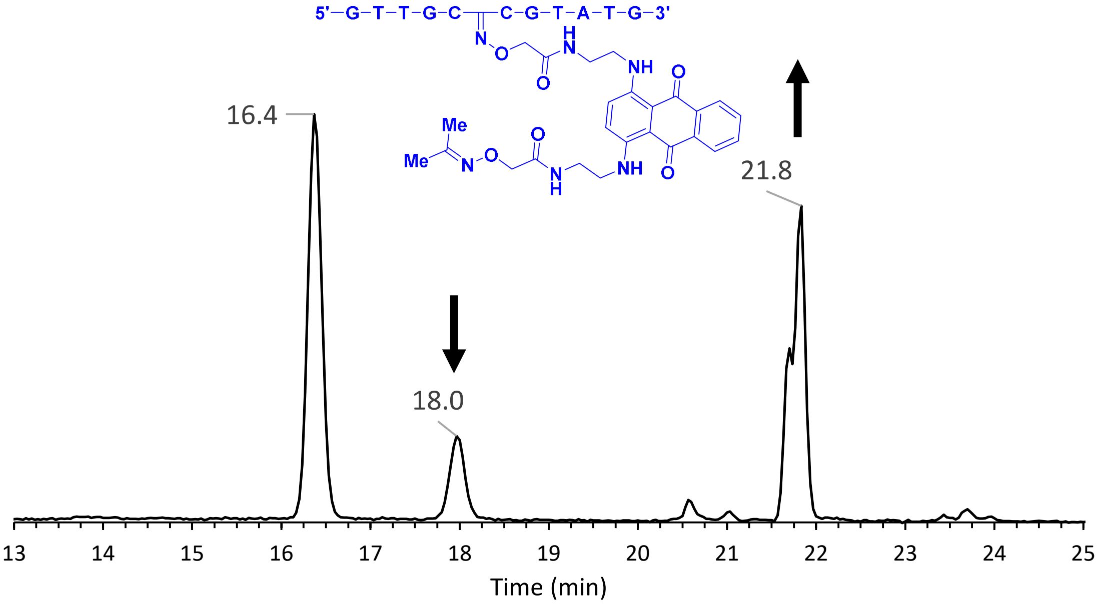

Figure 2.15: HPLC chromatogram monitoring the progress of the acetone-quenched conjugation reaction of 200 µM **2-2** to duplex APmer. The complementary strand elutes at 17.0 min, the APmer elutes at 18.6 min, and the acetone-capped oxime conjugate elutes at 21.8 min. The small peaks at 20.6 and 21.0 min are the byproducts. The structure of this oxime conjugate (**2-10**) is provided. Arrows indicate the growth or decrease in peaks over time.

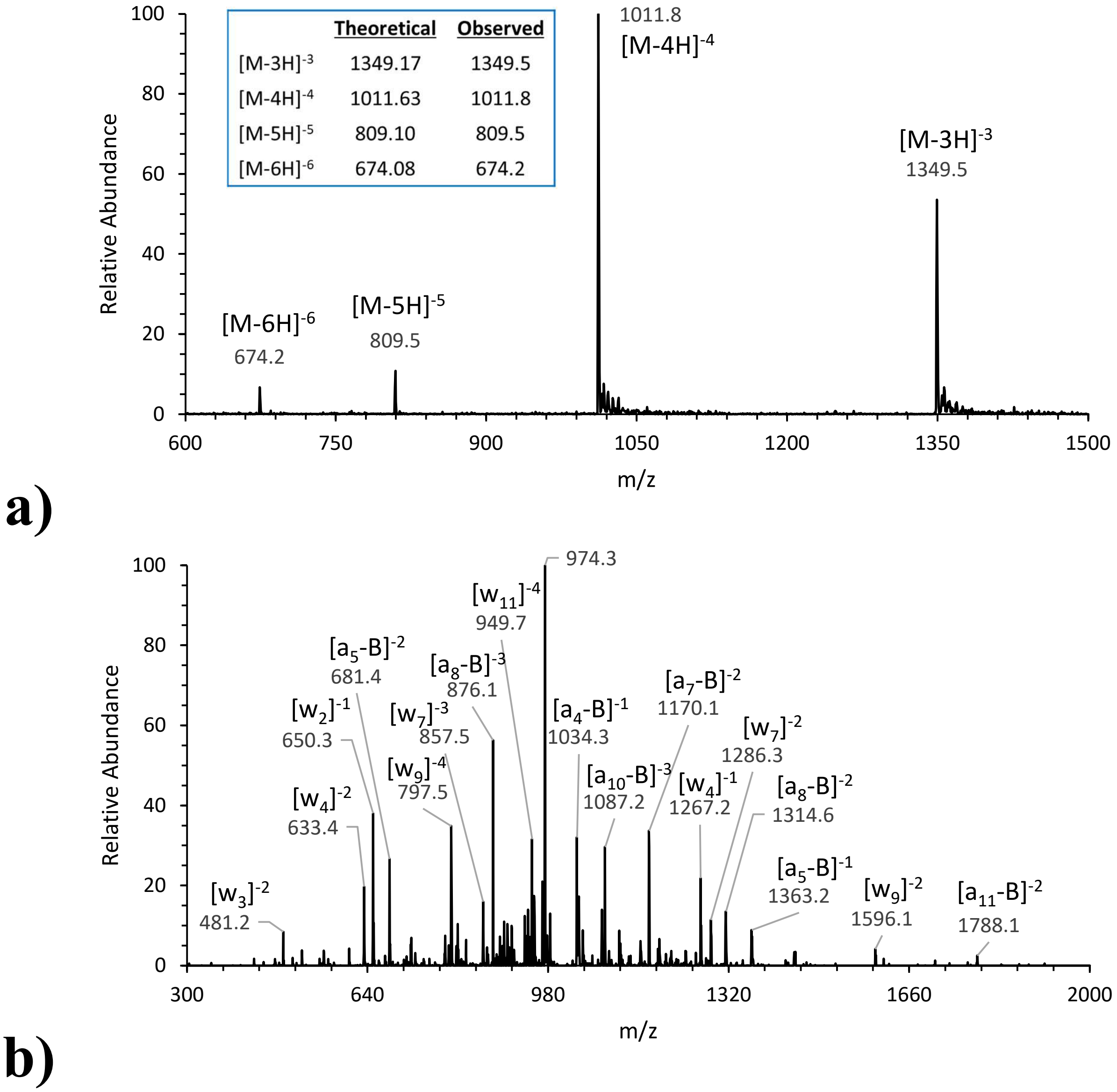
	Theoretical	Observed
$[M-3H]^{-3}$	1349.17	1349.5
$[M-4H]^{-4}$	1011.63	1011.8
$[M-5H]^{-5}$	809.10	809.5
$[M-6H]^{-6}$	674.08	674.2

Figure 2.16: Mass spectrum of HPLC-purified **2-10** oxime conjugate to the APmer. a) Full mass spectrum and table of important m/z data; and b) CID fragmentation MS^2 of m/z the 1011.6 (-4) ion. Important m/z data and the representative fragments are emphasized.

Table 2.3. Theoretical and observed mass spectrometric data for the CID fragmentation of the **2-10** oxime conjugate to the APmer. Theoretical values calculated by Mongo Oligo Mass Calculator v2.06. Names of the fragments and the sequences they represent are provided. X = conjugated AP site. (1 decimal point)

		Theoretical	**Observed**
GTTG	$[a_4\text{-B}]^{-1}$	1034.70	1034.3
GTTGC	$[a_5\text{-B}]^{-1}$	1363.91	1363.2
	$[a_5\text{-B}]^{-2}$	681.45	681.4
GTTGC**X**C	$[a_7\text{-B}]^{-2}$	1169.69	1170.1
GTTGC**X**CG	$[a_8\text{-B}]^{-2}$	1314.29	1314.6
	$[a_8\text{-B}]^{-3}$	875.85	876.1
GTTGC**X**CGTA	$[a_{10}\text{-B}]^{-3}$	1086.99	1087.2
GTTGC**X**CGTAT	$[a_{11}\text{-B}]^{-2}$	1787.59	1788.1
pTTGC**X**CGTATG	$[w_{11}]^{-4}$	949.32	949.7
pGC**X**CGTATG	$[w_9]^{-2}$	1595.45	1596.1
	$[w_9]^{-4}$	797.22	797.6
p**X**CGTATG	$[w_7]^{-2}$	1286.25	1286.3
	$[w_7]^{-3}$	857.17	857.6
pTATG	$[w_4]^{-1}$	1267.82	1267.2
	$[w_4]^{-2}$	633.41	633.4
pATG	$[w_3]^{-2}$	481.31	481.2
pTG	$[w_2]^{-1}$	650.41	650.3

Stability of the Oxime Conjugates of the 12-Base Pair DNA Oligonucleotide

With proof of the conjugates' existence, we sought to determine if these conjugates thermally stabilize the duplex compared to the same duplex but with an AP site analog. This analog replaces a nucleobase with tetrahydrofuran (THF). As such, the sequence dubbed THFmer is 5'– GTT GC<u>X</u> CGT ATG –3' where <u>X</u> is the THF analog of the AP site. Both the **2-1** and **2-2** conjugates (without acetone in the case of **2-2**) were purified by HPLC to isolate the

3'—C–A–A–C–G–C–G–C–A–T–A–C–5'
5'—G–T–T–G–C–<u>X</u>–C–G–T–A–T–G–3'

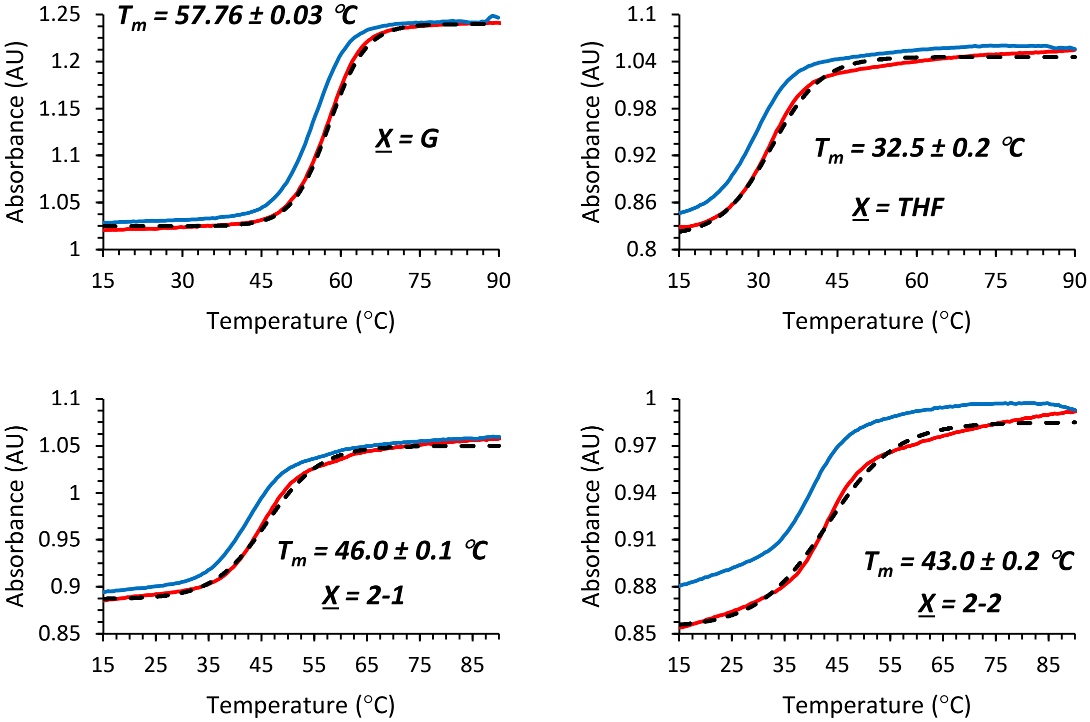

Figure 2.17: Melting (red) and cooling (blue) curves for the oligo conjugates. Data was collected for samples of 0.6 OD/mL from 15 °C to 90 °C at a rate of 1 °C/min measuring every 0.5 min. The curves from estimated sigmoidal parameters are in black. Samples are the unmodified control (X = G, top left), THFmer (top right), **2-1** (bottom left), and **2-2** (bottom right). Estimated T_m values are provided for each sample.

Table 2.4. Comparison of thermal melting temperatures between conjugate oligonucleotides and controls.

X =	**T_m (°C)**	**ΔT_m (°C)**	**$\Delta\Delta T_m$ (°C)**
G	57.76 ± 0.03		
THF	32.5 ± 0.2	-25.3 ± 0.2	
2-1	46.0 ± 0.1	-11.8 ± 0.1	13.5 ± 0.2
2-2	43.0 ± 0.2	-14.8 ± 0.2	10.5 ± 0.3

conjugates from the reaction mixtures. After drying the conjugates by lyophilization, both were prepped as described in the Experimental section of the chapter.

The thermal melting temperature (T_m) was determined for both compounds' oxime conjugates re-annealed to the complementary 12mer. As a control, the T_m of the THFmer and the unmodified control (5'– GTT GC<u>G</u> CGT ATG –3') also were measured. Presented in Figure 2.17 are the melting and cooling curves of each sample. The equations for the sigmoidal absorbance vs. temperature curves were estimated by KaleidaGraph to fit the equation:

$$y = A_f + \frac{A_i - A_f}{1 + e^{\frac{x - x_0}{dx}}} \qquad \textbf{Eq. 1}$$

where A_f is the higher absorbance asymptote, A_i is the lower absorbance asymptote, dx is the change in temperature corresponding to the greatest change in absorbance, and x_0 is the inflection point of the curve, (i.e., the T_m). The presence of the AP site analog significantly decreases the thermal stability of the DNA duplex. However, the formation of the oxime conjugates of **2-2** and **2-1** increase, in that order, the thermal stability from the THFmer (Table 2.4). However, the THFmer's and oxime conjugates' heating curves show broadening, indicating that the melting process was not as cooperative as it was for the control solution.

In each of the samples presented in Figure 2.17, the cooling curve is presented. These curves show how the samples reanneal after melting. If the cooling curve is smooth and similar to the melting curve, then the cooling transitions are similar to the melting transitions. This is the case for both controls as well as the **2-1** oxime conjugate's duplex. However, the cooling curve for the **2-2** oxime conjugate shows a modest hysteresis from its heating curve, indicating that the reannealing process does not follow an exact reversal of the melting mechanism.

While these T_m studies have given insight into the thermal stability of the conjugates' duplexes, a key tenet to our hypothesis is the stability of the oxime itself. As we did for the T_m studies, the oxime conjugates were purified by HPLC following the same conditions as previously reported in this dissertation. After lyophilization, the samples were reannealed to the complementary strand. After allowing the sample to cool to room temperature, the solution was transferred to a heat block set to 37 °C and allowed to react over the course of 1 week. Throughout the week, the samples were monitored by reverse-phase HPLC to check for reformation of the APmer. If APmer did reform, it would be the result of the hydrolysis of the oximes. Figure 2.18a shows an example of the chromatogram of the **2-1** oxime during the study, and Figure 2.18b shows the change in the percent **2-1** oxime concentration as a function of time. The data was fit to a linear regression using KaleidaGraph to estimate the slope. The slope of the regression is nonzero, indicating upon first glance that there was a significant change in oxime concentration over the course of a week. However, the magnitude of the uncertainty of the slope is greater than the magnitude of the slope itself. Since the slope ± uncertainty includes zero in its range, we concluded that our data suggests that there is *no* significant change in oxime concentration under these conditions over the course of the week.

As was previously done for the T_m study, the major product peak of the **2-2** conjugation reaction was purified from the complement strand and the smaller byproduct peaks shown in Figure 2.14. However, upon monitoring the first timepoint of the **2-2** oxime's stability, the initial chromatogram (Figure 2.19) shows the "reappearance" of the byproduct peaks that elute similarly to the purified peak. Additionally, as shown in Figure 2.19, the purified peak was much lower in intensity than it was when the reaction was purified initially. As shown in Figure 2.20, the *total* percent concentration of all three peaks remains constant over the course of the week from that point forward. This indicates that the byproduct peaks are in thermal equilibrium with the originally purified peak. This brings into question some of the results from the T_m study regarding the melting curve for the **2-2** conjugate. The T_m results for **2-2** actually are those of the

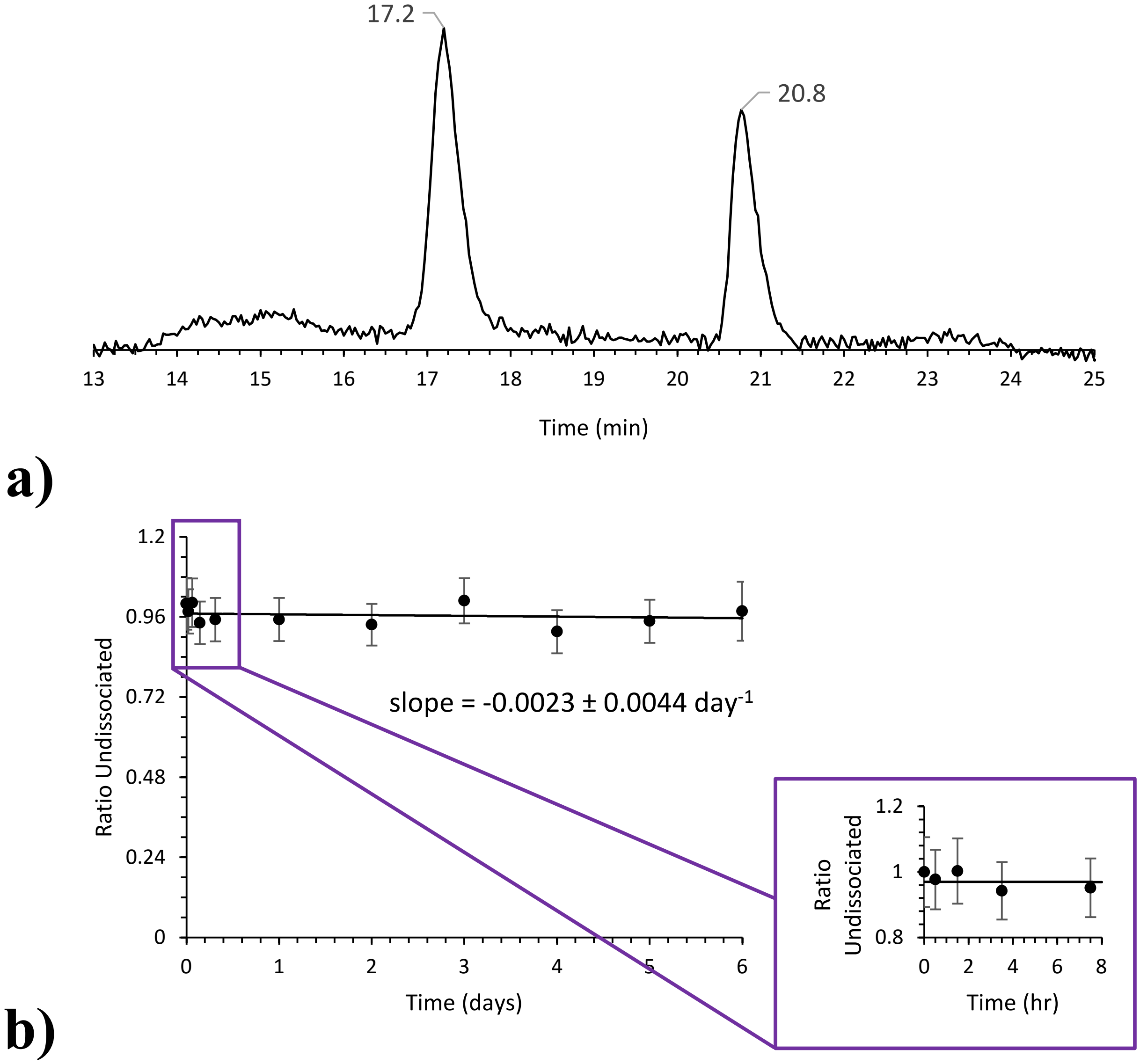

Figure 2.18: Stability of the **2-1** oxime conjugate to the APmer. a) Representative HPLC chromatogram demonstrating the relative amounts of each species in the reannealed duplex (the complementary strand elutes at 17.2 min, and the conjugate elutes at 20.8 min); and b) [APmer] vs. time for the reannealed conjugate. Error bars indicate deviation for technical replicates, not biological. Note how the slope of the linear regression includes 0 within one standard deviation.

thermal equilibrium between these peaks. Further work is needed to understand and prevent the onset of equilibrium so that the actual mono-conjugate can be studied.

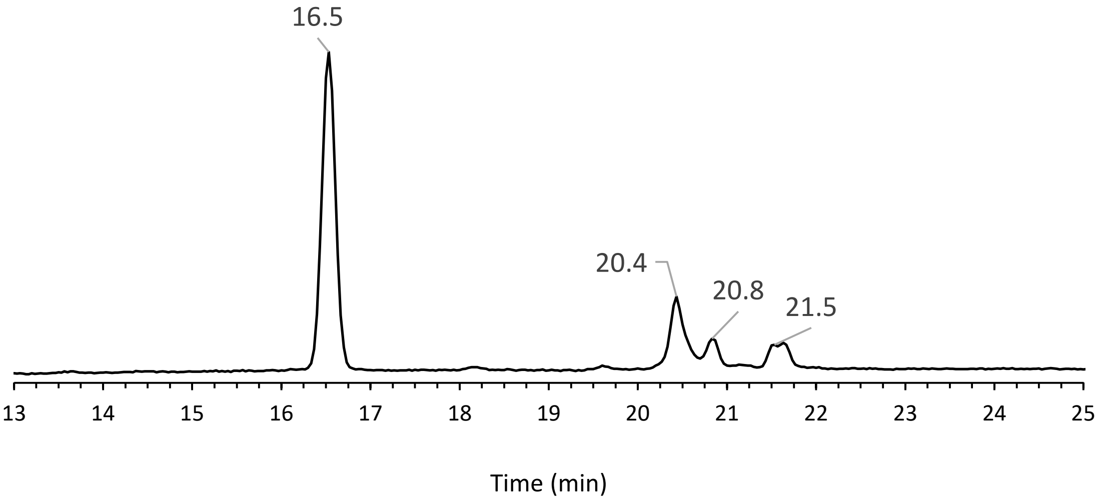

Figure 2.19: Initial timepoint of the **2-2** oxime conjugate's stability study. The complementary strand elutes at 16.5 min, and the oxime conjugate elutes at 20.4 min. The other eluants within that minute are the same unwanted byproducts as before. Their appearance here indicates that these products might be in equilibrium with each other.

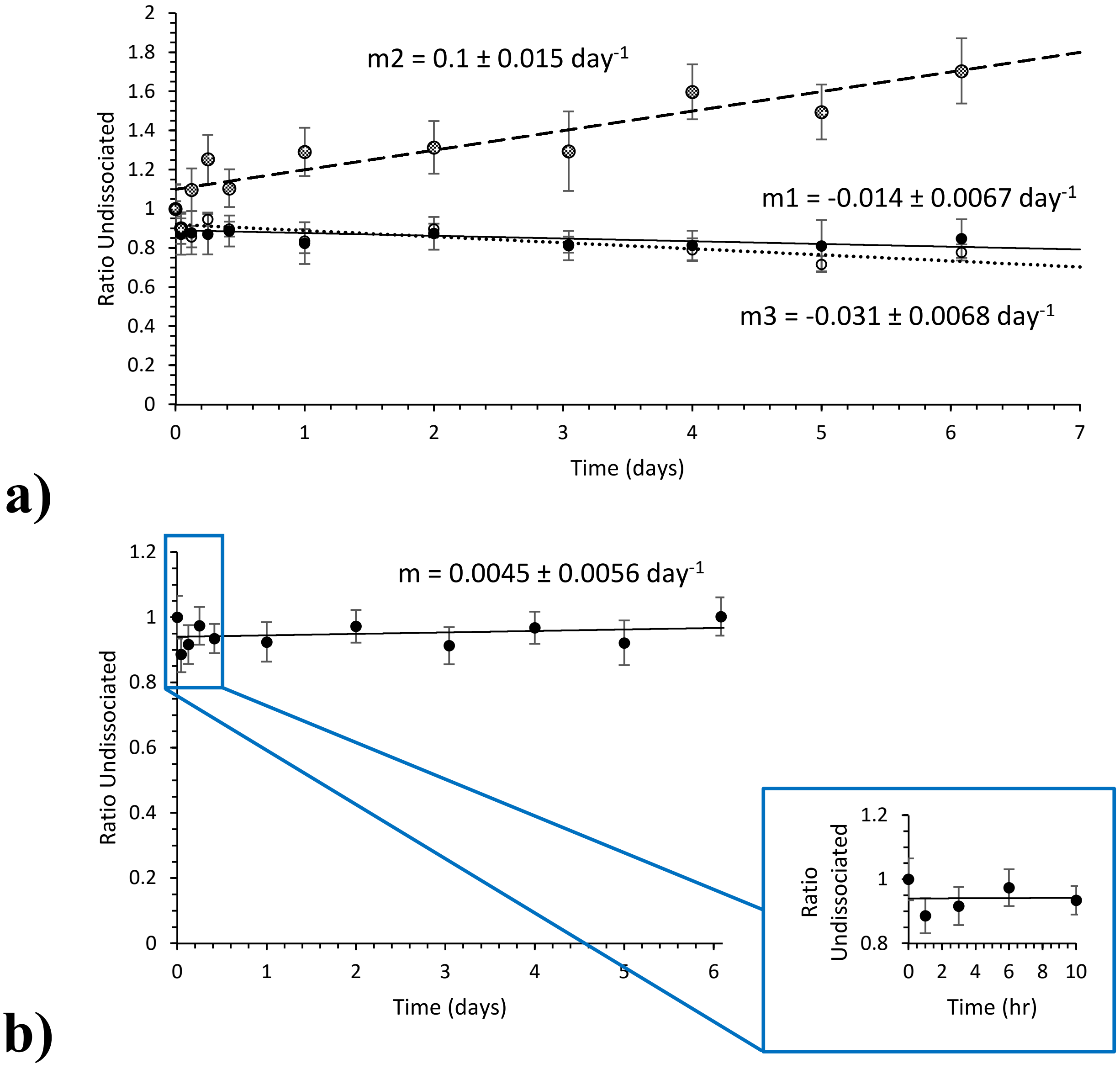

Figure 2.20: Stability of the **2-2** oxime conjugate to the APmer. a) Concentration versus time for the reannealed conjugate and the byproducts in the equilibrium; and b) Concentration versus time for <u>the sum</u> off all conjugate peaks. Note how the change of individual peaks is significant, but the overall change in the sum is not. Error bars indicate deviation for technical replicates, not biological.

Determining the Change in APmer Concentration as a Function of Time

Understanding the mechanism by which these compounds bind to AP sites in DNA is crucial because the rate laws will provide us concentration-based data to guide future studies. For example, if our research ever were to become a clinical chemotherapeutic option, then knowing the rate of adduct formation is imperative. As such, we performed initial kinetic studies to monitor the loss of APmer over time.

We employed the previously-described reaction conditions in triplicate for the reaction of **2-1** with duplex APmer made from degylcosylated Umer and its complement. The initial timepoints of the studies were taken before any anthraquinone was added. Reaction times began when the reactions were vortexed after addition of the drug. Aliquots of the reaction were collected at predetermined timepoints and mixed with a small amount of HPLC-grade acetone to quench the reaction. This quench was necessary to prevent systematic error in measuring the concentration of APmer. Each chromatogram was integrated manually in triplicate to perform calculations using technical replicates. Each technical replicate's data was processed as follows.

The peak areas of APmer and its complementary strand were averaged across technical replicates, and the standard deviation of these replicates was calculated. The average areas were divided by the respective strand's extinction coefficient at the measured wavelength to provide an effective concentration of each. In this dissertation, the effective concentration is labeled as $[\text{APmer}]_{\text{eff}}$ for the APmer, or similarly for other species. The ratio of $[\text{APmer}]_{\text{eff}}$ to $[\text{complement}]_{\text{eff}}$ was calculated to get an effective ratio of reaction completion. Each effective ratio was normalized by that of that biological replicate's timepoint at t = 0 hr – the one collected before the addition of any drug. This resulted in a graph of ratio undissociated (a measure of ratio completion) versus time, an example of which is shown in Figure 2.21. The error bars in Figure

2.21 represent the error between the technical replicates. The small size of the error bars indicates that the manual integration was consistent between replicates.

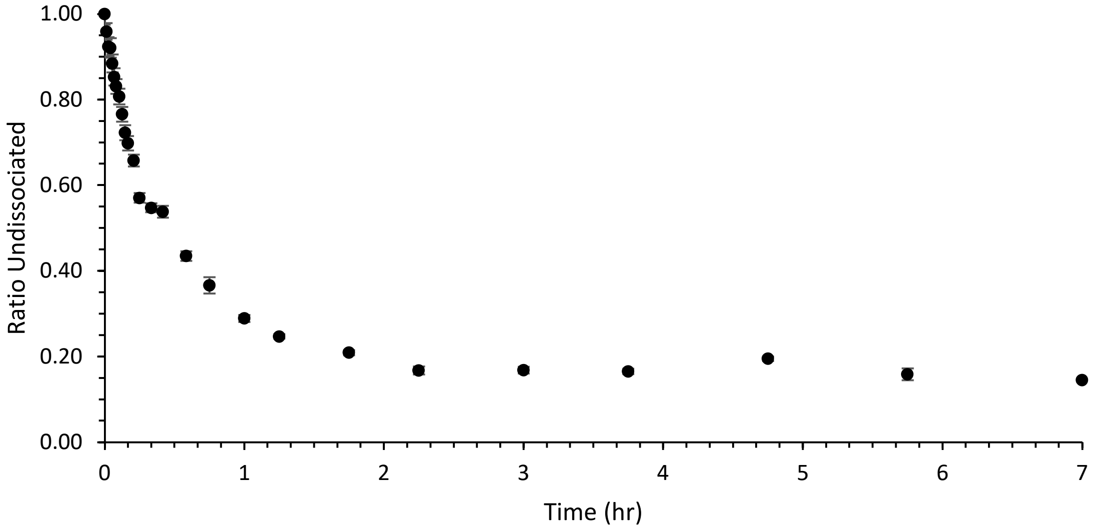

Figure 2.21: Ratio of undissociated APmer relative to the complementary strand versus time for a single biological replicate of **2-1** binding to the oligo. Error bars are the standard deviation of three technical replicates.

The average ratio completion across *biological* replicates was calculated by averaging the results of the calculations described in the previous paragraph for each replicate. This provided the data for our reported time course experiments. Each average ratio completion data point across biological replicates was calculated at each timepoint. These values were converted into concentrations of APmer and graphed as a function of time. This process was automated using Microsoft Excel; copies of the spreadsheet and the formulas used are presented in the Appendix of this dissertation. Figure 2.22a shows the time course for 40 μM **2-1** when the Umer and its complement are annealed at a concentration of 25 μM. The error bars on the data points are indicative of deviation between the biological replicates. The presence of these larger error bars indicates that further replicates may be needed to obtain a more precise dataset.

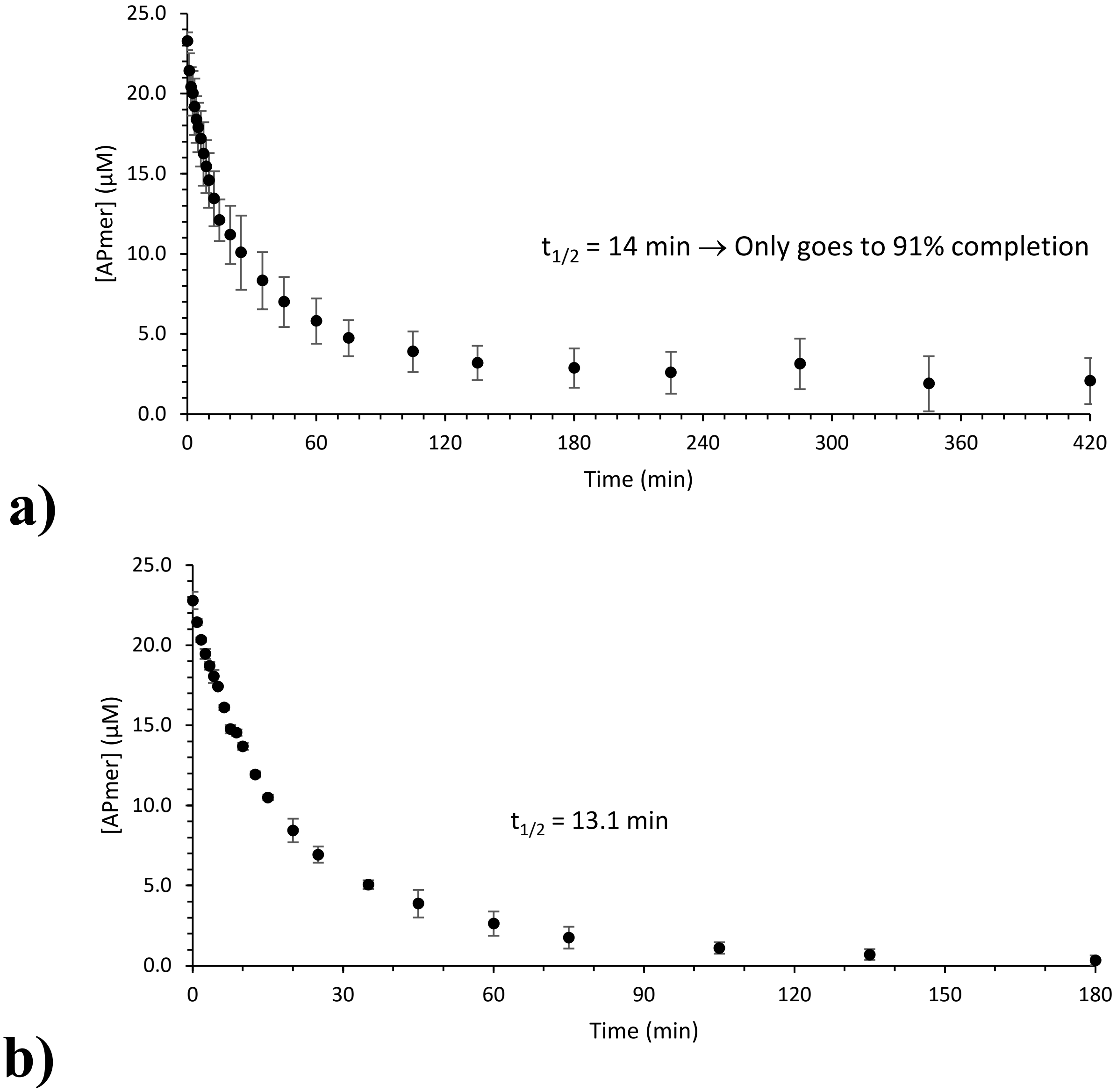

Figure 2.22: [APmer] versus time for the conjugation reactions of a) 40 μM **2-1** and b) 200 μM **2-2** to the oligo. Reactions were quenched with acetone before each timepoint. Error bars are the standard deviation of three biological replicates. Half-lives of the reactions are included.

As previously mentioned, the APmer reactions with **2-2** require a higher concentration of drug in order to lessen the competition between the conjugation and crosslinking reactions (Figure 2.14). As such, a similar procedure as that which is described in the previous paragraphs was performed using 200 μM **2-2** instead of 40 μM. These results are presented in Figure 2.22b.

From the data presented in Figure 2.22, the reaction times of these APmer reactions were set as described in the previous section (3 hr for optimal results).

For these data to be significant, they must be compared to datasets of some control experiments. Firstly, we measured the natural rate of fragmentation of an AP site for our duplex APmer using similar methods as previously described (Figure 2.23). Work done by John Terrell in our lab has shown that the APmer can fragment due to β-elimination at the AP site. Since loss of [APmer] was our measure of reaction rate, these data should tell us if there is any loss due to fragmentation instead of conjugation. As shown in the graph of [APmer] vs. time, this happens over the course of days, well beyond the timescale of the compounds' conjugation reactions in duplex APmer. As such, the β-elimation of APmer does not need to be considered a significant competing reaction for our compounds' time course data.

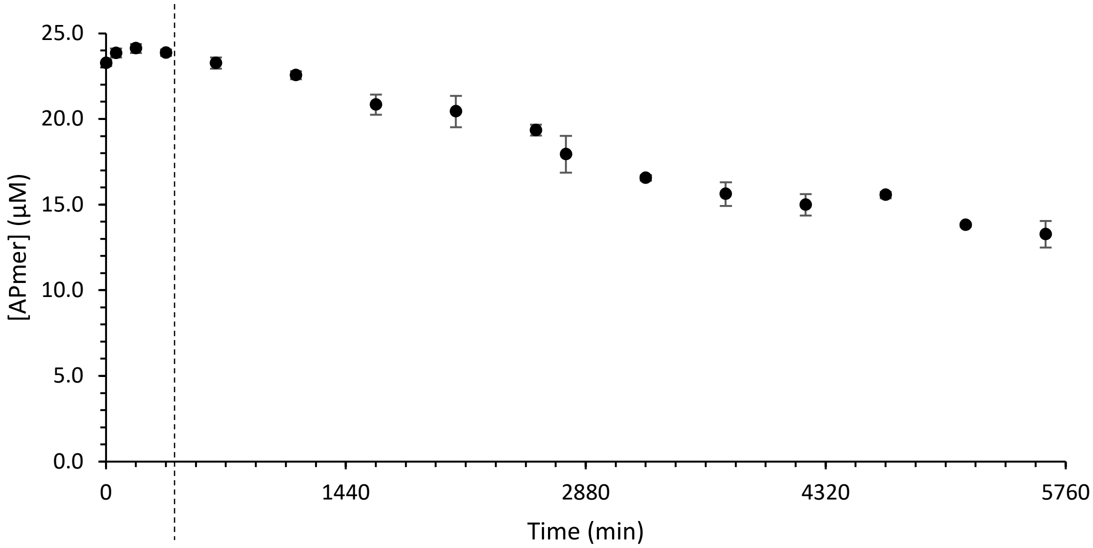

Figure 2.23: Loss of APmer over time due to β-elimination. Error bars are the standard deviation of three technical replicates – only one biological replicate was processed. A vertical line marks 7 hours, the length of time the reaction in Figure 2.22a ran.

Methoxyamine is the most basic alkoxyamine, and it already is present as a clinical option.[224–229] However, this compound does not intercalate like our compounds. As such, we measured the rate of conjugation of methoxyamine to duplex APmer as a function of [APmer] vs. time. Like the natural loss of APmer over time, the conjugation of methoxyamine to APmer also happens over the course of days. Because of this, loss of APmer due to β-elimination is a competing reaction to methoxyamine conjugation. The modeled equation for the data in Figure 2.23 was subtracted from the data to remove background loss of APmer. While the original data showed this reaction stalling at approximately 69% completion, adjusting these data to account for fragmentation predicts that the actual oxime formation stalls at approximately 21% completion (Figure 2.24).

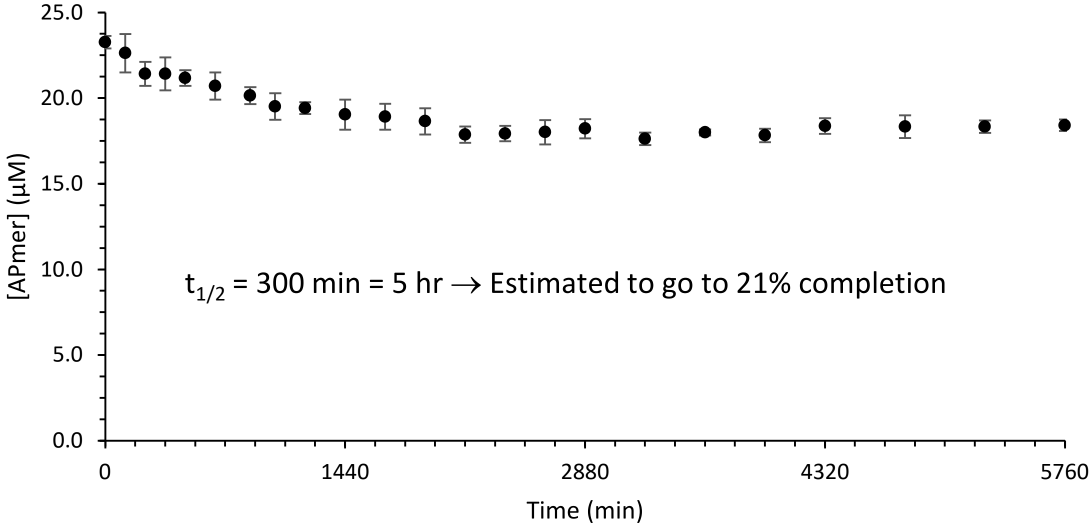

Figure 2.24: Loss of APmer over time as a result of methoxyamine binding to the AP site. Error bars are the standard deviation of three biological replicates. These results are adjusted from the acquired data to account for the background fragmentation of the APmer.

This also was done for the reaction of **2-1** to single-stranded APmer (Figure 2.25). While the original data showed this reaction stalling at approximately 81% completion, adjusting these

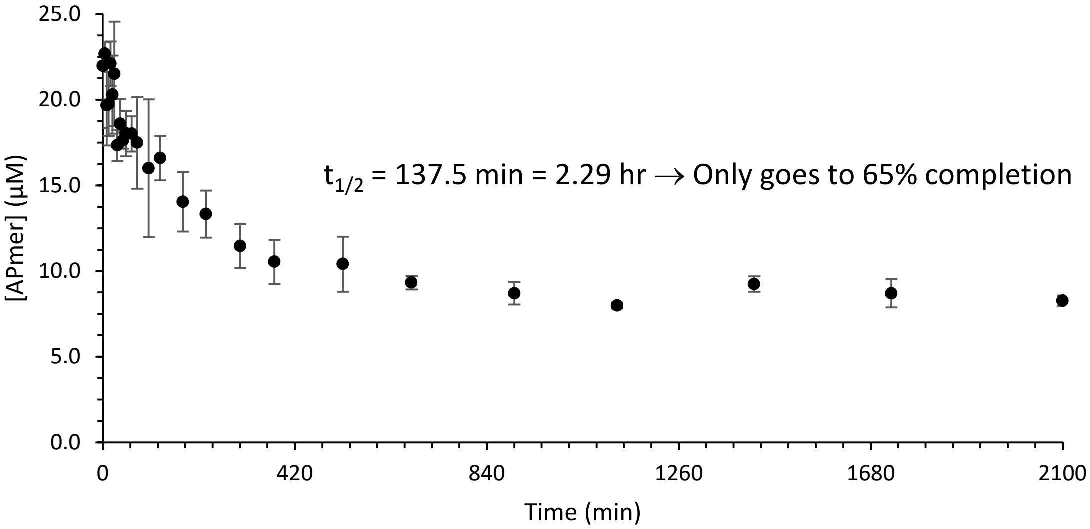

Figure 2.25: Loss of single-stranded APmer over time as a result of **2-1** binding to the AP site. Error bars are the standard deviation of three biological replicates. These results are adjusted from the acquired data to account for the background fragmentation of the APmer.

data to account for loss of APmer due to β-elimination predicts that the actual oxime formation stalls at approximately 65% completion. These conditions model the binding of our compound to an AP site; but, there is no intercalation that occurs with a single DNA strand, at least in the same way it occurs with duplex DNA. Additionally, we could not analyze our data the same as we did previously; we no longer have the complementary strand to act as an unchanging standard. Because of this, chromatograms were collected using full-loop injection. This process allowed us to measure the areas of the APmer peak as an absolute quantity, not a relative one. As can be seen in Figure 2.25, there was quite a bit of error associated with this method. We attribute this to slight variations in the HPLC sample volume with regards to the volume of acetone and the volume of sample due to water droplets on our HPLC syringe from washes. As such, Figure 2.25 should be considered a preliminary result with further testing required.

Additionally, while the reaction between single-stranded APmer and **2-1** does not span multiple days, there still is a significant loss of APmer due to fragmentation within this timeframe. As Figures 2.23-2.26 suggest, the rate of conjugation of **2-1** and **2-2** to duplex APmer is assisted by intercalation. This conclusion informed the mechanistic decisions that follow.

The analyses of these data are described in the following section. We employed COPASI, a software program from a collaboration between groups at the Biocomplexity Institute of Virginia Tech, the University of Heidelberg, and the University of Connecticut – UConn Health, to analyze the data as a model for the reactions' kinetics. By inputting our reaction conditions and uploading our dataset to the model, the software can estimate the rate constants of our model recursively. When we plug the estimated values into a theoretical time course experiment, we are given a curve that models our reaction.

Modeling the Rate of Conjugation of Aminoxyacetamides to AP Sites in DNA

The shape of the data presented in Figure 2.22 shows an exponential decay of the concentration of APmer over time, indicating that the conversion of APmer to conjugate is a concentration-dependent process. However, we cannot use an exponential regression to determine the rate constant of the binding process due to two factors. Firstly, we used different concentrations of the two drugs, so a rate constant for the binding of **2-1** cannot be compared to the concentration-dependent rate constant of **2-2**. Secondly, our current understanding of the mechanism of these drugs, as mentioned in Chapter 1, is that these intercalators will insert themselves into DNA duplexes and *then* covalently bind to DNA via formaldehyde. We would expect our compounds to behave similarly, following a mechanism as shown in Eq. 2 below:

$$APmer + Drug \rightleftharpoons [APmer \cdot Drug] \rightarrow Conjugate \qquad \textbf{Eq. 2}$$

where "[APmer · Drug]" is the intercalated drug complex. As this mechanism shows, the process of binding to an AP site in DNA is a two-step process. Performing an exponential regression *actually* provides an "observed rate constant" and makes the assumption either that the covalent binding is the rate-determining step or the reaction follows steady-state kinetics. In any case, the exponential decay is not an effective way of modeling this process.

To better model the kinetics of our drug-APmer system, we used COPASI for advanced chemical modeling. We labeled the forward rate of intercalation in Eq. 2 as k_1, the off-rate of the drug as k_2, and the covalent binding rate as k_3. For the reaction with **2-1**, the starting concentration of drug was 40 μM. While the starting concentration of Umer duplex was 25 μM, this value changed by the time the reaction began. When the UDG is added, the concentration of the duplex decreases to approximately 23.7 μM. This concentration further decreases to 23.3 μM when the drug is added. These were the starting concentrations used in the model.

An assumption we make in our model is that the calculated [APmer] outlined in the previous section solely represents that concentration. In reality, the presence of the [APmer · Drug] complex cannot be detected using HPLC, as the complex would dissociate on the column to give free drug and APmer. As such, the [APmer] used in the model actually is [APmer] + [APmer · Drug]. This aspect of the model is incorporated at a later point in this report.

Our data from the **2-1** time course was uploaded into COPASI. After adjusting the starting conditions as previously described, the system estimated that $k_1 = 1.37 \times 10^{-3}\ \mu M^{-1}\ min^{-1}$, $k_2 = 8.5 \times 10^{-3}\ min^{-1}$, and $k_3 = 4.8 \times 10^{-3}\ min^{-1}$. The uncertainties are presented along with these results in Table 2.5. While these errors are not insignificant, these results allow us to directly compare the k_3 values of **2-1** and **2-2** once the latter is modeled. Figure 2.26 shows the curve of a theoretical time course given our reaction conditions and the estimated rate constants set atop our data.

Table 2.5: First COPASI parameter estimation for the conjugation of **2-1** to the APmer by an intercalative mechanism (Eq. 2). These results do not consider [Conjugate] data.

Parameter	**Unit**	**Lower Bound**	**Start Value**	**Upper Bound**	**Value**	**Standard Deviation**	**Coeff. of Variation (%)**
k_1	$\mu M^{-1} \cdot min^{-1}$	-∞	0.01	∞	1.37×10^{-3}	0.03×10^{-3}	2.3
k_2	min^{-1}	-∞	0.01	∞	8.5×10^{-3}	0.9×10^{-3}	11.1
k_3	min^{-1}	-∞	0.01	∞	4.8×10^{-3}	0.8×10^{-3}	15.9

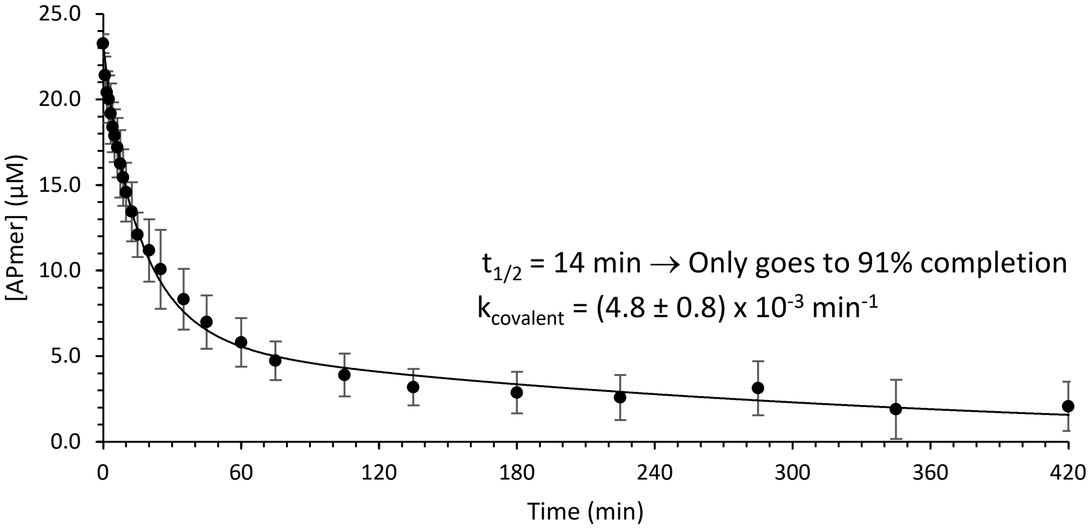

Figure 2.26: Data presented in Figure 2.22a with the curve predicted by COPASI. Curve shows [APmer] versus time of the model provided in Eq. 2 using the estimated rate constants in Table 2.5. The value for $k_{covalent}$ (k_3) is provided.

As a means of further improving the model's fit to the data, we went back to our HPLC chromatogram and manually integrated the conjugate's peak area on the second chromatogram of the diode array. For our experiments, this was set to a longer wavelength that is not shared between the drug and DNA. Since we previously had determined the extinction coefficients of our compound, we could perform similar calculations as previously described to calculate the average concentration of oxime conjugate at each timepoint. These data have been added to Figure 2.22a to create a new time course graph: Figure 2.27.

Unfortunately, when these data were added to the model in COPASI, the regressive estimations for the rate constants explode. When these new data are added to the model, the rate constants are estimated to be those in Table 2.6. While some of the values may seem reasonable, the uncertainties in each estimation significantly imply an imprecise guess due to highly correlated variables. When the conjugate growth is excluded from the model and the rate constants in Table 2.5 are used, COPASI predicts a sigmoidal shape for the concentration of conjugate. This is because the model predicts that the concentration of [APmer · Drug] is significant and changes over time (Figure 2.28). However, as shown in Figure 2.27, our growth data is logarithmic in shape. Forcing the sigmoidal shape to sharpen into a logarithmic shape most likely is the source of the large errors in COPASI's estimations.

Table 2.6: Second COPASI parameter estimation for the conjugation of **2-1** to the APmer by an intercalative mechanism (Eq. 2). These results do consider [Conjugate] data.

Parameter	Unit	Lower Bound	Start Value	Upper Bound	Value	Standard Deviation	Coeff. of Variation (%)
k_1	$\mu M^{-1} \cdot min^{-1}$	$-\infty$	0.01	∞	9.9×10^{-3}	25×10^{-3}	248.6
k_2	min^{-1}	$-\infty$	0.01	∞	4.7	14	294.3
k_3	min^{-1}	$-\infty$	0.01	∞	0.6	0.2	31.5

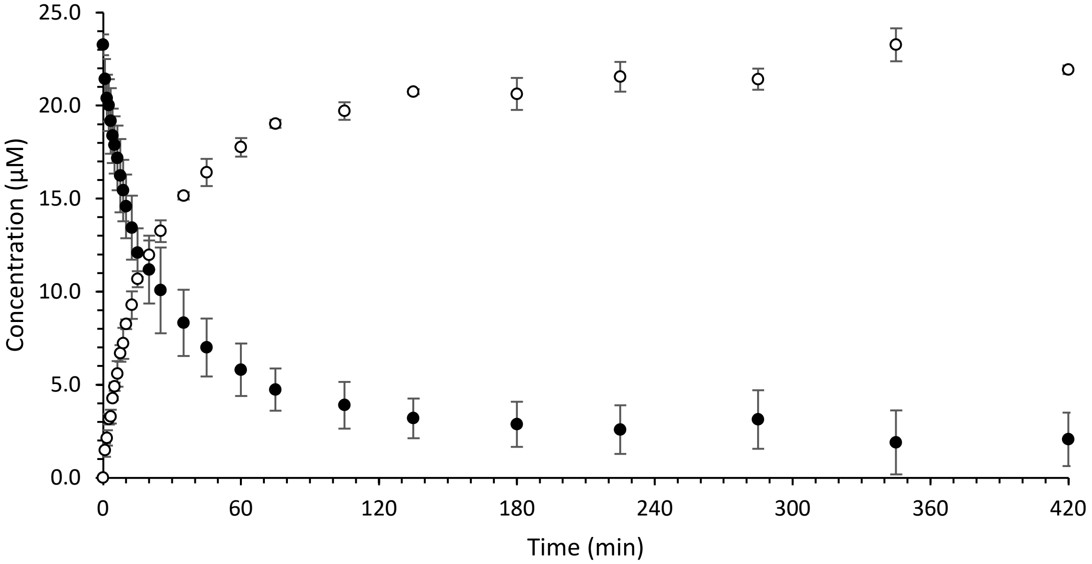

Figure 2.27: Loss of APmer over time (solid) compared to the growth of the **2-1** oxime conjugate over time (empty). Error bars are the standard deviation of three biological replicates. The growth of the oxime over time was calculated using areas from the long wavelength diode. The extinction coefficient at this wavelength was calculated using Table 2.1 where wavelength is 595 nm.

If we adjust the model so that the reaction is bimolecular, our mechanism becomes that shown in Eq. 3.

$$APmer + Drug \rightarrow Conjugate$$ **Eq. 3**

When this model is used in COPASI with both [APmer] and [Conjugate] datasets, the estimated rate constant becomes that reported in Table 2.7. As shown in Figure 2.29, the calculated time course data fit our data set well (with the exception that our reaction stalls and the model assumed a completed reaction). Additionally, the standard deviation of the estimated rate constant is lower than that of k_3 in the original model (Table 2.5).

Table 2.7: COPASI parameter estimation for the bimolecular conjugation of **2-1** to the APmer (Eq. 3). These results consider both the loss of APmer and the growth of Conjugate. Note that, in this case, k_1 either is the $k_{conjugation}$ or the k_{obs}.

Parameter	**Unit**	**Lower Bound**	**Start Value**	**Upper Bound**	**Value**	**Standard Deviation**	**Coeff. of Variation (%)**
k_1	$\mu M^{-1} \cdot min^{-1}$	-∞	0.01	∞	1.07 x 10^{-3}	0.03 x 10^{-3}	3.1

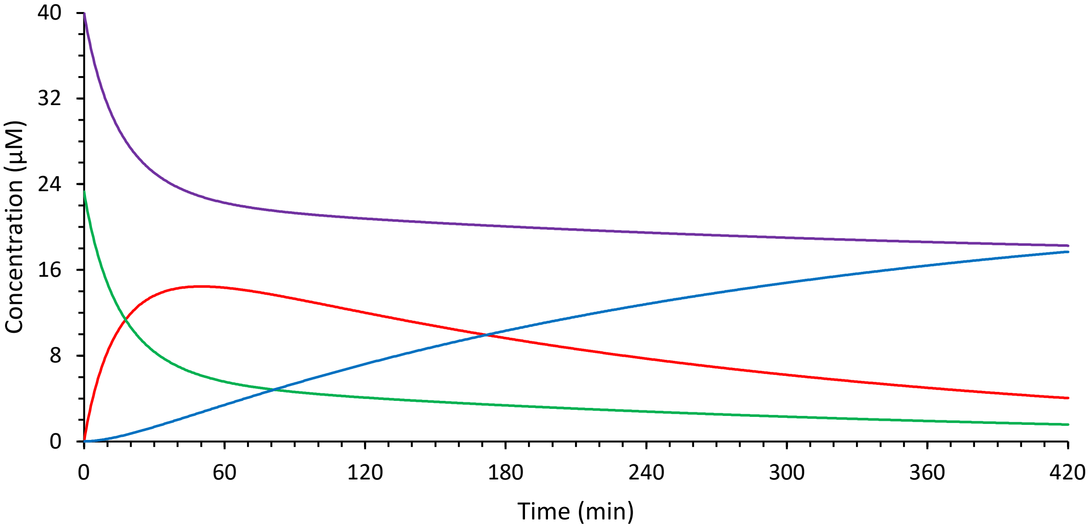

Figure 2.28: COPASI-generated time course plot. The model follows the mechanism outlined in Eq. 2, and the rate constants are those presented in Table 2.5. Reaction conditions are the same as those reported for Figure 2.22a. Color key: green = APmer, purple = **2-1**, red = [APmer · Drug], and blue = Conjugate. Note how [APmer · Drug] is <u>not</u> insignificant.

On one hand, the improved fit makes intuitive sense. We essentially have one variable and two datasets, so the variable cannot be confounded with another; estimating the variable now is a relatively simple process. However, the further implications that a bimolecular model fits the data better than the model expressed in Eq. 2 are baffling. To us, these results mean one of two things. The first possibility is that intercalation does not occur, or does occur as a competing reaction. This would mean that binding occurs *without* intercalation contrary to our understanding of these kinds of compounds based on published research. The estimated parameters in Table 2.5 lend support to this idea as the off-rate of intercalation, k_2, is approximately 6 times faster than the intercalation rate and a little less than 2 times faster than the estimated conjugation rate, k_3. While some conjugate may form from the [APmer · Drug] complex, these estimated values may imply that binding could occur outside of the complex.

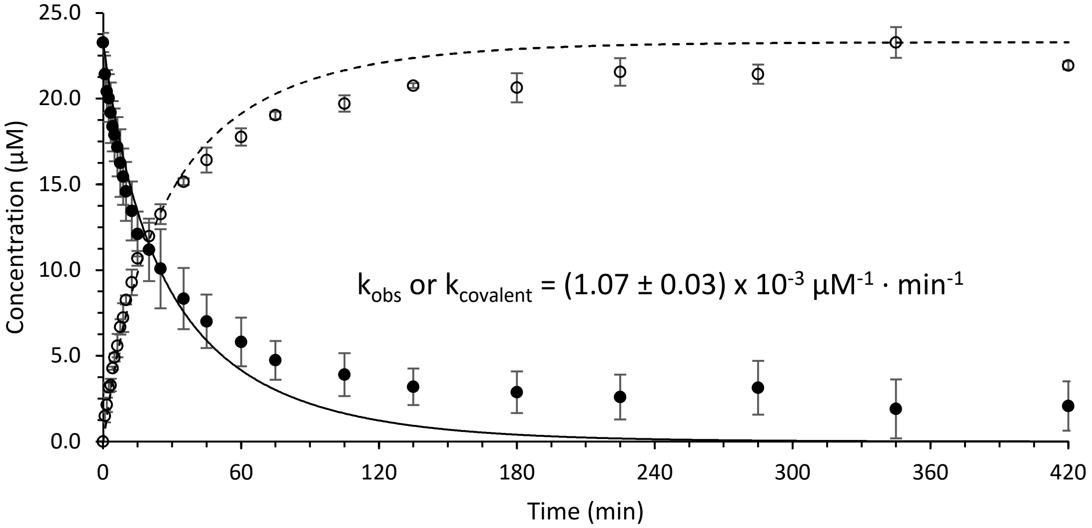

Figure 2.29: Data presented in Figure 2.27 with the curves predicted by COPASI. Curves show [APmer] versus time (solid) and [Conjugate] versus time (dashed) of the model provided in Eq. 3 using the estimated rate constant in Table 2.7. The value for k_1 is provided and represents either the observed k value (if steady-state) or the covalent k value (if truly bimolecular).

However, our methoxyamine and single stranded data negate this idea. This theory cannot be tested until more data is collected for reasons explained later.

The other possibility for the results in Table 2.7 and Figure 2.29 is that Eq. 2 still is the mechanism, but the reaction proceeds under steady-state conditions at the given concentrations of our model. The steady-state approximation of Eq. 2 concludes that the rate law for conjugate formation is:

$$\frac{d[Conjugate]}{dt} = k_{obs}[APmer][Drug] \qquad \textbf{Eq. 4}$$

where k_{obs} is equal to $(k_1k_3)/k_2$. As Eq. 4 suggests, making a steady-state assumption about our reaction mechanism also provides a bimolecular rate law that could result in the data shown in Table 2.7 and Figure 2.29.

Further experiments are required to elucidate the mechanics of this model. If we wish to test the steady-state hypothesis, for example, a circular dichroism study could give us the equilibrium concentrations of the intercalative step in Eq. 2. Under steady state conditions, $K_{intercalation}$ is equal to k_1/k_2. Therefore, $k_{obs} = K_{intercalation} \cdot k_3$, which would allow us to solve for k_3. Non-steady-state conditions also could benefit from the data of a circular dichroism study. As previously mentioned, we made the assumption that our recorded [APmer] is correct; however, the calculated values actually are the sum of [APmer] and [APmer · Drug]. Knowing the equilibrium concentration of the [APmer · Drug] complex could provide data helpful for measuring the true [APmer].

Another possible point of contention is that our current model may not be complex enough to fully characterize these compounds' reactivity with AP sites. Similar to earlier in this section, if the reaction truly is bimolecular and no intercalation is observed as predicted in the first possibility, a circular dichroism study would show that intercalation is not present. But, this model may not fully describe what actually is happening. For example, the drug may sample a number of different sites along the strand before find the optimal location for binding. Similarly, as shown in Figure 1.11, intercalation occurs over many different steps, not just one like Eq. 2 suggests. Adding steps like these to the mechanism is not feasible at this time. Each elementary step will add another unknown rate constant, two if the step is in equilibrium. The more unknowns added to the model, the more correlated each variable becomes leading to less reliable estimations by COPASI. In other words, one dataset cannot give enough information to separate, say, five different reaction steps. As such, more experiments and more data are needed to explore the theoretical space our model could inhabit.

Finally, progress has been made to apply these same mechanistic modeling steps to the conjugate formed by **2-2**. As of now, we only have modeled this reaction using Eq. 2. Additionally, we excluded the growth data of the **2.10** conjugate (as we did for Figure 2.26). These data and the model that accompanies them are preliminary. The estimated parameters by COPASI are presented in Table 2.8, and the COPASI curve fit to our data is shown in Figure 2.30. As can be seen in the table, while the on-rate for intercalation (k_1) is smaller than that of the **2-1** reaction, these data have led COPASI to estimate a $k_{covalent}$ (k_3) that is faster for **2-2** than **2-1**. Because of our use of kinetic modeling, these values can be compared directly even though the starting drug concentrations were different. However, more studies must be done in order to fully elucidate these rate constants and understand how these drugs bind to AP sites in DNA.

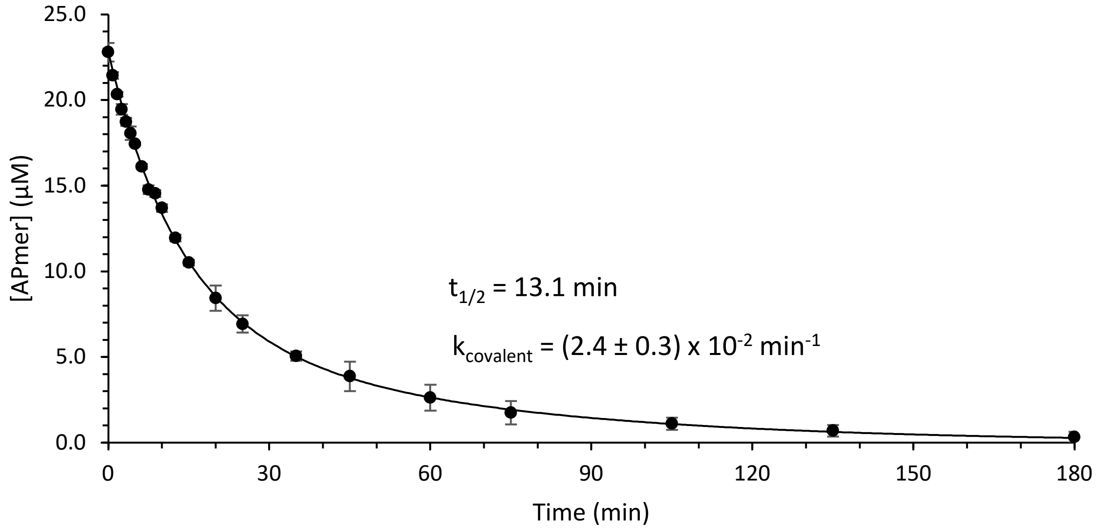

Figure 2.30: Data presented in Figure 2.22b with the curve predicted by COPASI. Curve shows [APmer] versus time of the model provided in Eq. 2 using the estimated rate constants in Table 2.8. The value for $k_{covalent}$ (k_3) is provided.

Table 2.8: First COPASI parameter estimation for the conjugation of **2-2** to the APmer by an intercalative mechanism (Eq. 2). These results do not consider [Conjugate] data.

Parameter	Unit	Lower Bound	Start Value	Upper Bound	Value	Standard Deviation	Coeff. of Variation (%)
k_1	$\mu M^{-1} \cdot min^{-1}$	-∞	0.01	∞	2.92×10^{-4}	0.04×10^{-3}	1.3
k_2	min^{-1}	-∞	0.01	∞	1.1×10^{-2}	0.1×10^{-2}	12.8
k_3	min^{-1}	-∞	0.01	∞	2.4×10^{-2}	0.3×10^{-2}	14.2

Summary

We have synthesized and characterized aminoxyacetamides **2-1** and **2-2** as their hydrochloride salts. Our divergent synthesis produces these compounds in four steps with overall yields of 11% and 2%, respectively. The lowest-yielding step of these compounds is the very first of the synthesis, which produces both substituted anthraquinones that are carried forward to the final products. Additionally, the critical step in these syntheses is the DCC coupling because small changes to the procedures drastically affect the yields. While the yields presented in this dissertation were suboptimal, Dr. Arjun Kafle, a postdoctoral researcher in our lab, has discovered that changing the second step from a TFA-mediated deprotection to an HCl/dioxane deprotection significantly improves the overall yield. This change produces the HCl salts of **2.5** and **2.8**, instead of the TFA salts (Figure 2.31). When the HCl salts are used for the DCC-mediated amide coupling, yields for that reaction improve too, and overall reaction time decreases. Additionally, the amount of time the DCC is allowed to react with HOBt and the acid is crucial since the activated ester needs to exist in an appreciable amount but hydrolyzes if left alone for too long (even in flame-dried glassware). Lastly, the rate of addition of the anthraquinone salts can affect the outcome of the reaction.

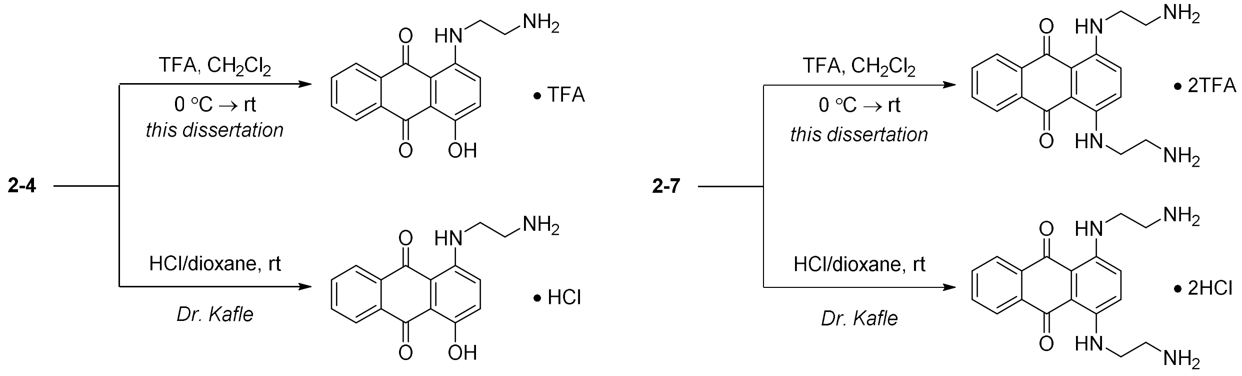

Figure 2.31: Dr. Arjun Kafle's update to the synthetic route in Figure 2.3.

Additionally, we have synthesized and characterized by mass spectrometry the different oxime-dR adducts of **2-1** and **2-2**. Care is needed to ensure that the mono-adduct of **2-2** is formed as the major product of its reaction. This is done by using a large excess of **2-2** with respect to dR. Because of this, HPLC purification takes a significant amount of time. Similarly, adducts formed between **2-1**/**2-2** and ^{13}C-labeled dR must be synthesized in a similar manner since the isotopically labeled sugar is more precious than its unlabeled counterpart. The ^{13}C-labeled dR oxime of **2-1** has been synthesized and characterized by mass spectrometry. Future work on this project requires these isotopically labeled adducts as mass spectrometric standards. The standards will be used for isotope-dilution LC-ESI/MS^3 experiments to quantitatively determine the extent of adduct formation in our cellular model.

The next model system we employed was a 12-base pair DNA oligonucleotide. By selectively inducing a single AP site within the oligonucleotide, we monitored and characterized the reaction of compounds **2-1** and **2-2** with the APmer. Reactions were quenched with acetone to allow for accurate timepoint data; and, as such, studies on **2-2** actually were representative of **2-10**, the singly acetone-capped oxime derivative of **2-2**. Each conjugate was formed, purified by reverse-phase HPLC, and characterized by LC-ESI/MS^2. While our typical reaction conditions worked for the APmer reaction with **2-1**, a 5-fold increase in drug concentration was needed to properly analyze the conjugation reaction between **2-2** and the APmer. This was due to the presence of byproducts at the lower concentration. Increasing the drug concentration to 200 μM promoted the singly-conjugated adduct formation over side reactions. For example, we showed that there is a non-negligible amount of crosslinking between two equivalents of APmer when 40 μM **2-2** is used. In any case, the stability of the duplex increased when our compounds bound to the AP site, as indicated by an increase in T_m from the AP site analog control.

Finally, we began an examination of the kinetics governing the reactivity of our compounds to the APmer. To begin, we measured the natural loss of APmer in our reaction conditions due to β-elimination. These values were subtracted from our model's control experiments as they proceeded within a similar timeframe to the fragmentation reaction. These rate constants are provided in Table 2.9. However, there was no significant loss of APmer due to fragmentation during the reactions of **2-1** and **2-2** with duplex APmer; as such, these data were not adjusted. When solely monitoring the loss of APmer over time as a means of divining the rate constants, our data provides a good fit to our current understanding of the binding mechanism (Eq. 2). However, when also considering the growth of the conjugate over time, our data began to take on characteristics of a one-step, bimolecular reaction profile (Eq. 3). This raises some questions about our data collection method and understanding of the binding mechanism. Three possibilities to explain the bimolecular fit are:

1. The bimolecular mechanism only has one step, so there are no confounding variables to interfere with COPASI's estimation.
2. The binding occurs via a bimolecular mechanism (i.e., does not bind from an intercalated state).
3. The reaction proceeds under steady-state-like conditions, providing a simplified rate law that is bimolecular. In this case, the divined rate constant actually is a k_{obs}, not a $k_{covalent}$.

Regardless of which option best explains the results of our kinetic modeling, more work is needed to fully elucidate the different components of the model.

Table 2.9. Comparison of COPASI rate constant predictions for each experiment. The experiments with adjusted rate constants show how incorporating the rate of hydrolysis (first data row) changes the rate prediction. Note that the model, itself, was not adjusted – just the data.

Drug	**Concentration Drug (μM)**	**Concentration APmer (μM)**	$k_{covalent}$	**Adjusted** $k_{covalent}$
---	---	23.3	$(9.3 \pm 0.4) \times 10^{-5}$ min^{-1}	
MeONH$_2$	40	23.3	$(6.2 \pm 0.1) \times 10^{-6}$ μM^{-1} min^{-1}	$(2.0 \pm 0.1) \times 10^{-6}$ μM^{-1} min^{-1}
2-1 (SS APmer)	40	23.6	$(7.2 \pm 0.6) \times 10^{-5}$ μM^{-1} min^{-1}	$(5.2 \pm 0.6) \times 10^{-5}$ μM^{-1} min^{-1}
2-1 (DS APmer)	40	23.3	$(1.07 \pm 0.03) \times 10^{-3}$ μM^{-1} min^{-1} (bimolecular model)	
2-2 (DS APmer)	200	22.8	$(2.4 \pm 0.3) \times 10^{-3}$ min^{-1}	

Future Work

There are many parts of this project that require attention for future work. Firstly, as previously mentioned, Dr. Arjun Kafle already has improved the synthetic route reported in this dissertation. Further optimization is needed to better improve the yields of the synthetic route. Secondly, further characterization of the dR adducts of **2-1** and **2-2** is needed before quantitative mass spectrometric studies are performed on the cellular model system. Namely, isotopically labeled standards of both dR oxime adducts of **2-2** are needed to perform the isotope dilution mass spectrometry required. Thirdly, before the cellular model even can be used, we must demonstrate that these adducts form readily *in vitro* in CT DNA. Preliminary work already has been done to demonstrate this with **2-1**. However, there were errors in the experimental design and the enrichment process by SPE. Therefore, there are no data to present in this dissertation. Further work must be done to prove the reactivity of <u>both</u> compounds in this next model.

Lastly, as previously mentioned, further experiments are needed to fully elucidate the mechanism of our compounds' binding to APmer using our kinetic models. While our models have given us *some* information about the reaction, more data is needed. For example, a circular dichroism study could help us figure out why the bimolecular model fits better than the intercalative one. Additionally, other kinetic studies can be done, namely, ones that employ steady-state conditions. By increasing the drug concentrations to abnormally large values, we could measure a k_{obs} for a pseudo-first order rate law. Additionally, we could perform concentration studies on how changing the concentration of **2-1** or **2-2** affects the rate. All of these experiments could contribute to the determination of the overall differential rate law of AP site oxime formation.

Experimental

General Methods

NMR spectra were recorded at 600 MHz on a Brucker AM Series NMR spectrometer in DMSO-d_6. All chemicals were the best available quality and used as received. Reagents were purchased from Millipore Sigma, Tokyo Chemical Industry, Oakwood Chemical, Alfa Aesar, Thermo Fisher Scientific, or Acros Organics. All enzymes were purchased from New England Biolabs or Millipore Sigma. All DNA oligonucleotides were ordered from and synthesized by Integrated DNA Technologies. Concentrations of stock oligonucleotide solutions were determined using a NanoDrop Microvolume Spectrophotometer from Thermo Fisher Scientific. Thin-layer chromatography was performed on silica gel glass plates (Millipore Sigma, TLC Silica gel 60 F_{254}). TLCs were visualized under UV light (254 nm). Flash column chromatography was performed using silica gel (Sorbtech, 60 Å porosity, 65x250 mesh). Reverse-phase flash column column chromatography was performed using reverse-phase silica gel (Silicycle, C18 (Carbon 17%) 60 Å, 40-63 μm). Solid phase extraction was performed using Sola HRP Polymeric Reversed Phase SPE cartridges (10 mg) purchased from Thermo Fisher Scientific. Desalting occurred by use of Sep-Pak cartridges (Waters). All Eppendorf tubes were purchased from eppendorf or Bio-Rad.

Synthetic Procedures

tert-butyl (2-((4-hydroxy-9,10-dioxo-9,10-dihydroanthracen-1-yl)amino)ethyl)carbamate (**2-4**) and di-*tert*-butyl (((9,10-dioxo-9,10-dihydroanthracene-1,4-diyl)bis(azanediyl))bis(ethane-2,1-diyl))dicarbamate (**2-7**)

These compounds were synthesized following a similar procedure to those reported in the literature.[266,267] To a round-bottom flask equipped with a stirbar was added *N*-Boc-ethylenediamine (0.8 mL, 5 mmol) and methanol (15 mL). The solution stirred at 55 °C for 20 min while argon gas was bubbled through the mixture. Anthracene-1,4,9,10-tetraol (242.2 mg, 1 mmol) was added to the reaction, which was left to stir at 55 °C under argon for 3 hr. The reaction was cooled to room temperature, and air was bubbled through the solution for 20 min. The reaction mixture was diluted with methylene chloride (10 mL) and washed with saturated aqueous copper (II) sulfate until the aqueous phase remained blue. The organic phase was dried over sodium sulfate and concentrated under vacuum to afford a dark blue/black solid. The crude product was dry-loaded onto silica gel and purified by column chromatography (EtOAc in hexanes; 2 x 0%, 5 x 25%, 7 x 35%, 2 x 50%), then triturated with diethyl ether and, then, pentane to yield **2-4** and **2-7** as purple and blue solids, respectively.

Characterization of **2-4**: (**Yield** = 27%). **^{1}H NMR** (600 MHz, DMSO-*d*$_6$): δ 10.31 (br t, J = 5.6 Hz, 1H, Ar-NH-), 8.25 (d, J = 7.9 Hz, 2H, H-5 & H-8), 7.94 (td, J_1 = 7.6 Hz, J_2 = 1.0 Hz, 1H, H-7), 7.86 (td, J_1 = 7.6 Hz, J_2 = 1.0 Hz, 1H, H-6), 7.56 (d, J = 9.7 Hz, 1H, H-2), 7.36 (d, J = 9.7 Hz, 1H, H-3), 7.04 (br t, J = 5.3 Hz, 1H, -NHC(=O)-C), 3.51 (br q, J = 6.2 Hz, 2H, H-1’), 3.20 (br q, J = 6.0 Hz, 2H, H-2’), 1.35 (s, 9H, H-5’ & H-6’ & H-7’). **^{13}C NMR** (150 MHz, DMSO-*d*$_6$): δ 186.8 (C-10), 180.8 (C-9), 156.2 (C-4), 155.8 (C-3’), 147.5 (C-1), 134.8 (C-7 & C-12), 133.0 (C-6), 131.9 (C-11), 128.7 (C-3), 126.3 (C-8), 126.0 (C-5), 125.5 (C-2), 112.9 (C-14), 107.6 (C-13), 77.8 (C-4’), 41.6 (C-1’), 39.7 (C-2’), 28.2 (C-5’ & C-6’ & C-7’). **Low Resolution [M+H]$^{+1}$** m/z 383.16 (*Theoretical*); 383.1 (*Actual*).

Characterization of **2-7**: (**Yield** = 8%). **^{1}H NMR** (600 MHz, DMSO-*d*$_6$): δ 10.84 (br t, J = 4.9 Hz, 2H, -NH-Ar-NH-), 8.23 (dd, J_1 = 5.5 Hz, J_2 = 3.3 Hz, 2H, H-5 & H-8), 7.79 (dd, J_1 = 5.5

Hz, J_2 = 3.3 Hz, 2H, H-6 & H-7), 7.54 (s, 2H, H-2 & H-3), 7.04 (br t, J = 4.4 Hz, 2H, -NHC(=O)-C), 3.52 (br q, J = 5.8 Hz, 4H, H-1' & H-1"), 3.19 (br q, J = 5.8 Hz, 4H, H-2' & H-2"), 1.37 (s, 18H, H-5' & H-6' & H-7' & H-5" & H-6" & H-7"). **^{13}C NMR** (150 MHz, DMSO-d_6): δ 180.7 (C-9 & C-10), 155.8 (C-3' & C-3"), 146.1 (C-1 & C-4), 133.8 (C-11 & C-12), 132.3 (C-5 & C-8), 125.7 (C-6 & C-7), 124.4 (C-2 & C-3), 108.7 (C-13 & C-14), 77.8 (C-4' & C-4"), 41.6 (C-1' & C-1"), 40.0 (C-2' & C-2"), 28.2 (C-5' & C-6' & C-7' & C-5" & C-6" & C-7"). **Low Resolution $[M+H]^{+1}$** m/z 525.27 (*Theoretical*); 525.2 (*Actual*).

2-((4-hydroxy-9,10-dioxo-9,10-dihydroanthracen-1-yl)amino)ethan-1-aminium trifluoroacetate (Anthra-OH) (**2-5**)

To a round-bottom flask equipped with a stirbar was added **2-4** (120 mg, 0.31 mmol) and methylene chloride (2 mL). The reaction was cooled in an ice bath, and trifluoroacetic acid (750 µL) was added dropwise. The ice bath was removed, and the reaction proceeded at room temperature for 2 hr. After concentrating the reaction under vacuum, the resultant solid was triturated with methylene chloride (x3) to remove all the remaining acid. The crude trifluoroacetate salt was carried forward to the next step of the synthesis without further purification (**Yield** = 92%). **^{1}H NMR** (600 MHz, DMSO-d_6): δ 10.23 (br t, J = 5.6 Hz, 1H, Ar-NH-), 8.28 (dd, J_1 = 7.5 Hz, J_2 = 1.3 Hz, 1H, H-8), 8.27 (dd, J_1 = 7.5 Hz, J_2 = 1.3 Hz, 1H, H-5), 7.96 (td, J_1 = 7.5 Hz, J_2 = 1.3 Hz, 1H, H-7), 7.90 (td, J_1 = 7.5 Hz, J_2 = 1.3 Hz, 1H, H-6), 7.93-7.84 (br), 7.58 (d, J = 9.6 Hz, 1H, H-2), 7.42 (d, J = 9.6 Hz, 1H, H-3), 4.70-3.54 (br), 3.72 (br q, J = 6.3 Hz, 2H, H-1'), 3.07 (br q, J = 6.0 Hz, 2H, H-2'). **^{13}C NMR** (150 MHz, DMSO-d_6): δ 187.0 (C-9), 181.4 (C-10), 156.2 (C-4), 146.8 (C-1), 135.0 (C-12), 134.6 (C-7), 133.3 (C-6), 132.0 (C-11), 128.7 (C-3), 126.4 (C-8), 126.2 (C-5), 125.2 (C-2), 113.2 (C-14), 108.5 (C-13), 39.6 (C-1’), 38.2 (C-2’). **Low Resolution $[M+H]^{+1}$** m/z 283.11 (*Theoretical*); 283.2 (*Actual*).

1,4-bis((2-aminoethyl)amino)anthracene-9,10-dione (Anthra) (**2-8**)

To a round-bottom flask equipped with a stirbar was added **2-7** (120 mg, 0.23 mmol) and methylene chloride (2 mL). The reaction was cooled in an ice bath, and trifluoroacetic acid (750 μL) was added dropwise. The ice bath was removed, and the reaction proceeded at room temperature for 2 hr. After concentrating the reaction under vacuum, the resultant solid was triturated with methylene chloride (x3) to remove all the remaining acid. The crude powder was dissolved in water and purified by reverse-phase column chromatography (MeOH in H_2O; 0% then 20%). The water fractions were concentrated by lyophilization to yield **2-8** as a blue solid (**Yield** = 61%). **^{1}H NMR** (600 MHz, DMSO-*d₆*): δ 10.67 (br t, J = 6.3 Hz, 2H, -NH-Ar-NH-), 8.25 (dd, J_1 = 5.8 Hz, J_2 = 3.3 Hz, 2H, H-5 & H-8), 7.84 (dd, J_1 = 5.8 Hz, J_2 = 3.3 Hz, 2H, H-6 & H-7), 7.52 (s, 2H, H-2 & H-3), 3.72 (br q, J = 6.4 Hz, 4H, H-1’ & H-1”), 3.07 (t, J = 6.4 Hz, 4H, H-2’ & H-2”). **^{13}C NMR** (150 MHz, DMSO-*d₆*): δ 181.6 (C-9 & C-10), 145.4 (C-1 & C-4), 133.7 (C-11 & C-12), 132.8 (C-5 & C-8), 125.8 (C-6 & C-7), 124.1 (C-2 & C-3),109.7 (C-13 & C-14), 39.9 (C-1’ & C-1”), 38.6 (C-2’ & C-2”). **Low Resolution $[M+H]^{+1}$** m/z 325.17 (*Theoretical*); 325.2 (*Actual*).

tert-butyl (2-((2-((4-hydroxy-9,10-dioxo-9,10-dihydroanthracen-1-yl)amino)ethyl)amino)-2-oxoethoxy)carbamate (**2-6**)

N-Boc-2-aminoxyacetic acid (24.8 mg, 0.13 mmol) was added to a flame-dried round-bottom flask equipped with a stirbar under an argon atmosphere. The acid was dissolved in a 1:1

(v/v) mixture of *N,N*-dimethylformamide and acetonitrile (1.6 mL). To the stirring solution was added 1-hydroxybenzotriazole monohydrate (32.8 mg, 0.22 mmol) and *N,N'*-dicyclohexylcarbodiimide (44.5 mg, 0.22 mmol). The reaction stirred for 30 min at room temperature. 2-5 (50 mg, 0.13 mmol) was dissolved in *N,N*-dimethylformamide (700 µL). To the anthraquinone solution was added *N,N*-diisopropylethylamine (26 µL, 0.15 mmol), after which the solution was added slowly, dropwise, to the stirred reaction. The reaction was left at room temperature to react overnight. The reaction was vacuum filtered to remove the formed precipitate, and the acetonitrile in the filtrate was removed under vacuum by rotary evaporation. The remains of the filtrate were diluted with water and extracted with ethyl acetate. The organic phase was washed with water (x3) and brine, then dried over sodium sulfate. After concentrating the organic phase under vacuum, the crude reaction mixture was dry-loaded onto silica gel and purified by column chromatography (MeOH in CH_2Cl_2; 4 x 0%, 1 x 1%, 2 x 2%, 4 x 3%, 1 x 4%, 2 x 5%). The product from the column was triturated with diethyl ether and, then, pentane to yield the Boc-protected aminoxyacetamide as a purple solid (**Yield** = 70%). **^{1}H NMR** (600 MHz, DMSO-d_6): δ 10.32 (br, t, 1H, Ar-NH-), 10.24 (br, s, 1H, Ar-OH), 8.27 (td, J_1 = 8.0 Hz, J_2 = 0.7 Hz, 2H, H-5 & H-8), 8.26 (br, s, 1H, -NHC(=O)-C), 7.94 (td, J_1 = 7.4 Hz, J_2 = 1.0 Hz, 1H, H-7), 7.88 (td, J_1 = 7.7 Hz, J_2 = 0.9 Hz, 1H, H-6), 7.61 (d, J = 9.6 Hz, 1H, H-2), 7.38 (d, J = 9.6 Hz, 1H, H-3), 4.17 (s, 2H, H-4'), 3.58 (br q, J = 6.3 Hz, 2H, H-1'), 3.40 (br q, J = 6.1 Hz, 2H, H-2'). **^{13}C NMR** (150 MHz, DMSO-d_6): δ 186.9 (C-10), 181.0 (C-9), 168.5 (C-3'), 156.7 (C-4), 156.2 (C-5'), 147.4 (C-1), 134.8 (C-12), 134.8 (C-7), 133.1 (C-6), 132.0 (C-11), 128.8 (C-3), 126.4 (C-8), 126.1 (C-5), 125.5 (C-2), 113.0 (C-14), 107.7 (C-13), 80.5 (C-6'), 74.7 (C-4'), 41.4 (C-1'), 38.2 (C-2'), 27.8 (C-7' & C-8' & C-9'). **Low Resolution $[M+H]^{+1}$** m/z 456.18 (*Theoretical*); 456.1 (*Actual*).

di-*tert*-butyl (((((((9,10-dioxo-9,10-dihydroanthracene-1,4-diyl)bis(azanediyl))bis(ethane-2,1-diyl))bis(azanediyl))bis(2-oxoethane-2,1-diyl))bis(oxy))dicarbamate (**2-9**)

N-Boc-2-aminoxyacetic acid (24.8 mg, 0.13 mmol) was added to a flame-dried round-bottom flask equipped with a stirbar under an argon atmosphere. The acid was dissolved in a 1:1 (v/v) mixture of *N,N*-dimethylformamide and acetonitrile (1.6 mL). To the stirring solution was added 1-hydroxybenzotriazole monohydrate (32.8 mg, 0.22 mmol) and *N,N'*-dicyclohexylcarbodiimide (44.5 mg, 0.22 mmol). The reaction stirred for 30 min at room temperature. **2-8** (34 mg, 0.062 mmol) was dissolved in *N,N*-dimethylformamide (700 μL). The solution was added slowly, dropwise, to the stirred reaction. The reaction was left at room temperature to react overnight. The reaction was vacuum filtered to remove the formed precipitate, and the acetonitrile in the filtrate was removed under vacuum by rotary evaporation. The remains of the filtrate were diluted with water and extracted with ethyl acetate. The organic phase was washed with water (x3) and brine, then dried over sodium sulfate. After concentrating under vacuum the organic phase, the crude reaction mixture was dry-loaded onto silica gel and purified by column chromatography (MeOH in CH_2Cl_2; 6 x 0%, 1 x 1%, 2 x 2%, 2 x 3%, 1 x 4%, 3 x 5%). The product from the column was triturated with diethyl ether and, then, pentane to yield the bis-aminoxyacetamide product as a blue solid (**Yield** = 42%). **^{1}H NMR** (600 MHz, DMSO-*d_6*): δ 10.81 (br t, *J* = 5.7 Hz, 2H, -NH-Ar-NH-), 8.26 (br m, 2H, -NHC(=O)-C), 8.24 (dd, J_1 = 5.8 Hz, J_2 = 3.3 Hz, 2H, H-5 & H-8), 7.80 (dd, J_1 = 5.8 Hz, J_2 = 3.3 Hz, 2H, H-6 & H-7), 7.58 (s, 2H, H-2 & H-3), 4.19 (s, 4H, H-4' & H-4"), 3.58 (br q, *J* = 6.3 Hz, 4H, H-1' & H-1"), 3.41 (*J* = 6.3 Hz, 4H, H-2' & H-2"), 1.37 (s, 18H, H-7' & H-8' & H-9' & H-7" & H-8" & H-9"). **^{13}C NMR** (150 MHz, DMSO-*d_6*): δ 180.9 (C-9 & C-10), 168.4 (C-3' & C-3"), 156.7 (C-5' & C-5"), 146.0 (C-1 & C-4), 133.8 (C-11 & C-12), 132.4 (C-5 & C-8), 125.7 (C-6 & C-7), 124.4 (C-2 & C-3), 108.8

(C-13 & C-14), 80.5 (C-6’ & C-6”), 74.7 (C-4’ & C-4”), 41.3 (C-1’ & C-1”), 38.3 (C-2’ & C-2”), 27.9 (C-7’ & C-8’ & C-9’ & C 7” & C-8” & C-9”). **Low Resolution $[M+H]^{+1}$** m/z 671.30 (*Theoretical*); 671.1 (*Actual*).

O-(2-((2-((4-hydroxy-9,10-dioxo-9,10-dihydroanthracen-1-yl)amino)ethyl)amino)-2-oxoethyl)hydroxylammonium chloride (**2-1**) and O,O'-(((((9,10-dioxo-9,10-dihydroanthracene-1,4-diyl)bis(azanediyl))bis(ethane-2,1-diyl))bis(azanediyl))bis(2-oxoethane-2,1-diyl))dihydroxylammonium dichloride (**2-2**)

These compounds were synthesized following a similar procedure to those reported in the literature.[268] Boc-protected aminoxyacetamides **2-6** and **2-9** (0.1 mmol) were respectively dissolved in chilled 4 M hydrochloric acid in dioxane (2 mL) under an argon atmosphere in a flame-dried round-bottom flask. The reaction was stirred at room temperature for 1 hr and concentrated under vacuum multiple times with methylene chloride. The crude solid was suspended in diethyl ether and transferred to a centrifuge tube. More diethyl ether was added (5 mL). The heterogenous mixture was centrifuged to collect all the precipitate at the bottom, and the solvent was removed. This process was performed 3 times, and then the solid was dried by rotary evaporation. The resultant salt was kept under vacuum to continue drying overnight. This yielded the hydrochloride salts of **2-1** and **2-2** as green and blue solids, respectively.

Characterization of **2-1**: (**Yield** = 64%). **^{1}H NMR** (600 MHz, DMSO-d_6): δ 11.00 (br, s, 1H, Ar-OH), 10.30 (br, s, 1H, Ar-NH-), 8.56 (br t, J = 5.5 Hz, 1H, -NHC(=O)-C), 8.27 (td, J_1 = 7.7 Hz, J_2 = 0.9 Hz, 2H, H-5 & H-8), 7.95 (td, J_1 = 7.5 Hz, J_2 = 1.3 Hz, 1H, H-7), 7.88 (td, J_1 = 7.5 Hz, J_2 = 1.3 Hz, 1H, H-6), 7.60 (d, J = 9.6 Hz, 1H, H-2), 7.39 (d, J = 9.6 Hz, 1H, H-3), 4.53 (s, 2H, H-4’), 4.16 (br s, $-NH_2$), 3.58 (br t, J = 6.3 Hz, 2H, H-1’), 3.40 (br q, J_1 = 6.1 Hz, 2H, H-

2’). **^{13}C NMR** (150 MHz, DMSO-*d_6*): δ 186.9 (C-10), 181.0 (C-9), 167.2 (C-3’), 156.2 (C-4), 147.3 (C-1), 134.8 (C-12), 134.7 (C-7), 133.1 (C-6), 132.0 (C-11), 128.8 (C-3), 126.4 (C-8), 126.1 (C-5), 125.4 (C-2), 113.0 (C-14), 107.8 (C-13), 71.3 (C-4’), 41.2 (C-1’), 38.3 (C-2’). **Low Resolution [M+H]$^{+1}$** m/z 356.12 (*Theoretical*); 356.2 (*Actual*).

Characterization of **2-2**: (**Yield** = 94%). **^{1}H NMR** (600 MHz, DMSO-*d_6*): δ 10.81 (br, s, 2H, -NH-Ar-NH-), 8.58 (br t, J = 5.5 Hz, 2H, -NHC(=O)-C), 8.25 (dd, J_1 = 5.8 Hz, J_2 = 3.3 Hz, 2H, H-5 & H-8), 7.81 (dd, J_1 = 5.9 Hz, J_2 = 3.3 Hz, 2H, H-6 & H-7), 7.59 (s, 2H, H-2 & H-3), 4.55 (s, 4H, H-4’ & H-4”), 4.00-3.50 (br s, -NH$_2$), 3.60 (br t, J = 6.3 Hz, 4H, H-1’ & H-1”), 3.41 (br q, J = 6.1 Hz, 4H, H-2’ & H-2”). **^{13}C NMR** (150 MHz, DMSO-*d_6*): δ 181.0 (C-9 & C-10), 167.2 (C-3’ & C-3”), 145.9 (C-1 & C-4), 133.8 (C-11 & C-12), 132.5 (C-6 & C-7), 125.8 (C-5 & C-8), 124.5 (C-2 & C-3), 108.8 (C-13 & C-14), 71.4 (C-4’ & C-4”), 41.2 (C-1’ & C-1”), 38.5 (C-2’ & C-2”). **Low Resolution [M+H]$^{+1}$** m/z 471.20 (*Theoretical*); 471.3 (*Actual*).

Reverse-Phase HPLC Methods

All chromatograms were collected on Beckman-Coulter HPLCs using 32 Karat software. Columns were purchased from Phenomenex, and solvents were purchased LCMS-grade from Thermo Fisher Scientific. The ammonium formate salt used to prepare the buffer solution was purchased from Acros Organics and Millipore Sigma. In all methods reported below, the difference between X.1 and X.2 methods are the size of the column and the flow rate. The method selected from these two options depended on the size and purpose of the run.

Method #1.1: Luna 5 μm C18(2) 100 Å column (250 x 4.6 mm), 1.5 mL/min flow rate. *Solvent A*: 0.1 M aqueous ammonium formate; *Solvent B*: Acetonitrile. *Gradient*: 1% B to 27.5% B over 5 min, 27.5% B isocratic flow for 10 min, 27.5% B to 35% B over 0.38 min, followed by isocratic flow for 8 min. The gradient increased to 40% B over 0.25 min and held isocratically for 5 min followed by an increase to 55% B over 0.75 min and isocratic flow for 4 min. Built into the method was a wash sequence wherein the gradient increases to 100% B over 5 sec, holds at 100% B for 5 min, decreases to 0% B over 10 sec, and holds at 0% B for 5.37 min (*total time = 44 min*).

<u>Method #1.2</u>: Follows the same gradient as Method #1.1, but uses a Luna 5 µm C18(2) 100 Å column (250 x 10 mm) and a flow rate of 5 mL/min.

<u>Method #2.1</u>: Luna 5 µm C18(2) 100 Å column (250 x 4.6 mm), 1.5 mL/min flow rate. *Solvent A*: 0.1 M aqueous ammonium formate; *Solvent B*: Acetonitrile. *Gradient*: 1% B to 27.5% B over 5 min, 27.5% B isocratic flow for 4 min, 27.5% B to 35% B over 0.38 min, followed by isocratic flow for 8 min. Lastly, the gradient increased to 40% B over 0.25 min and held isocratically for 1.37 min. Built into the method was a wash sequence wherein the gradient increases to 100% B over 6 sec, holds at 100% B for 5 min, decreases to 0% B over 10 sec, and holds at 0% B for 4.33 min (*total time = 29 min*).

<u>Method #2.2</u>: Follows the same gradient as Method #2.1, but uses a Luna 5 µm C18(2) 100 Å column (250 x 10 mm) and a flow rate of 5 mL/min.

<u>Method #2.3</u>: Follows the same gradient as Method #2.1, but uses a Luna 5 µm C8(2) 100 Å column (250 x 4.6 mm) and a flow rate of 1.5 mL/min. This method was used solely for the purification of isotopically labeled conjugates.

<u>Method #3.1</u>: Luna 5 µm C18(2) 100 Å column (250 x 4.6 mm), 1.5 mL/min flow rate. *Solvent A*: 0.1 M aqueous ammonium formate; *Solvent B*: Acetonitrile. *Gradient*: 1% B to 27.5% B over 5 min, followed by 27.5% B isocratic flow for 11 min. Built into the method was a wash sequence wherein the gradient increases to 100% B over 7.5 sec, holds at 100% B for 4.88 min, decreases to 0% B over 10 sec, and holds at 0% B for 4.83 min (*total time = 26 min*).

Method #3.2: Follows the same gradient as Method #3.1, but uses a Luna 5 µm C18(2) 100 Å column (250 x 10 mm) and a flow rate of 5 mL/min.

Method #4.1: Luna Clarity 10 µm Oligo-RP column (250 x 4.6 mm), 1.5 mL/min flow rate. *Solvent A*: 0.1 M aqueous ammonium formate; *Solvent B*: Acetonitrile. *Gradient*: 1% B to 10% B over 15 min, followed by an increase to 20% B over 5 min. The gradient is kept isocratic at 20% B for 5 min. Built into the method was a wash sequence wherein the gradient increases to 80% B over 3 min, holds at 80% B for 2 min, decreases to 0% B over 3 min, and holds at 0% B for 5 min (*total time = 38 min*).

Method #4.2: Follows the same gradient as Method #4.1, but uses a Luna Clarity 10 µm Oligo-RP column (250 x 10 mm) and a flow rate of 5 mL/min.

LC-ESI/MS^2 Methods

All chromatograms and spectra were collected on a Waters ACQITY LC and Finnigan LTQ MS using XCaliber software. Columns were purchased from Phenomenex, and solvents were purchased LCMS-grade from Thermo Fisher Scientific. The ammonium acetate salt used to prepare the buffer solution also was purchased from Thermo Fisher Scientific. Formic acid was purchased from Millipore Sigma. The mass spectrometry vials, caps, and silanized inserts were purchased from Thermo Fisher Scientific.

Method #1: Small molecules were analyzed by ESI/MS^2 without chromatographic separation. Samples were run through the spectrometer using 50% aqueous methanol (v/v) at a flow rate of 0.25 mL/min for 5 min. The spectrometer measured in positive-ion mode.

Method #2: DNA oligonucleotides were analyzed by LC-ESI/MS^2 with the following chromatographic conditions. Luna 3 µm C18(2) 100 Å column (150 x 2 mm), 0.125 mL/min flow rate. *Solvent A*: 1% (v/v) acetonitrile in 10 mM aqueous ammonium acetate; *Solvent B*: 90% (v/v) acetonitrile in 10 mM aqueous ammonium acetate. *Gradient*: Held isocratic at 0% B for 1 min. The gradient increased to 5% B over 3 min, 5% B to 20% B over 3 min, 20% B to 40% B over 2 min, 40% B to 50% B over 2 min, and 50% B to 100% B over 2 min. The gradient was held isocratically at 100% B for 1 min and decreased to 0% B over 1 min where it was kept isocratic for 3 min (*total time = 18 min*). The spectrometer measured in negative-ion mode.

Method #3: Enzyme digest hydrolysates were analyzed by LC-ESI/MS^2 with the following chromatographic conditions. Luna 3 μm C18(2) 100 Å column (150 x 2 mm), 0.125 mL/min flow rate. *Solvent A*: 0.05% aqueous formic acid; *Solvent B*: 0.05% formic acid in acetonitrile. *Gradient*: Held isocratic at 2% B for 2.5 min. The gradient increased to 15% B over 5.5 min, 15% B to 40% B over 4 min, and 40% B to 100% B over 1 min. The gradient was held isocratically at 100% B for 5 min and decreased to 0% B over 1 min where it was kept isocratic for 6 min (*total time = 25 min*). The spectrometer measured in positive-ion mode.

UV-vis Absorption

Three stock solutions of each drug were made by dissolving a measured amount of **2-1** or **2-2** in a precise volume of DMSO. Aliquots of these stock solutions were diluted with water to form five (six for **2-2**) stock solutions of varying μM concentrations. Each solution contained less than 4% DMSO by volume.

After all 15 samples (18 for **2-2**) were made, we began our UV-vis analysis. Spectral experiments were performed on a Varian Cary 4E spectrophotometer (Agilent Technologies) using a 1 mL quartz cuvette with a path length 1 cm. Each sample and a control were scanned from 800 nm to 230 nm. Data was exported from the software as a CSV file and analyzed on Microsoft Excel as described in the main text.

Deoxyribose Oxime Standards

All samples were analyzed by mass spectrometry (LC-ESI/MS^2 Method #1 or #3).

For the dR oxime conjugate of **2-1**, 1 mL of **2-1** in a 2 mM DMSO solution was added to an Eppendorf tube. To this solution was added a spatula tip of 2-deoxy-D-ribose. The solution was vortexed and sonicated to fully dissolve the sugar. The reaction was allowed to heat at 37 °C for 1 hour. The crude reaction was purified in aliquots by reverse-phase HPLC (Method #2). The eluants were collected and concentrated by lyophilization multiple times until all of the ammonium formate buffer was removed. **Low Resolution $[\mathbf{M+H}]^{+1}$** m/z 472.17 (*Theoretical*); 472.2 (*Actual*).

A similar procedure was followed for the bis-dR oxime conjugate of **2-2**. 1 mL of **2-2** in a 2 mM DMSO solution was added to an Eppendorf tube. To this solution was added a spatula tip of 2-deoxy-D-ribose. The solution was vortexed and sonicated to fully dissolve the sugar. The reaction was allowed to heat at 37 °C for 1 hour. The crude reaction was purified in aliquots by reverse-phase HPLC (Method #3). The eluants were collected and concentrated by lyophilization multiple times until all of the ammonium formate buffer was removed. **Low Resolution $[\mathbf{M+H}]^{+1}$** m/z 703.29 (*Theoretical*); 703.3 (*Actual*).

For the synthesis of the mono-dR oxime conjugate of **2-2**, a 1 mM stock solution of dR was prepared in HEPES buffer (0.1 M, 0.1 M NaCl, pH 7.4). A 500 μL aliquot of this solution was diluted to 1 mL by a 2 mM solution of **2-2** in DMSO. The reaction was allowed to react at 37 °C for 4 days. The crude reaction was purified by reverse-phase HPLC (Method #2). The eluants were collected and concentrated by lyophilization multiple times until all of the ammonium formate buffer was removed. **Low Resolution $[M+H]^{+1}$** m/z 587.25 (*Theoretical*); 587.3 (*Actual*).

For the isotopically labeled oxime conjugate between dR and **2-1** a similar procedure was followed as described in the previous paragraph. A 1 mM stock solution of ^{13}C-labeled dR was made in the same HEPES buffer as the previous paragraph. A 500 µL aliquot of this solution was diluted to 1 mL by a 2 mM solution of **2-2** in DMSO. The reaction was allowed to react at 37 °C for 1 hour. The crude reaction was purified by reverse-phase HPLC (Method #2.3) on a column used specifically for isotopically labeled compounds. The eluants were collected and concentrated by lyophilization multiple times until all of the ammonium formate buffer was removed. **Low Resolution $[M+H]^{+1}$** m/z 477.19 (*Theoretical*); 477.2 (*Actual*).

APmer Conjugation

Conditions for the reaction of our compounds with a 12-base pair DNA oligonucleotide varied depending on the size of the desired reaction. Equations used to determine these amounts are provided, but the procedure assumes a certain set of conditions typical to our experiments. Those are provided, as well.

HEPES buffer (0.1 M, 0.1 M NaCl, pH 7.4), Umer, and comp were added so that the concentrations of Umer and comp were each 25 µM. If one desired a certain amount of nanomoles of DNA in the reaction, the volumes of each reagent would be determined from the concentrations of stock solutions of the oligonucleotides determined by use of a NanoDrop Microvolume Spectrophotometer from Thermo Fisher Scientific. From the concentration data, we determined the volume of each solution that carries 5 nmol of DNA. Using these results, the formulas below provide the volumes necessary for annealing DNA at the desired concentration (25 µM, in this case).

$$Anneal\ Volume = Desired\ nmol\ Umer \times \left(\frac{1000\ \mu L}{25\ nmo\ \ Umer}\right) \qquad \textbf{Eq. 5}$$

$$Umer\ Volume = Desired\ nmol\ Umer \times \left(\frac{Volume\ of\ Umer\ from\ nanodrop}{5\ nmol\ Umer}\right) \qquad \textbf{Eq. 6}$$

$$Comp\ Volume = Desired\ nmol\ Comp \times \left(\frac{Volume\ of\ Comp\ from\ nanodrop}{5\ nmol\ Comp}\right) \qquad \textbf{Eq. 7}$$

$$HEPES\ Volume = Anneal\ Volume - Umer\ Volume - Comp\ Volume \qquad \textbf{Eq. 8}$$

Once the determined volumes are added to an Eppendorf tube, the reaction was vortexed and placed on a 90 °C heating block for 5 min. After heating, the heating block was turned off, and the reaction sat cooling in the powered-down heating block for 1.25 hr. The reaction was quickly centrifuged to remove all condensation from the cap of the Eppendorf. To the solution was added enough UDG (5 units/µL) to have a final UDG concentration of 0.25 units/µL. This volume was determined using Eq. 9.

$$Desired\ UDG\ Conc.\left(\frac{units}{\mu L}\right) = \frac{5\,\frac{units}{\mu L} \times UDG\ Volume}{Anneal\ Volume + UDG\ Volume} \qquad \textbf{Eq. 9}$$

Solving Eq. 9 for UDG Volume gives the needed volume. That result is added to the reaction, and the reaction is lightly vortexed to mix in the enzyme. The reaction was allowed to react at 37 °C on a heat block for 45 min.

When the enzymatic reaction was done, the sample was removed from the heating block, and stock drug solution was added to the reaction so that the final concentration of drug equaled what we desired. In most cases, this was 40 µM; however, in the case of **2-2**, we ended up using 200 µM for reasons discussed in Chapter 2. The volume of the stock solution added was determined using Eq. 10 and depends on the desired drug concentration and the stock solution concentration.

$$\mathit{Drug\ Volume\ in\ \mu L} = \frac{\mathit{Anneal\ Volume + UDG\ Volume}}{\left[1000\,\frac{\mu M}{mM} \times \left(\frac{\mathit{Drug\ Stock\ Conc.\ in\ mM}}{\mathit{Desired\ Drug\ Conc.\ in\ \mu M}}\right)\right] - 1} \qquad \textbf{Eq. 10}$$

If we ran a time course experiment and needed a t = 0 aliquot, that volume was subtracted from the numerator of Eq. 10 since the aliquot was taken before adding the drug. Since stock drug solutions were made in DMSO for better solubility, the final drug volumes needed to be small enough so that DMSO would not interfere with the reaction. If a larger amount of DNA was used, we used a higher concentration of stock solution so that the volume of drug added was smaller than it would have been.

After addition of the drug, the reaction was vortexed and placed on a 37 °C heating block and allowed to react. The reaction typically was done after 3 hr. When the reaction was complete, HPLC-grade acetone was added to the reaction to scavenge excess drug. The reaction was monitored and purified by reverse-phase HPLC (Method #4). When a 20 µL aliquot was removed from the reaction, we added it to a separate Eppendorf tube with 40 µL of HPLC-grade acetone. The aliquot tube was flicked a couple of times to mix, and the solution was injected onto the chromatograph. These aliquot volumes were necessary, especially for those experiments requiring full-loop injection. For those experiments, the HPLC was equipped with a 20 µL loop. For those experiments requiring peak data, peaks on the chromatogram were integrated manually using 32 Karat Software for HPLCs.

When reactions were purified by Method #4 on the HPLC, the eluants were collected and lyophilized multiple times until all of the ammonium formate buffer was removed. These samples were taken up in LCMS-grade water and analyzed by LC-ESI/MS^2 (Method #2). These data are presented in the main text of the dissertation. For experiments requiring crude analysis of the reaction, HEPES buffer and DMSO were removed by a Sep-Pak desalting procedure.

To desalt a sample by Sep-Pak, the Sep-Pak column first was washed with 5 mL of 50% MeCN in water (v/v) (x2), 5 mL of water (x2), and 5 mL of ammonium formate buffer (x2). The sample was diluted to 5 mL by the addition of water to the reaction. The reaction was loaded onto the column <u>slowly</u> so as to allow all DNA to stick properly to the solid phase. The column was washed with 5 mL of ammonium formate buffer <u>slowly</u> followed by 5 mL of water <u>slowly</u>. This step and the speed of washing were crucial as this was the step that removed salt from the sample. Finally, the sample was eluted normally with 5 mL of 50% MeCN in water (v/v), collected in 1 mL batches in Eppendorf tubes. The filled Eppendorf tubes were placed inside centrifuge tubes, sealed with lens paper, and concentrated *in vacuo* on a centrifugal evaporator. Once concentrated, the fractions were combined into one and analyzed by LC-ESI/MS^2 (Method #2).

Thermal Melting Experiments

Samples were prepared by reannealing purified APmer oxime conjugate to the complementary strand as described in the previous section of the Experimental. However, instead of the previously described HEPES buffer, these samples were annealed in sodium phosphate buffer (10 mM, 100 mM NaCl, 50 μM Na_2EDTA, pH 7.5). Control duplexes were annealed following this same procedure, as well. Once annealed, the samples were diluted with more sodium phosphate buffer so that the final concentration was approximately 0.6 A_{260}/mL of duplex oligonucleotide.

Thermal melting experiments were performed on a Varian Cary 4E spectrophotometer (Agilent Technologies) using a 1 mL quartz cuvette with a path length 1 cm. The temperature was increased from 15 °C to 90 °C at a rate of 0.5 °C/min with a hold time of 2 min. Subsequently, the temperature was decreased to the starting temperature at the same rate of temperature change. Absorbances of the samples were measured at 260 nm. Data was exported from the software as a CSV file and analyzed on Microsoft Excel and KaleidaGraph as described in the main text to determine the melting points (T_m).

Enzyme Digest

If an APmer conjugation reaction required enzymatic digestion, we performed the following protocol. Dried oligonucleotide was suspended in bis-tris digest buffer (5 mM, 10 mM $MgCl_2$, pH 7.10). A 10 µg aliquot was diluted so that the oligonucleotide concentration was approximately 120 ng/µL. DNAse I (10 µL, 0.1 mg/mL) and Nuclease P_1 (2 µL, 0.01 mg/mL) were added to the reaction. The reaction sat on a 37 °C heat block for 3.5 hr. After this time, Alkaline phosphatase (4 µL, 0.04 mg/mL) and Phosphodiesterase I (2 µL, 1 µg/mL) were added. The reaction incubated at 37 °C for an additional 12 hr/overnight. The next morning, Adenosine deaminase (5 µL, 1.25 µg/mL) was added and allowed to react at room temperature for 2 hr. The reaction was terminated by diluting it with twice the volume of chilled ethanol and standing on ice for 30 min. The sample was centrifuged for 30 min at 15,000 RPM to separate the enzymes from the supernatant. The supernatant was collected and dried by vacuum centrifugation. Once dry, the sample was dissolved in 100 μL of 0.05% aqueous formic acid (v/v) and enriched by SPE in 20 μL portions.

SPE Purification of Digested DNA

This protocol assumes a single run of SPE at a time. The vacuum chamber used allows for 12 samples to run at the same time and can be used accordingly. An SPE cartridge was equipped to the SPE vacuum chamber. The column was equilibrated with 3 mL of MeOH (x2) and 3 mL of 0.05% aqueous formic acid (v/v) (x2). The sample was diluted to 1 mL and loaded onto the cartridge. This was done with a slow drop rate to allow the samples to bind to the stationary phase. The cartridge was slowly eluted with 5 mL 0.05% aqueous formic acid (v/v) followed by 9 mL 6% aqueous methanol (v/v). Finally, the cartridge was washed with 1.5 mL 90% aqueous methanol (v/v). The eluents were collected and concentrated by vacuum centrifugation. The dried samples were redissolved in LCMS-grade water and analyzed by LC-ESI/MS^2 (Method #3).

COPASI Procedure

COPASI software was downloaded for free from the Internet. The process described herein uses the binding of **2-1** to duplex APmer via an intercalative mechanism as an example. When starting a new model, we adjusted the units so that time was measured in min, volume in L, and quantity in μmol (making the concentration μM). Under Model → Biochemical → Compartments, we created a new compartment and adjusted the Initial Size cell to be the reaction volume (in L) at timepoint t = 0 min.

Next, under Model → Biochemical → Reactions, we created a series of reactions to include in our model. These reactions are the elementary steps of the overall mechanism. As such, our first reaction (R1) was set to A + B = C (where A is the APmer, B is the drug, and C is the intercalative complex). The "=" is used in COPASI to represent equilibrium reactions. The rate law was manually adjusted to be Eq. 11.

$$\frac{d[C]}{dt} = k_1[A][B] - k_2[C] \qquad \textbf{Eq. 11}$$

The k values for this rate law are defined the same way as with Eq. 2. Uploading Eq. 11 as the rate law for R1 allowed us to assign A and B as substrates, C as a product, and k_1 and k_2 as parameters. We did something similar for R2, which we set as C → D. In this case, our rate law was Eq. 12.

$$\frac{d[D]}{dt} = k_3[C] \qquad \textbf{Eq. 12}$$

Assigning Eq. 12 to R2 allowed us to set C as a substrate, D as a product, and k_3 as a parameter.

Once the reactions were created, we clicked on Model → Biochemical → Species to set the starting concentrations of the reaction. For this example, we set [A] = 23.3 μM, [B] = 40 μM, and [C] = [D] = 0 μM. After completing this, we checked to make sure all was set up as desired by clicking Model → Mathematical → Differential Equations. This provides the differential rate laws for each species cited in our model.

Next, we selected Tasks → Parameter Estimation. In the top right corner, we selected "Experimental Data." Here, we uploaded a CSV file of our data for [APmer] versus time so that the parameters of our model could be estimated based on the data. Once uploaded, we unchecked the "<tab>" button and selected "Time Course" under "Experiment Type." The column headings from the CSV file appear in the screen with some blank cells in a table. In the table under "Type" for our [APmer] column, we selected “dependent,” which opens up a new screen. From the screen, we selected Species → Transient Concentrations → [A](t) to tell the program that those data represented that species. Selecting “OK” set the experimental data to the parameter estimation. Following this, we could input the parameters we wanted to estimate. By clicking the icon, we added all the reaction parameters. Next, we changed the upper and lower bounds as indicated in the tables for this chapter, and we set the Start Value to 0.01. By clicking “Run” on the bottom left of the screen, COPASI recursively estimates what these parameters could be. Going to Tasks → Parameter Estimation → Results, we got a table similar to Table 2.5.

Clicking “Update Model” transfers these estimations into the mechanism we previously created. Next, by going to Tasks → Time Course, we created the parameters of the computational experiment. By setting the duration and interval size, we could control the number of data points calculated using our model. Before running the experiment, however, we clicked “Output Assistant” in the bottom right corner and chose “Concentrations, Volumes, and Global Quantity Values” under the “Plots” option. This tells COPASI to create a graph of concentration versus time for all species in the model. By selecting “Create” and then “Run,” COPASI generates a graph like the one in Figure 2.30. To see the data points and export them as a TXT file, we clicked Tasks → Time Course → Results.

There are other features of COPASI software that might prove useful to us in the future, but these are the SOPs for our current purposes.

References

231. Kassa, J. Review of Oximes in the Antidotal Treatment of Poisoning by Organophosphorus Nerve Agents. *J. Toxicol. Clin. Toxicol.* **40**, 803–816 (2002).

232. Sørensen, M., Neilson, E. H. J. & Møller, B. L. Oximes: Unrecognized Chameleons in General and Specialized Plant Metabolism. *Mol. Plant* **11**, 95–117 (2018).

233. Schepetkin, I. A., Plotnikov, M. B., Khlebnikov, A. I., Plotnikova, T. M. & Quinn, M. T. Oximes: Novel Therapeutics with Anticancer and Anti-Inflammatory Potential. *Biomolecules* **11**, 777 (2021).

234. Souza, L. G. da S. *et al.* Synthesis, antibacterial and cytotoxic activities of new biflorin-based hydrazones and oximes. *Bioorg. Med. Chem. Lett.* **26**, 435–439 (2016).

235. Reddy, D. S. *et al.* Synthesis and evaluation of novel coumarin-oxime ethers as potential anti-tubercular agents: Their DNA cleavage ability and BSA interaction study. *Eur. J. Med. Chem.* **150**, 864–875 (2018).

236. Hwang, T.-L., Wang, W.-H., Wang, T.-Y., Yu, H.-P. & Hsieh, P.-W. Synthesis and pharmacological characterization of 2-aminobenzaldehyde oxime analogs as dual inhibitors of neutrophil elastase and proteinase 3. *Bioorg. Med. Chem.* **23**, 1123–1134 (2015).

237. Komai, T. *et al.* Inhibition of HIV-1 Protease by Oxim Derivatives. *Biochem. Biophys. Res. Commun.* **230**, 557–561 (1997).

238. Chiou, C.-T. *et al.* Synthesis and evaluation of 3-ylideneoxindole acetamides as potent anticancer agents. *Eur. J. Med. Chem.* **98**, 1–12 (2015).

239. Blažević, T. *et al.* Indirubin and Indirubin Derivatives for Counteracting Proliferative Diseases. *Evidence-based Complement. Altern. Med.* **2015**, 654098 (2015).

240. Yuskaitis, C. J. & Jope, R. S. Glycogen synthase kinase-3 regulates microglial migration, inflammation, and inflammation-induced neurotoxicity. *Cell. Signal.* **21**, 264–273 (2009).

241. Kalia, J. & Raines, R. T. Hydrolytic stability of hydrazones and oximes. *Angew. Chemie -*

Int. Ed. **47**, 7523–7526 (2008).

242. Wiberg, K. B. & Glased, R. Stereochemistry, Energetics, and Electron Distributions in 3-Center Four-Pi-Electron Systems A=B-C. *J. Am. Chem. Soc.* **114**, 841–850 (1992).

243. Liu, L., Nakatsuru, Y. & Gerson, S. L. Base Excision Repair as a Therapeutic Target in Colon Cancer. *Clin. Cancer Res.* **8**, 2985–2991 (2002).

244. Rinne, M. L., He, Y., Pachkowski, B. F., Nakamura, J. & Kelley, M. R. N-methylpurine DNA glycosylase overexpression increases alkylation sensitivity by rapidly removing non-toxic 7-methylguanine adducts. *Nucleic Acids Res.* **33**, 2859–2867 (2005).

245. Matyjaszewski, K., Woodworth, B. E., Zhang, X., Gaynor, S. G. & Metzner, Z. Simple and efficient synthesis of various alkoxyamines for stable free radical polymerization. *Macromolecules* **31**, 5955–5957 (1998).

246. Braslau, R., Tsimelzon, A. & Gewandter, J. Novel methodology for the synthesis of N-alkoxyamines. *Org. Lett.* **6**, 2233–2235 (2004).

247. Tamura, Y., Minamikawa, J. & Ikeda, M. O-mesitylenesulfonylhydroxylamine and related compounds - Powerful aminating reagents. *Synthesis (Stuttg).* **1977**, 1–17 (1977).

248. Boche, G. *et al.* O-(Mesitylsulfonyl)hydroxylamine. *Encycl. Reagents Org. Synth.* (2011). doi:10.1002/047084289X.RM055M.PUB2

249. Sun, R. *et al.* Design, synthesis, bioactivity, and structure-activity relationship (SAR) studies of novel benzoylphenylureas containing oxime ether group. *J. Agric. Food Chem.* **56**, 11376–11391 (2008).

250. Diamond, L. H. & Audrieth, L. F. Preparation of N-Substituted Hydrazines from Amines and Chloramine. *J. Am. Chem. Soc.* **77**, 3131 (1955).

251. Rowe, R. A. & Audrieth, L. F. Preparation of Some N-Disubstituted Hydrazines by

Reaction of Chloramine with Secondary Amines. *J. Am. Chem. Soc.* **78**, 563–564 (1956).

252. Krapcho, A. P. *et al.* Aza and diaza bioisosteric anthracene-9,10-diones as antitumor agents. *Acta Biochim. Pol.* **42**, 427–432 (1995).

253. Krapcho, A. P. *et al.* Anthracene-9,10-Diones and Aza Bioisosteres as Antitumor Agents. *Curr. Med. Chem.* **2**, 803–824 (1995).

254. Khomutov, A. R. *et al.* Synthesis of hydroxylamine analogues of polyamides. *Tetrahedron* **52**, 13751–13766 (1996).

255. Malik, G., Ferry, A., Guinchard, X. & Crich, D. Synthesis of β-hydroxy O-alkyl hydroxylamines from epoxides using a convenient and versatile two-step procedure. *Synthesis (Stuttg).* **45**, 65–74 (2013).

256. Kubo, K., Ide, H., Wallace, S. S. & Kow, Y. W. A Novel, Sensitive, and Specific Assay for Abasic Sites, the Most Commonly Produced DNA Lesion. *Biochemistry* **31**, 3703–3708 (1992).

257. Nakamura, J. *et al.* Highly Sensitive Apurinic/Apyrimidinic Site Assay Can Detect Spontaneous and Chemically Induced Depurination under Physiological Conditions. *Cancer Res.* **58**, 222–225 (1998).

258. Nakamura, J. & Swenberg, J. A. Endogenous Apurinic/Apyrimidinic Sites in Genomic DNA of Mammalian Tissues. *Cancer Res.* **59**, 2522–2526 (1999).

259. Pastor, W. A. *et al.* Genome-wide mapping of 5-hydroxymethylcytosine in embryonic stem cells. *Nature* **473**, 394–397 (2011).

260. Tjhung, K. F. *et al.* Silent Encoding of Chemical Post-Translational Modifications in Phage-Displayed Libraries. *J. Am. Chem. Soc.* **138**, 32–35 (2016).

261. Trévisiol, E. T., Defrancq, E. D., Lhomme, J. L., Laayoun, A. L. & Cros, P. C. Synthesis

of Methylketone Containing Nucleoside Triphosphates for RNA Labelling. *Tetrahedron* **56**, 6501–6510 (2000).

262. Ghosh, S., Defrancq, E., Lhomme, J. H., Dumy, P. & Bhattacharya, S. Efficient conjugation and characterization of distamycin-based peptides with selected oligonucleotide stretches. *Bioconjug. Chem.* **15**, 520–529 (2004).

263. Cipolla, L. *et al.* Novel Tn antigen-containing neoglycopeptides: Synthesis and evaluation as anti tumor vaccines. *Bioorganic Med. Chem.* **10**, 1639–1646 (2002).

264. Anderson, R. J. *et al.* NKT cell-dependent glycolipid–peptide vaccines with potent anti-tumour activity. *Chem. Sci.* **6**, 5120–5127 (2015).

265. Garanger, E., Boturyn, D., Renaudet, O., Defrancq, E. & Dumy, P. Chemoselectively addressable template: A valuable tool for the engineering of molecular conjugates. *J. Org. Chem.* **71**, 2402–2410 (2006).

266. Routier, S. *et al.* Salen-anthraquinone Conjugates. Synthesis, DNA-binding and cleaving properties, effects on topoisomerases and cytotoxicity. *Bioorg. Med. Chem.* **4**, 1185–1196 (1996).

267. Morier-Teissier, E. *et al.* Synthesis and Antitumor Properties of an Anthraquinone Bisubstituted by the Copper Chelating Peptide Gly-Gly-l-His. *J. Med. Chem.* **36**, 2084–2090 (1993).

268. Han, G., Tamaki, M. & Hruby, V. J. Fast, efficient and selective deprotection of the tert-butoxycarbonyl (Boc) group using HCl/dioxane (4 M). *J. Pept. Res.* **58**, 338–341 (2001).

Appendix I

1D and 2D NMR Spectra for Chapter 2

^{1}H NMR of 2-4

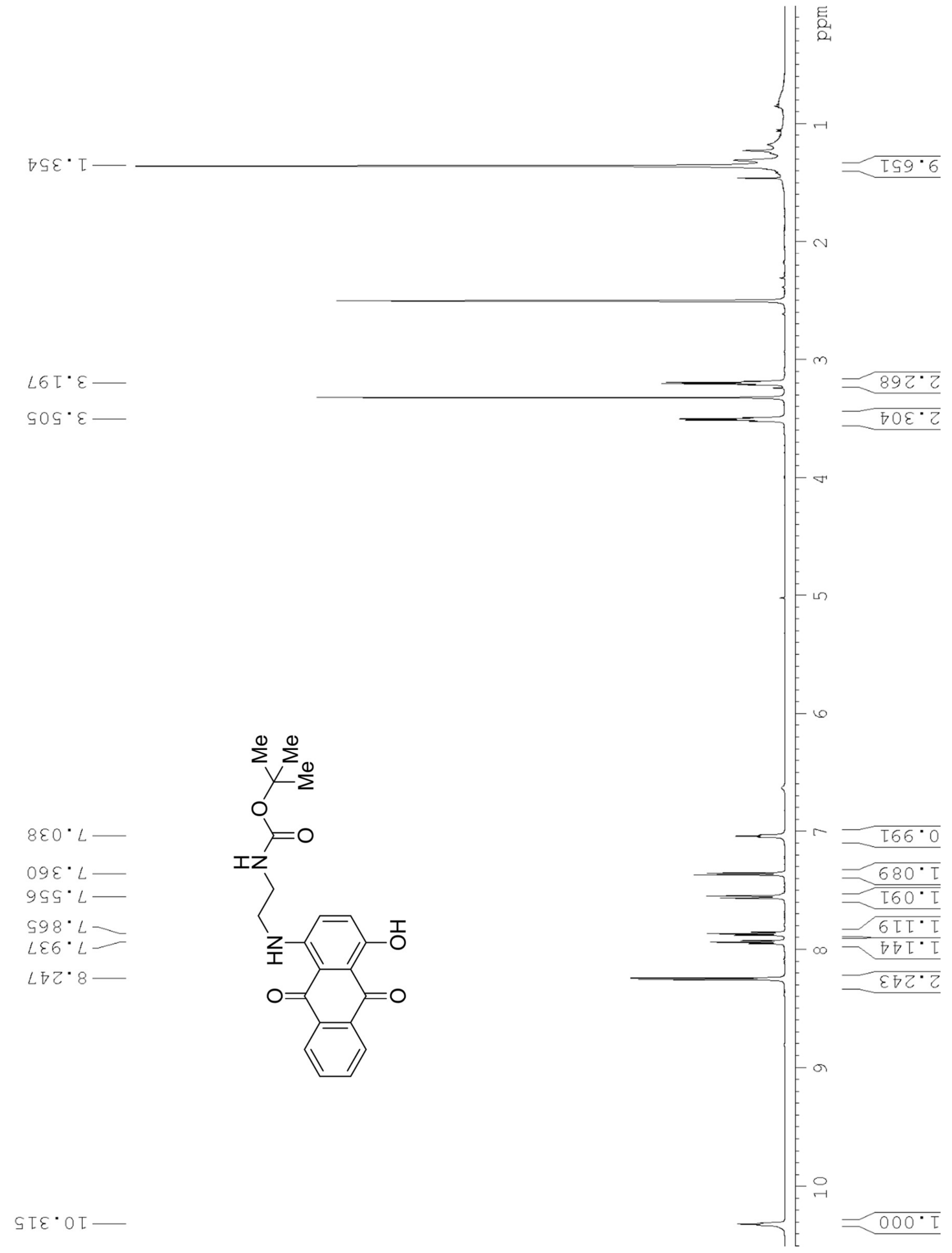
ppm
1
2
3
4
5
6
7
8
9
10
1.354
3.197
3.505
7.038
7.360
7.556
7.865
7.937
8.247
10.315
9.651
2.268
2.304
0.991
1.089
1.091
1.119
1.144
2.243
1.000
Me
Me
Me
O
O
H
N
HN
OH
O
O

^{13}C NMR of 2-4

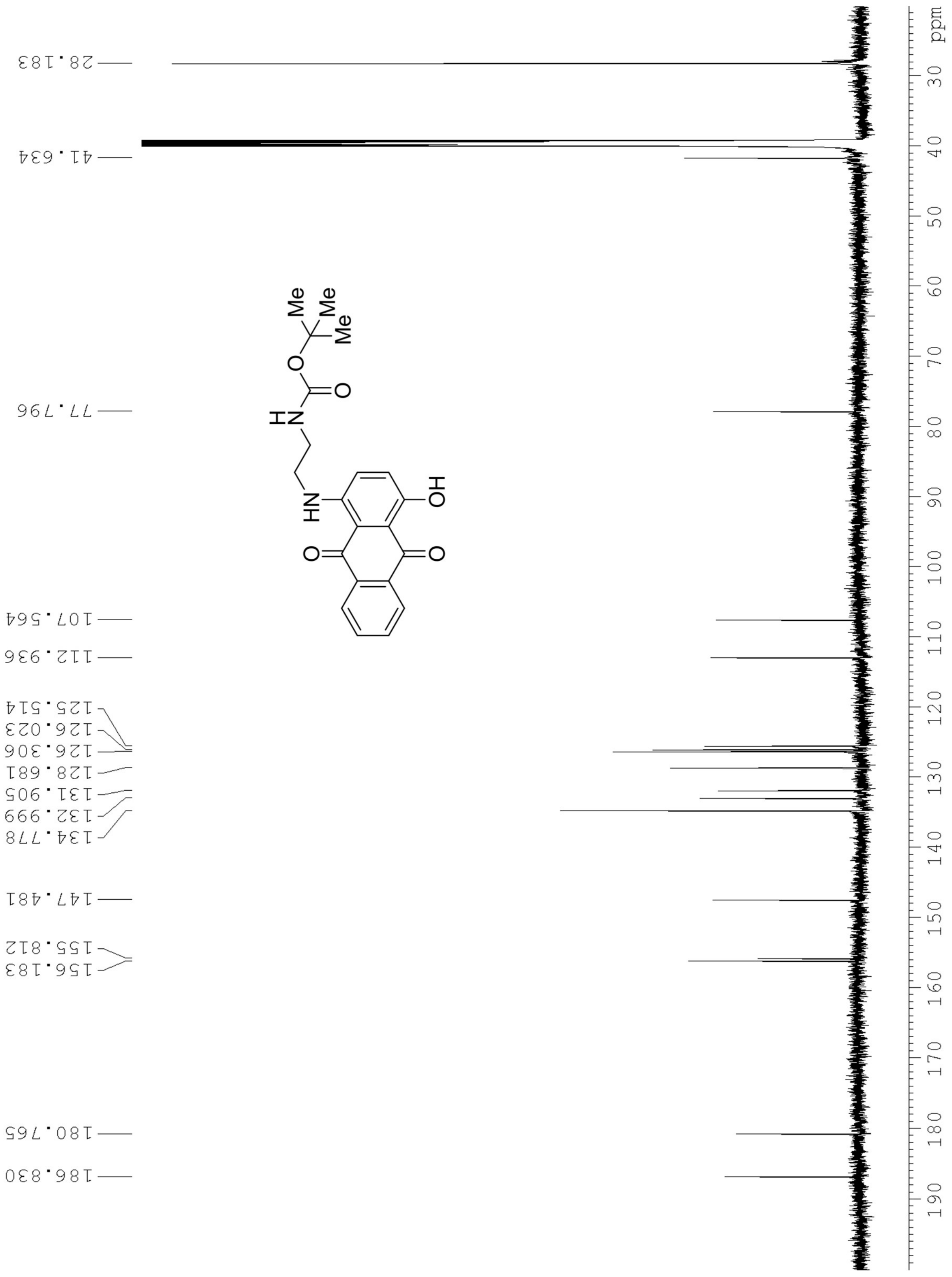
28.183
41.634
77.796
107.564
112.936
125.514
126.023
126.306
128.681
131.905
132.999
134.778
147.481
155.812
156.183
180.765
186.830
ppm
30
40
50
60
70
80
90
100
110
120
130
140
150
160
170
180
190
Me
Me
Me
O
O
H
N
HN
OH
O
O

HSQC NMR of 2-4

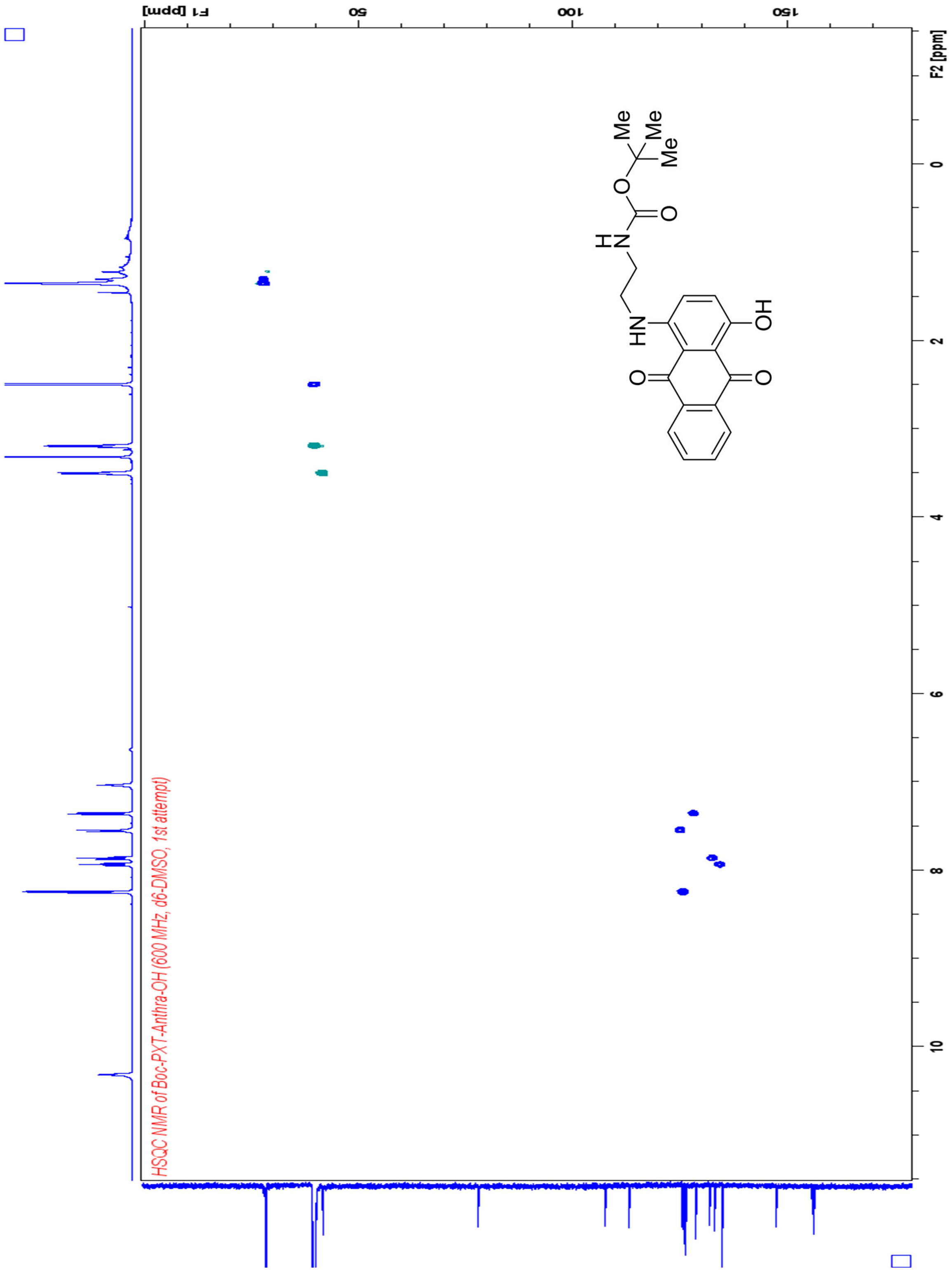

HMBC NMR of 2-4

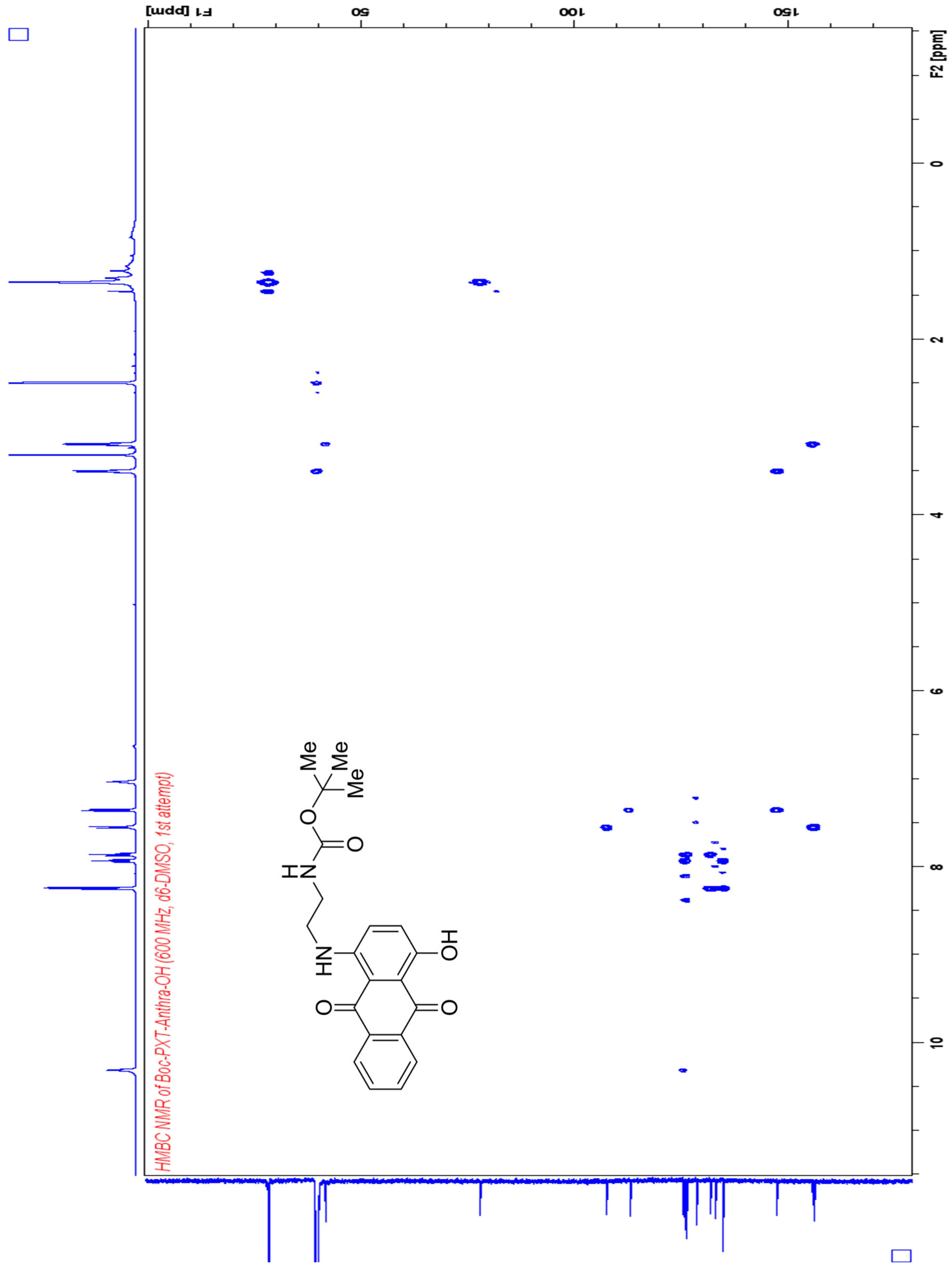

COSY NMR of 2-4

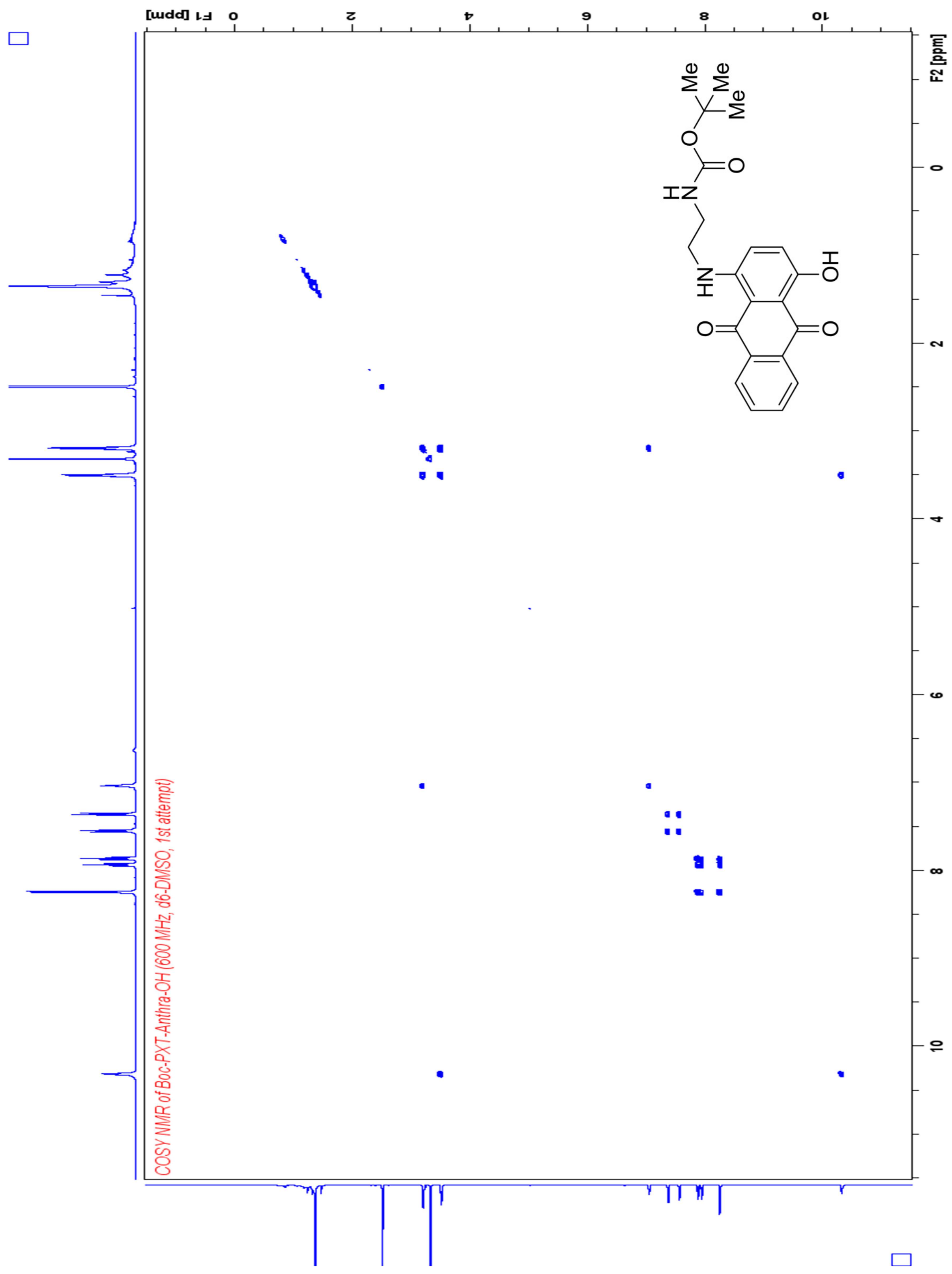

^{1}H NMR of 2-7

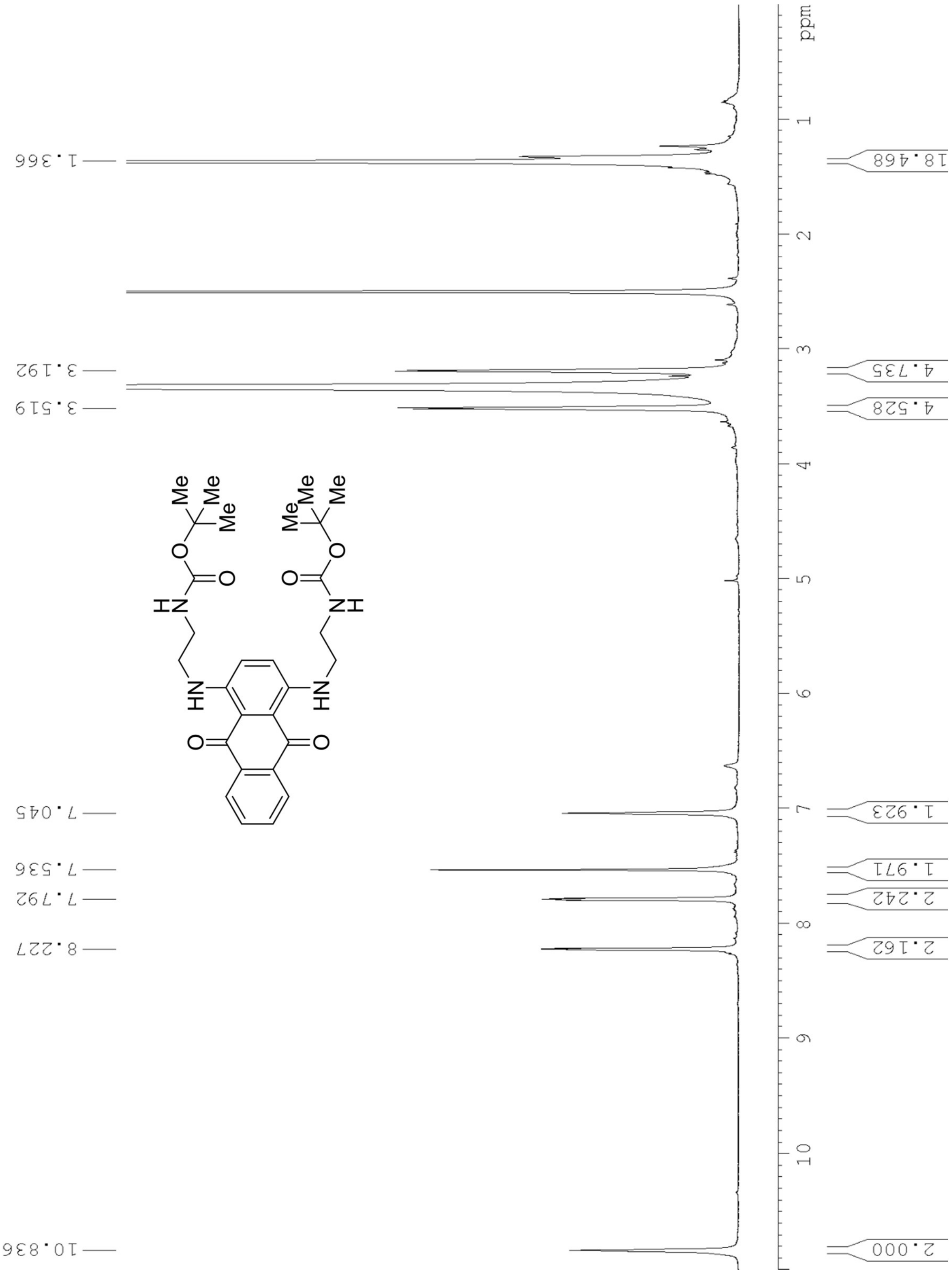
1.366
3.192
3.519
7.045
7.536
7.792
8.227
10.836
18.468
4.735
4.528
1.923
1.971
2.242
2.162
2.000
ppm
1
2
3
4
5
6
7
8
9
10
Me
Me
Me
O
O
HN
HN
O
O
NH
NH
O
O
Me
Me
Me

^{13}C NMR of 2-7

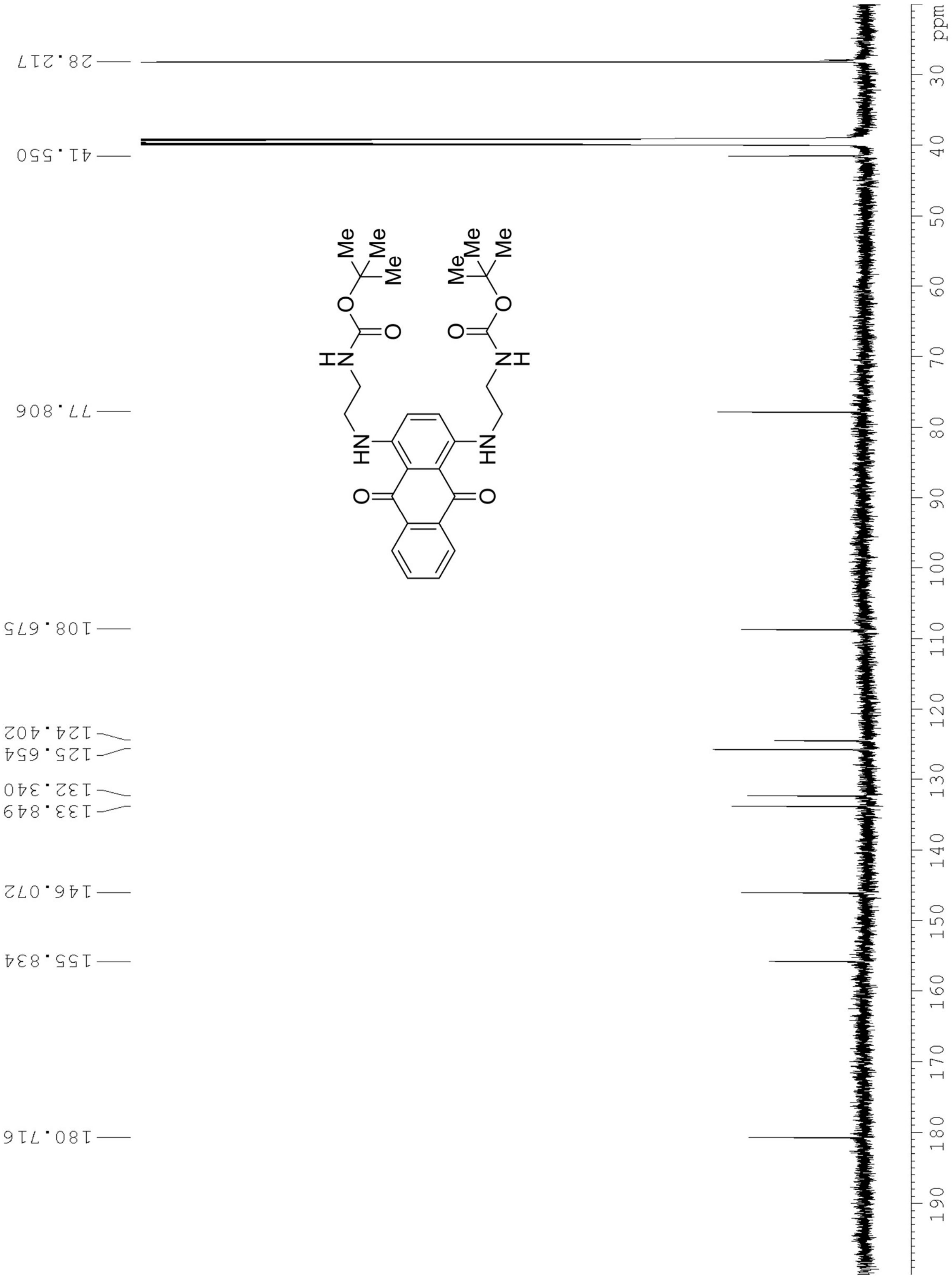
28.217
41.550
77.806
108.675
124.402
125.654
132.340
133.849
146.072
155.834
180.716
ppm
30
40
50
60
70
80
90
100
110
120
130
140
150
160
170
180
190
Me
Me
Me
Me
Me
Me
O
O
O
O
HN
HN
HN
HN
O
O

HSQC NMR of 2-7

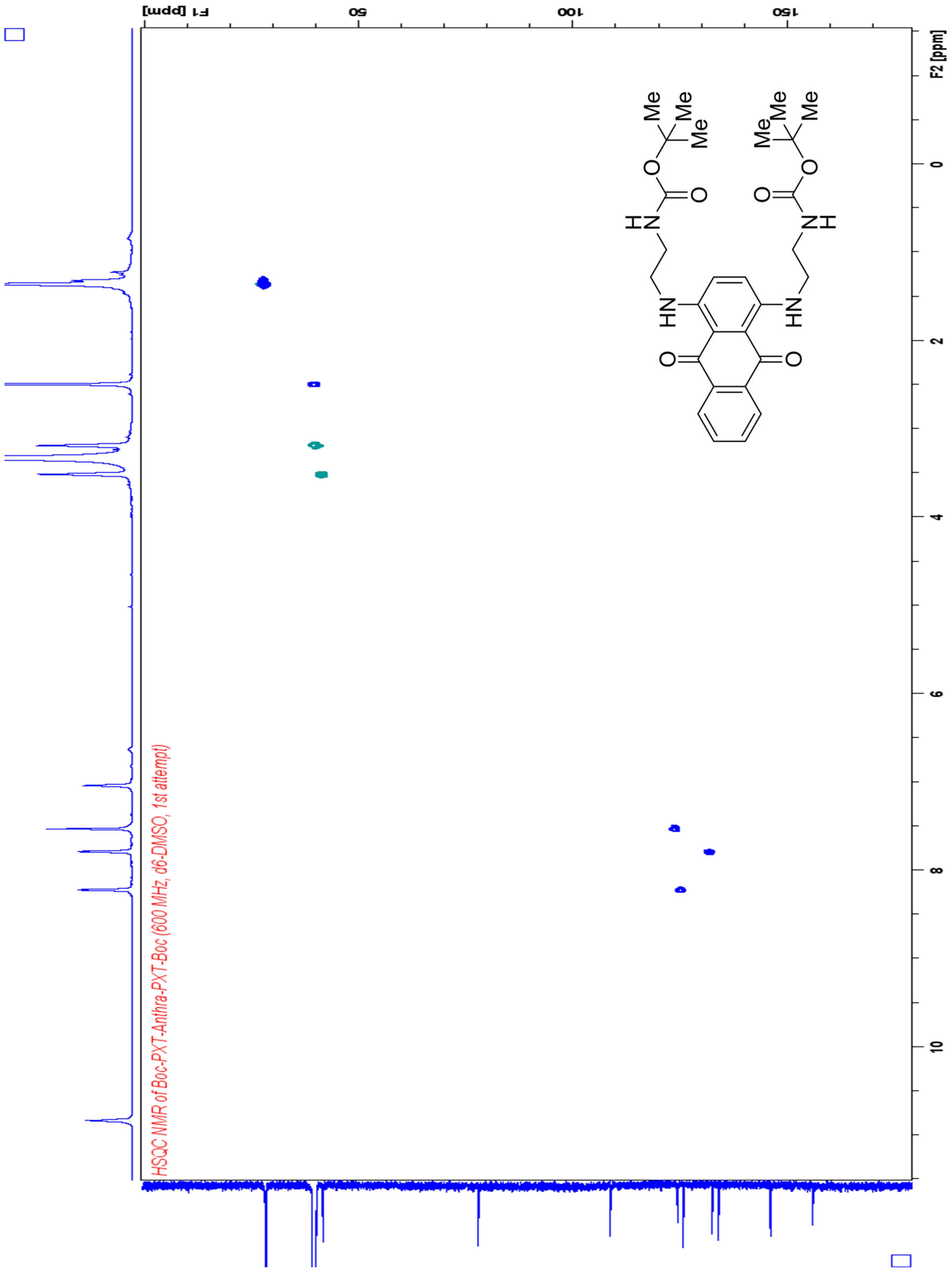

HMBC NMR of 2-7

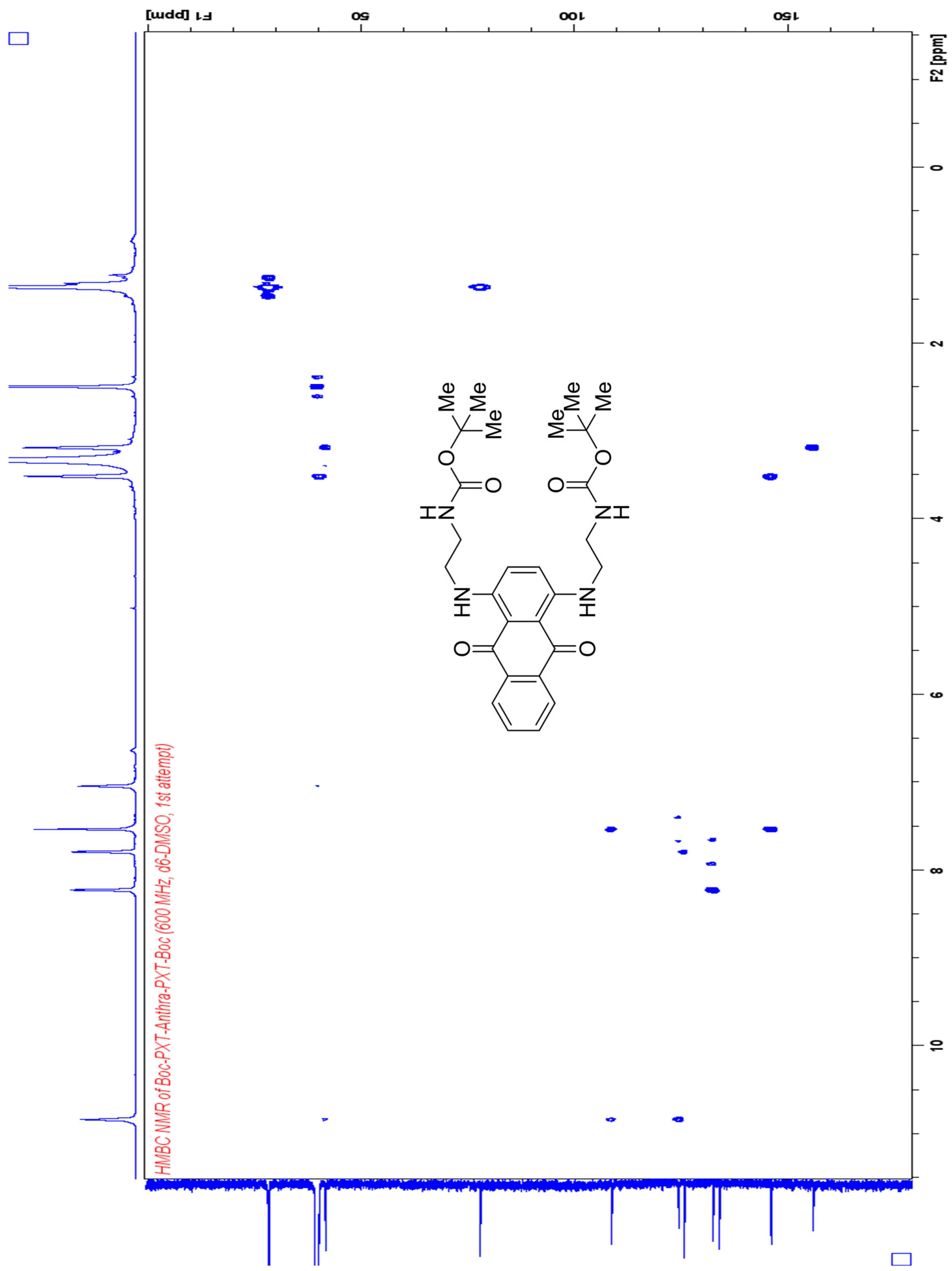

COSY NMR of 2-7

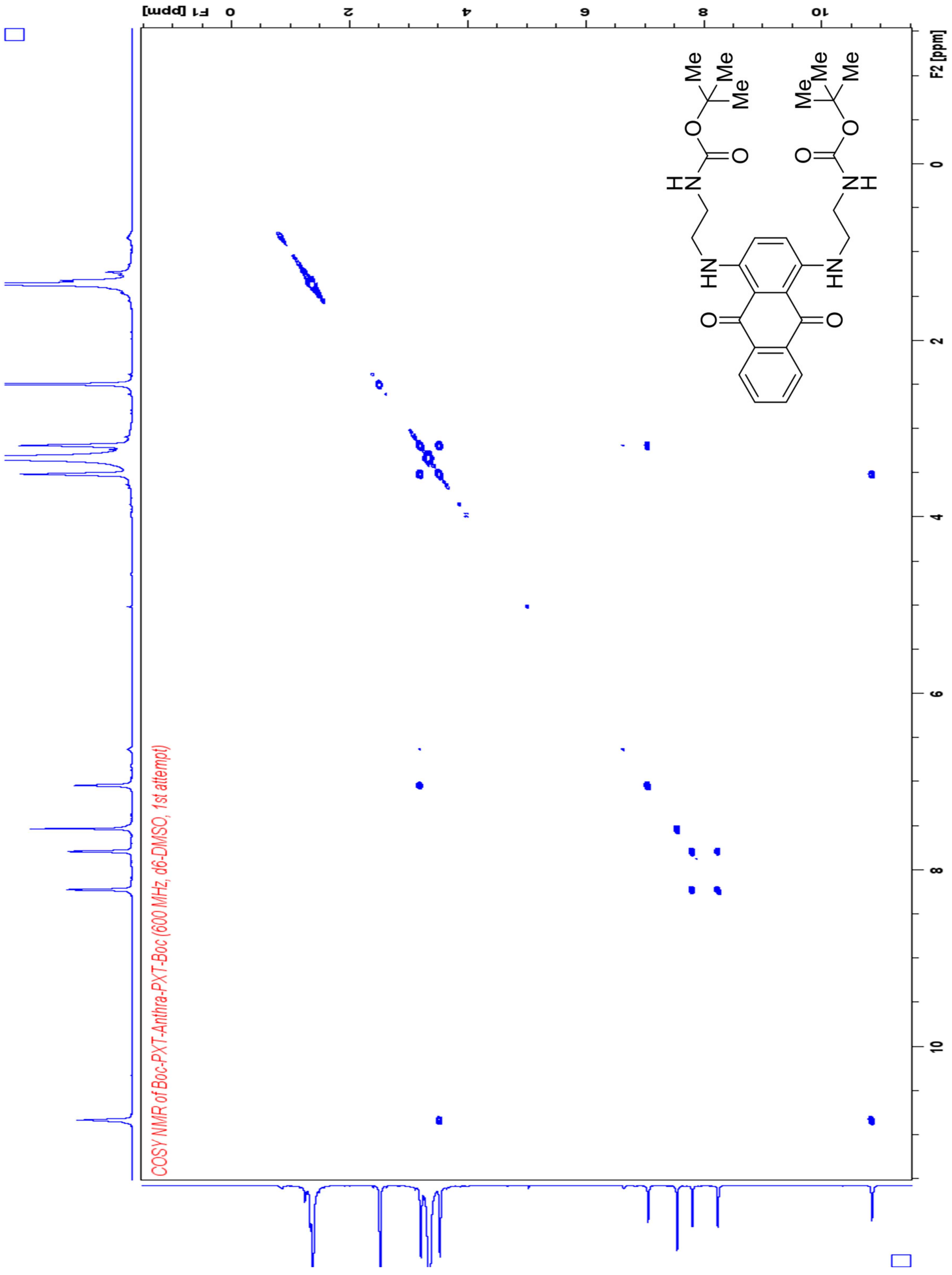

^{1}H NMR of 2-5

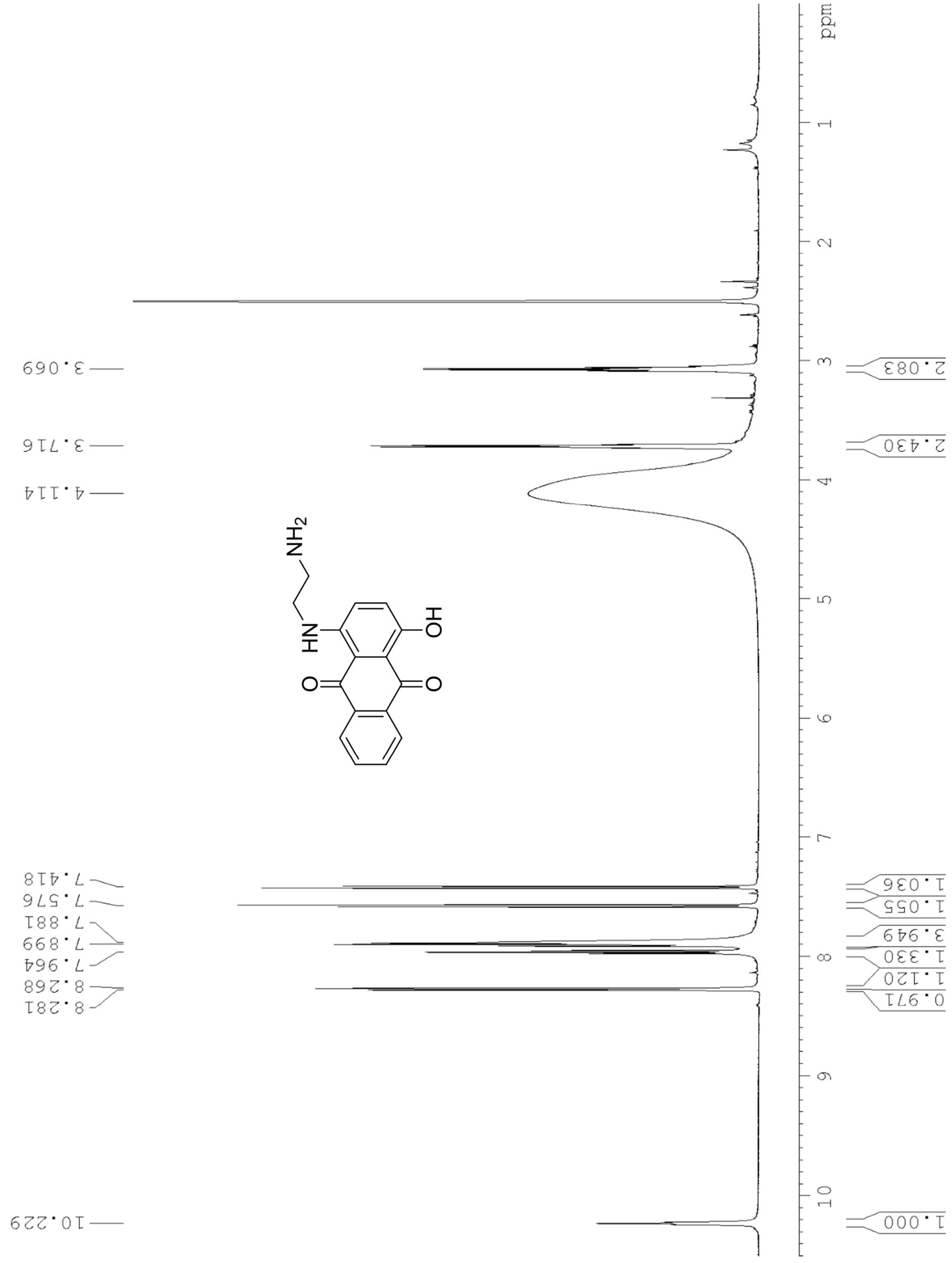
ppm
1
2
3
4
5
6
7
8
9
10
3.069
3.716
4.114
7.418
7.576
7.881
7.899
7.964
8.268
8.281
10.229
2.083
2.430
1.036
1.055
3.949
1.330
1.120
0.971
1.000
NH2
HN
OH
O
O

^{13}C NMR of 2-5

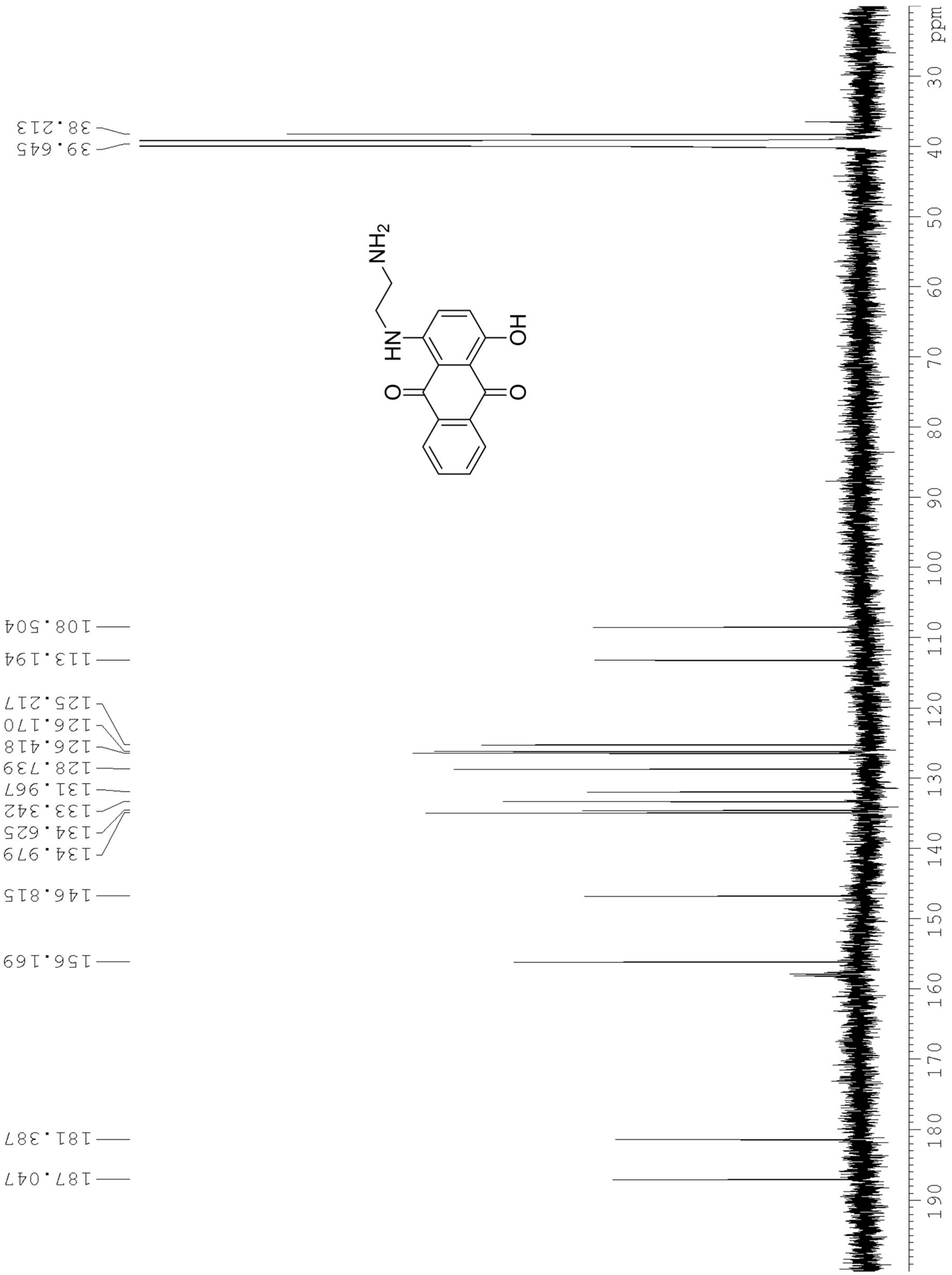
38.213
39.645
108.504
113.194
125.217
126.170
126.418
128.739
131.967
133.342
134.625
134.979
146.815
156.169
181.387
187.047
ppm
30
40
50
60
70
80
90
100
110
120
130
140
150
160
170
180
190
NH2
HN
OH
O
O

HSQC NMR of 2-5

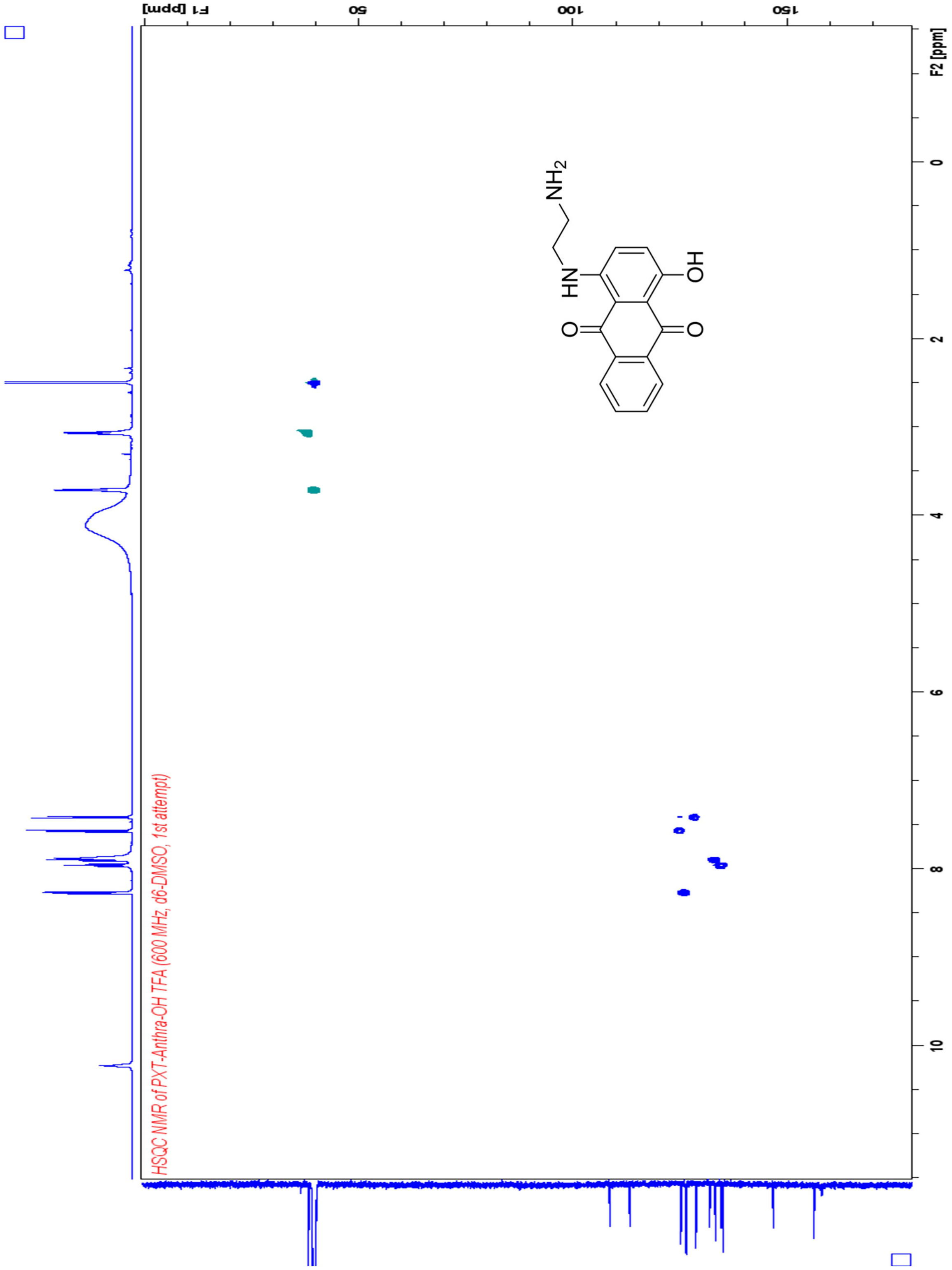

HMBC NMR of 2-5

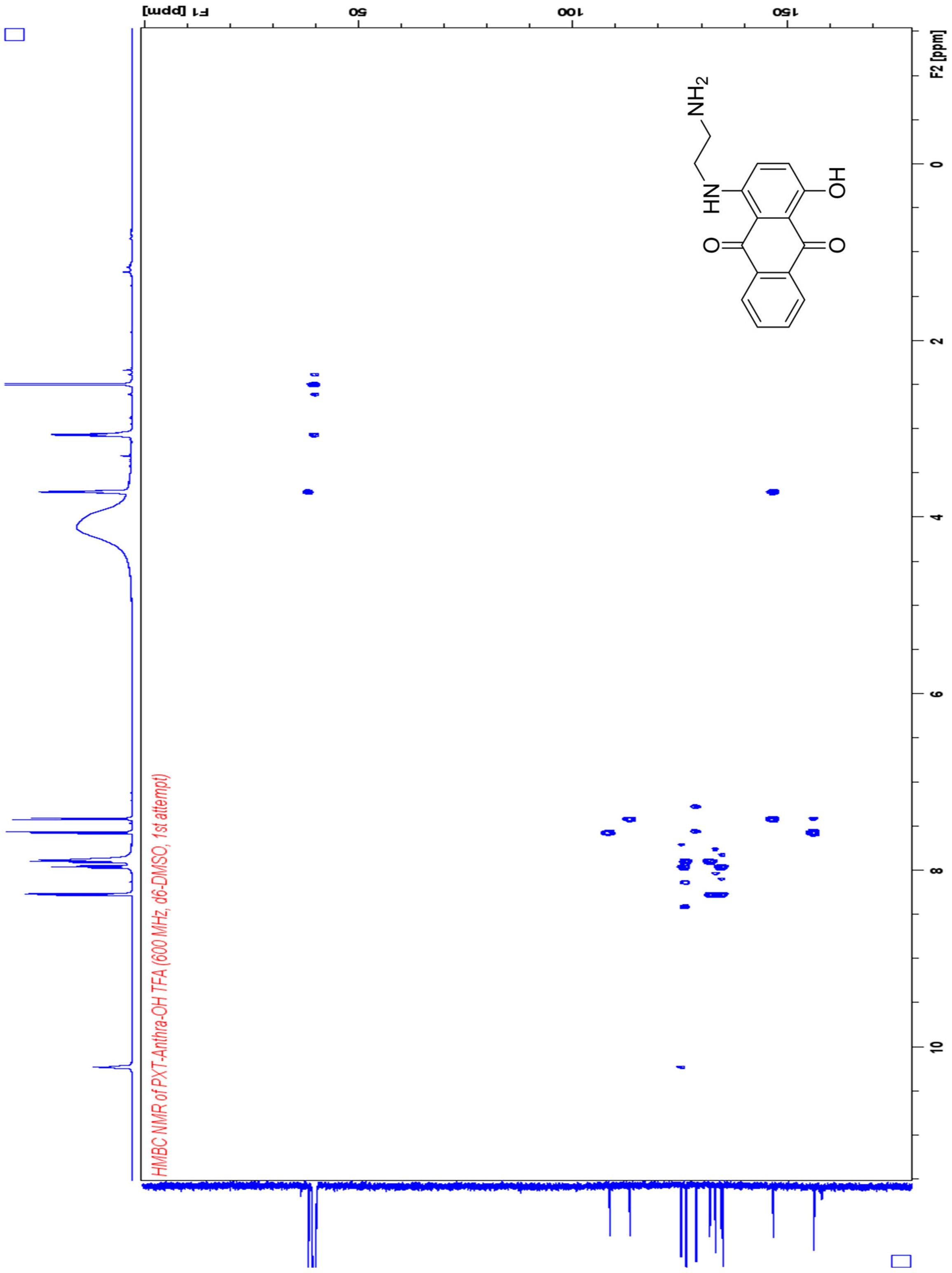

COSY NMR of 2-5

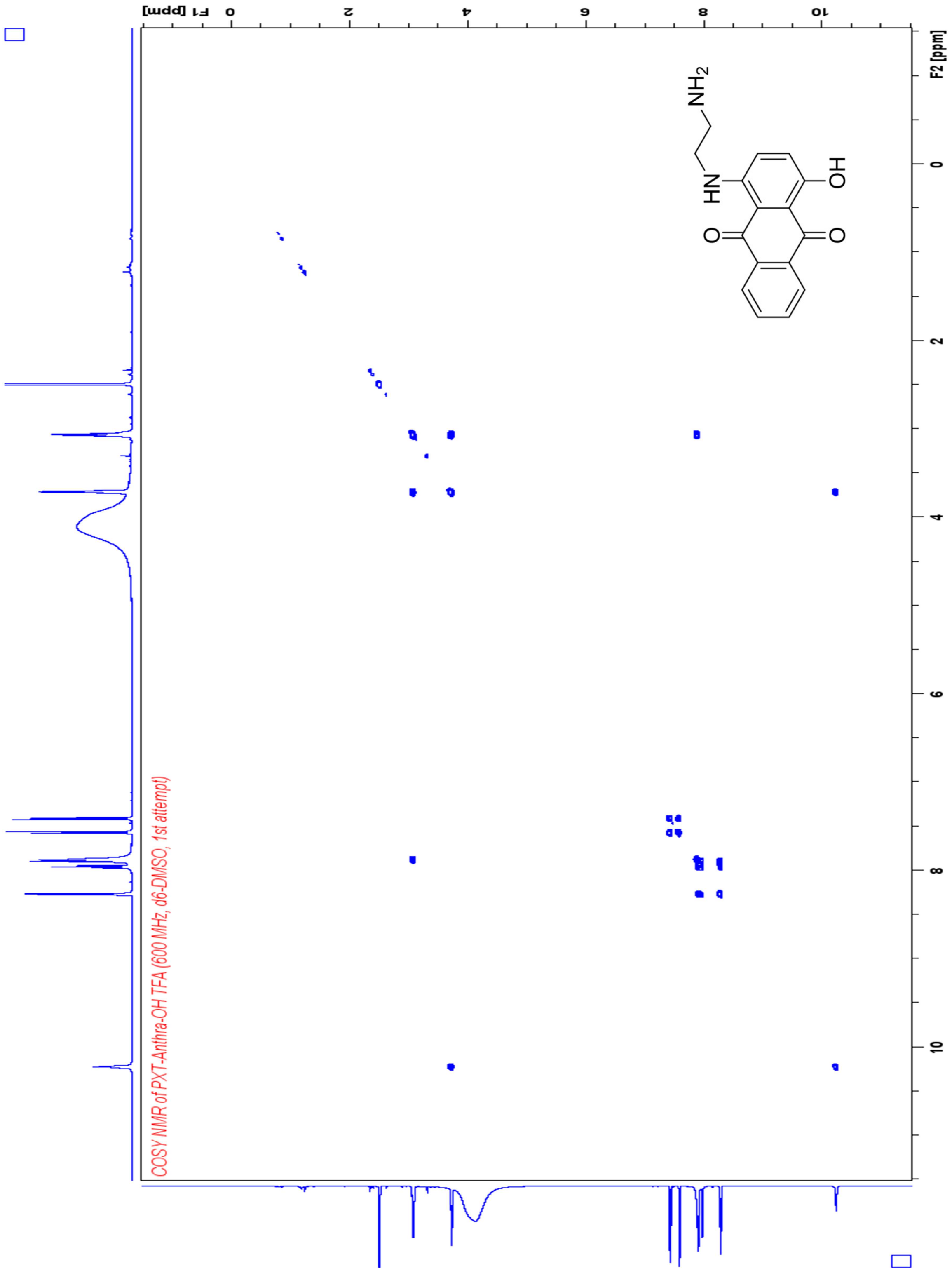

^{1}H NMR of 2-8

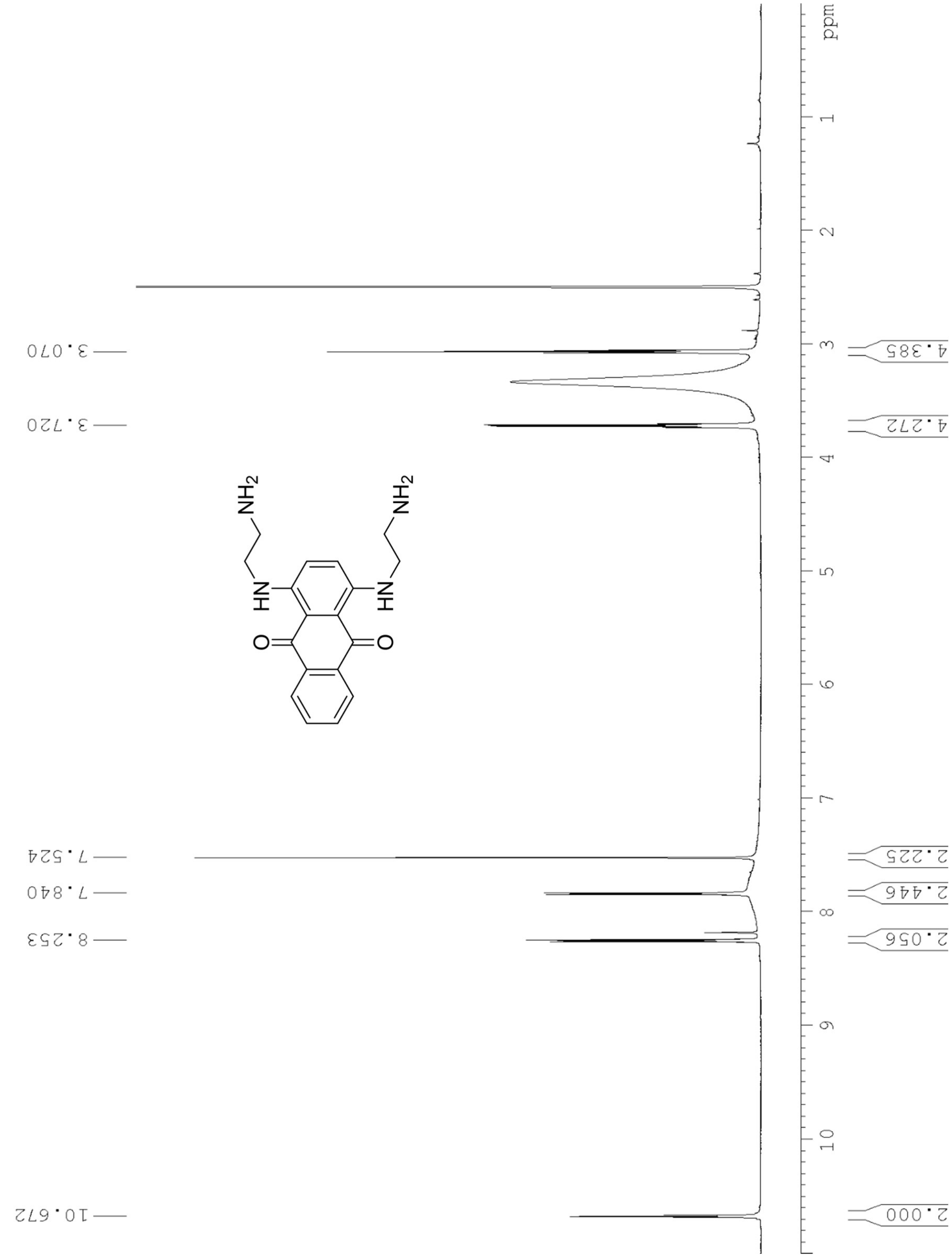
3.070
3.720
7.524
7.840
8.253
10.672
4.385
4.272
2.225
2.446
2.056
2.000
ppm
1
2
3
4
5
6
7
8
9
10
NH2
NH2
HN
HN
O
O

^{13}C NMR of 2-8

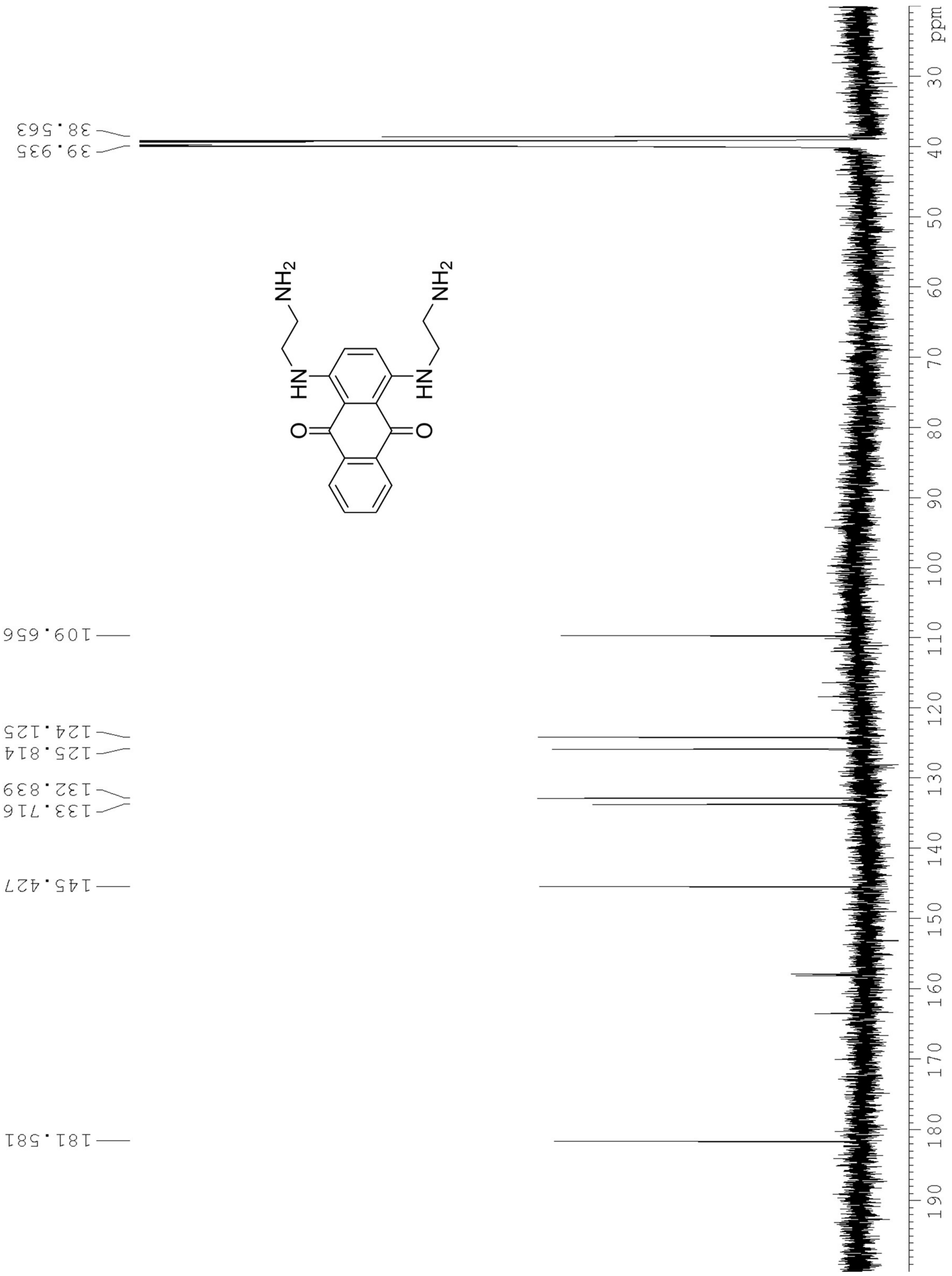

38.563
39.935
109.656
124.125
125.814
132.839
133.716
145.427
181.581
NH$_2$
NH$_2$
HN
HN
O
O
ppm
30
40
50
60
70
80
90
100
110
120
130
140
150
160
170
180
190

HSQC NMR of 2-8

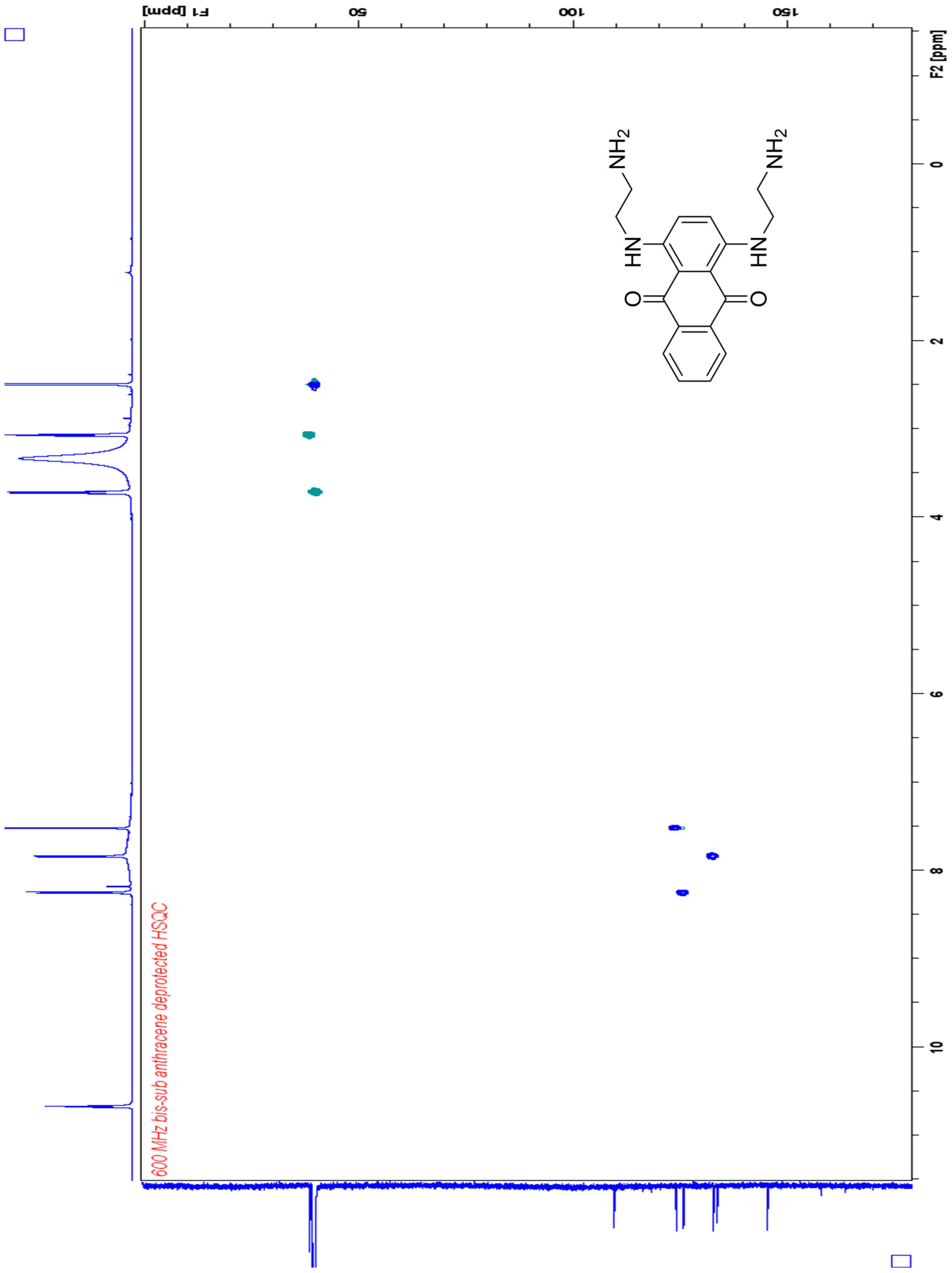

HMBC NMR of 2-8

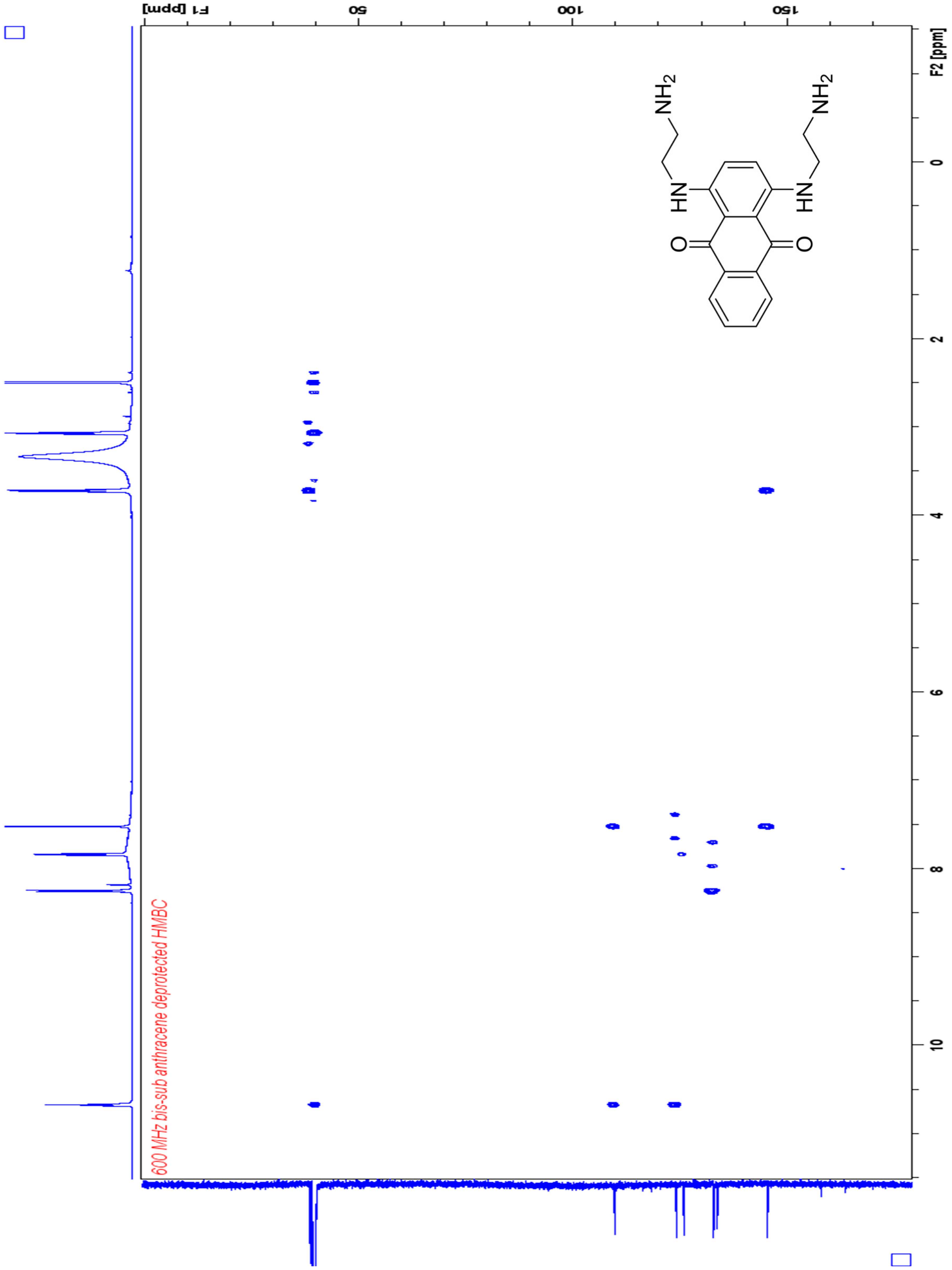

COSY NMR of 2-8

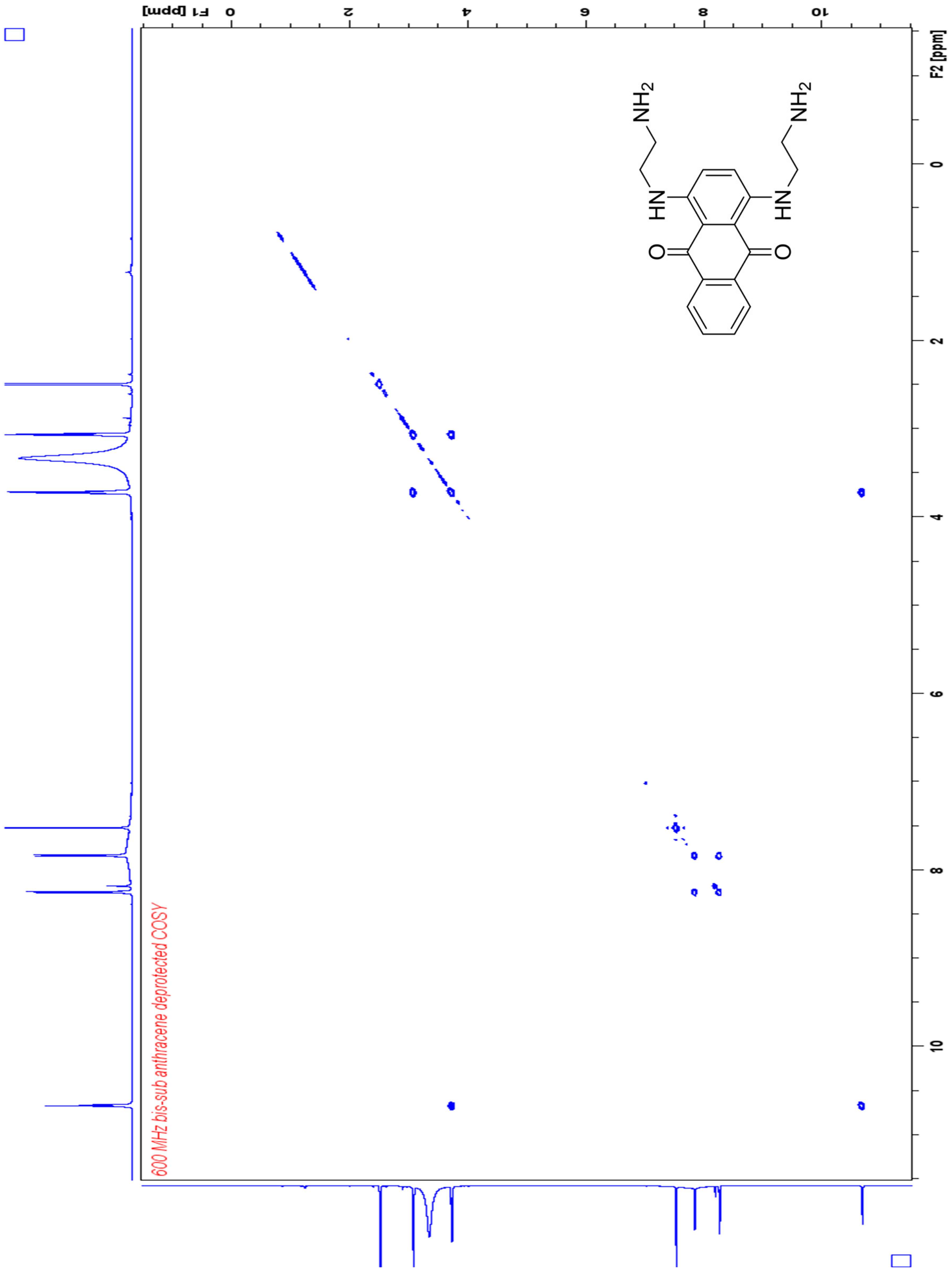

^{1}**H NMR of 2-6** (contains trace amounts of *N,N'*-dicyclohexylurea)

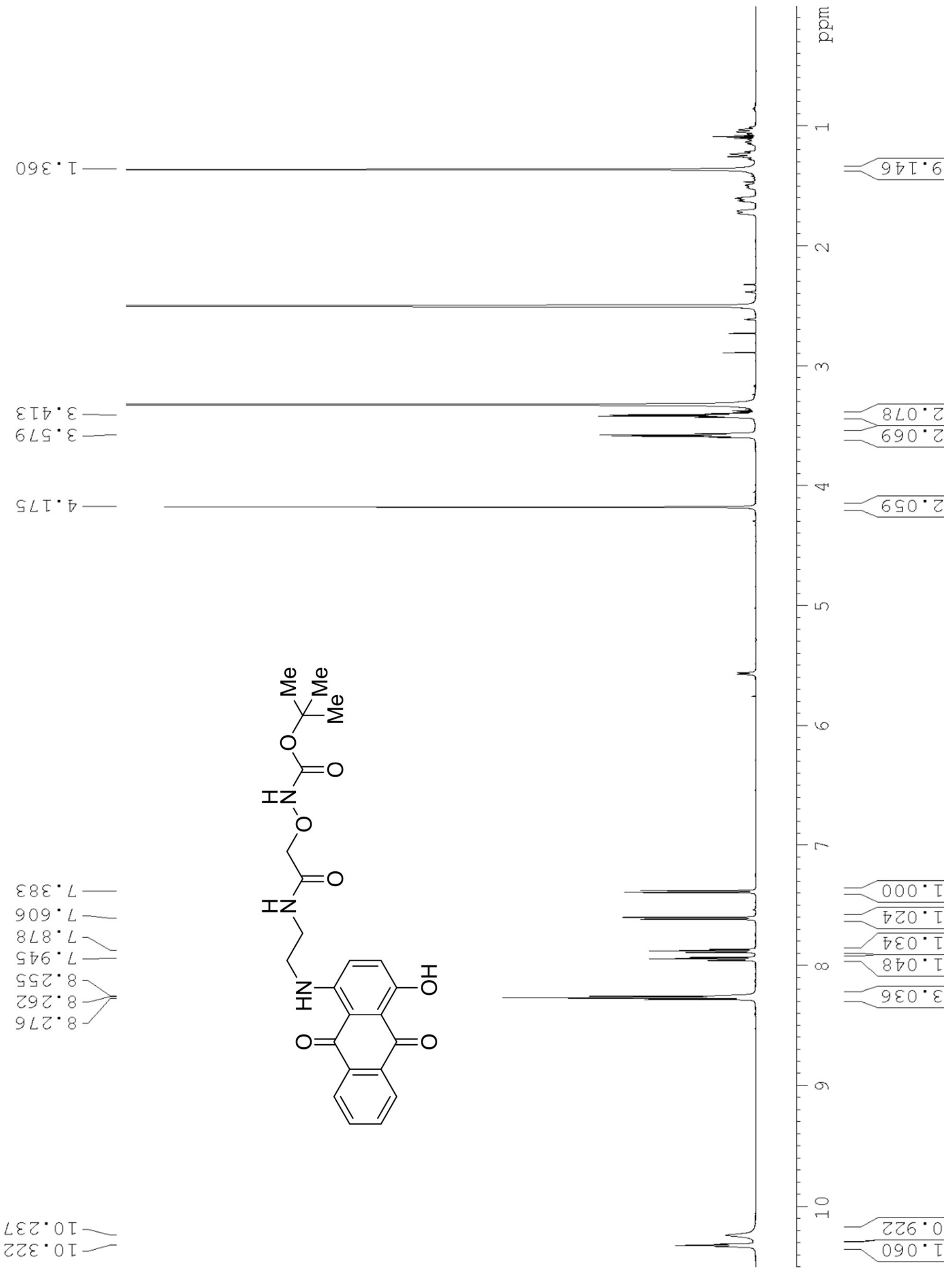

^{13}C NMR of 2-6 (contains trace amounts of *N,N'*-dicyclohexylurea)

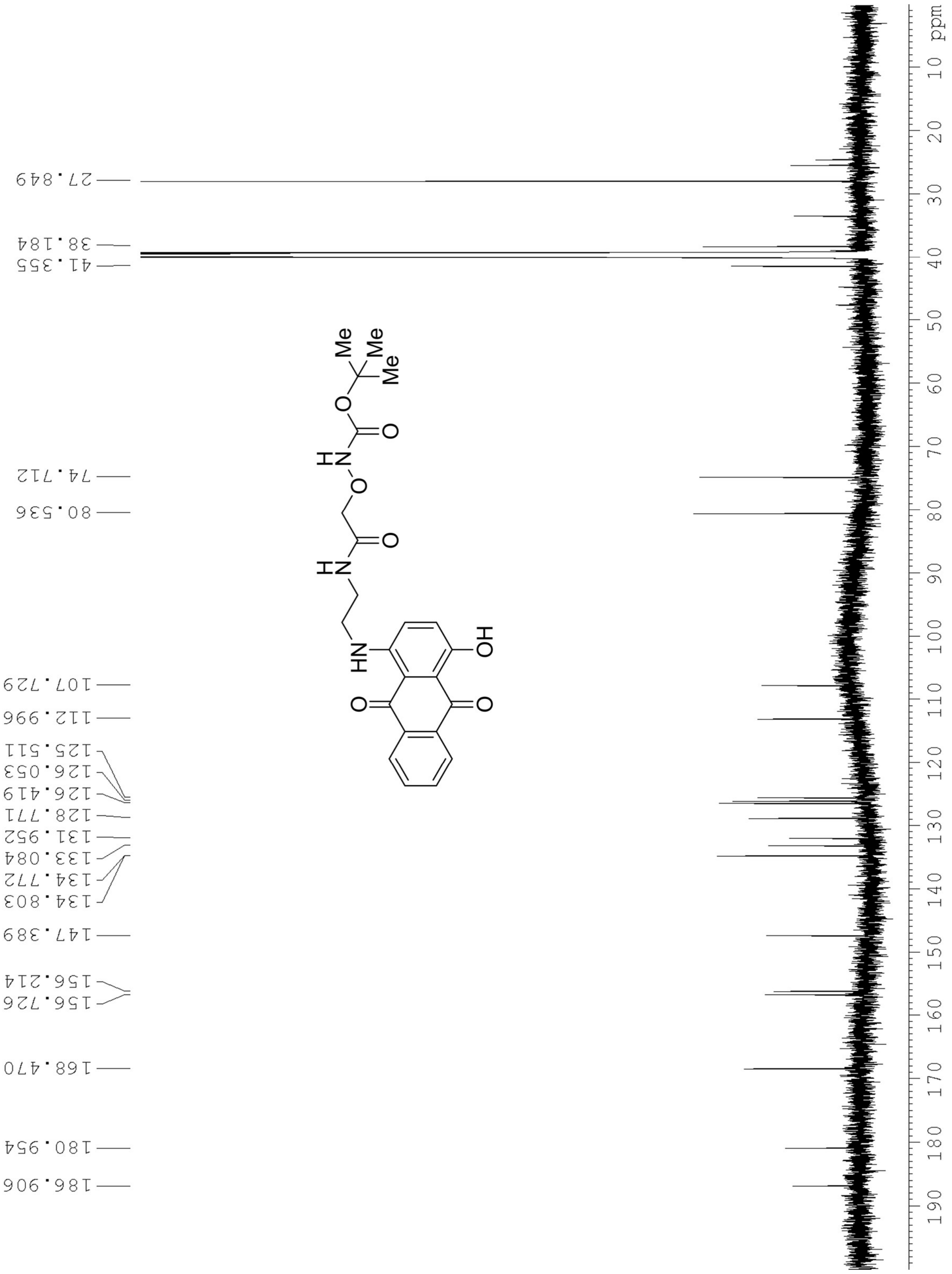

HSQC NMR of 2-6 (contains trace amounts of *N,N'*-dicyclohexylurea)

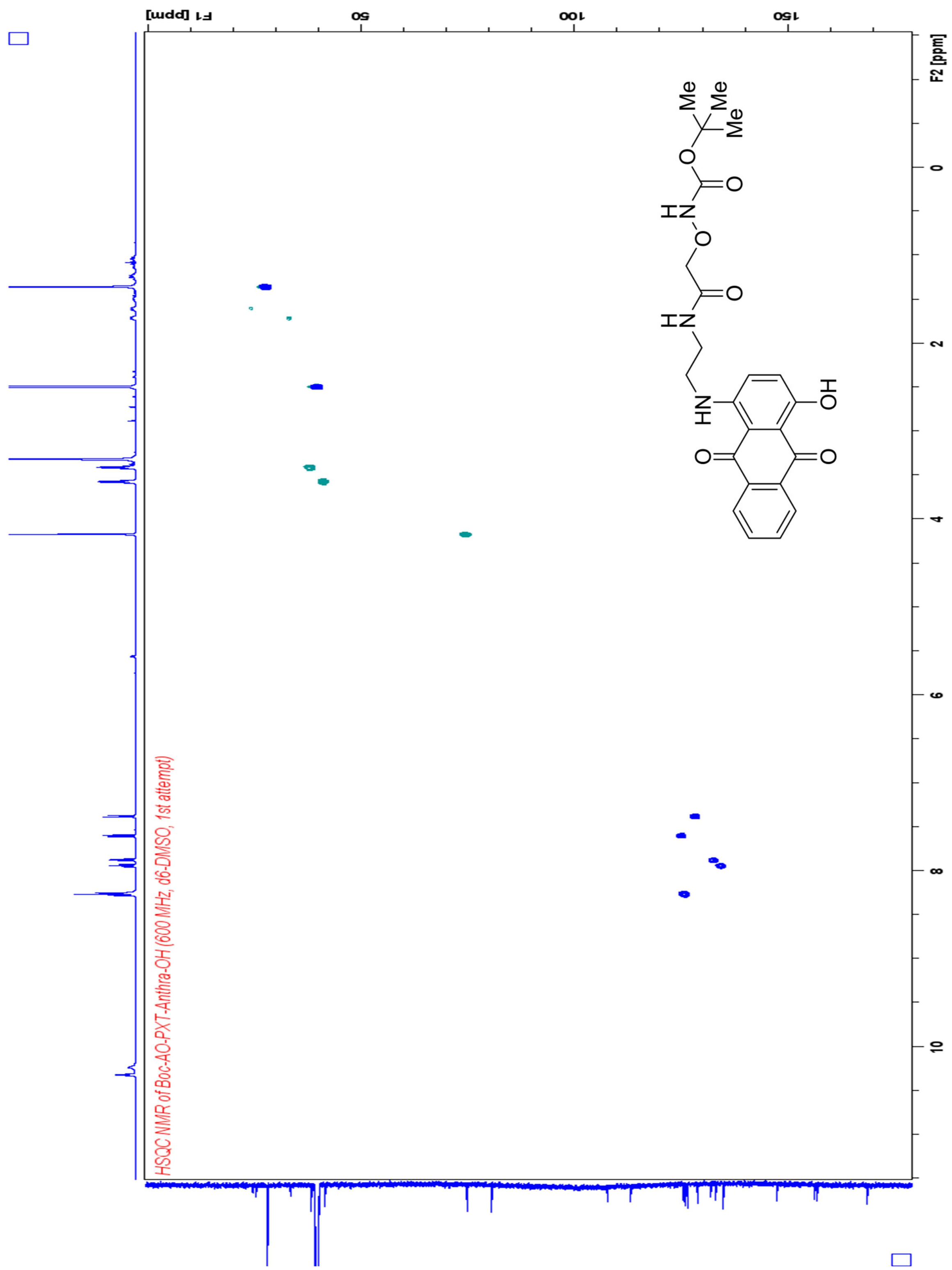

HMBC NMR of 2-6 (contains trace amounts of *N,N'*-dicyclohexylurea)

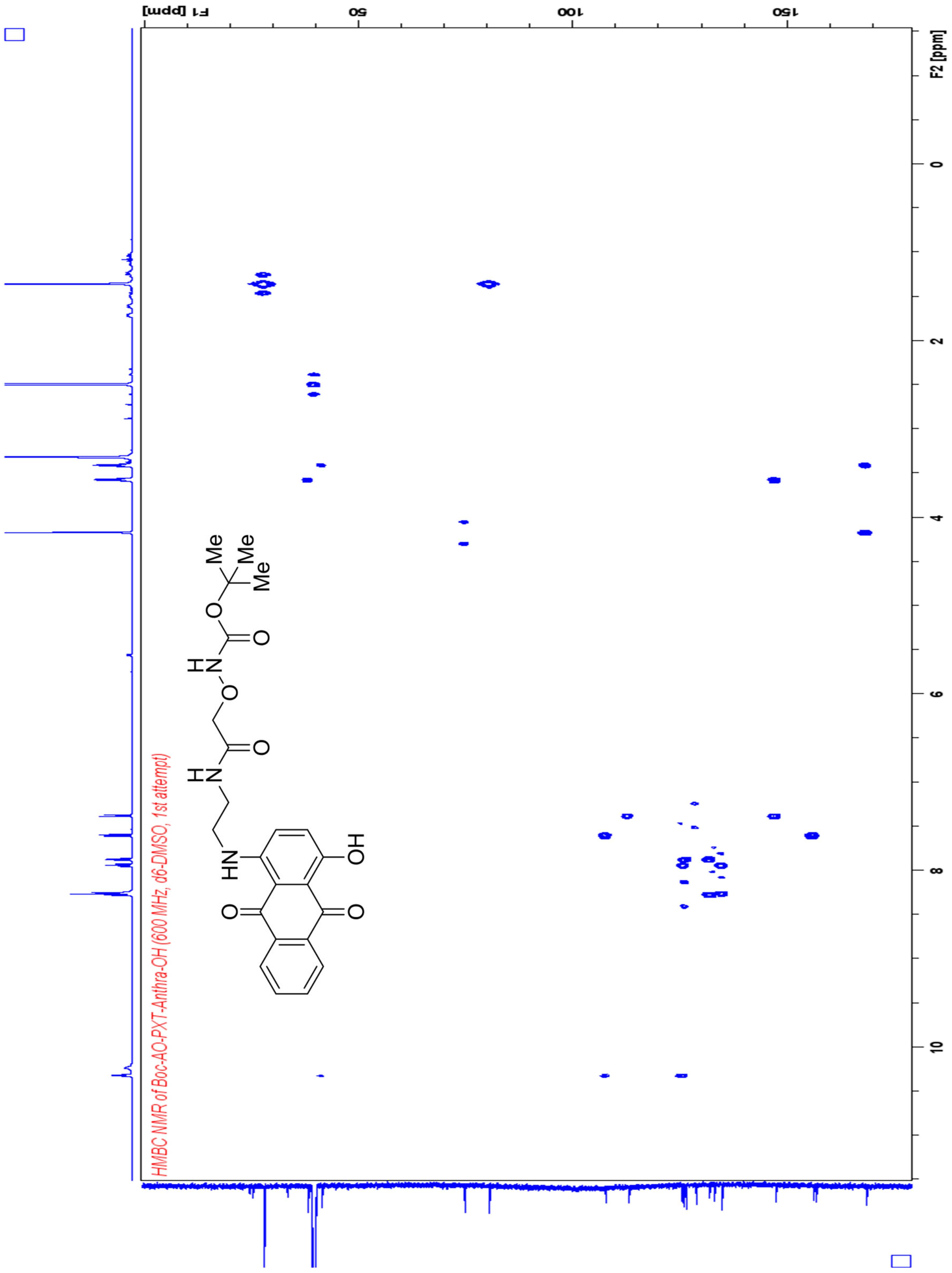

COSY NMR of 2-6 (contains trace amounts of *N,N'*-dicyclohexylurea)

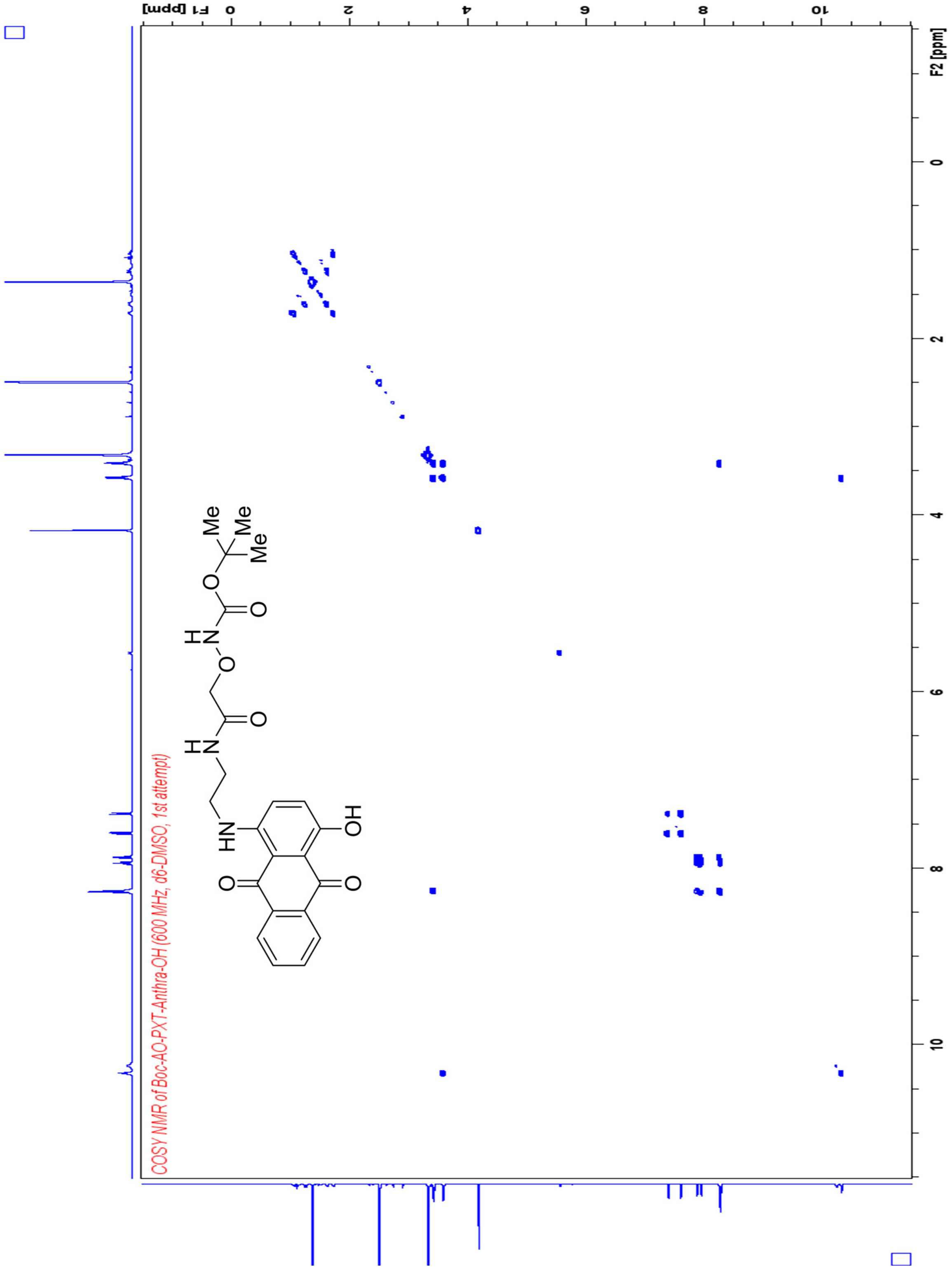

^{1}H NMR of 2-9

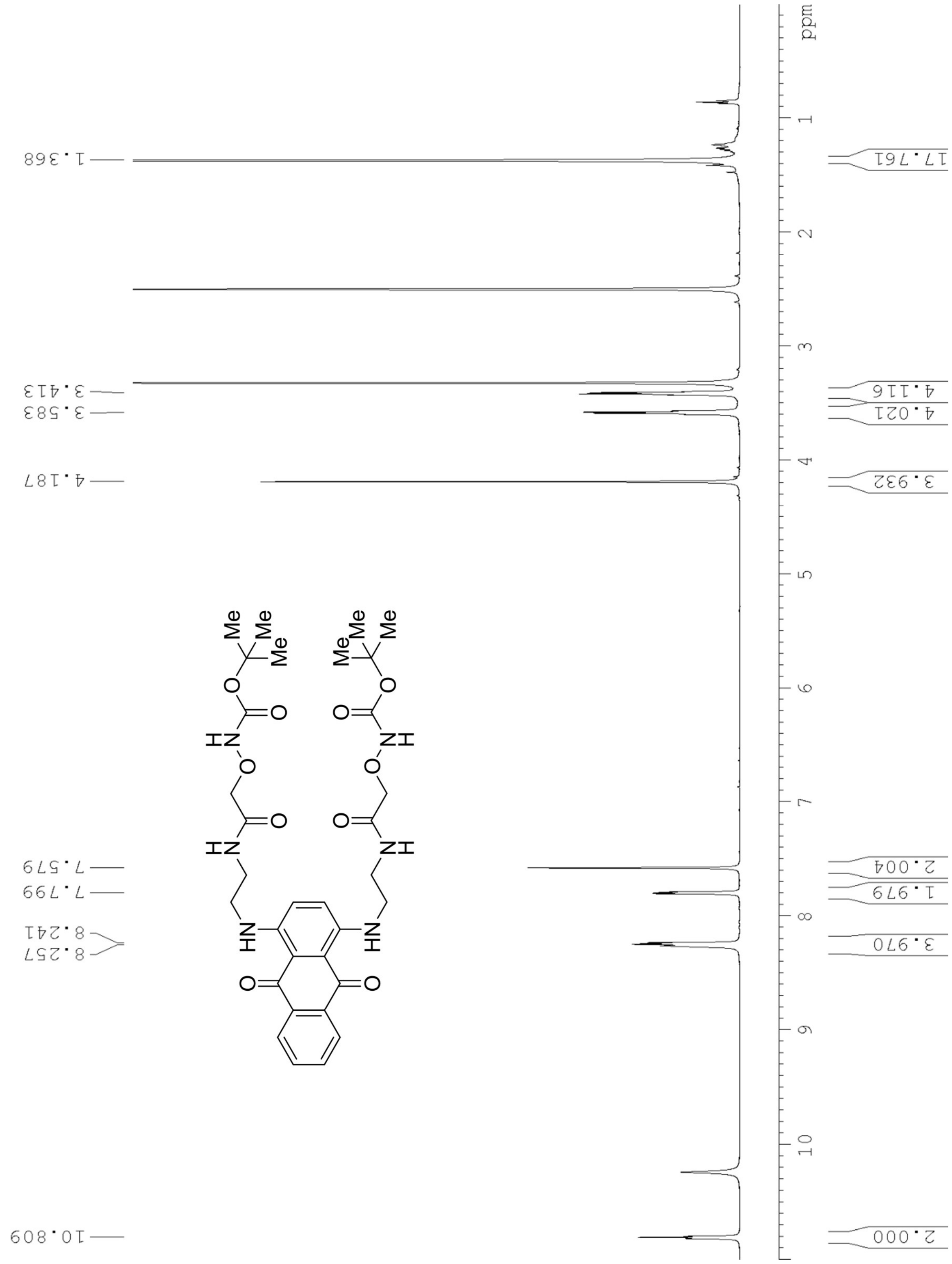
1.368
3.413
3.583
4.187
7.579
7.799
8.241
8.257
10.809
17.761
4.116
4.021
3.932
2.004
1.979
3.970
2.000
ppm
1
2
3
4
5
6
7
8
9
10
Me
Me
Me
O
O
NH
O
O
NH
HN
O
O

^{13}C NMR of 2-9

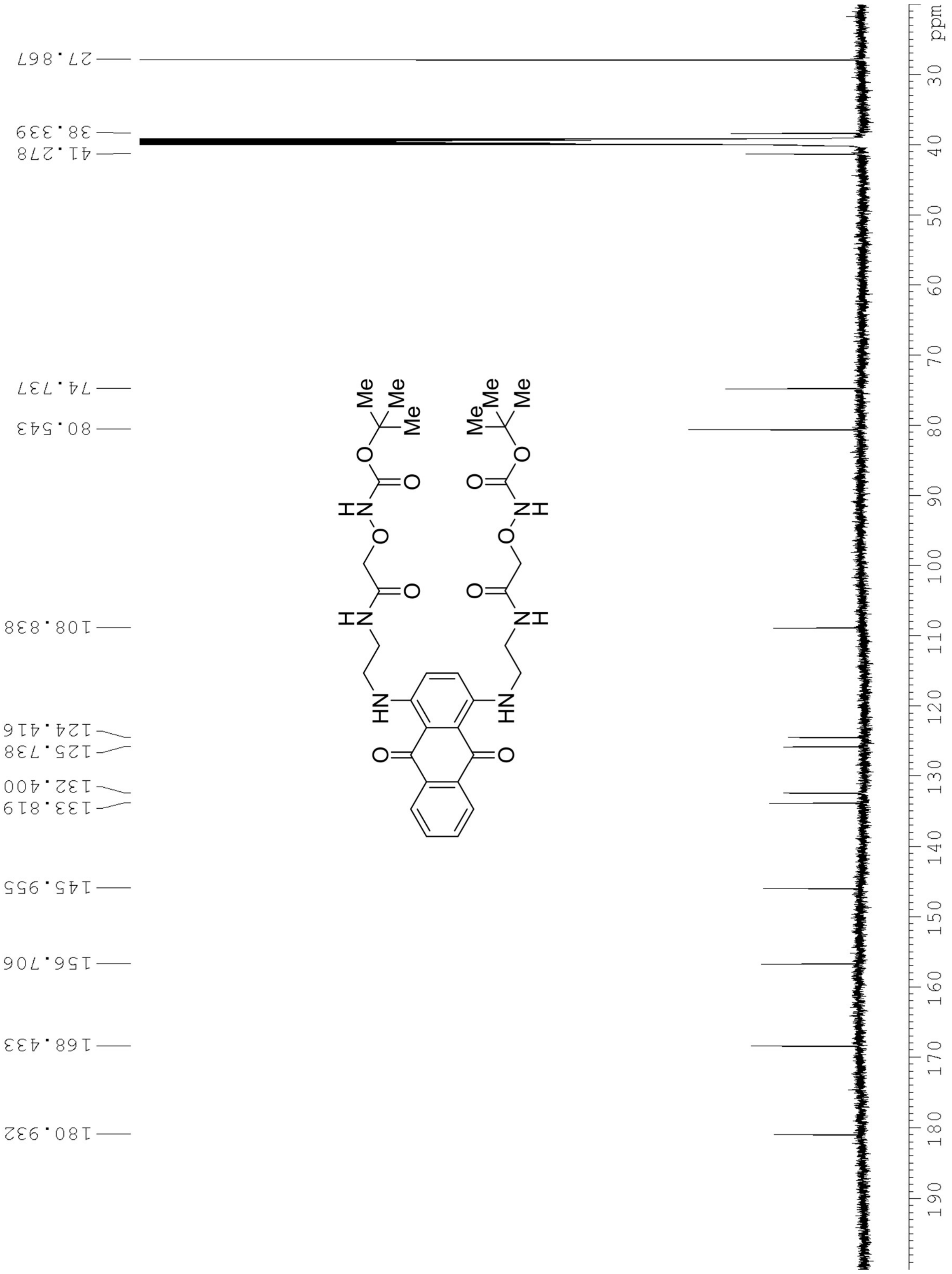

27.867
38.339
41.278
74.737
80.543
108.838
124.416
125.738
132.400
133.819
145.955
156.706
168.433
180.932
ppm
30
40
50
60
70
80
90
100
110
120
130
140
150
160
170
180
190
Me
O
NH
HN

HSQC NMR of 2-9

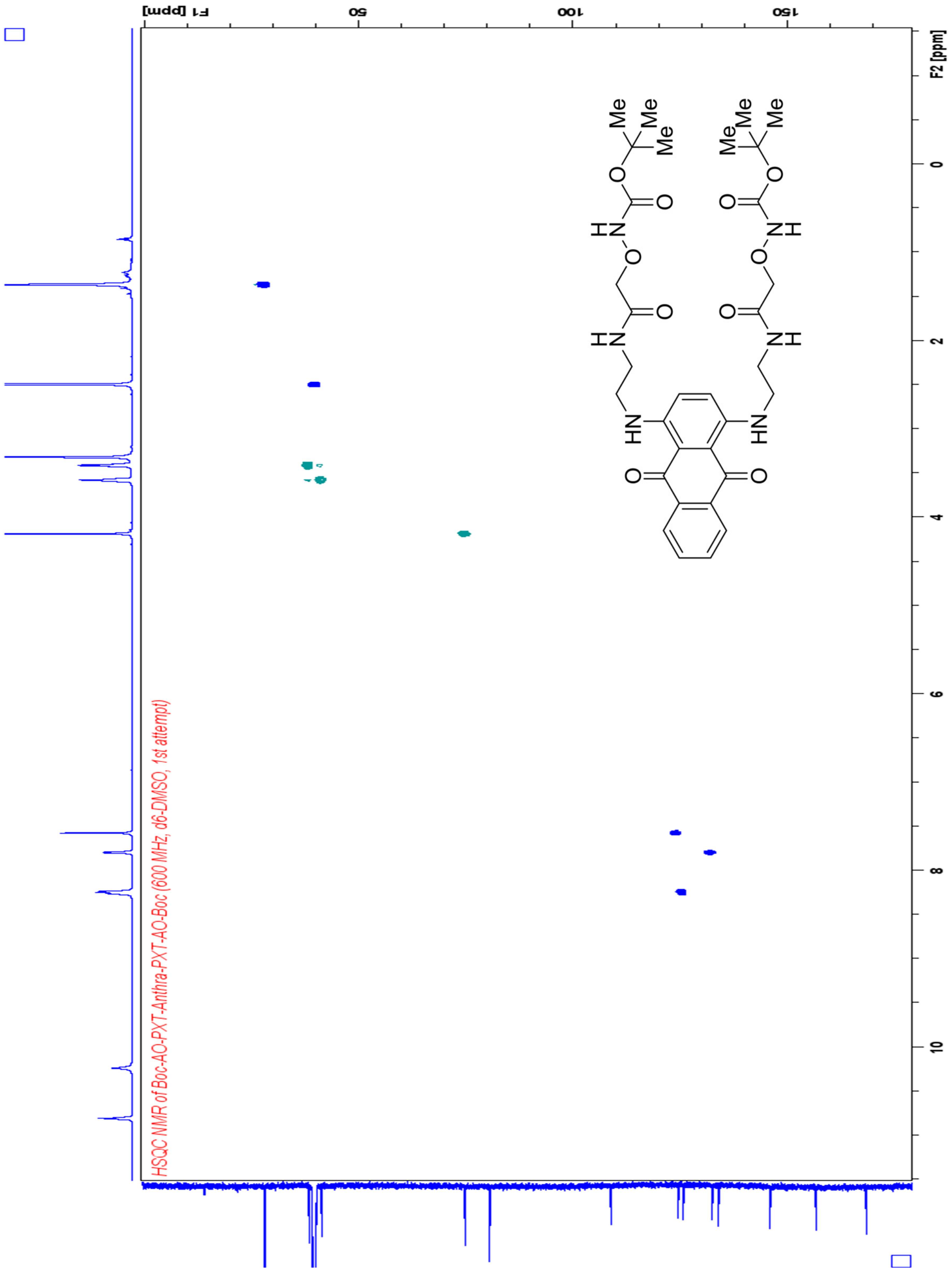

HMBC NMR of 2-9

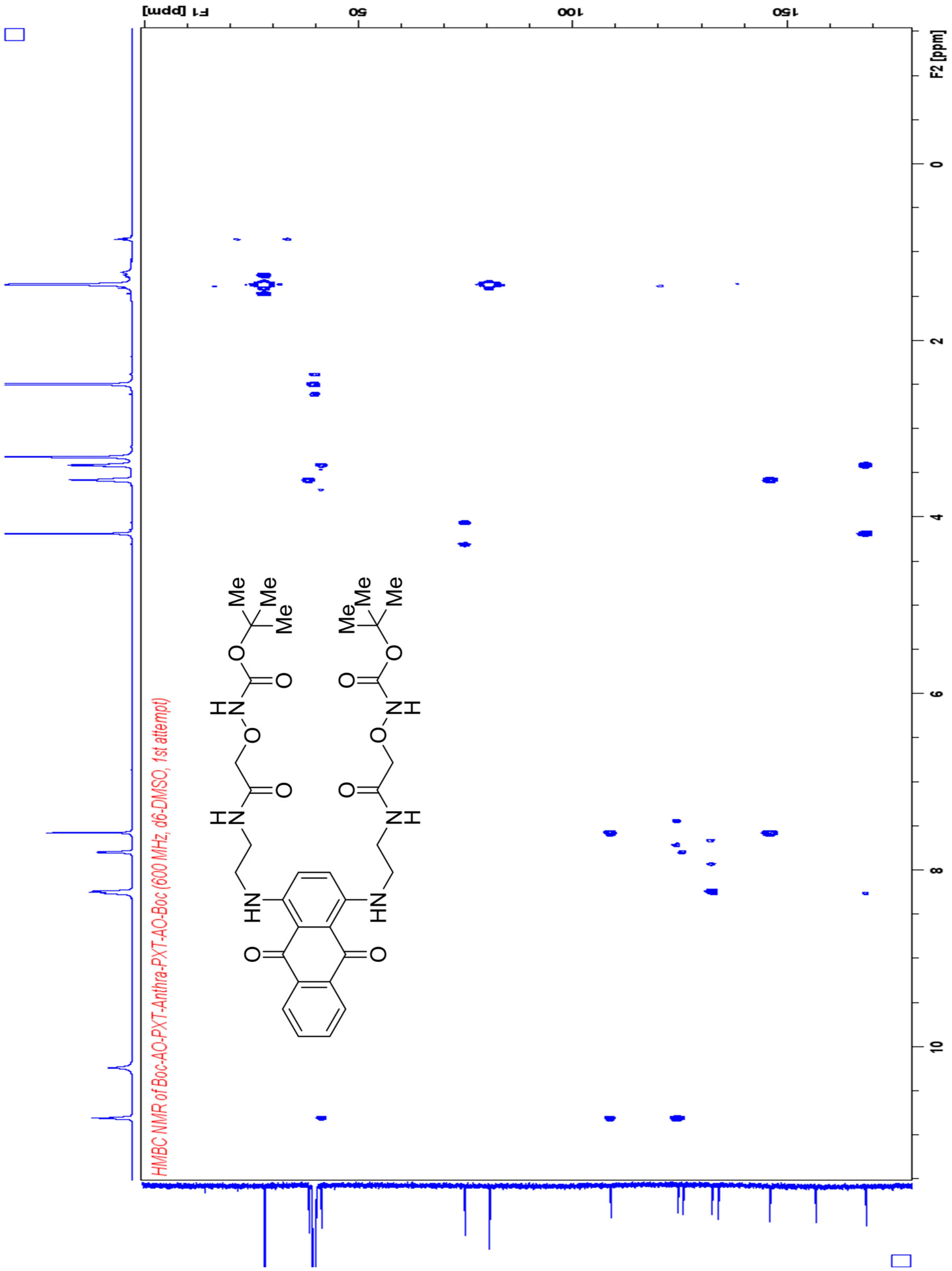

COSY NMR of 2-9

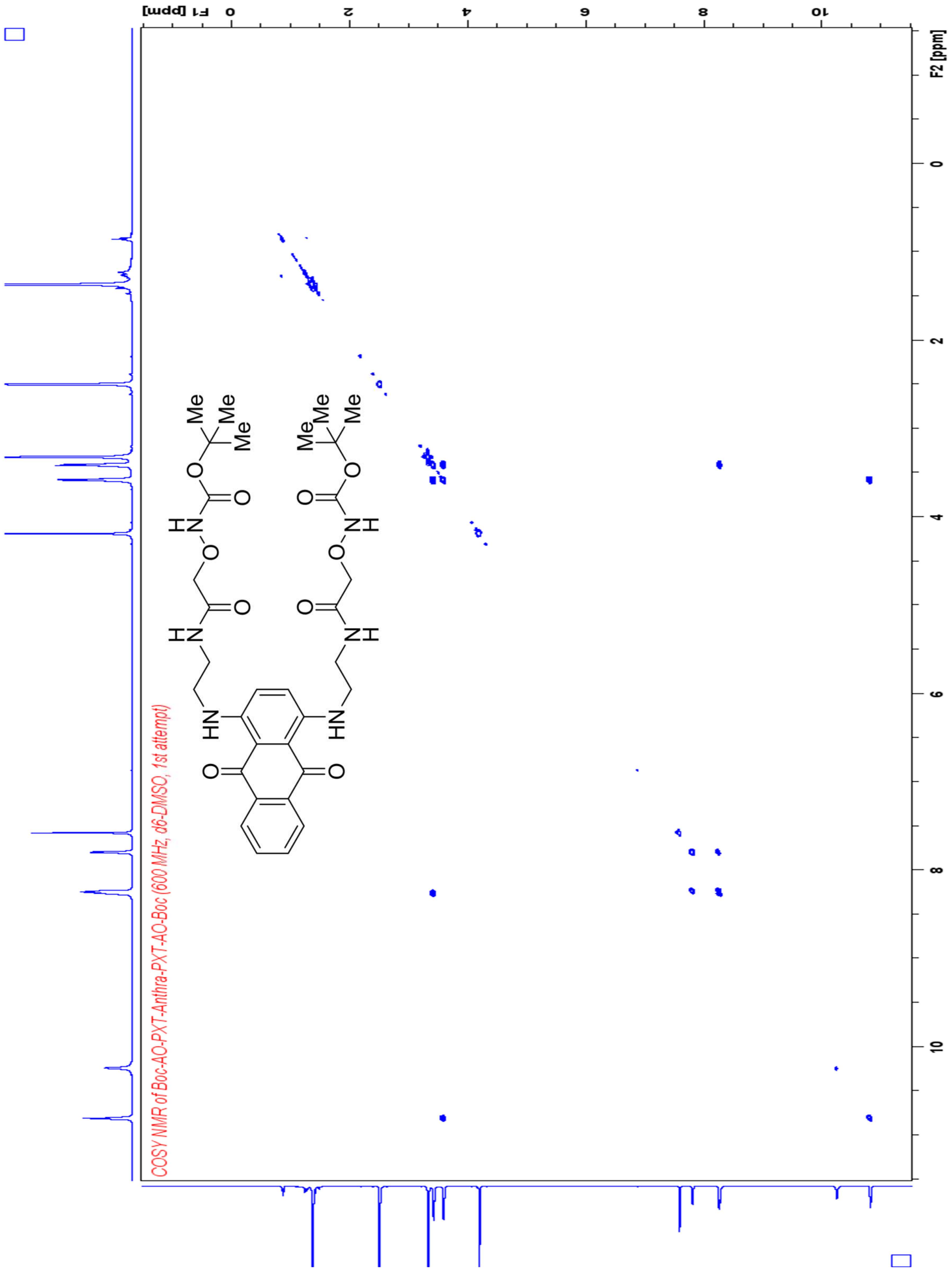

^{1}H NMR of 2-1

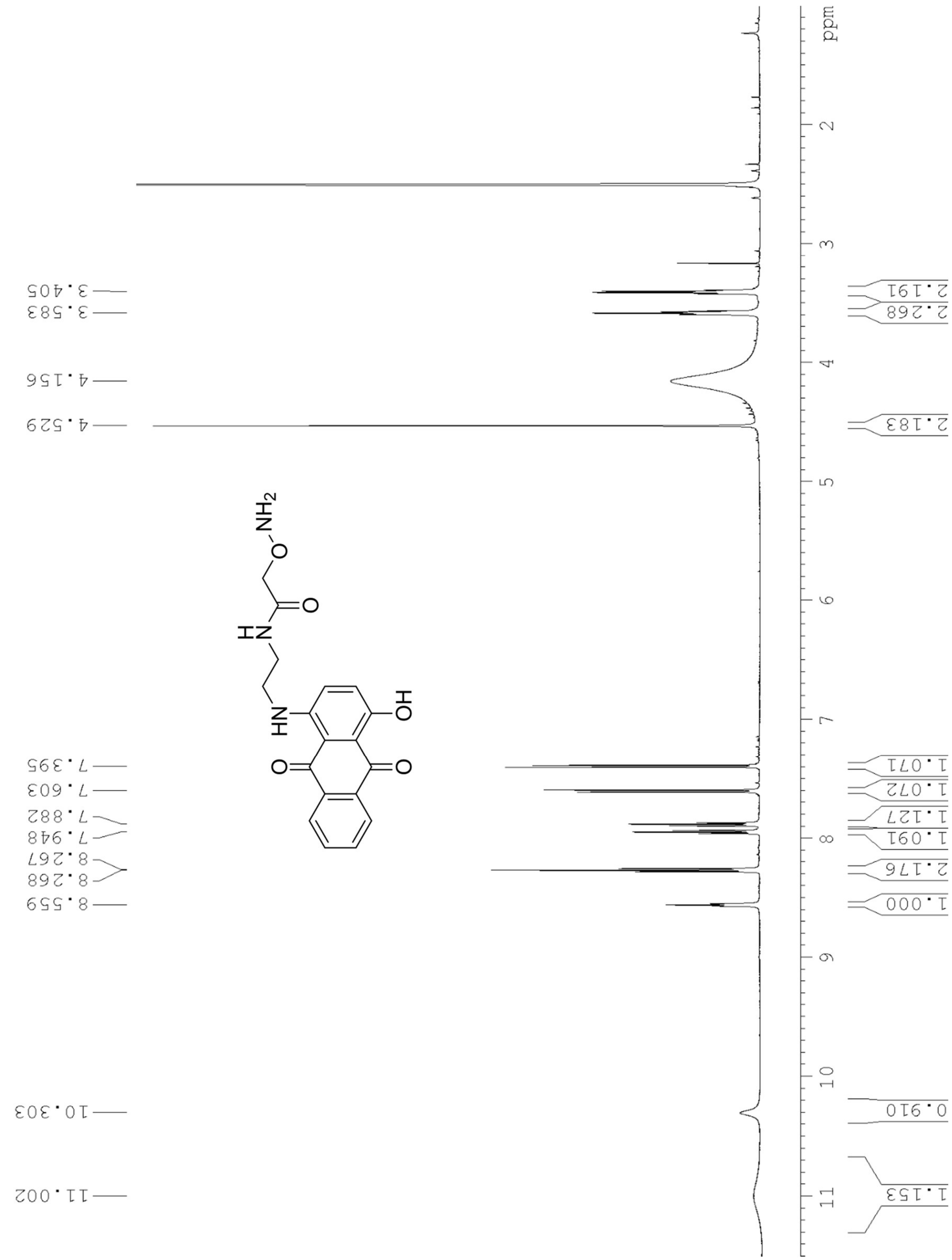

3.405
3.583
4.156
4.529
7.395
7.603
7.882
7.948
8.267
8.268
8.559
10.303
11.002
2.191
2.268
2.183
1.071
1.072
1.127
1.091
2.176
1.000
0.910
1.153
ppm
2
3
4
5
6
7
8
9
10
11
NH2
O
H
N
HN
OH

^{13}C NMR of 2-1

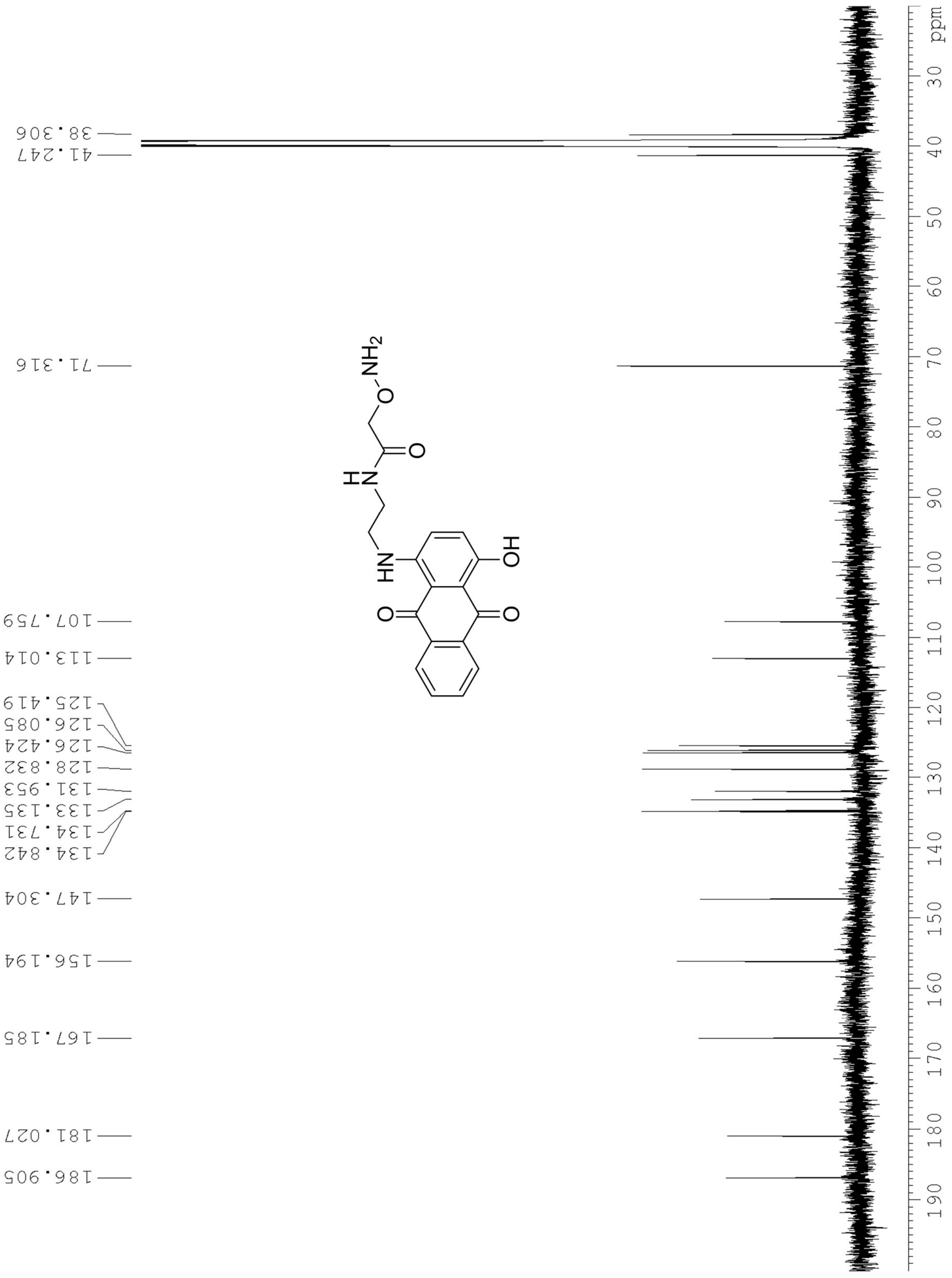

38.306
41.247
71.316
107.759
113.014
125.419
126.085
126.424
128.832
131.953
133.135
134.731
134.842
147.304
156.194
167.185
181.027
186.905
ppm
30
40
50
60
70
80
90
100
110
120
130
140
150
160
170
180
190
NH2
O
H
N
O
HN
OH
O
O

HSQC NMR of 2-1

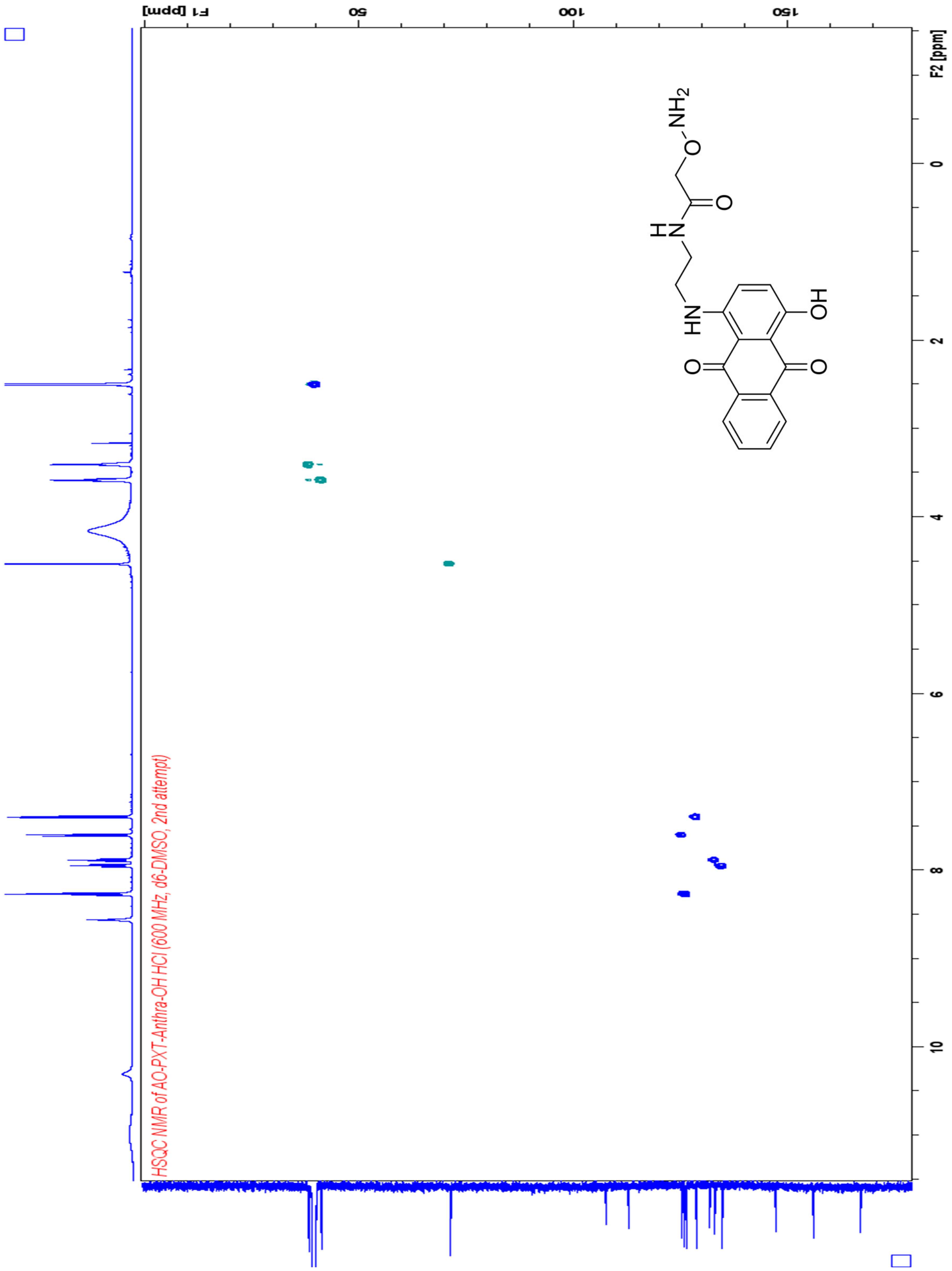

HMBC NMR of 2-1

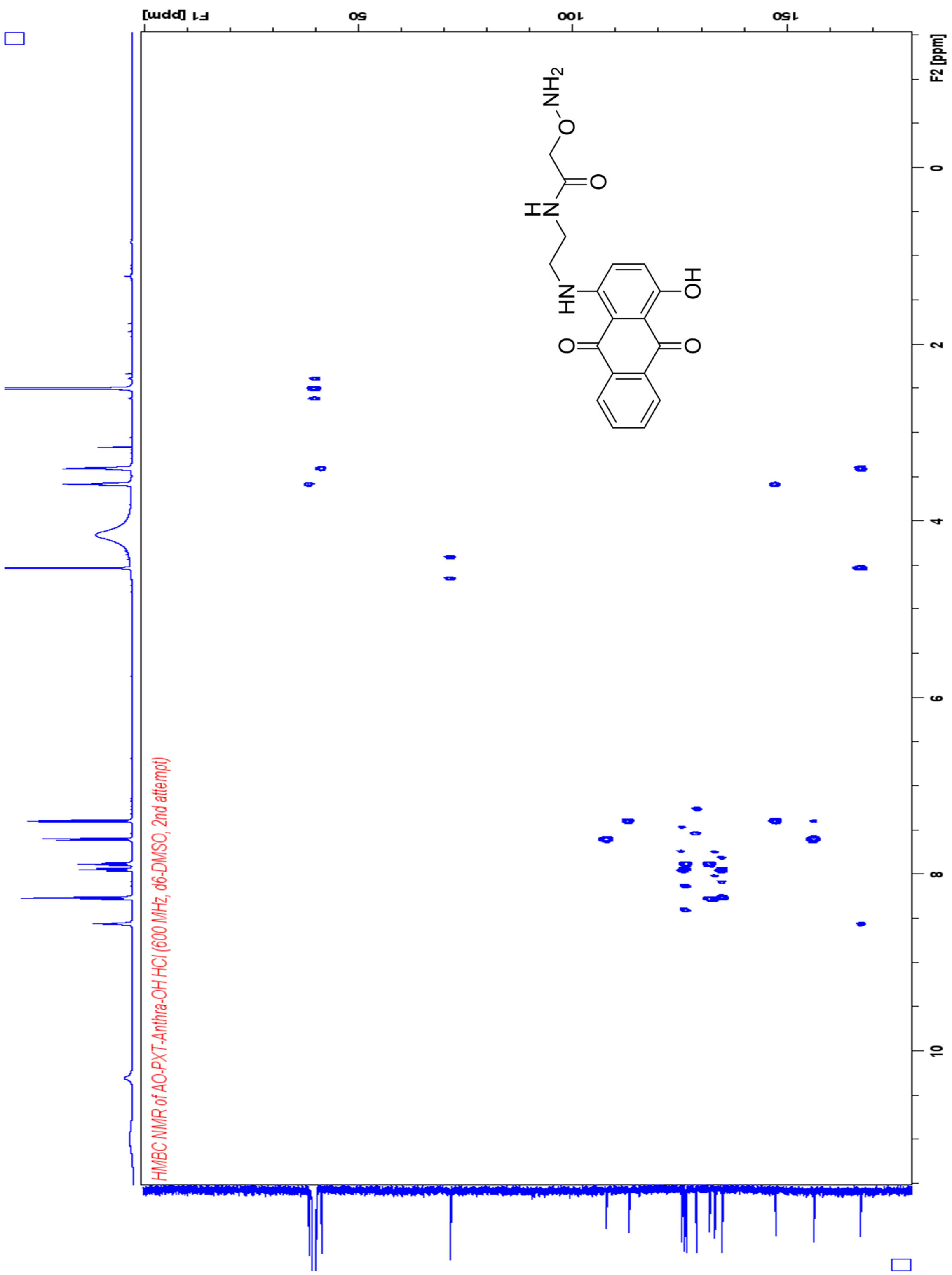

COSY NMR of 2-1

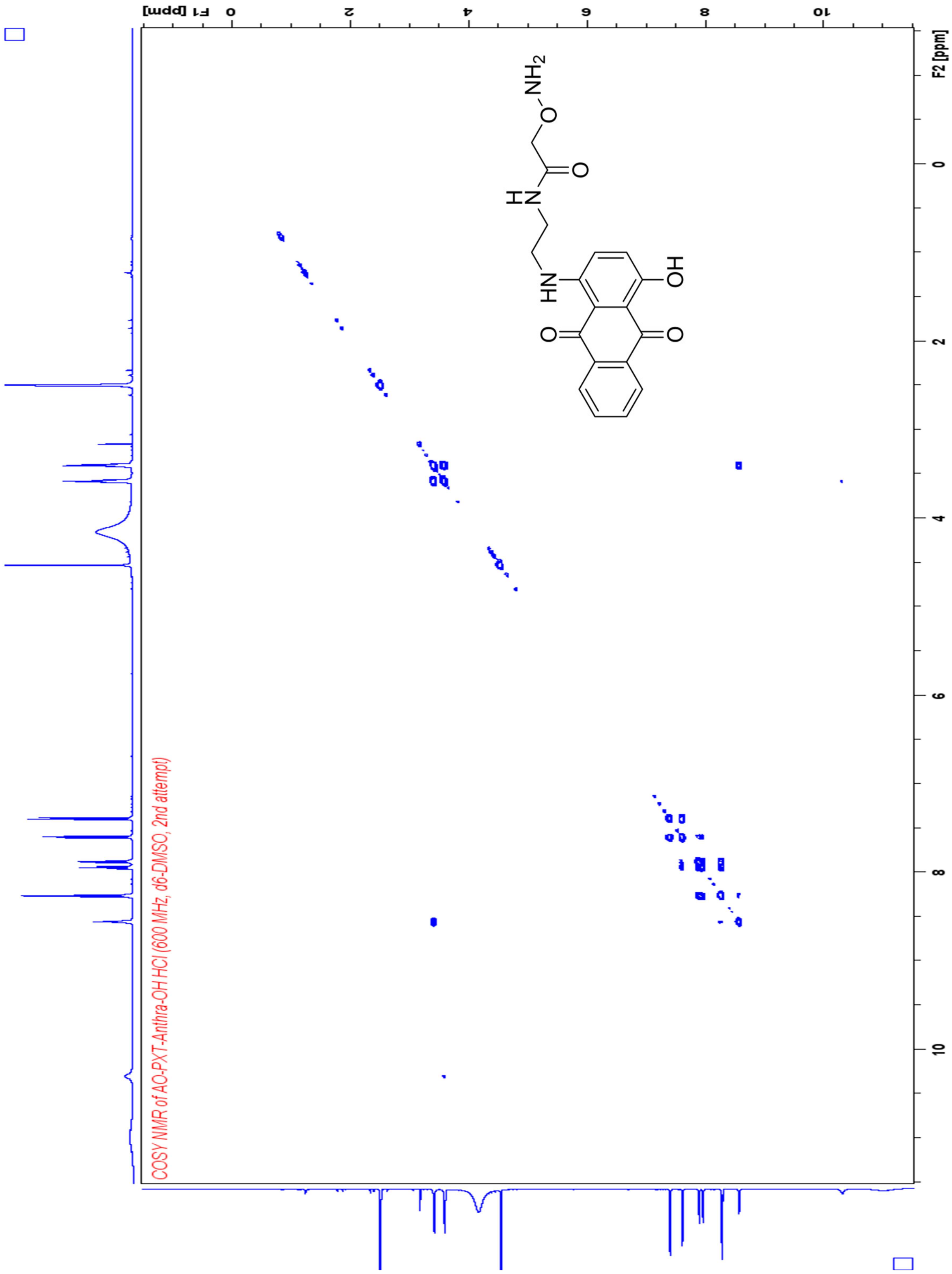

^{1}H NMR of 2-2

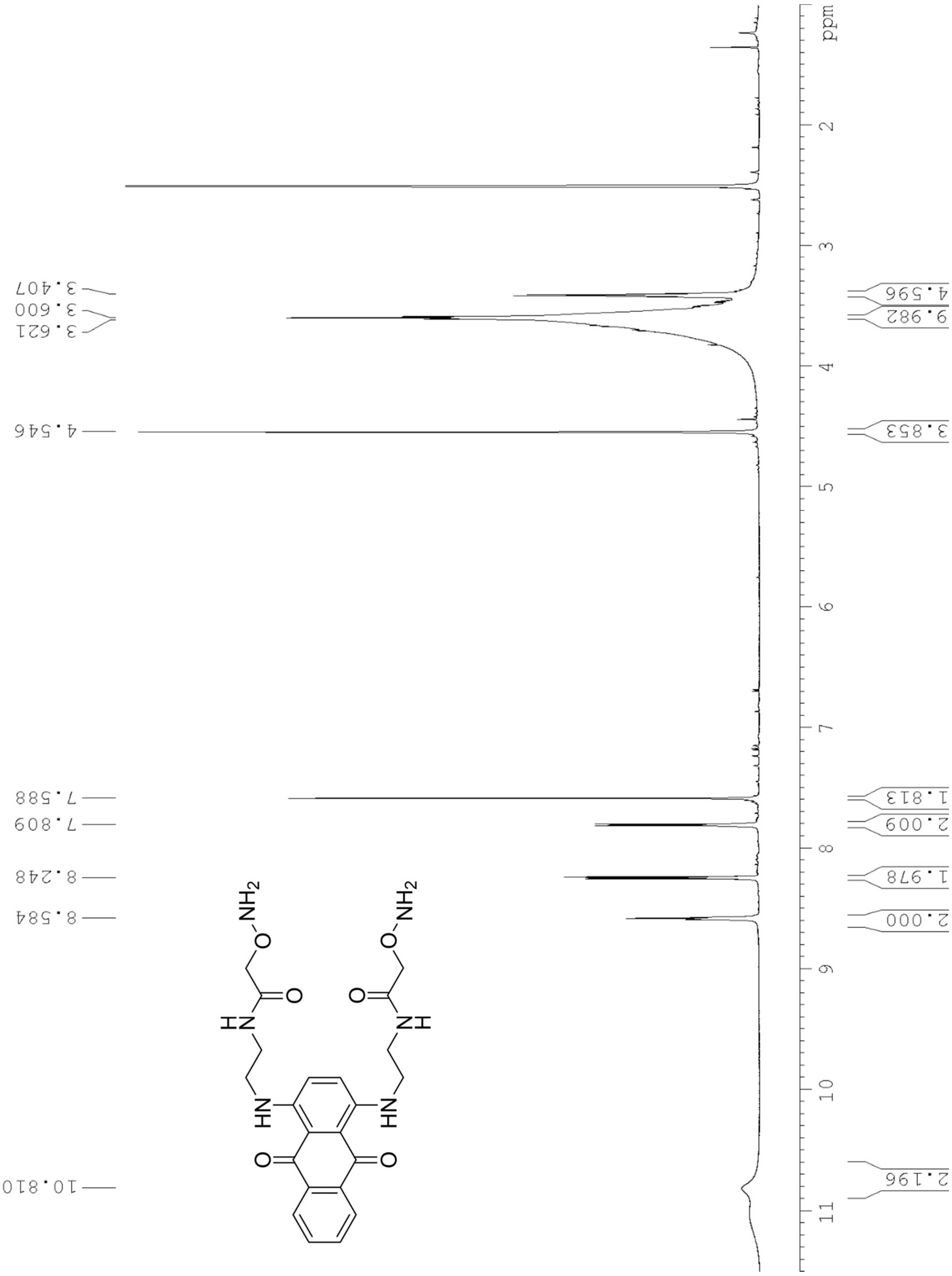
3.407
3.600
3.621
4.546
7.588
7.809
8.248
8.584
10.810
4.596
9.982
3.853
1.813
2.009
1.978
2.000
2.196
ppm
2
3
4
5
6
7
8
9
10
11
NH$_2$
O
HN
NH
O

^{13}C NMR of 2-2

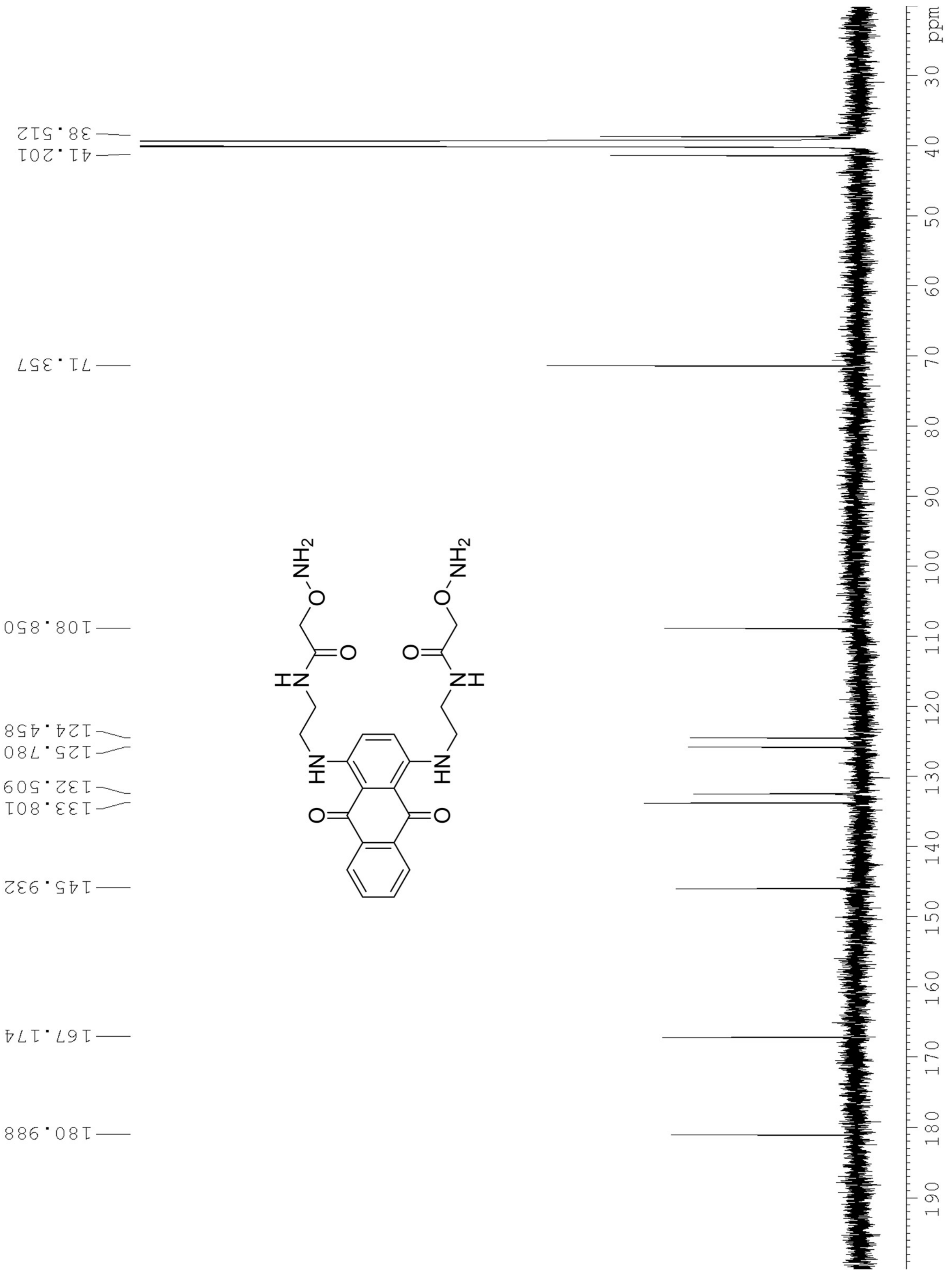

38.512
41.201
71.357
108.850
124.458
125.780
132.509
133.801
145.932
167.174
180.988
ppm
30
40
50
60
70
80
90
100
110
120
130
140
150
160
170
180
190
NH2
O
HN
NH
HN
NH
O
O
O
O
O
NH2

HSQC NMR of 2-2

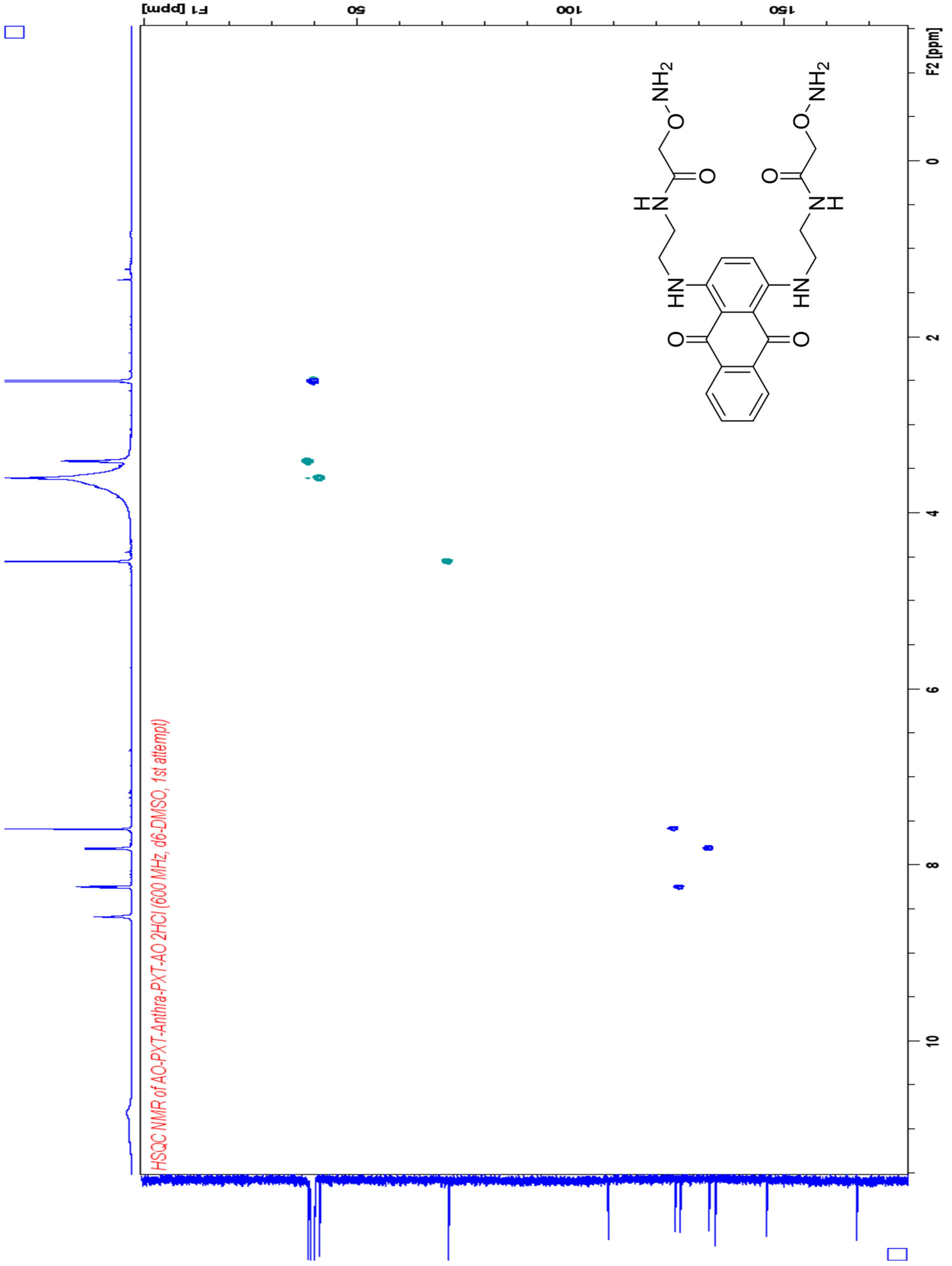

HMBC NMR of 2-2

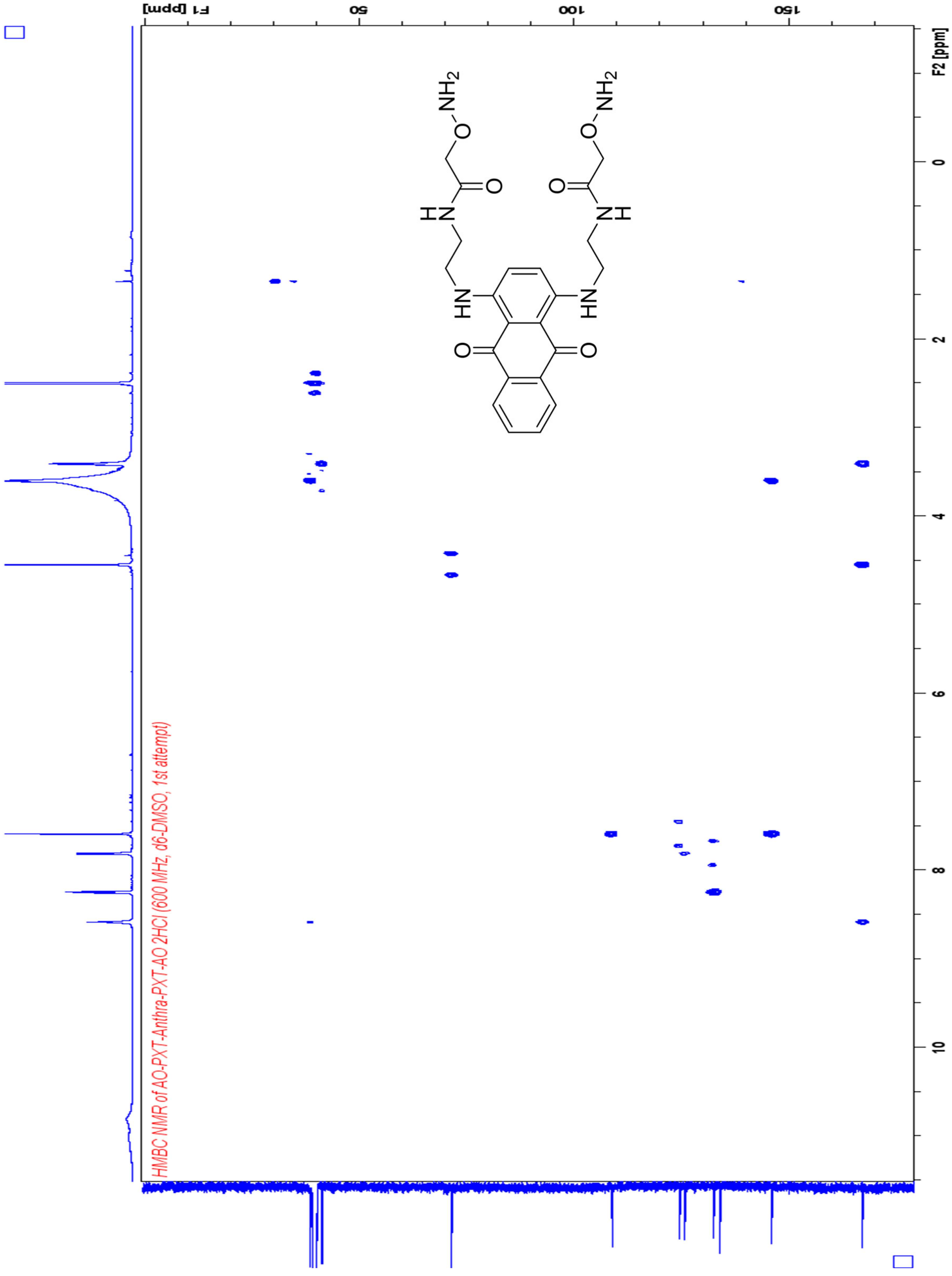

COSY NMR of 2-2

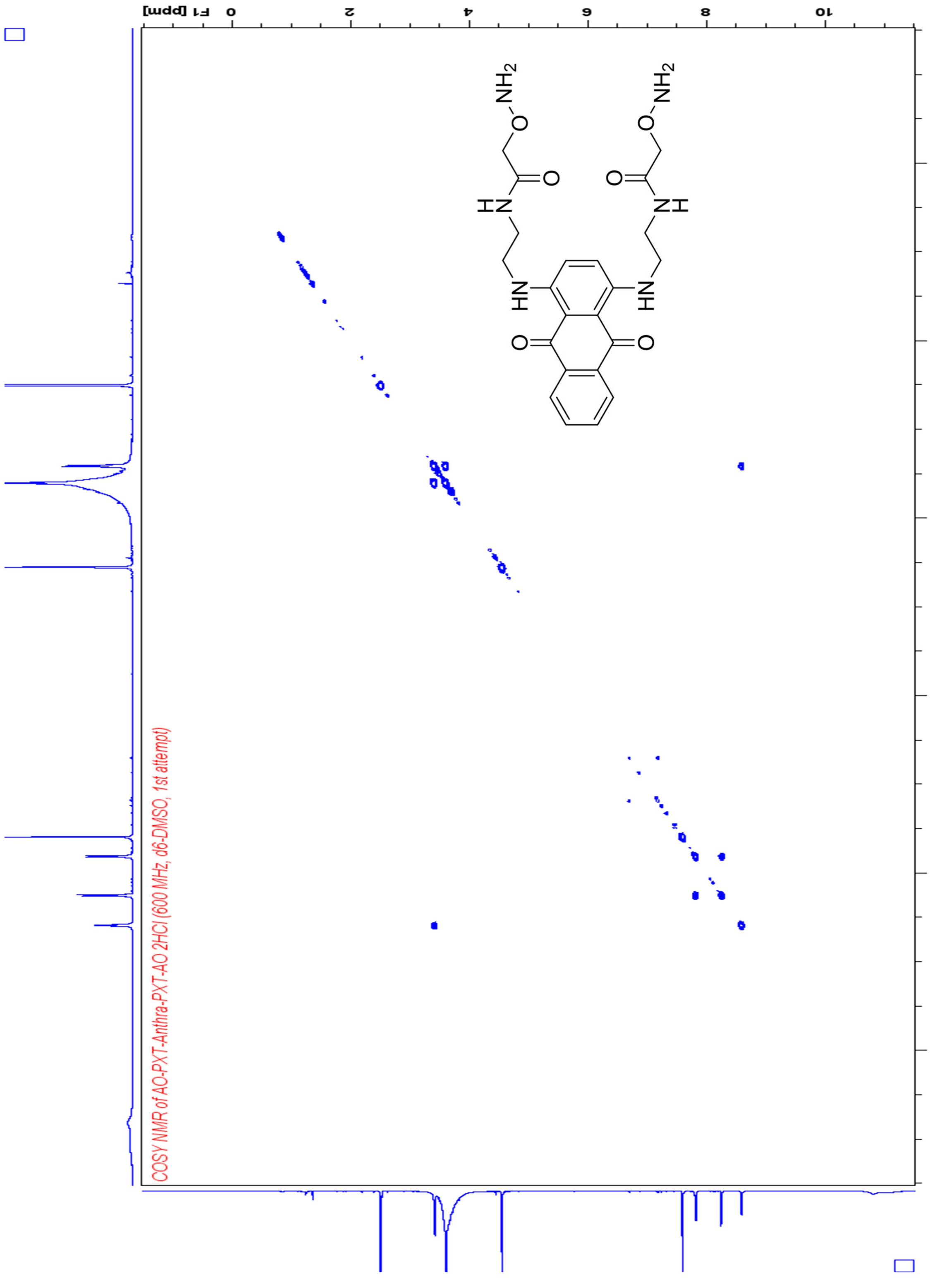

Appendix II

ESI/MS^2 Spectra for Chapter 2

ESI/MS^2 of 2-4

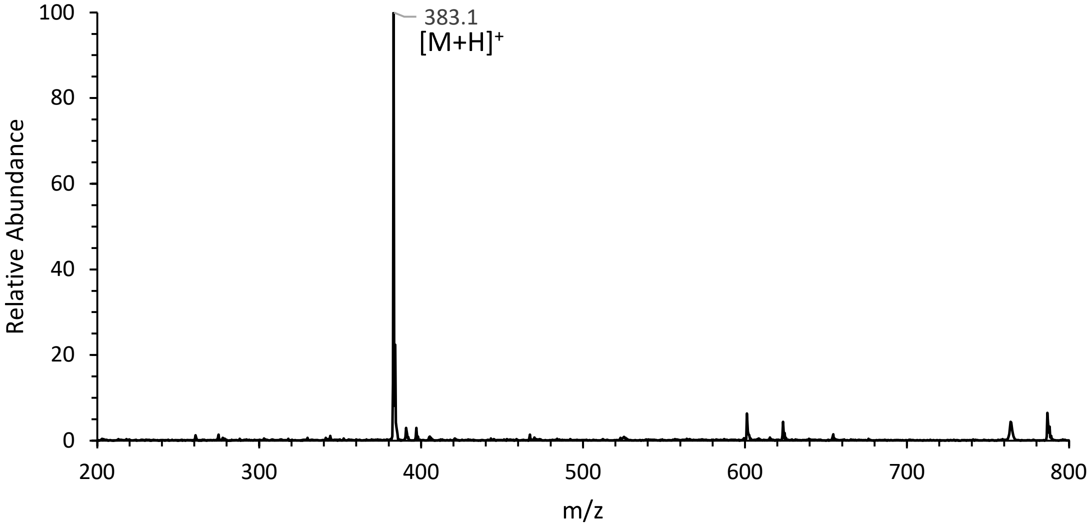

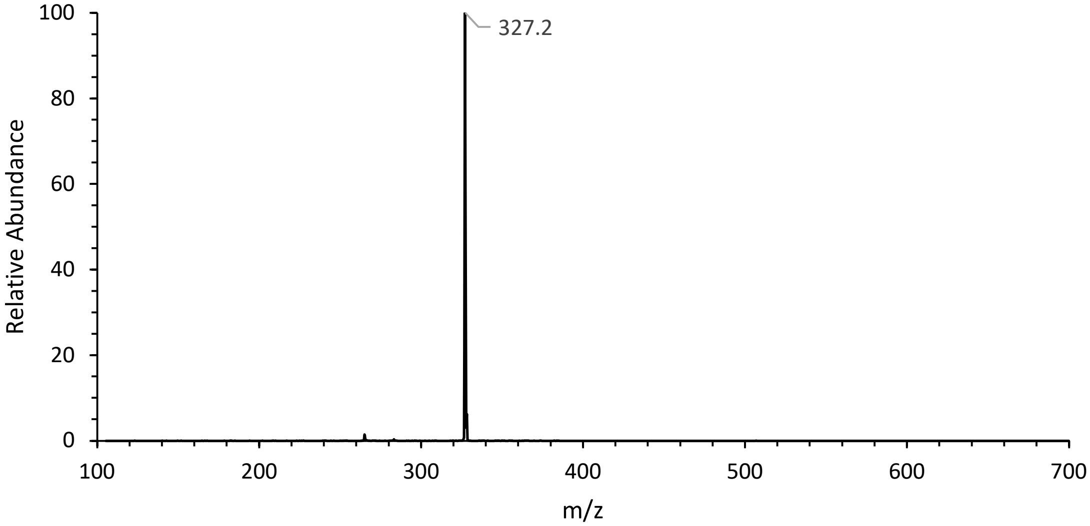

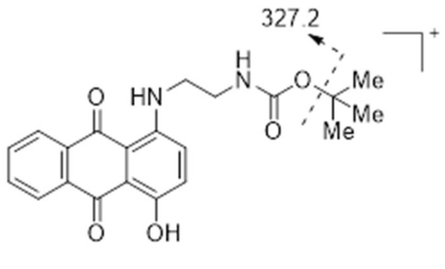

m/z **383.1**

ESI/MS^2 of 2-7

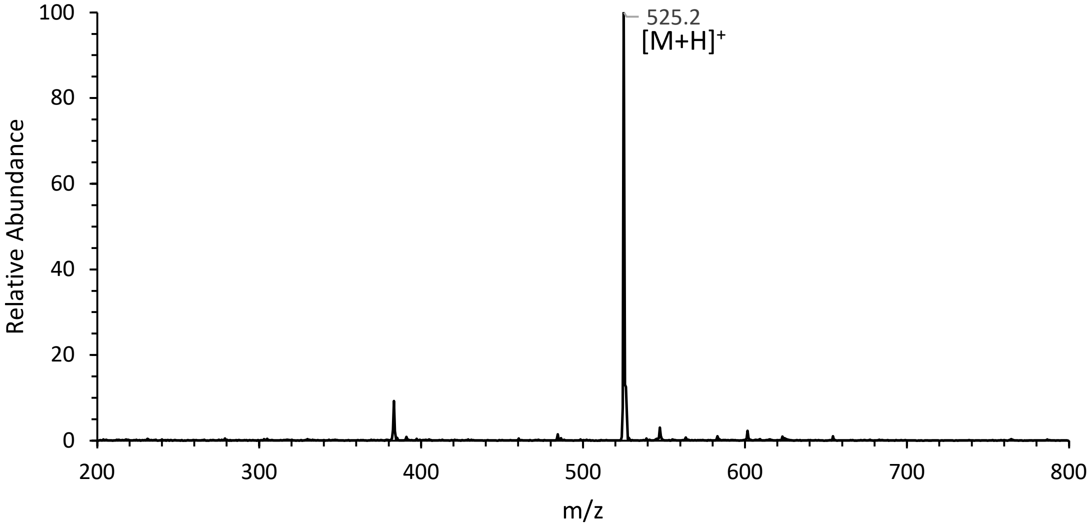

525.2
[M+H]+
Relative Abundance
0
20
40
60
80
100
200
300
400
500
600
700
800
m/z

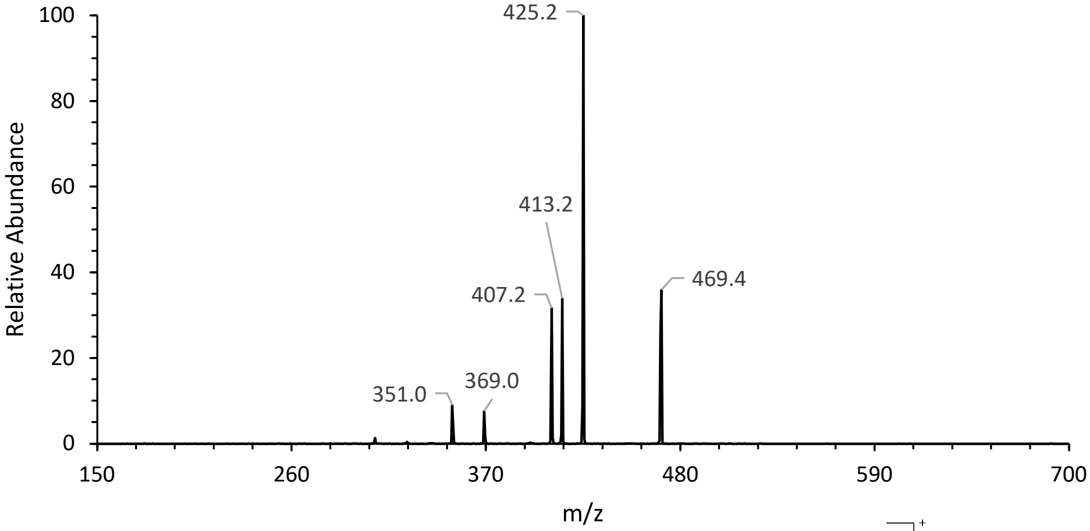

425.2
413.2
407.2
469.4
351.0
369.0
Relative Abundance
0
20
40
60
80
100
150
260
370
480
590
700
m/z

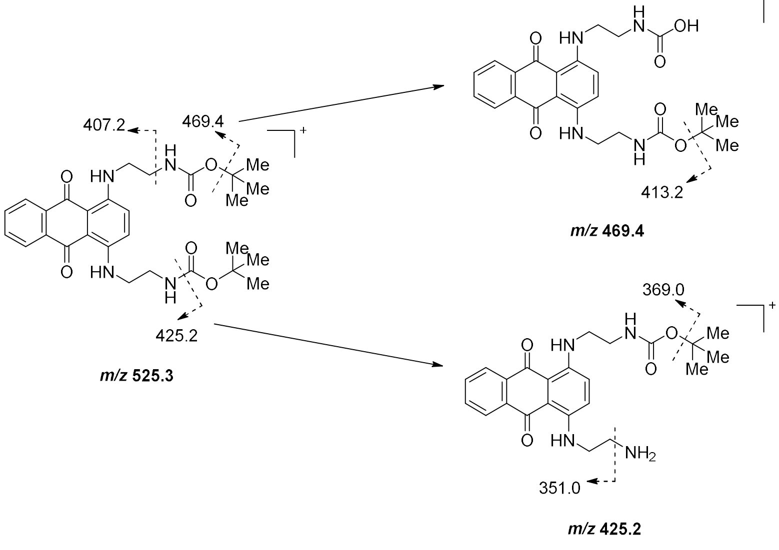

407.2
469.4
425.2
413.2
369.0
351.0
m/z 525.3
m/z 469.4
m/z 425.2

ESI/MS^2 of 2-5

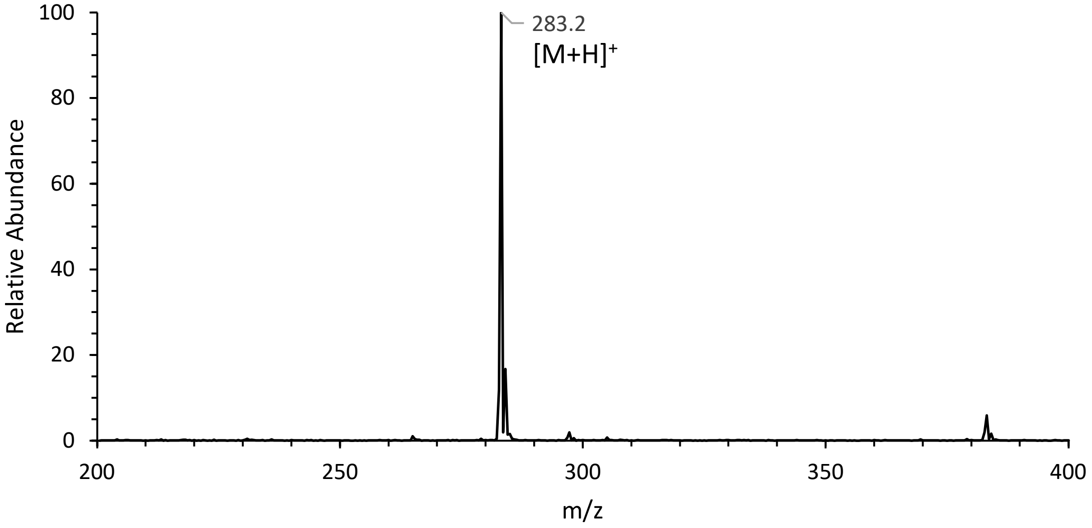

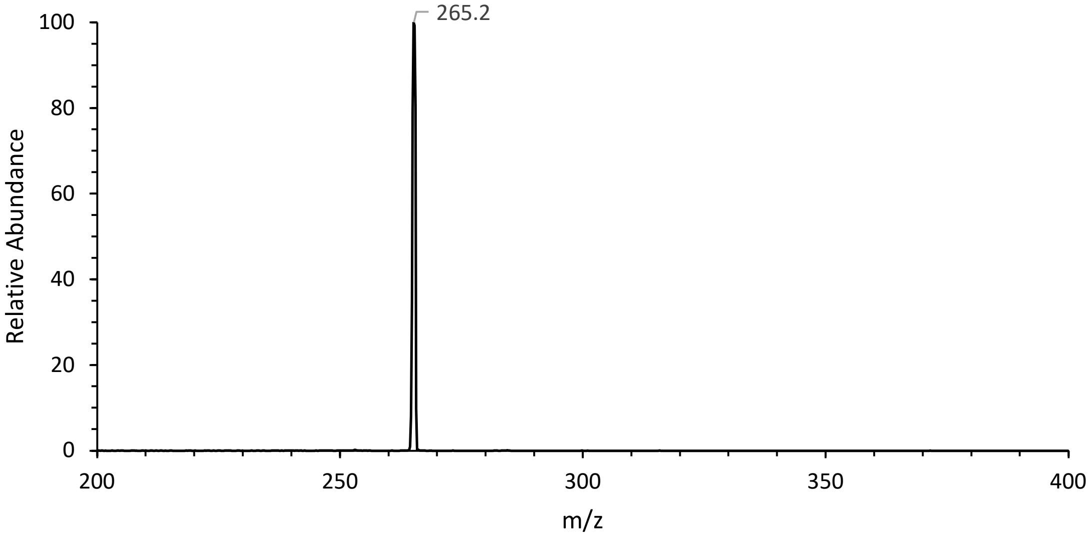

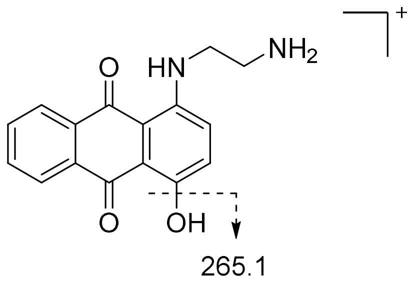

***m/z* 283.1**

ESI/MS^2 of 2-8

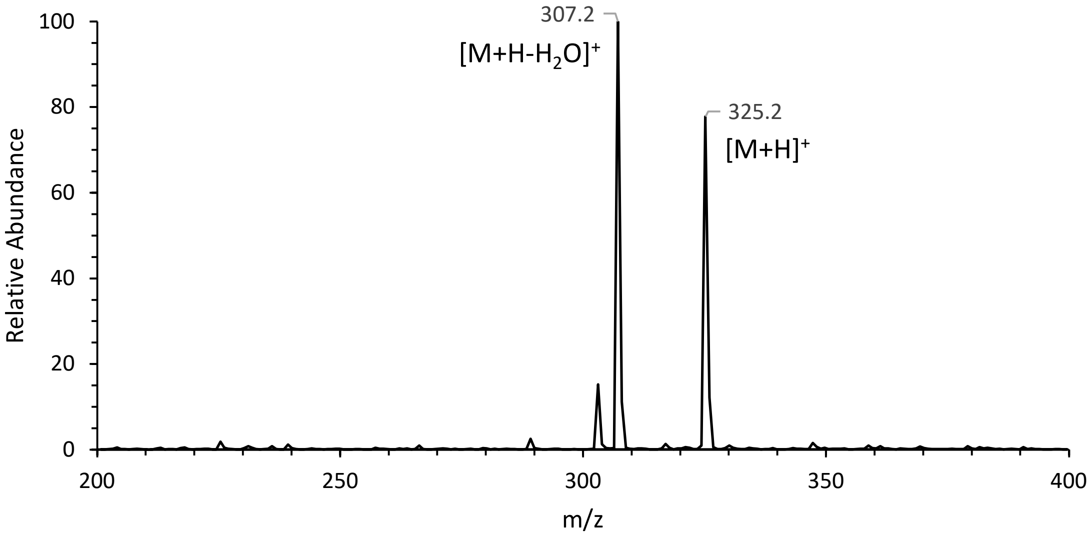

307.2
[M+H-H$_2$O]$^+$
325.2
[M+H]$^+$
Relative Abundance
0
20
40
60
80
100
200
250
300
350
400
m/z

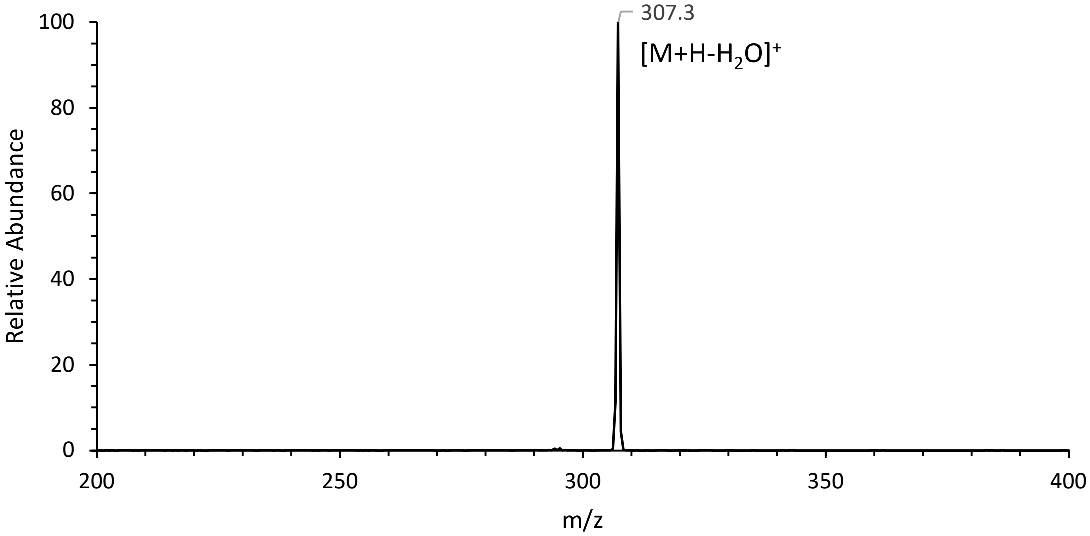

307.3
[M+H-H$_2$O]$^+$
Relative Abundance
0
20
40
60
80
100
200
250
300
350
400
m/z

ESI/MS^2 of 2-6

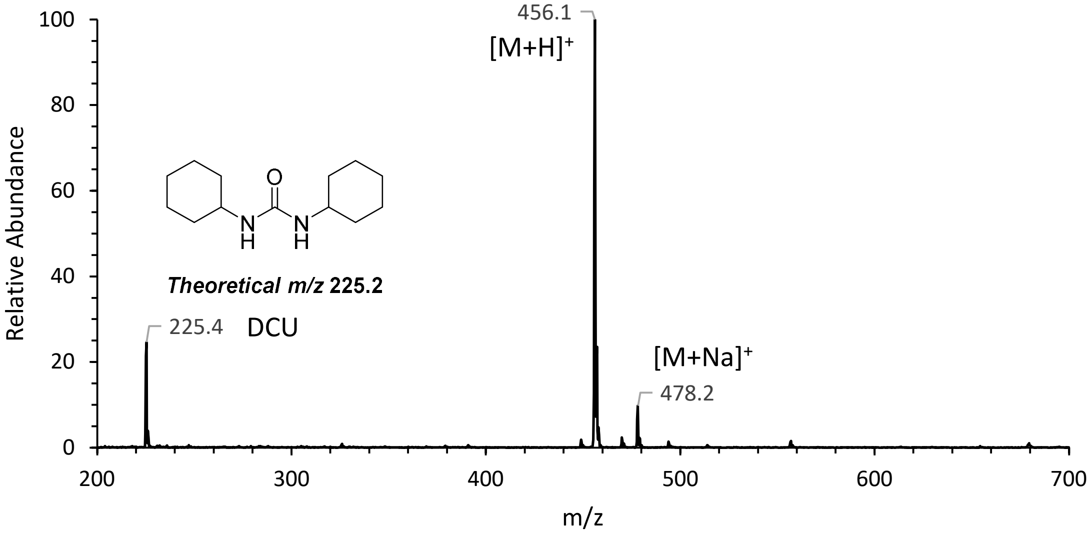

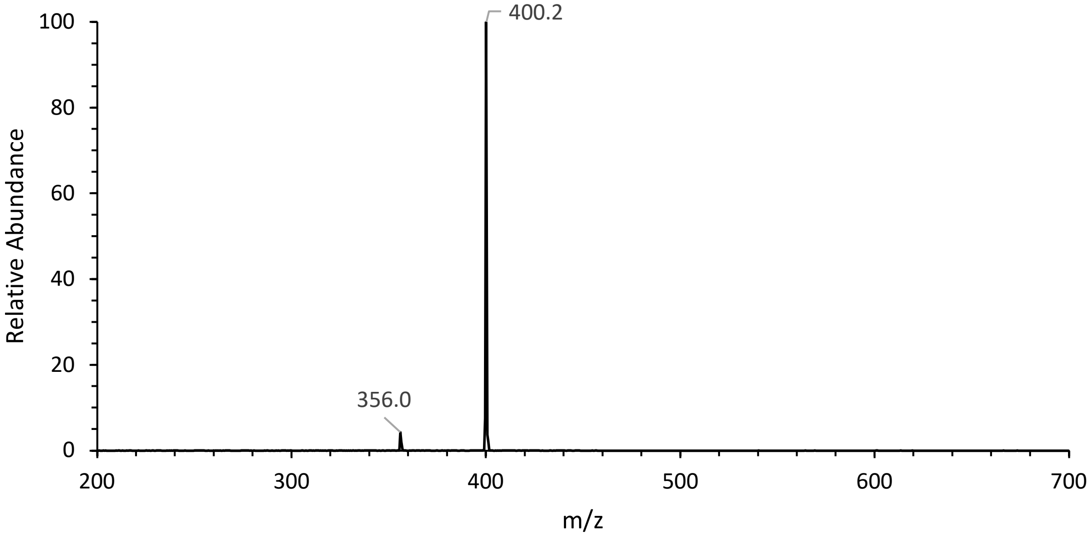

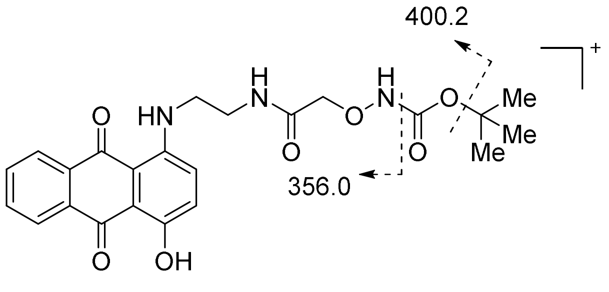

***m/z* 456.1**

ESI/MS^2 of 2-9

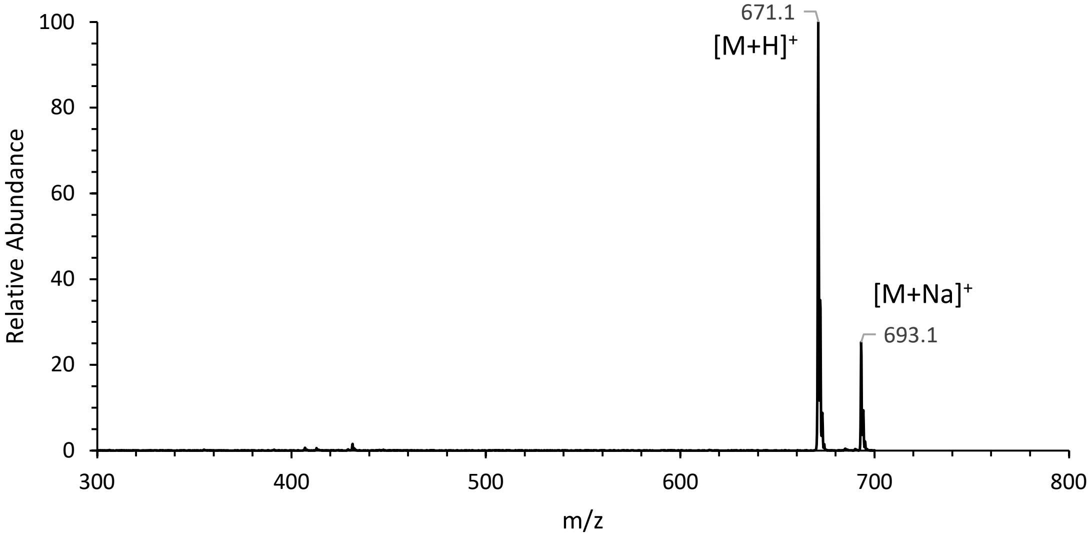

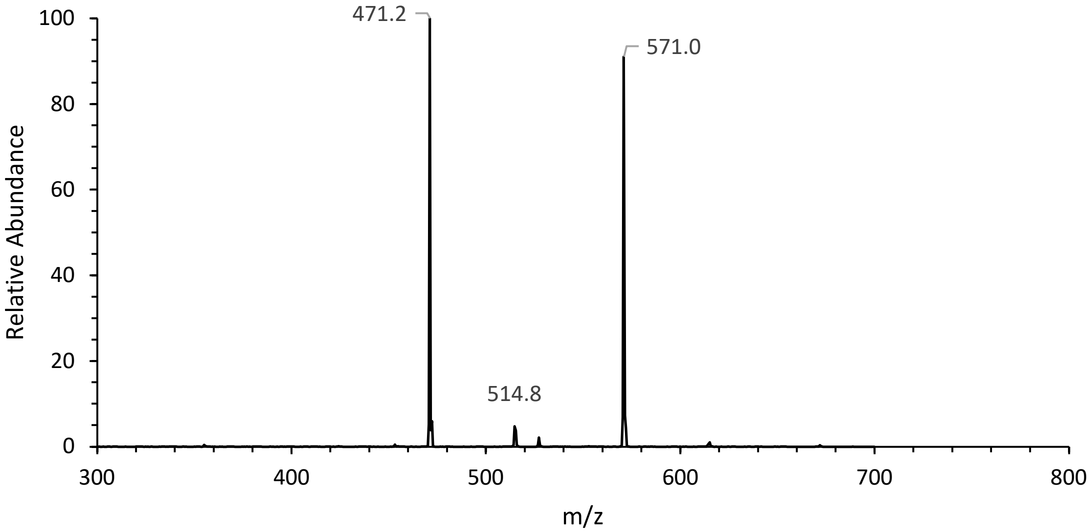

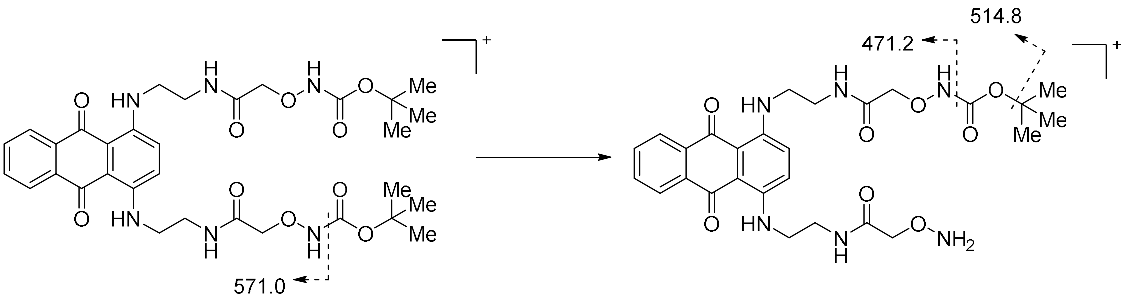

m/z **671.3**

m/z **571.0**

ESI/MS^2 of 2-1

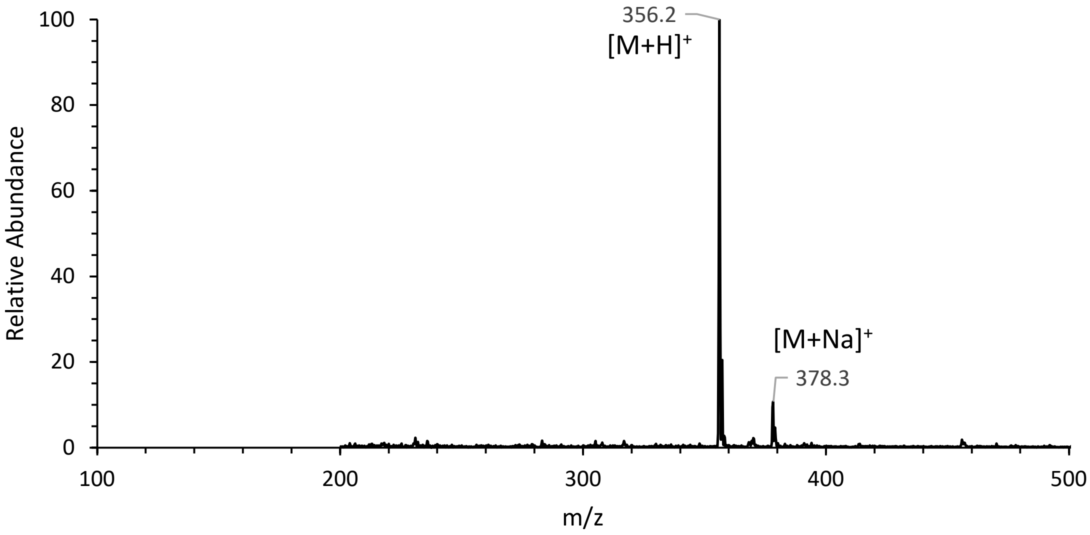

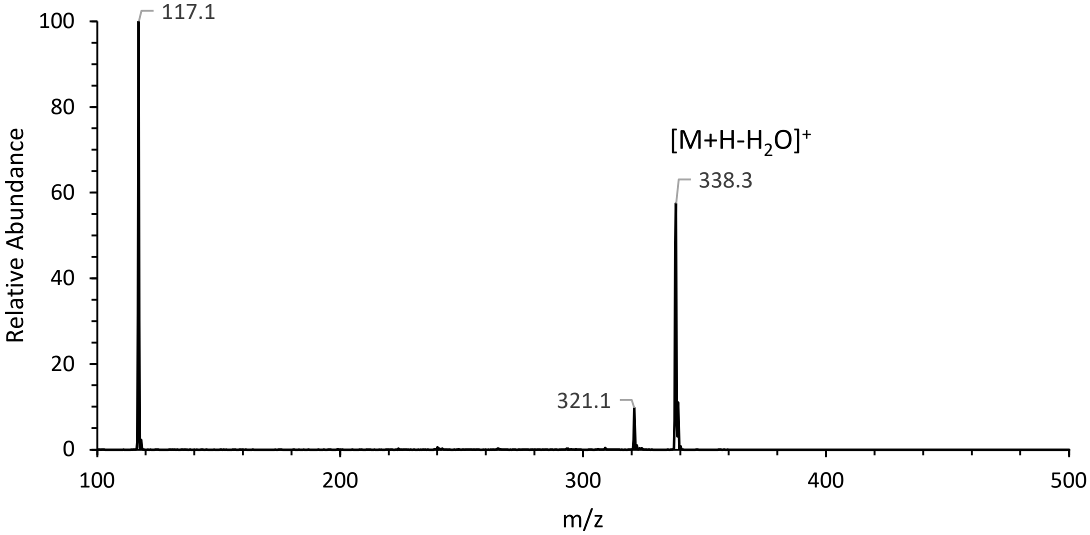

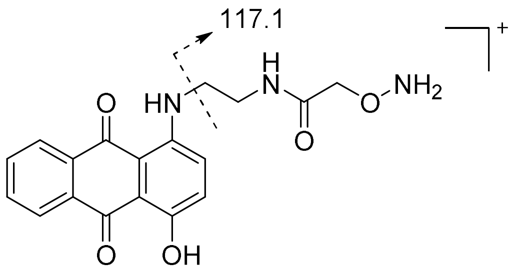

m/z **356.2**

ESI/MS^2 of 2-2

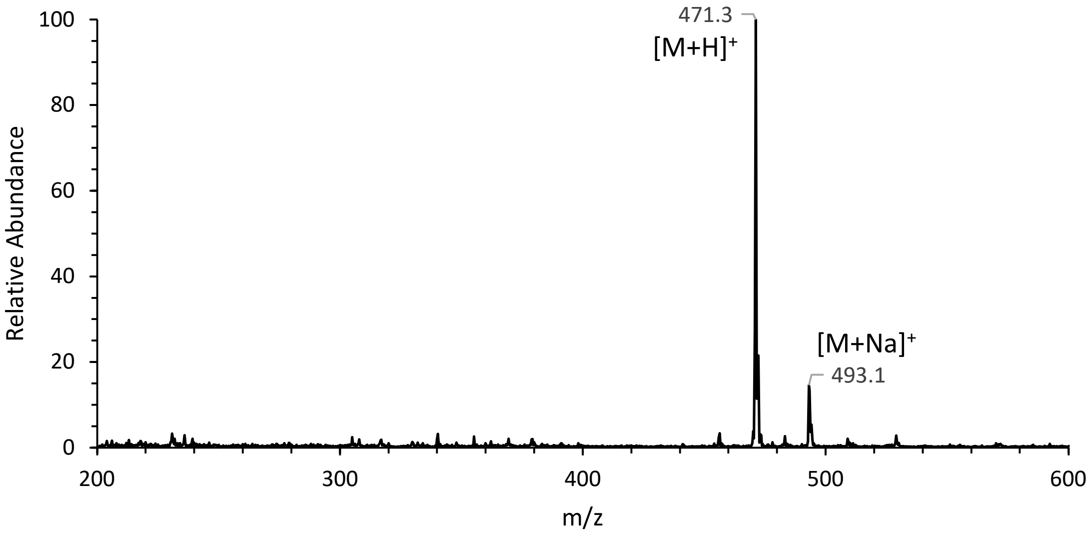

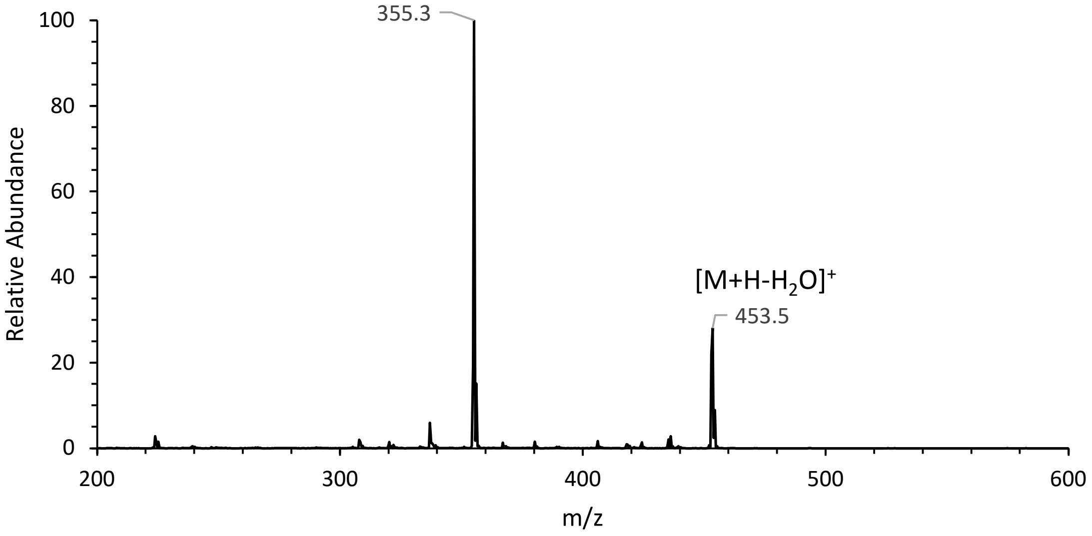

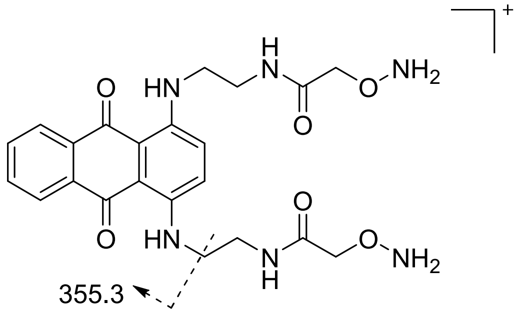

***m/z* 471.3**

ESI/MS^2 of the dR oxime of 2-1

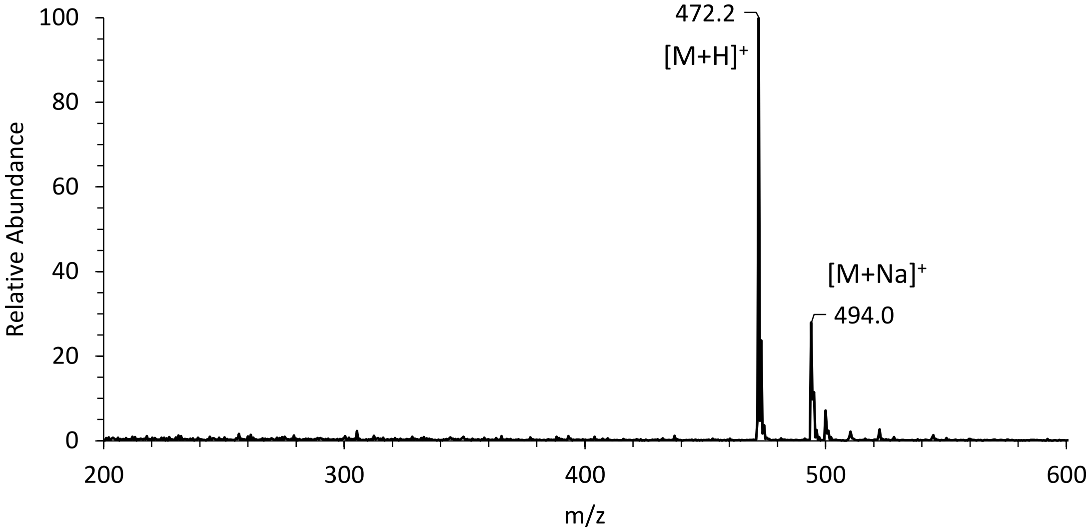

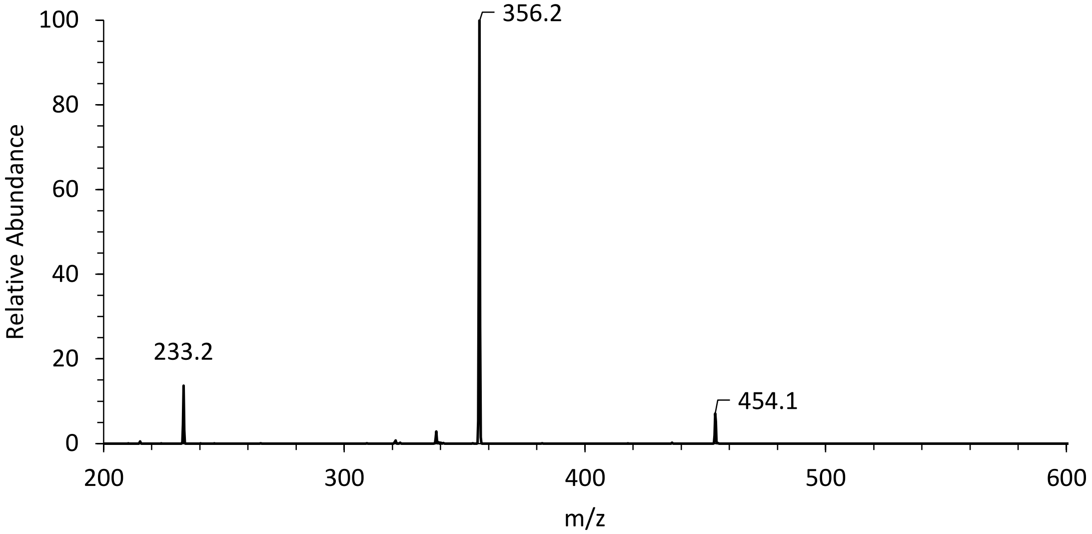

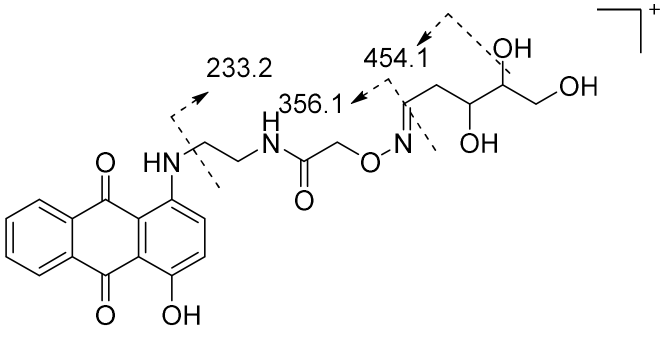

***m/z* 472.2**

ESI/MS^2 of the mono-dR oxime of 2-2

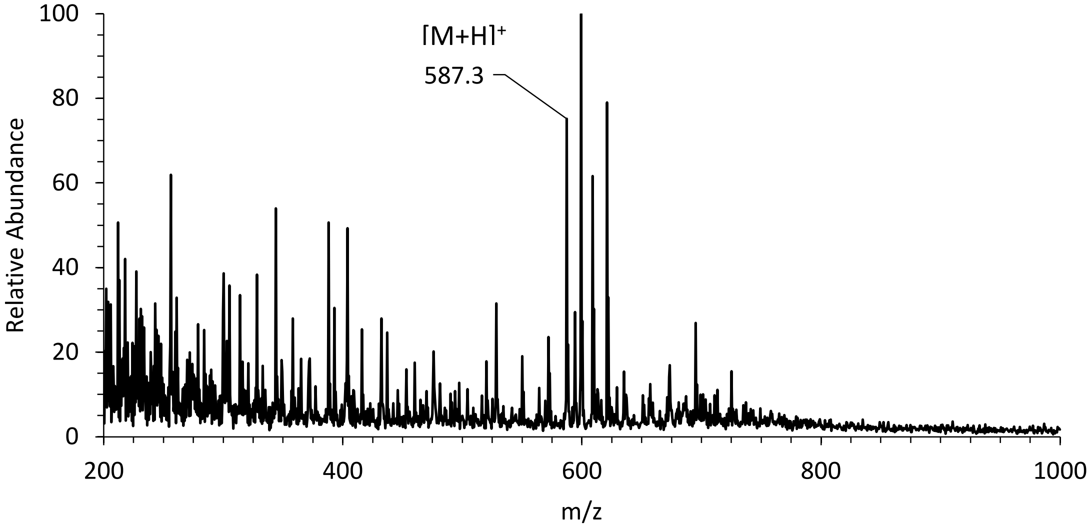

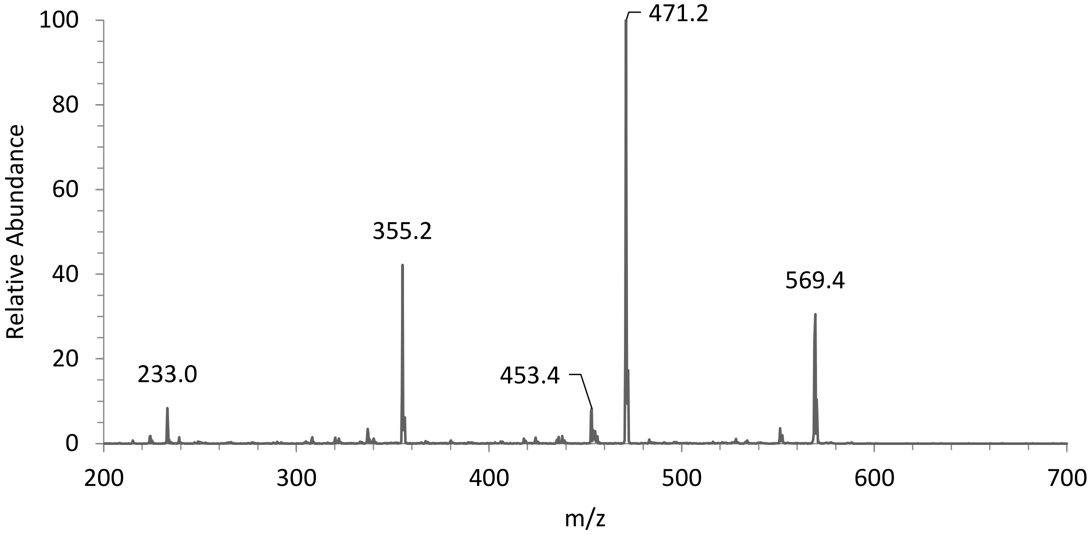

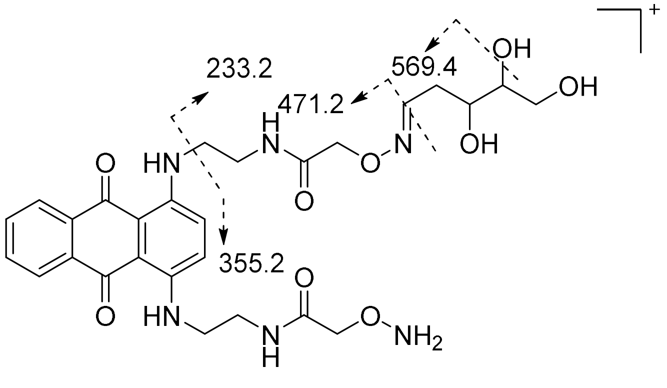

***m/z* 587.3**

ESI/MS^2 of the bis-dR oxime of 2-2

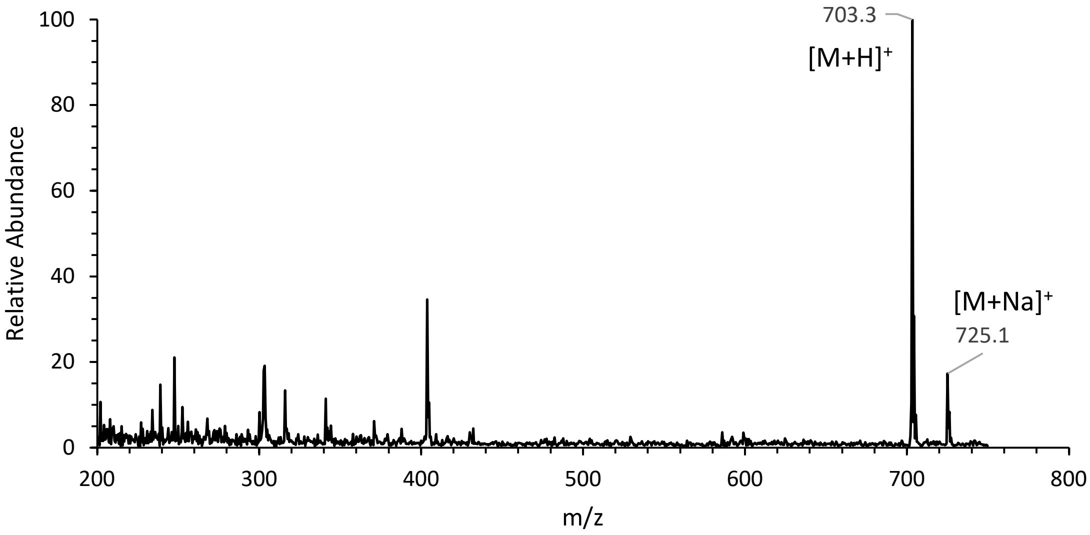

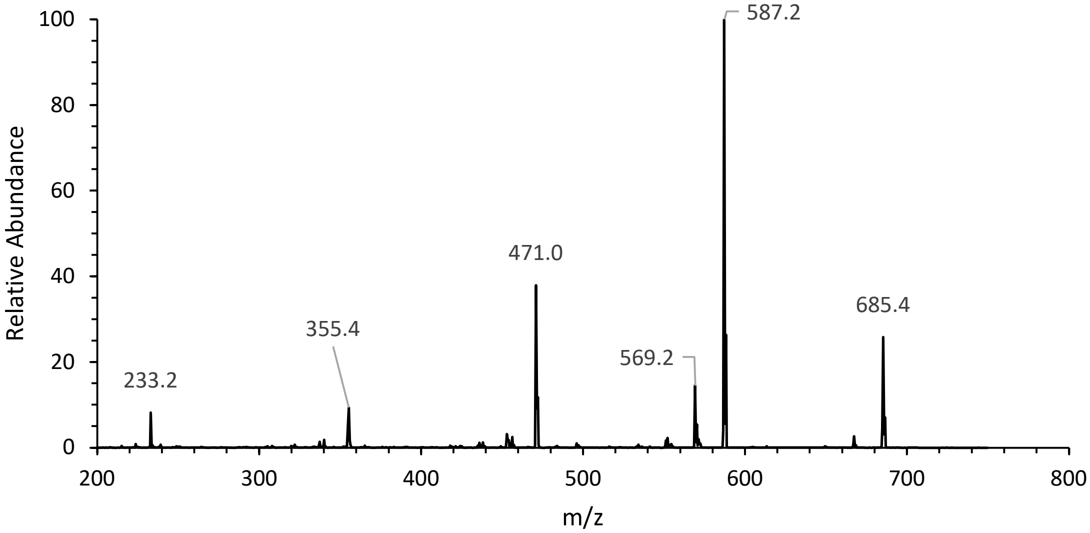

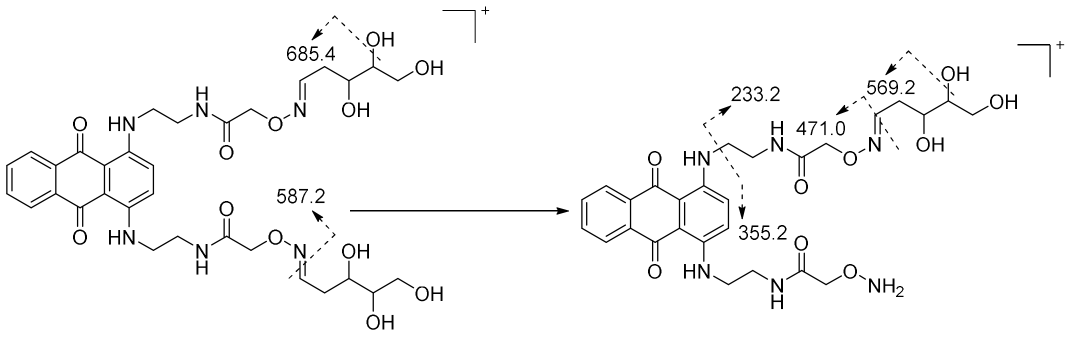

m/z **703.3**

m/z **587.2**

ESI/MS^2 of the ^{13}C-labeled dR oxime of 2-1 (red dots are isotopically labeled carbons)

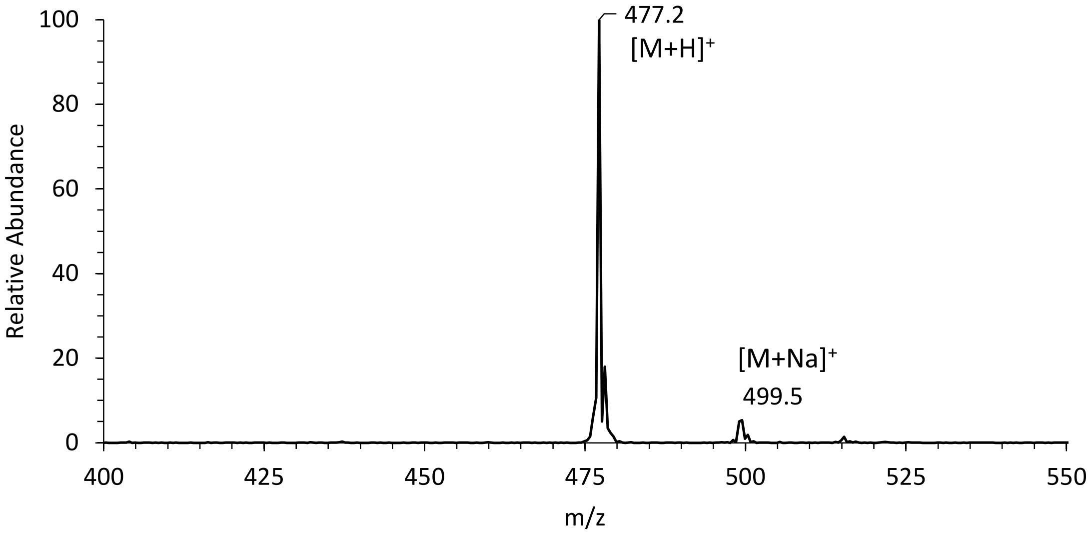

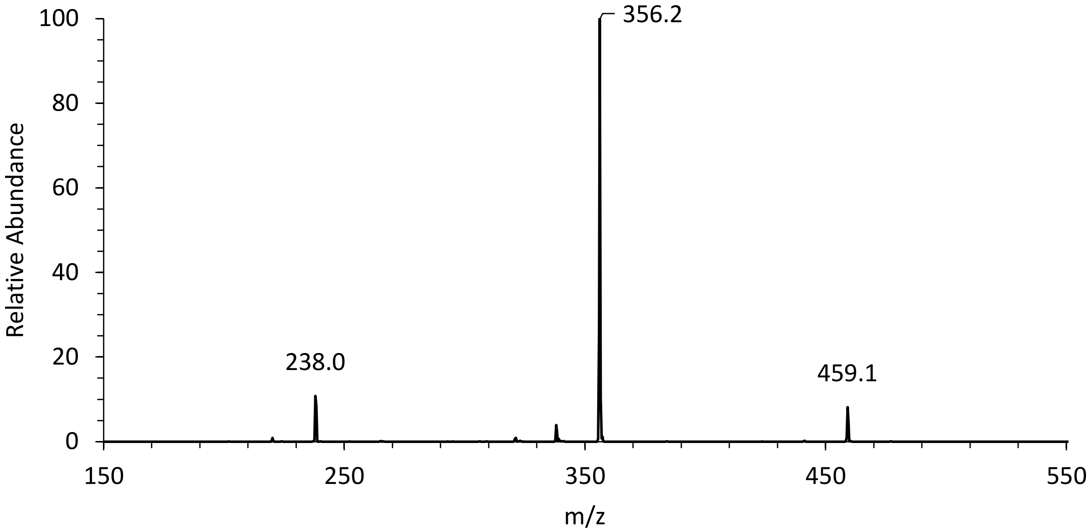

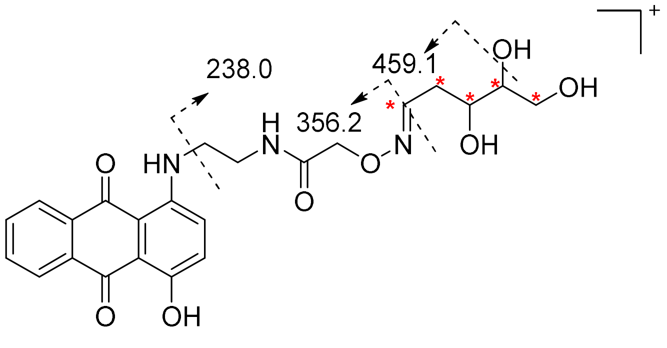

***m/z* 477.2**

ESI-MS^2 of the 2-1 oxime conjugate to the APmer

Explanation of fragment peaks is provided in the tables of the main text.

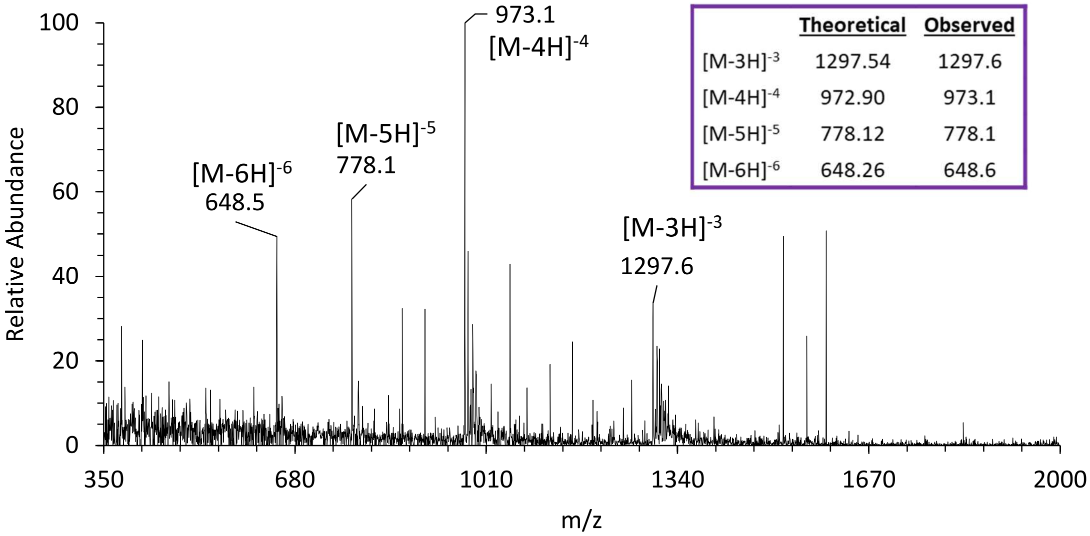

	Theoretical	Observed
[M-3H]$^{-3}$	1297.54	1297.6
[M-4H]$^{-4}$	972.90	973.1
[M-5H]$^{-5}$	778.12	778.1
[M-6H]$^{-6}$	648.26	648.6

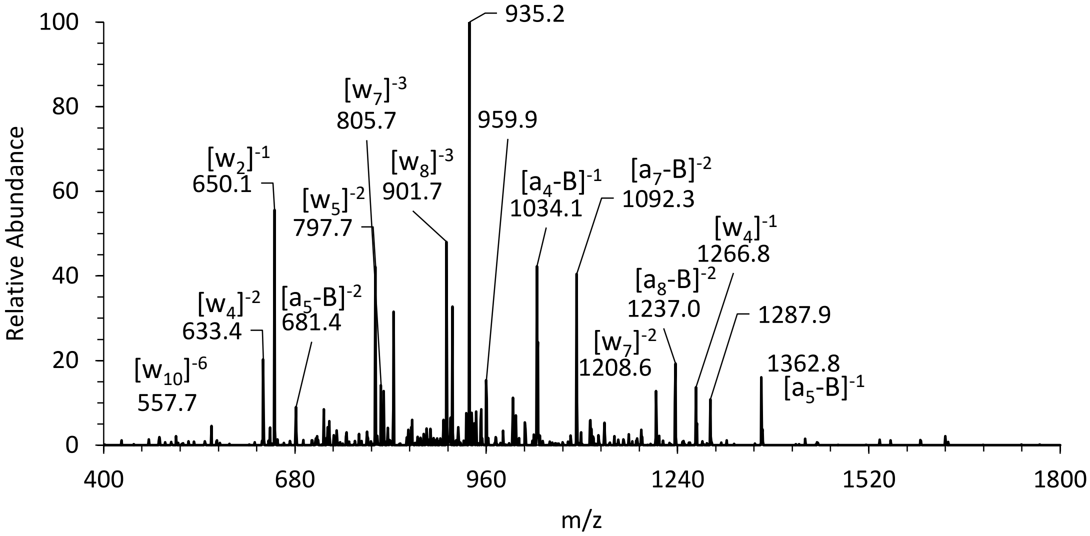

ESI-MS^2 of the acetone-capped 2-2 oxime conjugate to the APmer

Explanation of fragment peaks is provided in the tables of the main text.

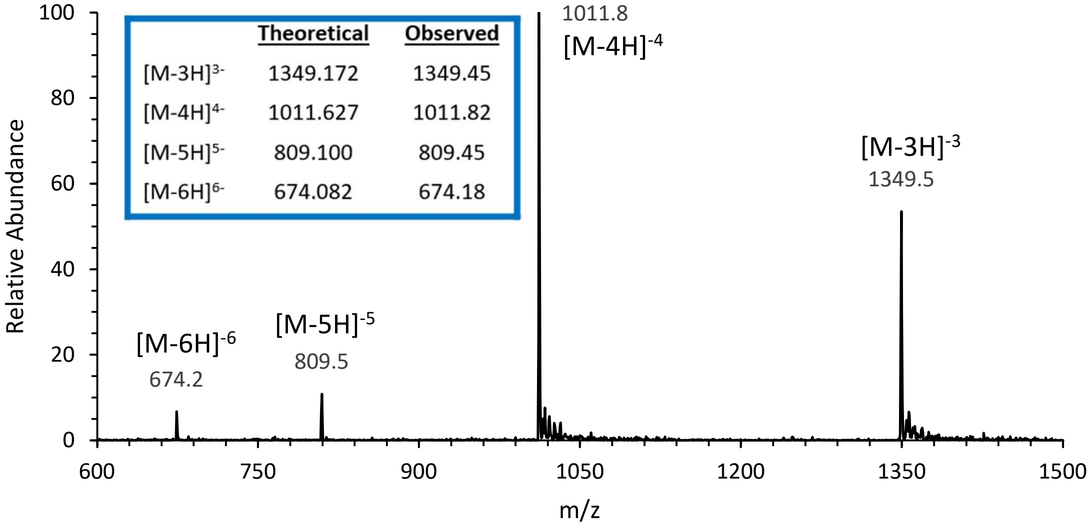

	Theoretical	Observed
$[M-3H]^{3-}$	1349.172	1349.45
$[M-4H]^{4-}$	1011.627	1011.82
$[M-5H]^{5-}$	809.100	809.45
$[M-6H]^{6-}$	674.082	674.18

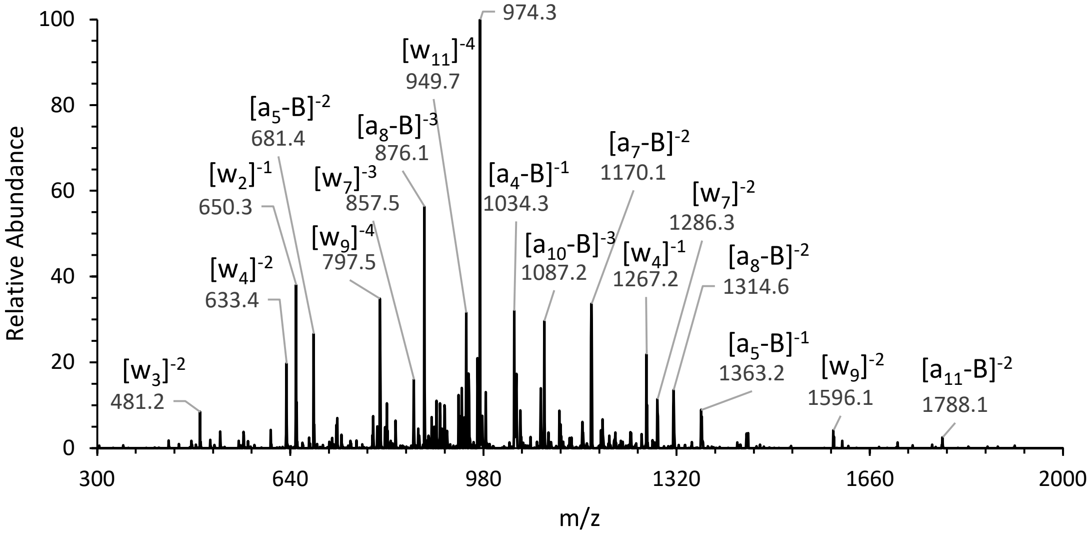

Appendix III

Liquid Chromatograms for Chapter 2

HPLC Chromatogram of 2-1

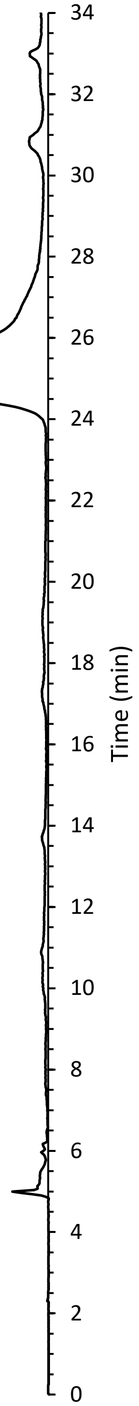

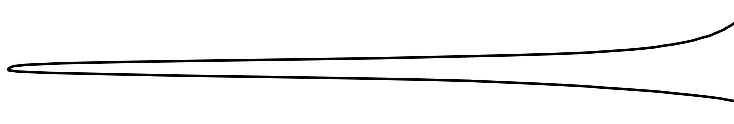

HPLC Chromatogram of 2-2

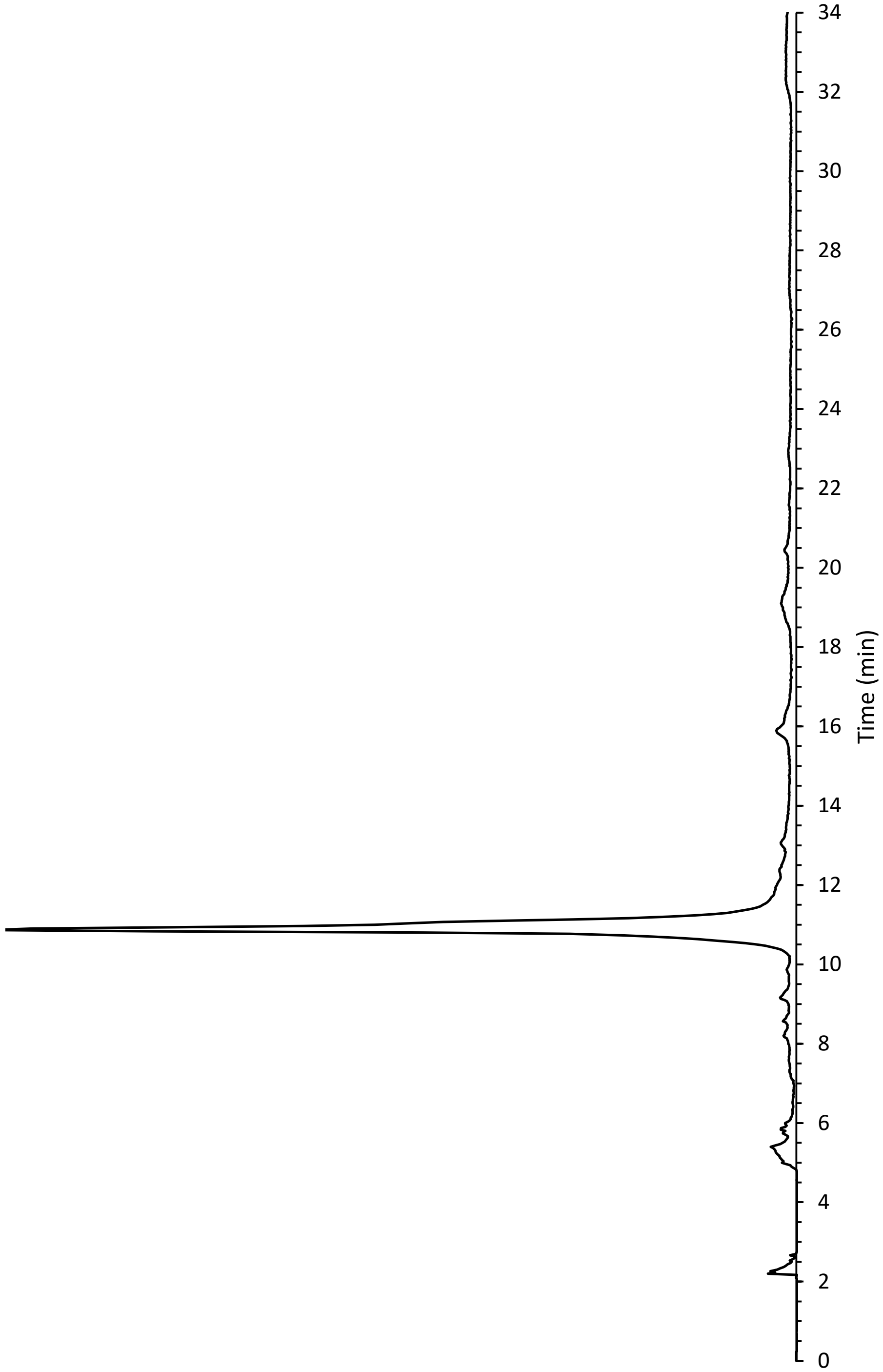

HPLC Chromatogram of Crude Reaction for Mono-dR Oxime of 2-1

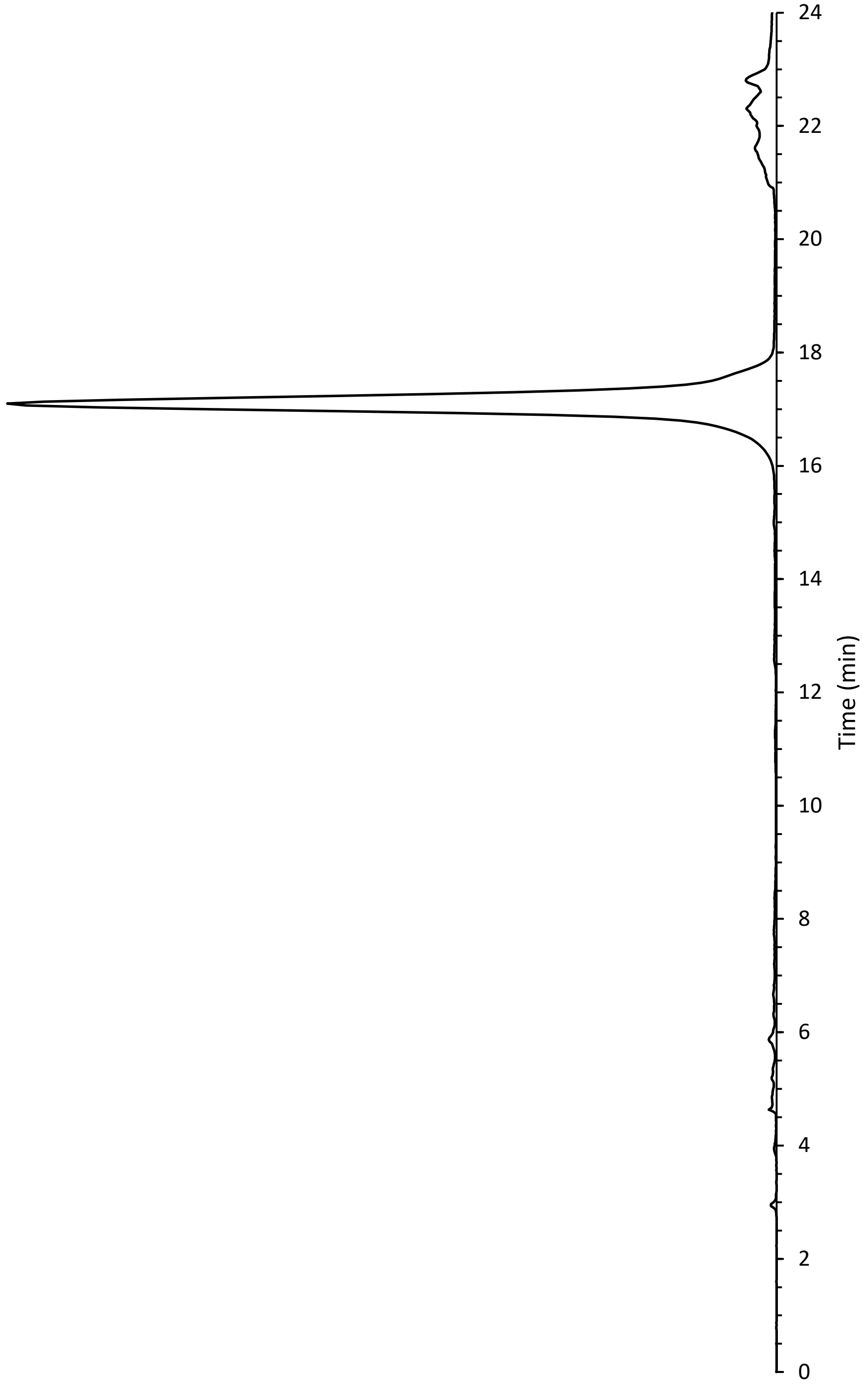

HPLC Chromatogram of Crude Reaction for Bis-dR Oxime of 2-2

The peak at ~10 min is the oxime conjugate, and the peak at ~11 min is **2-2**

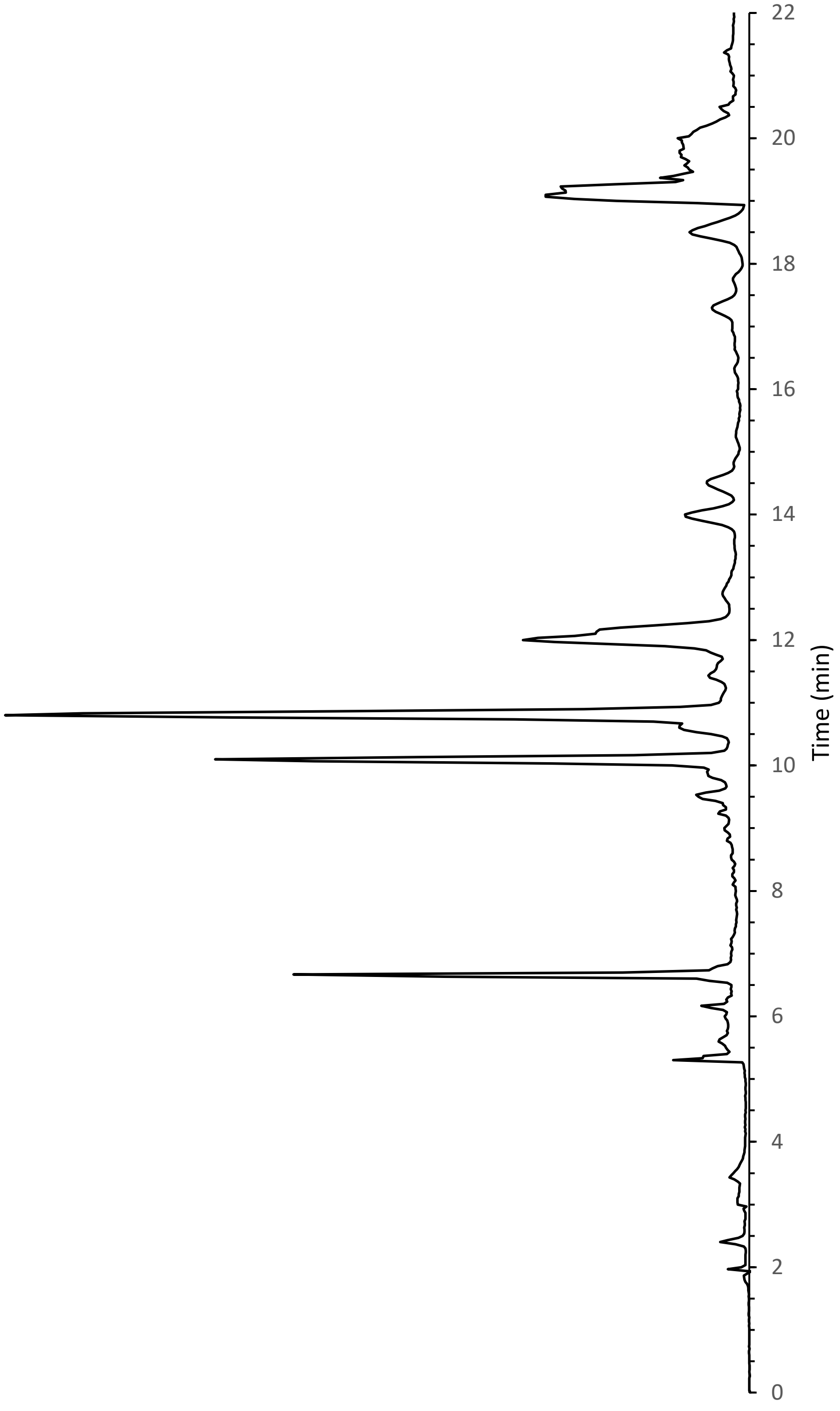

HPLC Chromatogram of Crude Reaction for Mono-dR Oxime of 2-2

The peak at ~9.8 min is the oxime conjugate, and the peak ata ~11 min is **2-2**

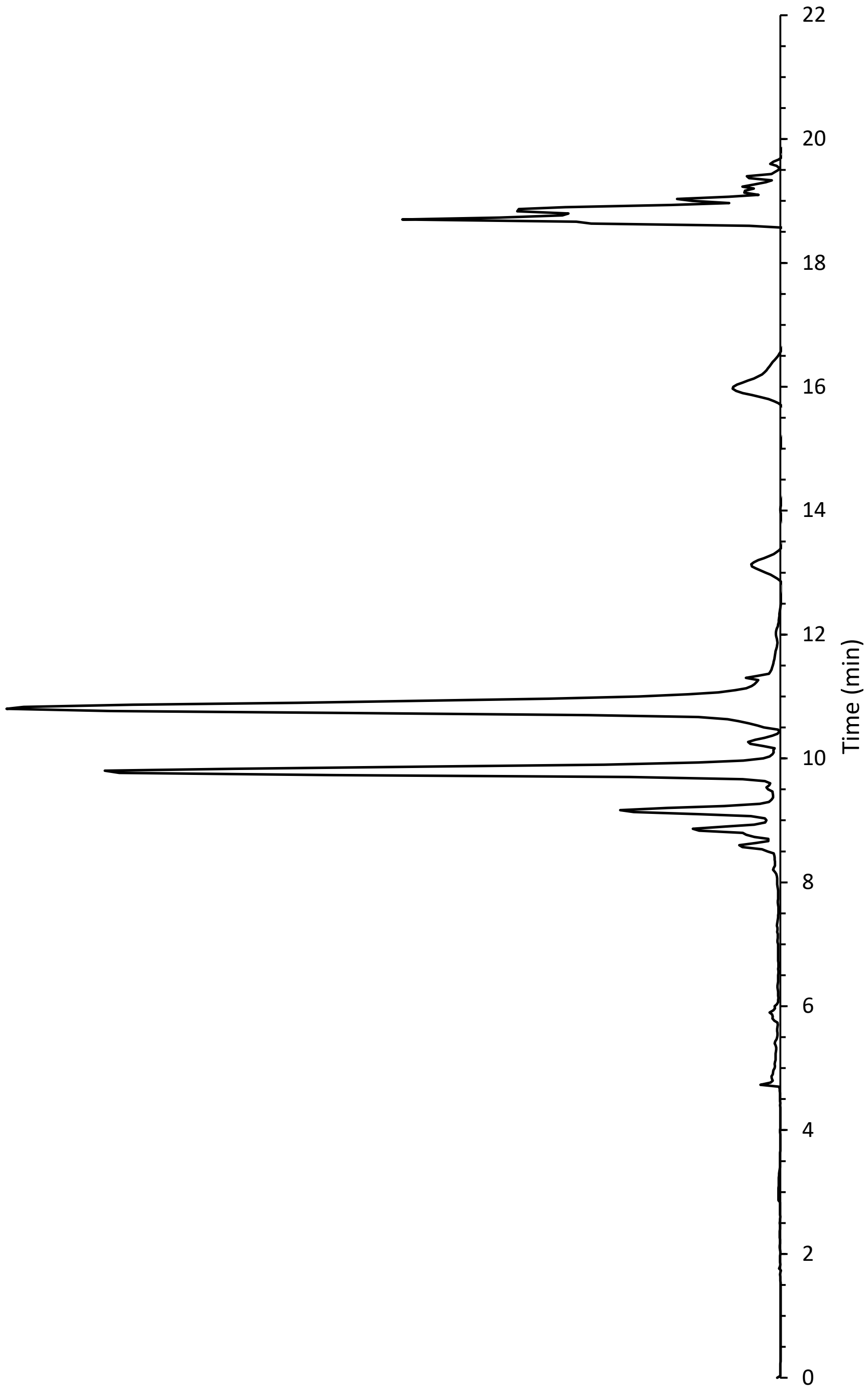

HPLC Chromatogram of Crude Reaction for ^{13}C-labeled dR Oxime of 2-1

The peak at ~15 min is the oxime conjugate

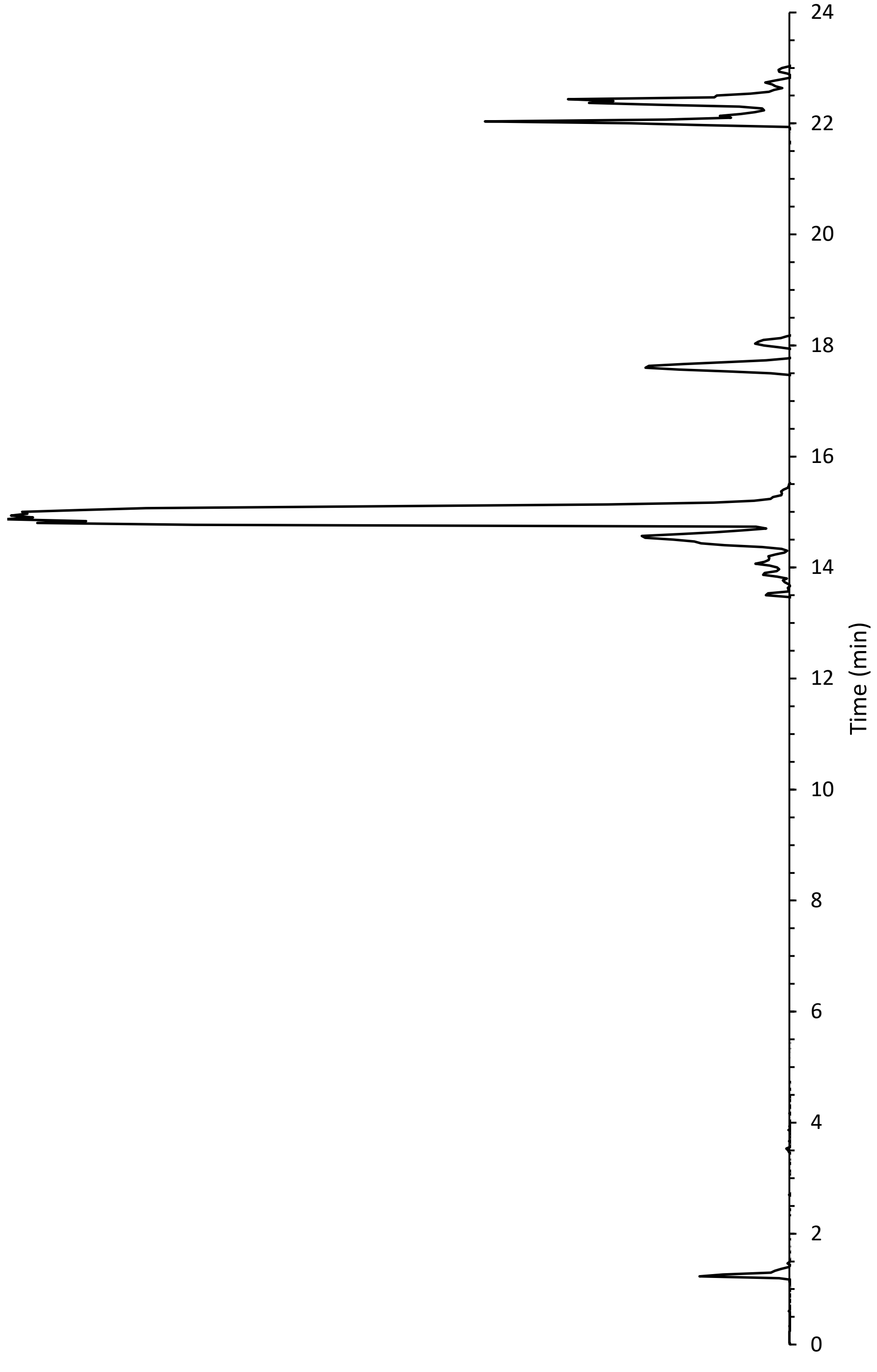

HPLC Chromatogram of Crude Reaction of 2-1 (40 µM) with APmer (25 µM)

The peak at ~17 min is the complementary strand, the peak at ~18.5 min is the APmer, and the peak at ~21 min is the oxime conjugate

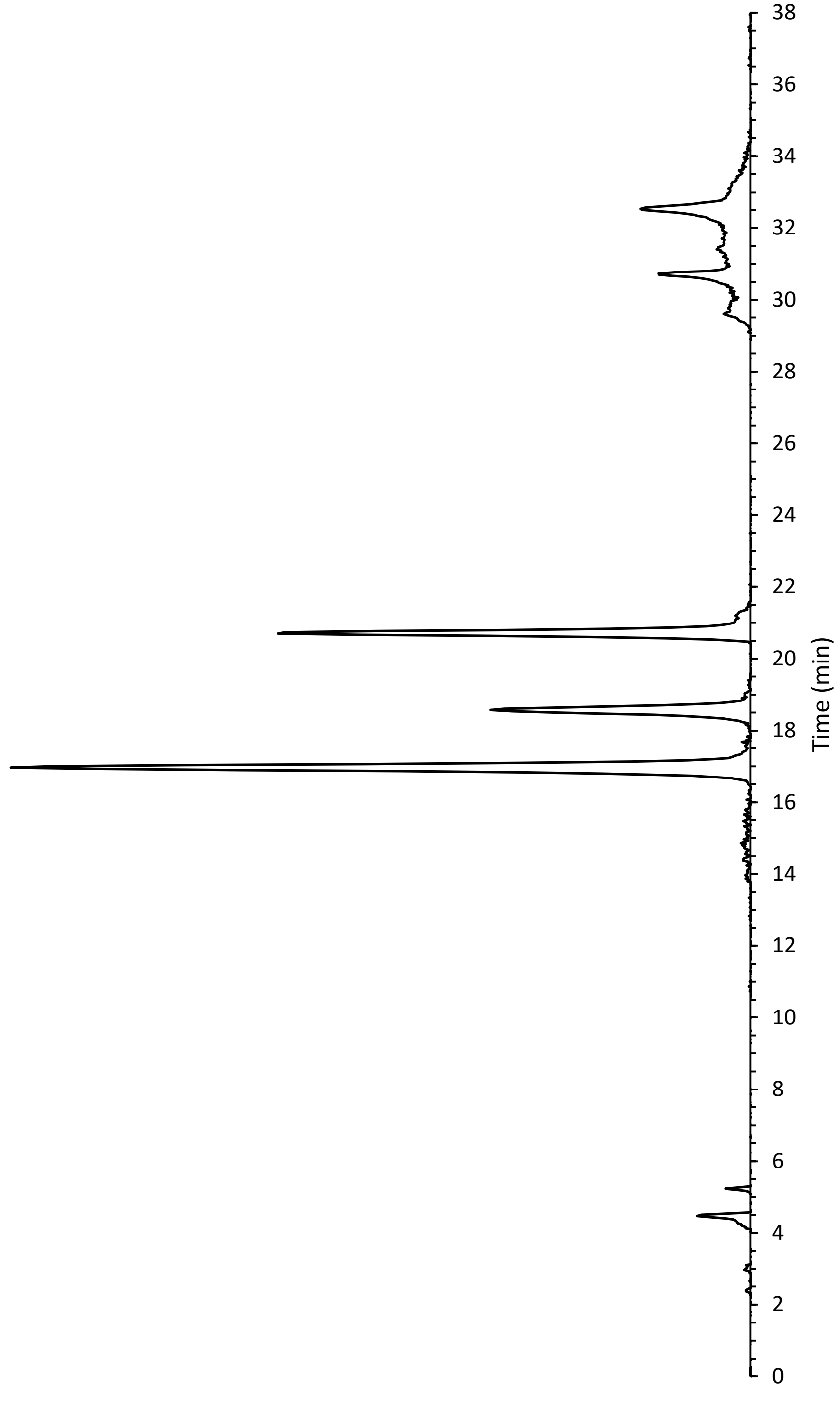

HPLC Chromatogram of Crude Reaction of 2-2 (40 µM) with APmer (25 µM)

The peak at ~17 min is the complementary strand, the peak at ~18.5 min is the APmer, the peak at ~21 min is the oxime conjugate, and the peaks after 21 min are the byproducts.

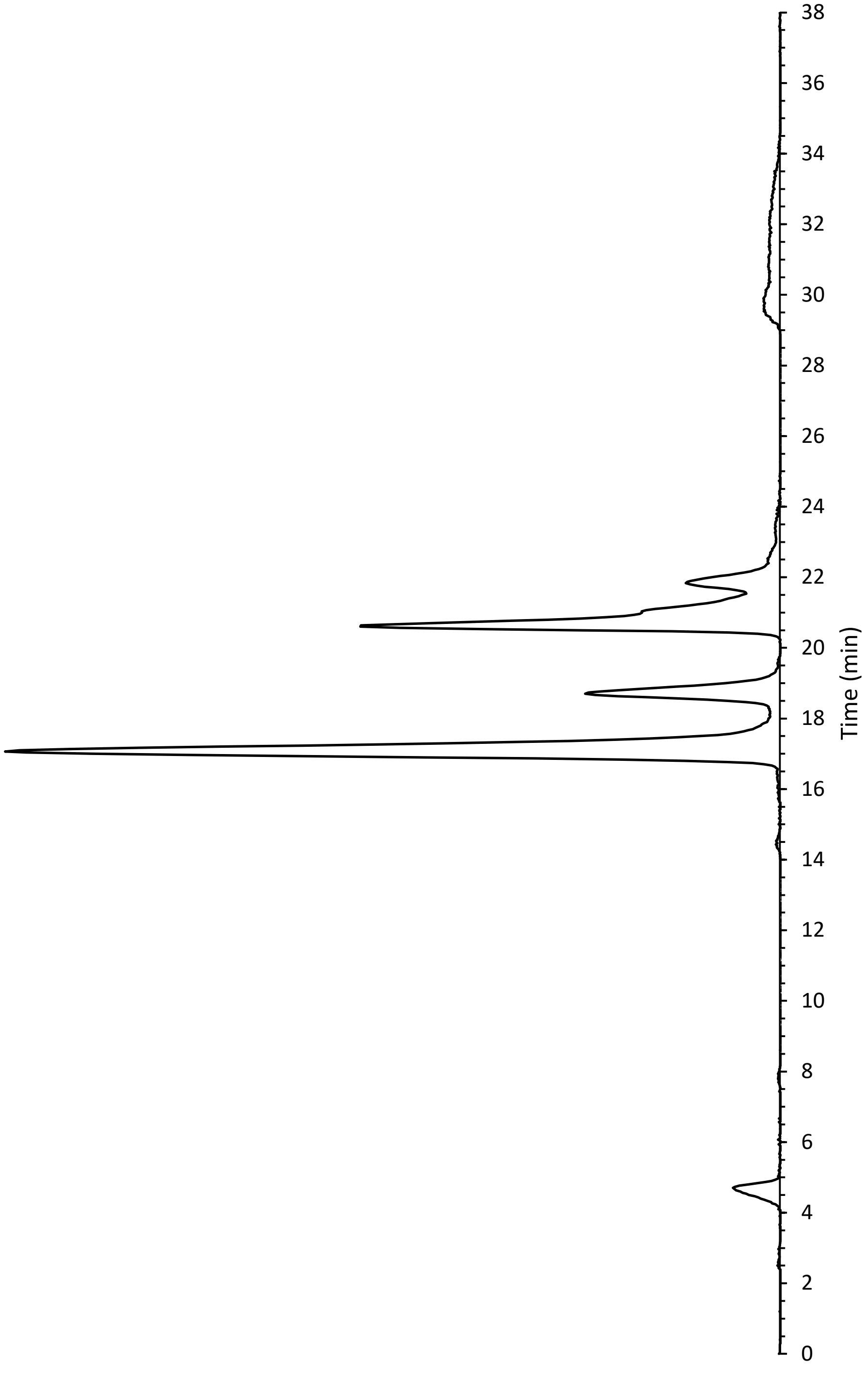

HPLC Chromatogram of Crude Reaction of 2-2 (200 µM) with APmer (25 µM)

The peak at ~16.5 min is the complementary strand, the tiny peak at ~18 min is the APmer, the peak at ~20.5 min is the oxime conjugate, and the peaks on and after 21 min are the byprducts.

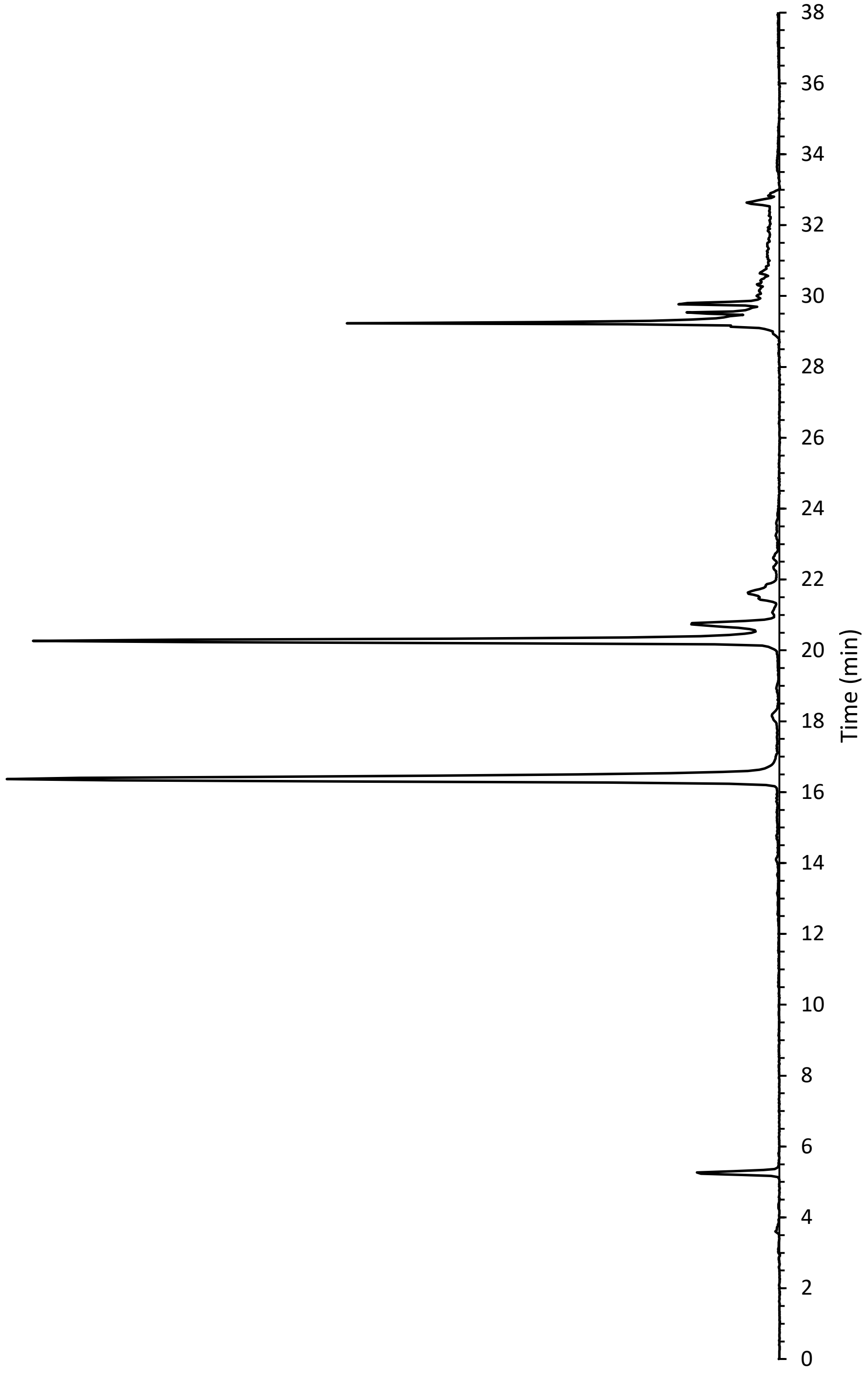

HPLC Chromatogram of Crude Reaction of 2-2 (200 µM) with APmer (25 µM) Capped with Acetone

The peak at ~16.5 min is the complementary strand, the tiny peak at ~18 min is the APmer, the peak at ~22 min is the oxime conjugate with acetone capping the unbound side. The peak at ~6 min is acetone.

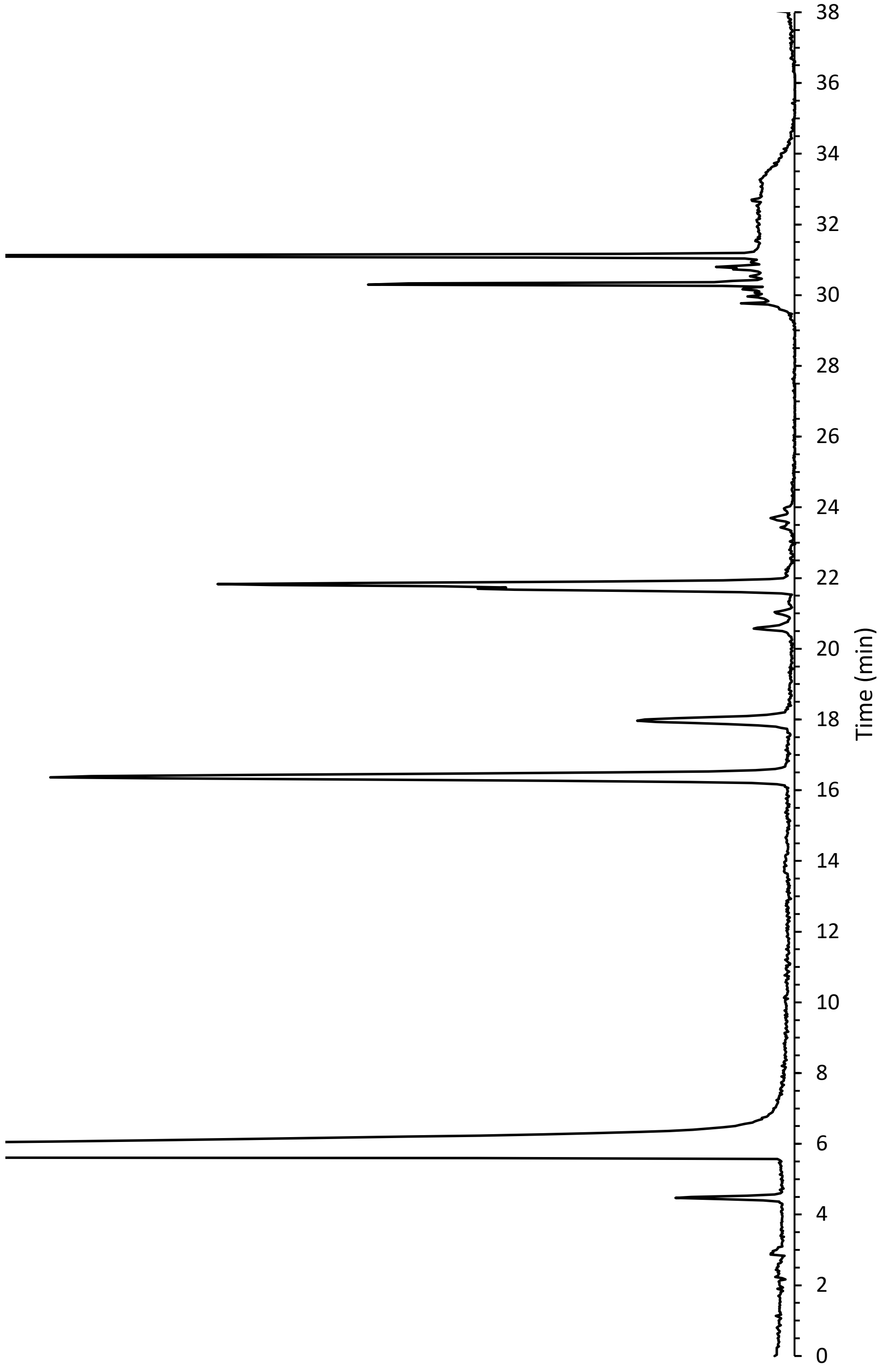

LC Chromatogram of Purified APmer Oxime with 2-1
(These data were collected by the LTQ Mass Spectrometer)
The top chromatogram is the full mass spectrum, the middle one measures the $[M-4]^{-4}$ ion fragmentation, and the bottom one measures the $[M-3]^{-3}$ ion fragmentation.

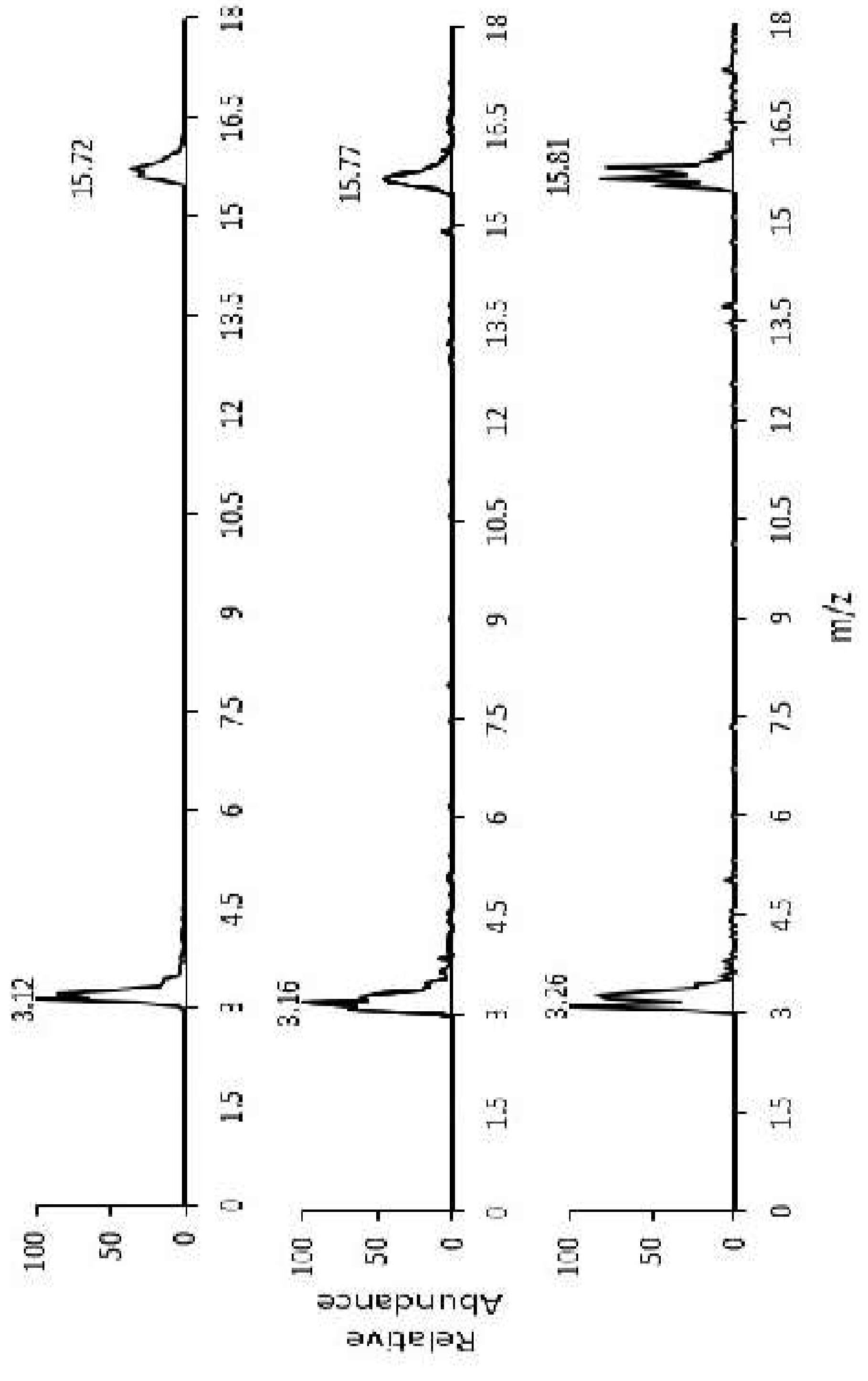

LC Chromatogram of Purified APmer Oxime with 2-2 Capped with Acetone

(These data were collected by the LTQ Mass Spectrometer)

The top chromatogram is the full mass spectrum, the middle one measures the $[M-3]^{-4}$ ion fragmentation, and the bottom one measures the $[M-2]^{-3}$ ion fragmentation

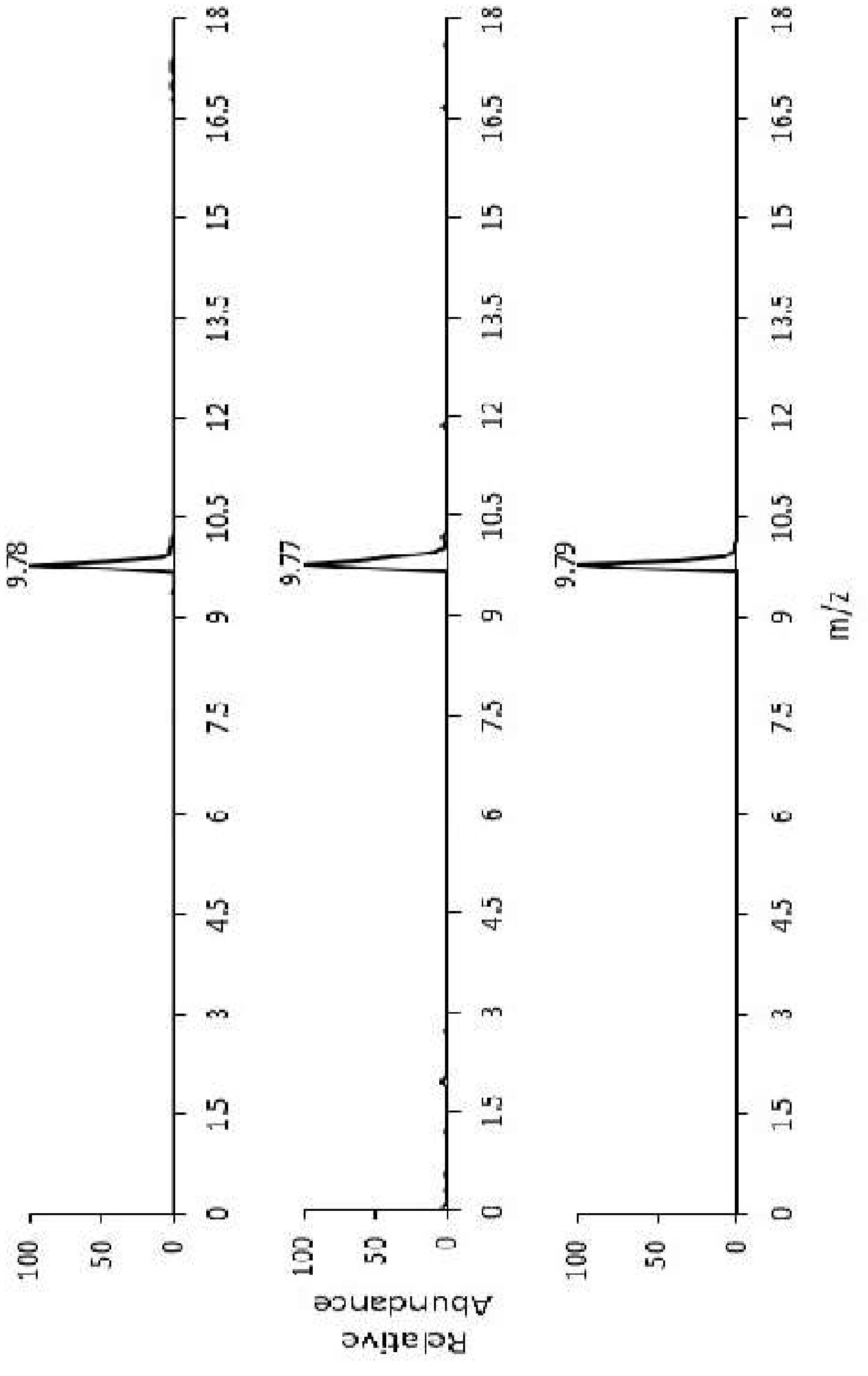

LC Chromatogram of Purified APmer Oxime with 2-2 Digested and Enriched by SPE
(These data were collected by the LTQ Mass Spectrometer)

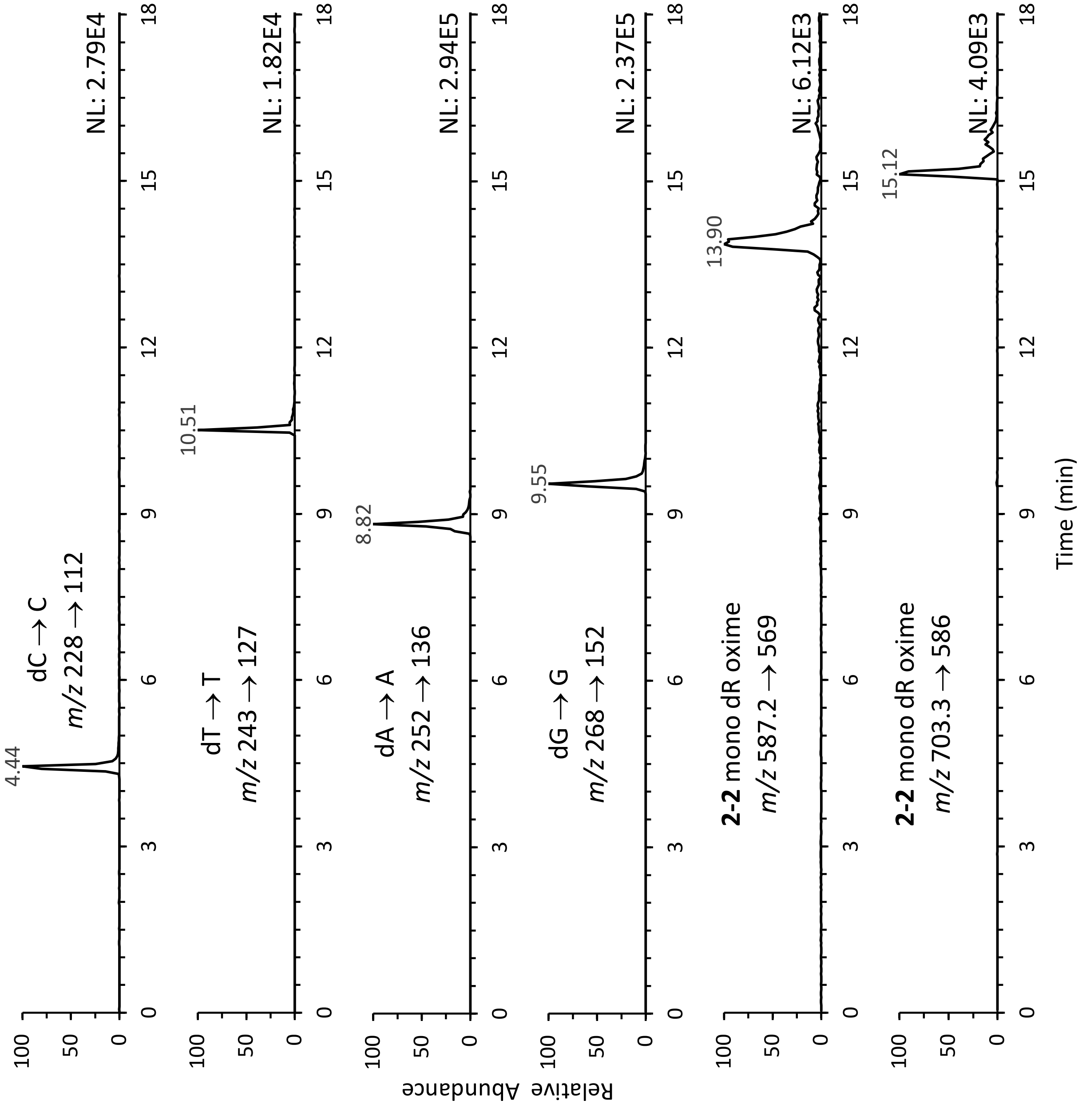

HPLC Chromatogram of the Fragmentation of APmer (25 µM)

The peak at ~16 min is the complementary strand, and the peak at ~17.5 min is the APmer. The peak at ~6 min is acetone, and the small peaks between 12 min and 16 min are the result of β-elimination.

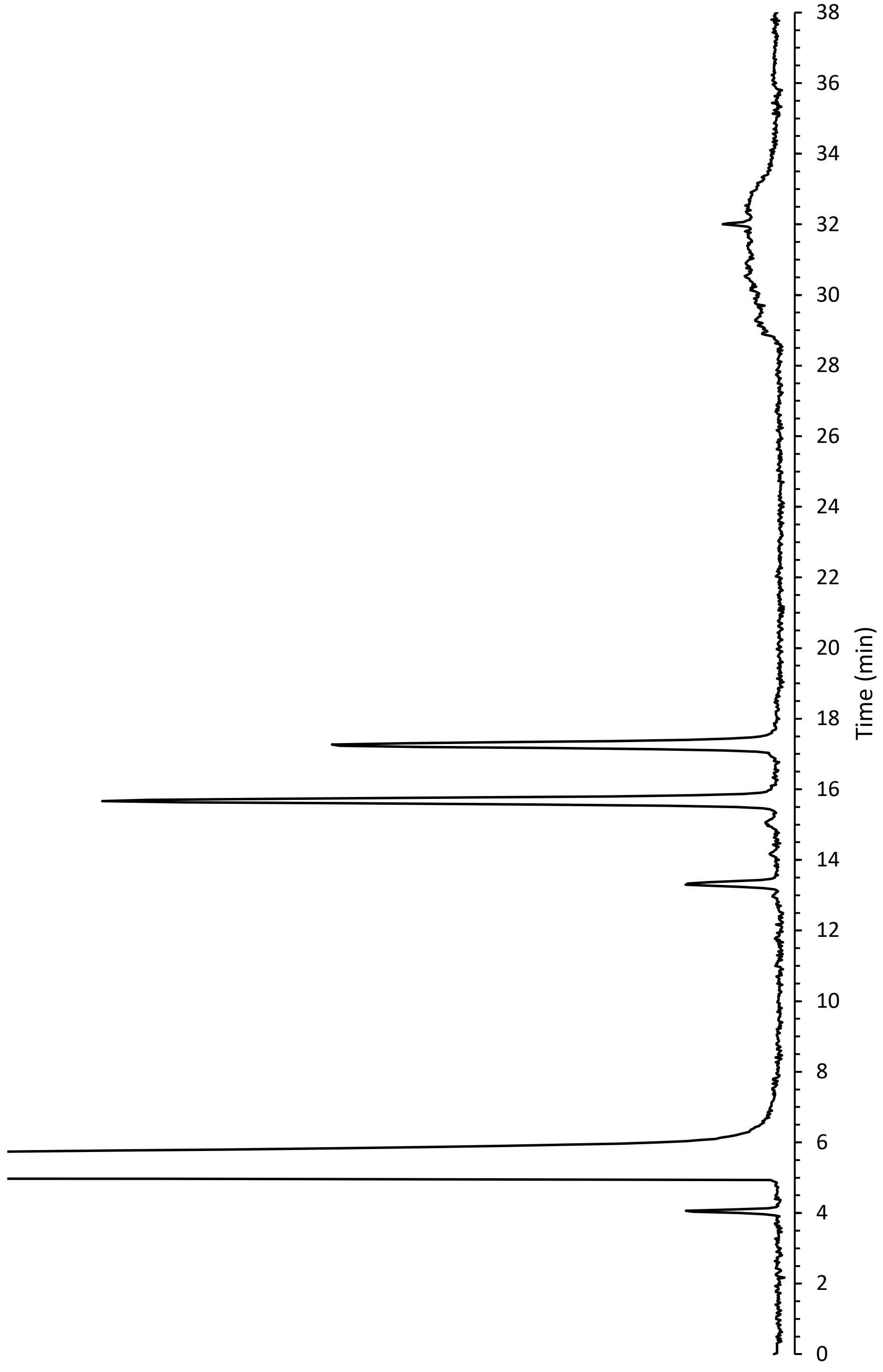

HPLC Chromatogram of Crude Reaction of Methoxyamine (40 µM) with APmer (25 µM)
The peak at ~16 min is the complementary strand, and the peak at ~17.5 min is the APmer. The peak at ~6 min is acetone, and the small peaks between 12 min and 16 min are the result of β-elimination. The peak at ~19 min is the methoxyamine oxime conjugate.

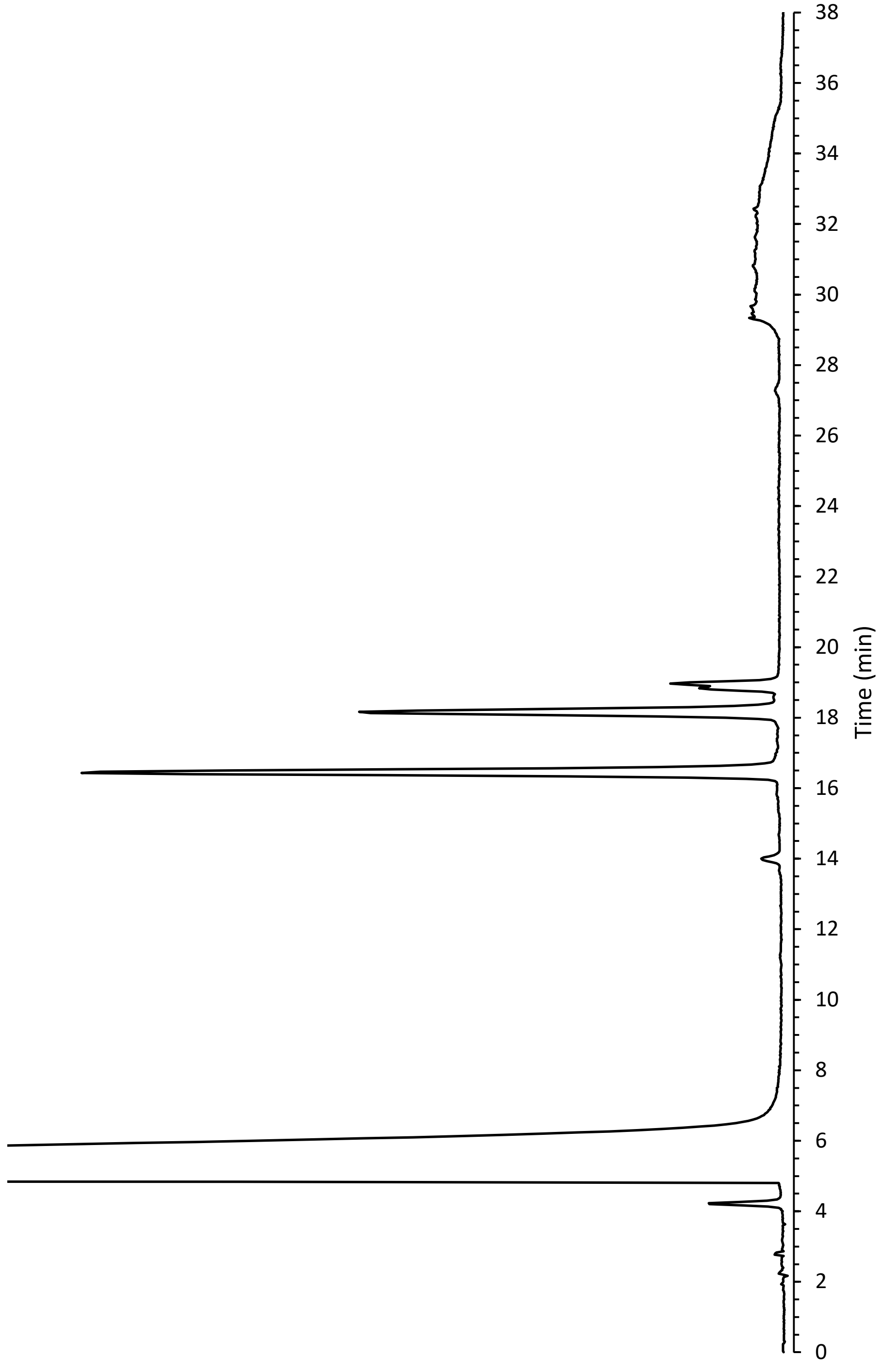

HPLC Chromatogram of Crude Reaction of 2-1 (40 µM) with SS APmer (25 µM)
The peak at ~17 min is the APmer. The peak at ~6 min is acetone, and the small peaks between 12 min and 16 min are the result of β-elimination. The peak at ~20 min is the oxime conjugate.

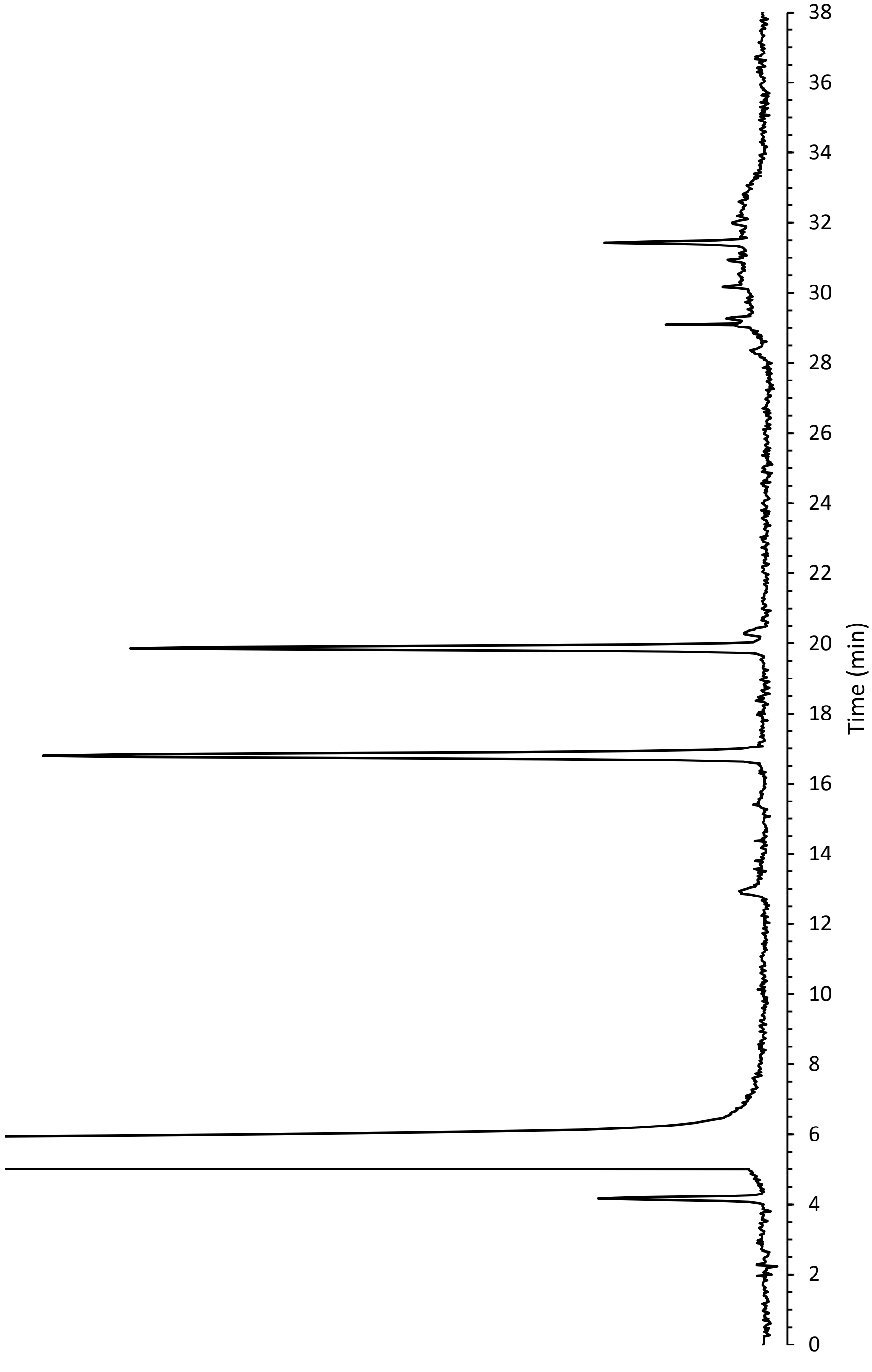

HPLC Chromatogram of Reannealed 2-1 Oxime of APmer after 6 days

The peak at ~17.5 min is the complementary peak, and the peak at ~21 min is the oxime conjugate.

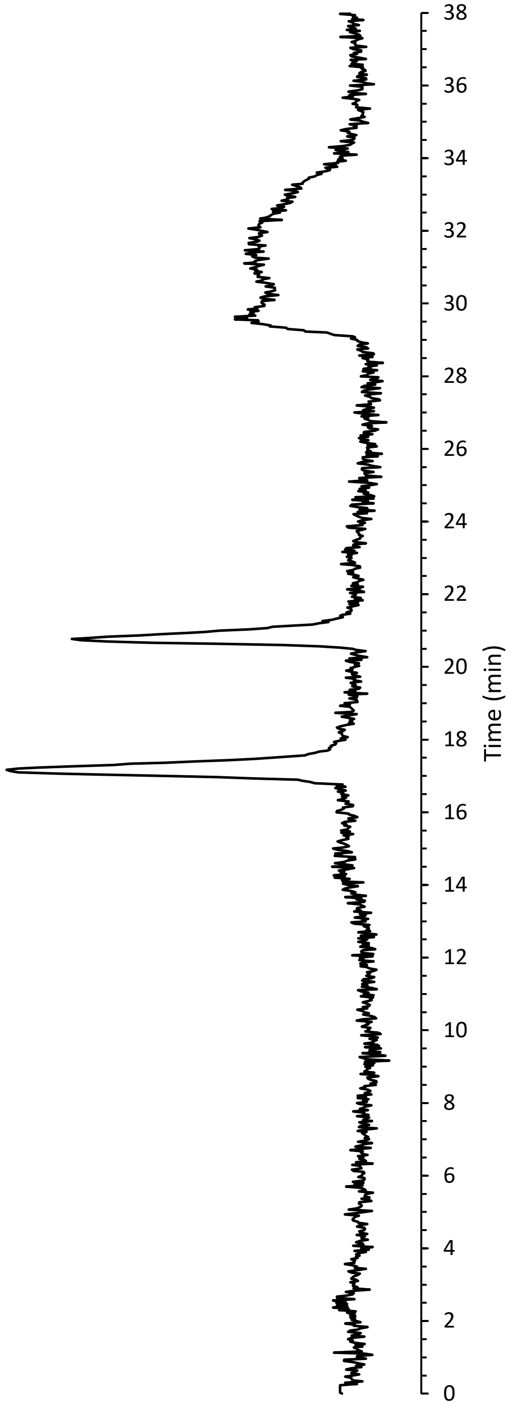

HPLC Chromatogram of Reannealed 2-2 Oxime of APmer (Acetone Capped) after 6 days

The peak at ~16 min is the complementary strand, and the peaks between 20 min and 22 min are the peaks that are in thermal equilibrium with each other (see main text). The baseline is increasing due to instrumental error at the time of the experiment.

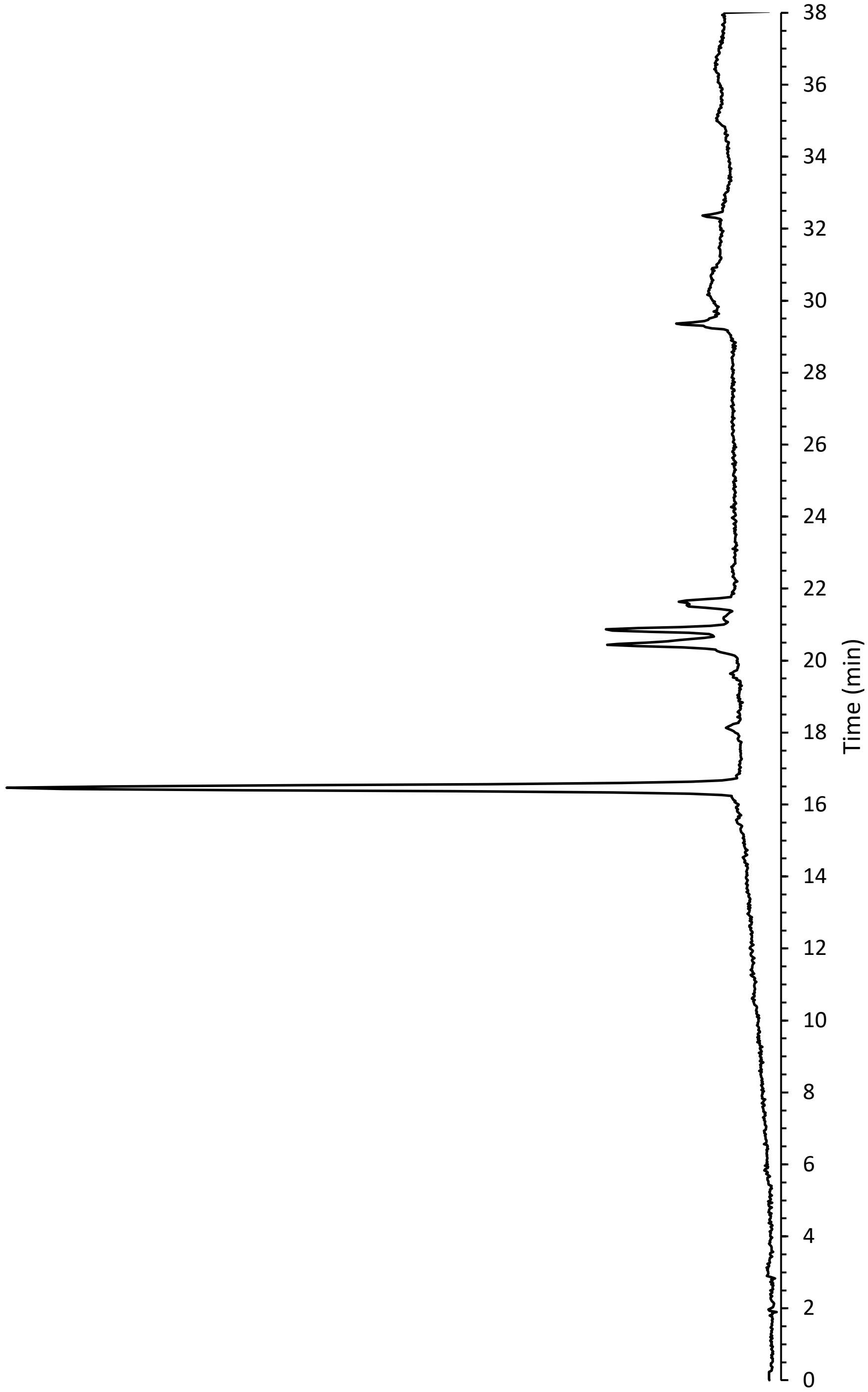

Appendix IV

Microsoft Excel Formulas for Chapter 2

Excel Process for Determining Extinction Coefficients

One of these tables was made for each concentration (Tables IV.1.1 – IV.1.5 for **2-1** and Tables IV.1.1 – IV.1.6 for **2-2**). Each concentration had 3 replicates made, and the averages and standard deviations were used to determine the extinction coefficients. This document assumes that each table is on a separate sheet within the same document, and that the sheets are labeled using the names of the Tables.

Table IV.1.1

	A	B	C	D	E	F	G	H	I
1	**Concentration 1.1**		**Concentration 1.2**		**Concentration 1.3**		**Average of Concentration 1**		
2	**λ (nm)**	**Abs.**	**λ (nm)**	**Abs.**	**λ (nm)**	**Abs.**	**λ (nm)**	**Abs.**	**Abs. s.d.**
3									

A3:A573 – Decreasing wavelength by 1 nm per cell, starting at 800 nm and ending at 230 nm, copied from the ASCII file of data.

B3:B573 – Absorbance data for each wavelength, copied from the ASCII file of data.

C3:C573 – Same as column A for replicate #2

D3:D573 – Same as column B for replicate #2

E3:E573 – Same as column A for replicate #3

F3:F573 – Same as column B for replicate #3

G3:G573 – “=A3” carried down throughout the entire column

H3:H573 – “=AVERAGE(B3,D3,F3)” carried down throughout the entire column

I3:I573 – “=STDEV.S(B3,D3,F3)” carried down throughout the entire column

The next table was made once, and it references each of the tables designed above (5 of them for **2-1** and 6 of them for **2-2).**

Table IV.2 (Designed for **2.1**)

	A	B	C	D	E	F	G	H
1	**λ (nm)**	**Concentration (M)**	**Abs.**	**Abs. s.d.**	**LINEST**		**Ext. Coeff. $(M^{-1}\ cm^{-1})$**	**Ext. Coeff. s.d. $(M^{-1}\ cm^{-1})$**
2								
3								
4								
5								
6								

A2 – Type the wavelength for which you wish to determine the extinction coefficient.

B2:B6 – Concentrations 1-5

C2:C6 – “=INDEX(‘Table IV.1.1’!$A$1:$I$573,MATCH($A$2,’Table IV.1.1’!$A$1:$A$573,0),COLUMN(H1))” carried down throughout the entire column (When the name of a Table is listed, change the formula to reference the correct tab for the desired concentration)

D2:D6 – “=INDEX(‘Table IV.1.1’!$A$1:$I$573,MATCH($A$2,’Table IV.1.1’!$A$1:$A$573,0),COLUMN(H1))” carried down throughout the entire column (When the name of a Table is listed, change the formula to reference the correct tab for the desired concentration)

E2:F6 – “{=LINEST(C2:C6,B2:B6,TRUE,TRUE)}” This is not carried down throughout the column, but you must have the entire region selected when you enter the formula. The {} brackets come from setting the formula to an array (CTRL+SHIFT+ENTER on PC’s version of Excel)

G2 – “=E2”

H2 – “=E3”

By typing a wavelength into the yellow box (A2), Table IV.2 calculates the linear regression of the data at the measured concentrations and provides the slope of the graph. If the path length of the cuvette is 1 cm, then G2 is the extinction coefficient with a standard deviation of H2.

Excel Process for Time Course Experiments in DS APmer

Each biological replicate will get its own table like the one shown below, where the final number represents the number of the biological replicate. These are sheets within a single document, each named after the table.

Table IV.3.1

	A	B	C	D	E	F	G	H	I	J	K
1	**Time (hr)**	**Time (min)**	**Area comp (1)**	**Area AP (1)**	**Area drug (1)**	**Area comp (2)**	**Area AP (2)**	**Area drug (2)**	**Area comp (3)**	**Area AP (3)**	**Area drug (3)**
2											

A2:___ – Input the timepoints that you wish to use for your experiment.

B2:___ – “=A2*60” carried down throughout the column

C2:___ – Input area data of Technical Replicate 1 for the complementary strand’s peak on the chromatogram

D2:___ – Input area data of Technical Replicate 1 for APmer’s peak on the chromatogram

E2:___ – Input area data of Technical Replicate 1 for the oxime conjugate strand’s peak on the chromatogram

F2:___ – Input area data of Technical Replicate 2 for the complementary strand’s peak on the chromatogram

G2:___ – Input area data of Technical Replicate 2 for APmer’s peak on the chromatogram

H2:___ – Input area data of Technical Replicate 2 for the oxime conjugate strand’s peak on the chromatogram

I2:___ – Input area data of Technical Replicate 3 for the complementary strand’s peak on the chromatogram

J2:___ – Input area data of Technical Replicate 3 for APmer’s peak on the chromatogram

K2:___ – Input area data of Technical Replicate 3 for the oxime conjugate strand’s peak on the chromatogram

Like the previous table, there is one of these tables for each biological replicate. And, each table is on a separate sheet within the document.

Table IV.4.1

	A	B	C	D	E	F	G	H
1	**Time (hr)**	**Time (min)**	**Area comp (avg)**	**Area comp (s.d.)**	**Area AP (avg)**	**Area AP (s.d.)**	**Area drug (avg)**	**Area drug (s.d.)**
2								

A2:___ – Input the timepoints that you wish to use for your experiment.

B2:___ – “=A2*60” carried down throughout the column

C2:___ – “=AVERAGE(‘Table IV.3.1’!C2:___,’Table IV.3.1’!F2:___,’Table IV.3.1’!I2:___)” carried down throughout the column

D2:___ – “=STDEV.S(‘Table IV.3.1’!C2:___,’Table IV.3.1’!F2:___,’Table IV.3.1’!I2:___)” carried down throughout the column

E2:___ – “=AVERAGE(‘Table IV.3.1’!D2:___,’Table IV.3.1’!G2:___,’Table IV.3.1’!J2:___)” carried down throughout the column

F2:___ – “=STDEV.S(‘Table IV.3.1’!D2:___,’Table IV.3.1’!G2:___,’Table IV.3.1’!J2:___)” carried down throughout the column

G2:___ – “=AVERAGE(‘Table IV.3.1’!E2:___,’Table IV.3.1’!H2:___,’Table IV.3.1’!K2:___)” carried down throughout the column

H2:___ – “=STDEV.S(‘Table IV.3.1’!E2:___,’Table IV.3.1’!H2:___,’Table IV.3.1’!k2:___)” carried down throughout the column

There is a new version of this table that is created for each biological replicate. The example below shows just a single biological replicate. The output of these data is a normalized ratio of reaction completion that can be plotted as a function of time. The error is propagated and provides the standard deviation of *technical replicates* (i.e., how precise is our manual integration).

Table IV.5.1

	A	B	C	D	E	F	G	H	I	J
1	**Time (hr)**	**Time (min)**	**Area/e comp**	**Area/e comp (s.d.)**	**Area/e AP**	**Area/e AP (s.d.)**	**Ratio AP Lost**	**Ratio AP Lost (s.d.)**	**Norm.**	**Norm. (s.d.)**
2										

A2:___ – Input the timepoints that you wish to use for your experiment.

B2:___ – “=A2*60” carried down throughout the column

C2:___ – “=‘Table IV.4.1’!C2/X” for the complementary strand’s extinction coefficient (“X”). This is carried down throughout the column

D2:___ – “=C2*(‘Table IV.4.1’!D2/‘Table IV.4.1’!C2)” carried down throughout the column

E2:___ – “=‘Table IV.4.1’!E2/Y” for APmer’s extinction coefficient (“Y”). This is carried down throughout the column

F2:___ – “=E2*(‘Table IV.4.1’!F2/‘Table IV.4.1’!E2)” carried down throughout the column

G2:___ – “=E2/C2” carried down throughout the column

H2:___ – “=G2*(SQRT(((D2/C2)^2)+((F2/E2)^2)))” carried down throughout the column

I2:___ – “=I2/$I$2” carried down throughout the column

J2:___ – “=I2*(SQRT(((H2/G2)^2)+(($H$2/$G$2)^2)))” carried down throughout the column

After finishing Tables IV.5.1 – IV.5.3 for the 3 biological replicates, the average normalized ratio of completion is determined. These data are converted to [APmer] data and graphed as a function of time. Column F of Table IV.6 is the data used for the error bars representing variation across biological replicates. Lastly, it is the data in column E of Table IV.6 that is uploaded to COPASI for kinetic modeling experiments.

Table IV.6

	A	B	C	D	E	F
1	**Average**					
2	**Time (hr)**	**Time (min)**	**Normalized Ratio**	**Normalized Ratio (s.d.)**	**[APmer] (µM)**	**[APmer] s.d. (µM)**
3						

A3:___ – Input the timepoints that you wish to use for your experiment.

B3:___ – "=A3*60" carried down throughout the column

C3:___ – "=AVERAGE('Table IV.5.1'!I2,'Table IV.5.2'!I2,'Talbe IV.5.3'!I2)" carried down throughout the column

D3:___ – "=STDEV.S('Table IV.5.1'!I2,'Table IV.5.2'!I2,'Talbe IV.5.3'!I2)" carried down throughout the column

E3:___ – Nanomoles of the t=0 hr HPLC aliquot subtracted from the total number of nanomoles at t=0 hr, divided by the "initial volume" after drug is added, multiplied by "C3," and adjusted to make sure the final answer is in µM. This is carried down throughout the column

F3:___ – "E3*(D3/C3)" carried down throughout the column

The practices outlined in this part of Appendix IV can be applied to other situations. For example, similar procedures can be used to determine the growth of the conjugate over time (like what is done in this dissertation).

There are slightly different procedures that one would use to employ Excel in automating the calculations for experiments done in SS APmer. Because there is no complementary strand, the normalized ratio of completion cannot be calculated. As such, full loop injection HPLC is used to get absolute concentrations. To do this, a calibration curve is needed. This process is not outlined in the Appendix since the process still is being worked out; as mentioned in the main text of the dissertation, the work presented for SS APmer was preliminary.

Additionally, similar processes were employed to calculate the results for the stability of the oxime conjugates over the course of approximately 6 days.